UNIVERSITÉ CÔTE D'AZUR

ÉCOLE DOCTORALE
SCIENCES FONDAMENTALES ET APPLIQUÉES

THÈSE DE DOCTORAT

Vers un laser à cascade quantique à base d'oxyde de zinc

Nolwenn LE BIAVAN

Centre de Recherche sur l'Hétéro-Epitaxie et ses Applications

Présentée en vue de l'obtention du grade de docteur en physique d'Université Côté d'Azur
Dirigée par : Jean-Michel Chauveau
Co-encadrée par : Maxime Hugues
Soutenue le : 13 novembre 2019

Devant le jury, composé de :
Jérôme Faist, Professeur, Institut d'Electronique Quantique, ETH Zurich
Marius Grundmann, Professeur, Université de Leipzig
Isabelle Sagnes, Directeur de Recherche, Centre de Nanosciences et Nanotechnologies, Université Paris Saclay
Roland Teissier, Directeur de Recherche, Institut d'Electronique et des Systèmes, Université de Montpellier
Michel Vincent, Directeur de Recherche, Centre de Mise en Forme des Matériaux (CEMEF), Mines ParisTech

Vers un laser à cascade quantique à base d'oxyde de zinc

Jury :

Président du jury

Isabelle Sagnes, Directeur de Recherche, Centre de Nanosciences et Nanotechnologies (C2N), Université Paris Saclay

Rapporteurs

Jérôme Faist, Professeur, Institute for Quantum Electronics, ETH Zurich
Roland Teissier, Directeur de Recherche, Institut d'Electronique et Systèmes (IES), University of Montpellier

Examinateurs

Marius Grundmann, Professeur, Université de Leipzig
Isabelle Sagnes, Directeur de Recherche, Centre de Nanosciences et Nanotechnologies (C2N), Université Paris Saclay
Michel Vincent, Directeur de Recherche, Centre de Mise en Forme des Matériaux (CEMEF), Mines ParisTech

Toward a zinc oxide based quantum cascade laser

Jury:

Président du jury

Isabelle Sagnes, Research Director, Centre for Nanosciences and Nanotechnologies (C2N), University Paris Saclay

Rapporteurs

Jérôme Faist, Professor, Institute for Quantum Electronics, ETH Zurich
Roland Teissier, Research Director, Institut d'Electronique et Systèmes (IES), University of Montpellier

Examinateurs

Marius Grundmann, Professor, University of Leipzig
Isabelle Sagnes, Research Director, Centre for Nanosciences and Nanotechnologies (C2N), University Paris Saclay
Michel Vincent, Research Director, Centre de Mise en Forme des Matériaux (CEMEF), Mines ParisTech

Vers un laser à cascade quantique à base d'oxyde de zinc

Le domaine Terahertz (THz), situé entre le domaine visible et micro-ondes, se révèle être très prometteur du point de vue des applications. Cependant, ce potentiel n'est pas totalement exploité à cause du manque de sources compactes capables de couvrir un part importante de cette gamme d'énergie. Les Lasers à Cascade Quantiques (LQC) sont considéré comme de bons candidats, car ils sont à la fois compacts et accordables. Mais dans le domaine THz, les LQCs existants souffrent d'une limite de leur température de fonctionnement ($\sim 200\,K$), ce qui restreint fortement le champ des applications possibles. Cela vient d'une propriété intrinsèque des matériaux qui sont communément utilisés pour concevoir les LQCs : l'énergie de phonon-LO. Par conséquent, une forte compétition entre la transition assistée par LO-phonon et la transition radiative à la base du LQC survient à température ambiante, ce qui réduit l'efficacité du processus laser. Pour contrer ce problème, nous avons choisi d'utiliser le ZnO, car son énergie de phonon-LO est deux fois plus large que celle des matériaux cités précédemment, ce qui permet au laser de fonctionner jusqu'à température ambiante.

Même si le ZnO et ses alliages ne sont pas nouveaux dans le domaine des semiconducteurs, ils sont complètement exotiques dans le domaine des LQCs. Les LQCs reposent sur des hétérostructures hautement périodiques, desquelles les propriétés clés du dispositif final découlent. Par conséquent, ces hétérostructures doivent être contrôlées à la monocouche atomique près et cette précision doit être reproductible sur une centaine de périodes, ce qui fait de la croissance des LQCs un véritable challenge. Cette thèses vise à relever ce défi en portant les hétérostructures ZnO/(Zn, Mg)O a un degré de contrôle ultime. Nous mettons en oeuvre la croissance d'hétérostructures ZnO/(Zn, Mg)O sur substrats ZnO à l'aide d'un nouveau bâti d'épitaxie par jets moléculaires et nous avons démontré qu'elles sont de qualité compatible avec celle requise par les LQCs. Ce premier pas nous a permis de démontrer l'observation des transitions intersousbandes dans le moyen infrarouge jusqu'à température ambiante, ainsi que leur couplage dans des structures à puits quantiques asymétriques. Des structures à cascade complètes ont aussi été crû et ont mené à la première démonstration d'un détecteur à cascade quantique à base de ZnO dans l'infrarouge à température ambiante. Des structures LQC ont aussi été réalisées et des expériences de microscopie électronique en transmission en mode balayage montrent un excellent contrôle des hétérostructures.

Mots clés : Laser à cascade quantique, oxyde de zinc, hétérostructure, épitaxie par jets moléculaires, transition intersousbande.

Toward a zinc oxide based quantum cascade laser

The Terahertz domain (THz), situated between the visible and microwave energy range, turns out to be very promissing in terms of applications. However its application potential is not fully used because of the lack for compact sources able to cover a large part of its energy range. Quantum Cascade Lasers (QCL) are good candidates for this purpose, because there are both compact and highly tunable. But in the THz range, the existing QCLs suffer from the operation temperature limitation ($\sim 200\,K$), which is very restricting from the application viewpoint. It comes from an intrinsic property of the materials commonly used to build QCLs: the LO-phonon energy. As a consequence a strong competition between the LO-phonon transition and the QCL radiative transition arise at room temperature, which hinder the lasing efficiency. To tackle this issue, we choose to make use of ZnO, because its LO-phonon energy is twice larger compared to the aforementioned materials, thus enabling to keep the lasing action efficient at room temperature.

Even if ZnO and its related alloys are not new in the field of semiconductor science, they are totally exotic for the QCL field. Indeed, QCL are build from highly periodic heterostructures, from which all the key device properties come from. Therefore, the heterostructure should be controlled at the monolayer scale and this precision should be reproducible on hundred of periods, which made QCL growth an indubitabble challenge. This thesis aims at take up this challenge by bringing ZnO/(Zn, Mg)O heterostructures to this ultime degree of control. We are growing ZnO/(Zn, Mg)O heterostructures on ZnO substrates with a new molecular beam epitaxy system and we demonstrate that the heterostructures quality matche the QCL material requirements. This first step enables us to demonstrate the observation of intersubband transitions in the mid-infrared range until room temperature, as well as their coupling within asymmetric quantum well structures. Complete cascade structures were also grown and lead to the first demonstration of a ZnO based Quantum Cascade Detector in the infrared range until room temperature. QCL structures were also grown and shows very good heterostructure control as stated by scanning transmission electron microscopy experiments.

Key words: Quantum cascade laser, zinc oxide, heterostructure, molecular beam epitaxy, intersubband transition.

Acknowledgment

This work may not have been possible without the involvment of many people that I would like to thank here.

- My thesis directors Jean-Michel Chauveau and Maxime Hugues. Without them nothing of this work would have been possible. I appreciated that you immediately believe in me such that I had freedom to make my own choice concerning this work. I am very grateful to the many opportunities you gave me to present my work during conferences and workshops.
- Jury members: Prof. Dr. Jérôme Faist, Prof. Dr. Marius Grundmann, HDR Dr. Isabelle Sagnes, HDR Dr. Roland Teissier and HDR Dr. Michel Vincent who kindly accepted to evaluate this work.
- The CRHEA former lab director Jean-Yves Duboz for supporting my application at the doctoral school.
- Prof. Dr. Marius Grundmann for his help and for the nice discussions about mechanical properties of (Zn, Mg)O.
- The partners of the Zoterac project for sharing their experience and ideas during meeting projects and conferences. It was very enriching to work in such an environnment and this work would not have been achieved without these collaborations.
- My engineer collegues of CRHEA for the time they spend teaching me various characterisation techniques and to always be available when I had questions.
- Our administrative and informatics staff: so many things would have been much more difficult without your kind help.
- Denis Lefebvre, member of the CRHEA's Zoterac team for his every day work at the ZOE molecular beam epitaxy growing samples but also for taking the time to explain me technical details. It has been a real pleasure to work every day with you on this project.
- IMRA Europe and CNME in Madrid for giving access to their transmission electron microscope facilities.
- Prof. Dr. Andreas Wieck and HDR Dr. Nathan Jukam for invited me to spend one month at RUB Bochum to discover terahertz time domain spectrocopy.
- Prof. Borge Vinter for having kindly accepted to proofread this manuscript.
- Prof. Dr. Sergio Di Matteo for being an incredible inspiring professor during my Bachelor studies at Rennes 1 University.
- Dr. Almudena Torres-Pardo for her determination to look into atomic details at the transmission electron microscope. I always appreciate to work with you not only because you were able to get the best of our samples, but also because you are the type of person that everyone would like to work with.

- All the PhD students at CRHEA for the nice moments we share in the office and also outside.
- PhD students from Bochum: Charlotte, Carsten, Julian, Carlos, and Marcel for the nice atmosphere during my stay in Bochum and for the nice moments around a Glühwein glass at the Weihnachtsmarkt. I am also very grateful to Natalie, who took a lot of time to show me how is working the terahertz time domain spectroscopy setup and gives me insights about cleaning room processes.
- Stefanie Tecklenburg from the Max Planck Institute in Düsseldorf for the pleasant time at Lac de Prals and at Düsseldorf Weihnachtsmarkt.
- Dr. Pavel Kuzhir for his kindness and involvment concerning my teaching experience at the engineer school Polytech'Nice.
- My collegues Patrice Camelin and François Mondain for the nice moments we spent together teaching in practical courses at Polytech'Nice.
- Laurie Chiara, Ugo Bellagamba and Franck Rainaut, our mentors during "Ma Thèse en 180 secondes" for their precious advice and their entire involvment so that we were able to give the best of our research to the public. For sure I will never forget this experience as well as my text!
- Charlotte Ménager for her complete support when I had not so nice moments in the lab, and for her frienship since our Master degree. I would like also to thank you for having pushed me to participate to "Ma Thèse en 180 secondes", and for the many tips you gave me.
- My parents and my aunt for their unfailing support since always, no matter what the choices I made. If my parents were not there every evening, taking care that my homework was properly done when I was a child, I would probably not having such success in my studies.
- Patrice Camelin: again you! If you were not here every evening to distract me from my daily life lab problems, I would not be able to fight everyday for this thesis to be completed.

Contents

Nomenclature

AFM Atomic Force Microscopy

C-V Current Voltage measurement

CL Cathodoluminescence

DME Domain Matching Epitaxy

EDX Energy Dispersive X–ray spectroscopy

FWHM Full Width at Half Maximum

GaAs Gallium Arsenide

GaN Gallium Nitride

Ge Germanium

I-V Current-Voltage

ICL Interband Cascade Laser

InAs Indium Arsenide

InSb Indium Antimonide

IQE Internal Quantum Efficiency

IR Infrared

ISB Intersubband

ISBT Intersubband transition

J-V Current density - Voltage

J-V Current density - Voltage

LA Longitudinal Acoustic

LME Lattice Matching Epitaxy

MBE Molecular Beam Epitaxy

MgO Magnesium Oxide

MIS Metal - Insulator - Semiconductor

ML Monolayer

MOVPE Metallorganic Vapor Phase Epitaxy

MQWs Mutil Quantum Wells

MSP Multisubband Plasmons

nid Non intentionaly doped

PC Photoconductive

PL Photoluminescence

QCD Quantum Cascade Detector

QCL Quantum Cascade Laser

QSE Quantum Stark Effect

QW Quantum Well

QWIP Quantum Well Infrared Photodetector

RHEED Reflection High Energy Electron Diffraction

RMS Root Mean Square

RSM Reciprocal Space Map

RT Room Temperature

RTA Rapid Thermal Annealing

SC Semiconductor

SEM Scanning Electron Microscopy

SIMS Secondary Ion Mass Spectroscopy

STEM-HAADF Scanning Transmission Electron Microscopy - High Angle Annular Dark Field

TDS Time Domain Spectroscopy

TEM Transmission Electron Microscopy

TES Two Electron Satellites

TO-phonon Transverse Optic phonon

XRR X-Ray Reflectivity

ZnO Zinc Oxide

ZOTERAC Zinc Oxide for Terahertz Cascade

List of Figures

List of Tables

Part I.

Introduction

This introduction is organized as answers to the following questions:

1. What is the THz domain? Why is this domain interesting from a scientific and application point of view? What are the THz sources that already exist? What are the current limitations to deploying the THz domain in our daily life through mainstream applications? How can we tackle them?

2. How does a QCL (Quantum Cascade Laser) work? What can be the different approaches implemented for QCL design? What are the crucial parameters? What exists already? What are the particularities and/or difficulties to go toward the THz range? And again, how can we overcome them?

3. Why can a ZnO based QCL be a good candidate to tackle the problem of operating temperature for a THz QCL? What are the alternative material systems to ZnO?

4. What are the typical properties of ZnO? What are the possibilities in order to create ZnO based heterostructures?

0.1. The Terahertz domain

Applications

The THz domain lies between the infrared domain for the photonic part, and the microwave domain for the electronic part as illustrated in figure 0.1. Alternative names for this part of the electromagnetic spectrum that can be encountered are "far infrared", "submillimeter waves" or "T-rays". Its common name of "THz radiations" comes form the fact that the typical frequency order of magnitude is the THz, more precisely between 0.3 to $30\,THz$. It is equivalent to a wavelength range between 1000 and $10\,\mu m$ and to an energy range of 1.25 and $125\,meV$. These boundaries can slightly change from one author to another because THz domain does not possess a standard definition.

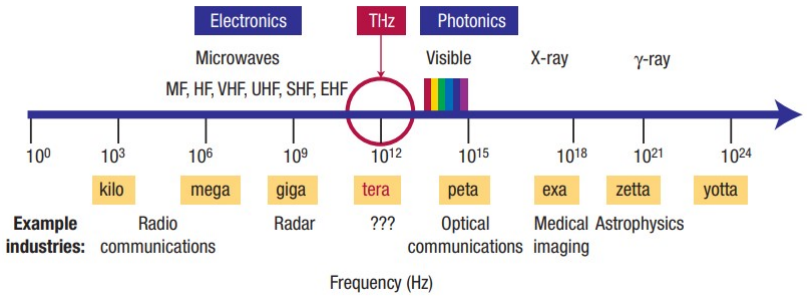

Figure 0.1.: THz domain within other parts of the electromagnetic spectrum. *Reprinted by permission from Springer Nature Customer Service Centre GmbH: Springer Nature, Nature Materials, (Ferguson & Zhang, 2002), Copyright 2002*

THz radiations have noticeable properties when interacting with various materials, which has rapidly led researchers to imagine numerous applications using this frequency range. Among them is the strong absorption of THz radiations by water because of the strong polarity of water molecules.

Figure 0.2 provides an illustration of this property: the left part of the image shows a THz constrast that enhances the leaf veins due to their higher water content (in blue in figure 0.2). This property can be used in medicine to distinguish tissues according to their water content (Han *et al.*, 2000).

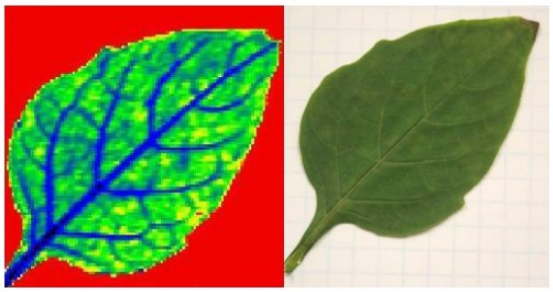

Figure 0.2.: THz image (left) and optical image of a fresh leaf. The contrast on the THz image is due to the difference of water content in different leaf parts. *(Du* et al.*, 2009), URL, © IOP Publishing. Reproduced with permission. All rights reserved.*

Promissing medical applications are possible like tumor detection using THz imaging (Löffler *et al.*, 2001). Whereas THz radiations are completly reflected by metals, they are easily transmitted through non-polar dielectric as plastic, clothes, paper and many others. This explains why THz radiation through imaging systems would be very efficient for security control, in order to detect hidden metallic weapons for instance (Federici *et al.*, 2005) as illustrated in figure 0.3 or in industry for quality control. It is even more relevant since many of the above-mentioned materials are not transparent at optical frequencies and give a poor contrast when using X-Rays (Ferguson & Zhang, 2002).

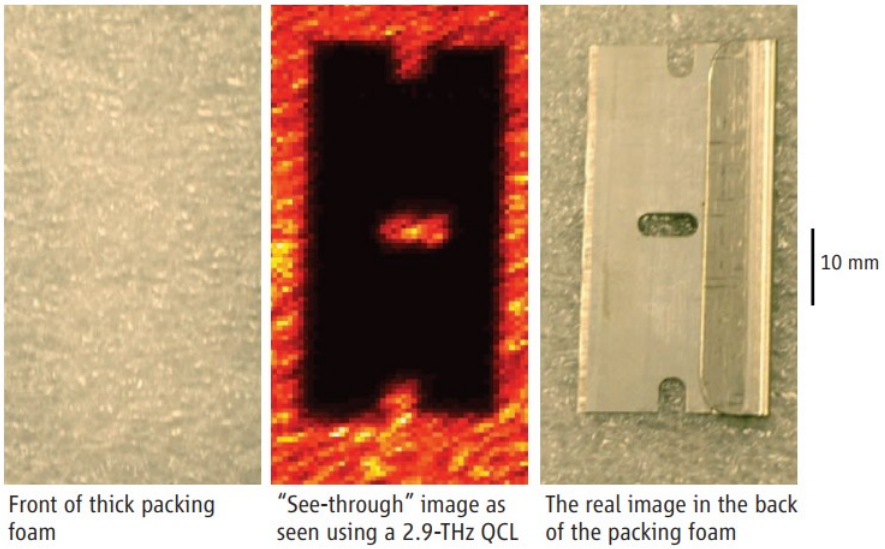

Figure 0.3.: Demonstration of the use of THz imaging for hidden weapons detection. From left to right: picture of the packing foam, THz image using a 2.9 THz quantum cascade laser (QCL), image of the hidden rasor blade from the back of the packing foam. *From (Lee & Wanke, 2007). Reprinted with permission from AAAS.*

A large proportion of molecules have their rotational and/or vibrationnal modes lying in THz range, which can be viewed as a fingerprint to identify them. It opens wide perspectives for drug detection and identification (Kawase *et al.*, 2003), as well as medicine quality evaluation in pharmaceutical

industry (Taday, 2004). For more details about the applications in the THz domain, one could refer for instance to the roadmap in the following review article (Tonouchi, 2007).

THz sources

Despite a lot of research dedicated to THz for several years, this field has difficulties to take off in terms of mainstream applications. The THz domain is often referred to the "THz gap" because of the lack of low cost, compact and RT (Room Temperature) operating THz sources and detectors. For detectors as well as a more complete description of THz sources, the reader can turn to the following books and reviews: (Bründermann *et al.*, 2012; Ferguson & Zhang, 2002; Lee, 2009; Siegel, 2002; Tonouchi, 2007).

We have seen that the THz domain is sandwiched between the microwave and the infrared frequency domains. In these domains, waves are generated by electronic and optical approaches respectively. For the electronic part, microwaves are converted to THz waves by increasing the frequency. However, this frequency conversion leads to a low output power and/or low conversion efficiency. For the optical part, the idea is to start from higher frequencies and to convert them to THz frequencies by optical means. We see that some of them can be suitable for mainstream applications.

Electronic approaches

Frequency multiplication starts from a microwave signal, typically in the range of $10-100\,GHz$, generated by an oscillator. This microwave signal is then converted into THz waves thanks to Schottky diodes through their non-linearities (Maestrini *et al.*, 2008; Porterfield, 2007). The drawback of this method is the reduced output power when it goes further into the THz range.

Some electronic approaches take advantage of accelerated charges that emit radiations as for **transient photoconductive switching**, **photomixing**, and **free electron laser** (Lee, 2009). The **transient photoconductive switching** method is based on the properties of a photoconductive antenna (Mourou *et al.*, 1981). The antenna is fabricated using a bulk SC on which two electrodes are deposited. A constant bias is applied to the antenna using the electrodes and a femtosecond laser is used to send short photon pulses on the antenna. If the photon energy is higher than the semiconductor bandgap, it creates an electron-hole pair which is accelerated towards one of the electrodes thanks to the applied bias. The acceleration of the charges produces an electric field whose frequency lies in the THz range. For one femtosecond laser pulse that impinges on the PC (Photoconductive) antenna, a single broad THz pulse is emitted. These antennae are widely used in THz Time Domain Spectrocopy (TDS).

Photomixing makes also use of PC antennae, and the mecanism at the root of the THz generation is the same as for the transient photoconductive switching. The difference is that two lasers with different frequencies are required to create a beating (Verghese *et al.*, 1997). This beating is sent to a PC antenna which is converted into THz radiations. But instead of a broad pulse as for

transient photoconductive switching, the outcome is a continuous THz wave thanks to the repetitive beat pattern in input.

The **free electron laser** approach is realized in a synchrotron environment because it needs high acceleration values (Williams, 2002). Bunches of electrons that are accelerated emit a radiation whose emitted wavelength depends on the acceleration process. This explains why free electron lasers are probably the most tunable lasers. Indeed they can cover from the soft-X-Rays to the microwaves, from 10^{-4} to $10^{6}\,THz$ (Bründermann *et al.*, 2012). Thus the whole THz region can be covered with a high output power. But the synchrotron environment makes it impossible to use for mainstream applications.

Optical approaches

On the optical side, some approaches use non-linear crystals as a THz converter. This is the case in **optical rectification** and **difference frequency generation**. In **optical rectification**, or generation (Bass *et al.*, 1962), a femtosecond laser pulse impinges on a non-linear crystal and converts the incoming pulse into THz emission.

For **difference frequency generation**, two lasers with different frequencies ω_1 and ω_2 are sent to a non-linear crystal which converts the incoming waves into a wave of frequency $\omega_1 - \omega_2$. The advantage of this technique is its flexibility since the output frequency can be changed by shifting one of the two lasers' frequency. However, they suffer from a low conversion efficiency because they are based on a high order optical phenomenon due to the non-linear crystal. This limitation tends to lower the output power of the THz wave (Ferguson & Zhang, 2002).

Another optical method to generate THz waves is to use **gas lasers**. Two gas lasers are needed: the first one is used a an optical pump to trigger the population inversion within the second laser. In general a CO_2 laser emitting at a wavelength of $\sim 10\,\mu m$ is used as the optical pump. The radiative transition is based on the different rotational states of the gas molecules. In order to target a specific wavelength, either different sets of rotational transitions can be used while keeping the same gas, or the gas nature of the second laser can be changed. The accessible frequencies are ranging from 0.2 to $8\,THz$ (Lee, 2009).

Solid laser sources operating in the THz range also exist: **the p-Ge (germanium) laser** was the first laser which emits in this range and was invented in the years 1980 (Andronov *et al.*, 1982, 1985). It is made out of p-doped bulk Ge and is electrically pumped. The radiative transition lies between Landau levels that arise from the application of a strong magnetic field ($0.2 - 6\,T$). Holes are pumped until they reach the bottom of the heavy hole valence band. Thanks to a crossed electric and magnetic field, holes are transfered from the light hole to the heavy hole band and undergo a radiative transition in the THz range. This complex laser has the advantage to be accordable in the range between $1.5 - 4.3\,THz$. But it has two main drawbacks: a high magnetic field must be applied as well as cryogenic conditions ($\sim 40\,K$), which makes this laser not suitable for mainstream

applications (Bründermann *et al.*, 2012).

The **interband cascade laser** (ICL) is also in the family of solid laser sources. However, it relies on the concept of quantum engineering. This concept states that the main laser properties are determined by the manner the heterostructure is build. The radiative transition is achieved by the radiative recombinaison of an electron of the conduction band and a hole of the valence band. The concept of ICL was proposed in 1995 Yang (1995). The first continuous and RT operation ICL was demonstrated in 2008 and emits at $80\,THz$ Kim *et al.* (2008). After this demonstration in the IR range, the ICL research tried to shift toward longer wavelength, ie THz. The shortest emission frequency achieved is $27\,THz$ but this device is limited to $\sim 100\,K$ in continuous mode operation Li *et al.* (2015). The difficulties that ICLs encounter when going toward the THz are related to the bandgap limitations, the increase of free carrier absorption loss as well as Auger recombinaison Li *et al.* (2015).

The **quantum cascade laser** (QCL), also relies on the concept of quantum engineering. Its operation as well as its history will be presented in detail in the next section. Due to its tunability, the high output power achievable and its compactness, the QCL is a very promissing candidate to approach the whole THz range.

Table 0.1 summarizes the THz sources described above with their main advantages and limitations.

THz source	Advantages	Disadvantages / Limitations
Frequency multiplication	Continuous emission, compact	Reduced output power when increasing the frequency ($10 - 100\,\mu W$ at $1\,THz$)
Transient photoconductive switching	Compact	Pulsed emission, material dependant
Photomixing	Continuous emission, compact	Low output power ($\sim \mu W$ range, material limitation) due to a low conversion efficiency ($\sim 10^{-5} - 10^{-6}$)
Free electron laser	High tunability ($0.88 - 100\,THz$) and high peak output power ($\sim MW$ range)	Not compact (synchrotron environment), pulsed emission
Optical rectification	Tunability	Low conversion efficiency (second order optical phenomenon), pulsed emission
Difference frequency generation	Tunability, continuous emission	Low conversion efficiency ($\sim 10^{-4}$)
Gas laser	High output power ($10 - 100\,mW$)	Discrete frequencies between 0.2 and $8\,THz$ achievable
p-Ge laser	Output power in the mW range	Need a magnetic field ($0.2 - 6\,T$), limited tunability thanks to the electric and magnetic fields ($1 - 4\,THz$), cryogenic condition ($\sim 40\,K$)
ICL	Tunability, continuous emission, compact	Long wavelength emission difficult (material issue)
QCL	Tunability, continous emission, compact, output power $\geq 10\,mW$ at $1\,THz$	Temperature operation limited to $210\,K$. Need for cooling.

Table 0.1.: Advantages and disadvantages of a few THz sources.

0.2. Quantum Cascade Laser

In this part I detail physical principles on which a QCL is based and I go through the 3 design approaches that can be implemented. After that, I switch from the material point of view. We see that even if the QCL interest lies in the fact that the architecture is more important than the SCs used, some clue material parameters need to be taken into account to optimize the design. I describe few of them and explain how they can impact the device performances.

Then I review the key elements of the QCL history and and how QCLs have evolved to go towards the THz range. I put a special emphasis on the comparison between an IR QCL and a THz one to

highlight the specificities and difficulties related to the translation of QCL from the IR to the THz range. It leads me to the final part in which I expose why ZnO is a good candidate to tackle the main current limitation of THz QCL.

0.2.1. How does it work?

A QCL is an unipolar device, meaning that only one type of carrier is involved. It needs two main physical phenomena to operate: ISBT (intersubband transition) and tunnel transport. They take place within superlattices in which the single building block is called a QW (Quantum Well). To build a QW, two SC with dictinct bandgaps are required. The SC with the lower bandgap is referred to the well material and the SC with the higher one as the barrier material. When one layer of QW material is sandwiched between two layers of barrier materials, the energy within the QW is lower than in the surround barriers, which allow carriers to be trapped inside the QW. In addition, quantum confinement arises inside the QW and creates discrete energy levels. When carriers are trapped inside a QW, they can only take energy values according to these discrete energy levels (Paiella, 2006; Rosencher & Vinter, 2002). The discrete levels belong to the same band and are called subband energy levels.

Intersubband transition

The ISBT takes place when a carrier - let us say an electron - changes from one subband level to another within the same band (see figure 0.4). If the electron loses energy, as represented in figure 0.4, it emits a photon whose energy is the energy difference between the subbands levels $e_2 - e_1$. Thus the photon energy is governed by the energy separation between the subband levels considered. These subband levels come from the quantum confinement, ie how the QW is built. Thus it makes devices based on ISBT very tunable through mainly the QW thickness and the barrier height (linked to the barrier bandoffset).

Before the QCL invention, most of SC lasers were based on interband transitions, ie from the radiative recombinaison of a hole within the valence band and an electron within the conduction band (figure 0.4). In this case the emission wavelength is mainly determined by the SC bandgap, which is an intrinsic material property. Here lies precisely the strength of QCL compared to interband SC lasers for which the THz range is impossible to reach. Since intersubband transition is used, the emission wavelength depends mainly on the QW architecture rather than on the SC used to create this architecture (figure 0.4).

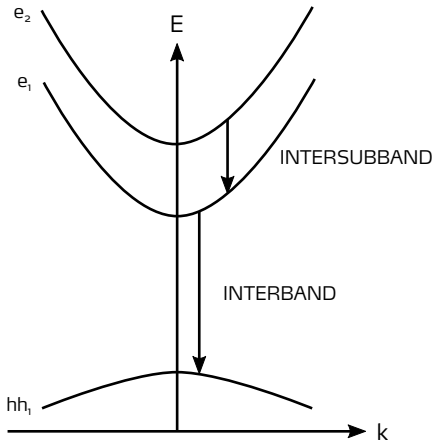

Figure 0.4.: Schematic of interband and intersubband transitions.

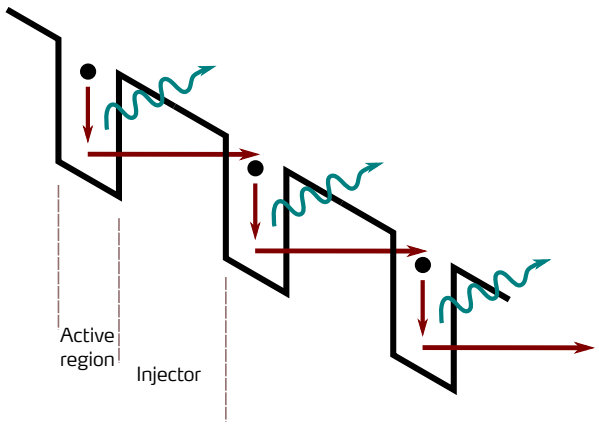

Figure 0.5.: Schematic of the QCL operation principle.

Tunnel transport

In a QCL, many identical active regions - where an electron undergoes a ISBT and releases a photon - are repeated. The overall structure is under bias in order to make possible the use of one electron to ideally produce as many photons as the number of periods. To do so, a transport mecanism from one active region to the next one is required. This transport is obtained by the tunnel effect within a series of coupled MQWs called the injector. The tunnel effect appears when the barrier which separates two adjacent QWs is thin (typically few ML), allowing electron to go through it.

Figure 0.5 shows a simplified view, which displays the operation principle of a QCL with the alternance of the two zones: the active region where the ISBT takes place, and the tunnel transport in the injector region. If we follow the electron path from the top to the bottom of the structure, we can clearly see the cascade appear.

QCL history

The first studies on the use of superlattices, referred as coupled MQWs, to tailor quantum effects such as ISBT or tunnel transport were done in the 1970s by (Esaki & Tsu, 1970), where they studied the properties of superlattices to trigger radiative transitions. They were followed rapidly by (Kazarinov & Suris, 1971), who studied theoretically the electronic properties of such superlattices. They found out that in case of a resonant tunnel transfert from one QW to the next one, a negative differential resistance should be observed in the I-V(Current-Voltage) characteristics. Moreover, they propose a first design principle for an emitter based on superlattices, which is very similar to the actual QCL working principle.

In 1985 the first absorption due to an ISBT within a QW is observed using GaAs QWs (West & Eglash, 1985). At this time, the authors did not refer to ISBT but to QWEST for "Quantum Well Envelope State Transition", which are spectrally peaked contrary to interband transitions (Rosencher & Vinter, 2002). In 1986, (Capasso *et al.*, 1986) bring a new notion in the field of tunnel effect by clarifying the concept of the resonant tunnel effect.

The first QCL laser was realized in 1994 and was made from GaInAs/AlInAs layers grown by MBE

(Faist *et al.*, 1994). It emitted in the IR range at $71\,THz$ in pulsed mode up to $90\,K$. After this first demonstration, researchers put at lot of efforts to go towards QCLs that are able to work continuously and at RT. The first RT QCL laser was demonstrated two years later (Faist *et al.*, 1996), as well as the first continuous wave operation (Sirtori *et al.*, 1996). Few years later, the first continuous wave QCL operating at RT was demonstrated (Beck *et al.*, 2002). As the first QCL, it was based on GaInAs/AlInAs heterostructures with an optical power of $3\,mW$ at $312\,K$. In parallel to this race for continuous wave and RT operation, there was both an improvement of the output power as well as an extension of the emission frequency in the IR range. For the output power, $1\,W$ has been obtained for QCLs emitting in the range between 19 to $75\,THz$ in the same period when the continuous wave and RT operation was demonstrated (Faist *et al.*, 2002; Sirtori *et al.*, 2002). Concerning the emission range, continuous wave and RT operation together were demonstrated between 33 and $62\,THz$ (Beck *et al.*, 2002; Evans *et al.*, 2004). Strenghened by all these demonstrations, QCLs in the IR range were quickly commercialized and some research groups have orientated their research to adapt QCL to industrial production. For instance, there are demonstrations of QCL grown on Si substrate, because Si is the reference material for large scale process (Borak, 2005; Nguyen-Van *et al.*, 2018). In the same spirit, QCLs grown by MOVPE were demonstrated and show very encouraging results for the large scale production (Roberts *et al.*, 2003; Diehl *et al.*, 2006; Sirigu *et al.*, 2008). QCL history has taken a turning point in 2002, when the first THz QCL was demonstrated (Köhler *et al.*, 2002). GaAs/AlGaAs heterostructures were implemented in a "chirped superlattice" design and pulsed emission at $4.4\,THz$ up to $50\,K$ was observed. Since then, a lot of efforts were oriented in this direction, partly because of the numerous applications linked to the THz domain.

Designs

The occurence of radiative transition in a device is not sufficient to call it a laser: a population inversion is required. It means that the lower energy level involved in the ISBT should be ideally empty such that electrons on the higher energy level continue to undergo an ISBT. A fast transfer mecanism should be involved to quickly remove electrons from the lower subband to another one to keep the ISBT going. This is a key point to consider when optimizing a QCL design.

Three main design types exist to make carriers cascade. The first one is called "chirped superlattices" and is based on transitions between two minibands (see grey areas in figure 0.6). A miniband is the result of several QWs separated by a thin barrier so that they are coupled. When each of the single QWs becomes coupled, they form what is called a miniband because energy states are very close. For the chirped superlattice design, there are two minibands separated by a minigap and the radiative transition takes place between the lower energy level of the upper miniband and the upper energy level of the lower miniband. This configuration is very similar to band to band transition but with minibands (Williams, 2007). The advantage of this design is that the miniband used for the radiative transition gives rise to a large dipole matrix, which is an advantage to maximize the laser gain (Tredicucci *et al.*, 1998). After the radiative transition, an efficient population inversion takes place inside the lower miniband by scattering in order to transport the electron to the bottom of the miniband.

The second approach called "bound to continuum" is derived from the "chirped superlattice design"

(figure 0.6). The difference lies in the upper radiative state position. Here, it lies in the minigap. This upper state can be seen as a defect state within the minigap. The lower radiative state, as well as the depopulation process inside the lower miniband stay the same as for the "chirped superlattice" design. Compared to "chirped superlattice", "bound to continuum" shows a lower oscillator strength between the energy levels involved in the radiative transition because the transition is diagonal. This disadvantage is compensated by a more selective injection in the upper radiative state, because it lies within the minigap (Paiella, 2006; Williams, 2007).

While "chirped superlattice" and "bound to continuum" are very similar because they are based on minibands, the third design is totally different. It is called the "resonant phonon" approach because the lower radiative state depopulation is obtained by a transition involving an optical phonon (figure 0.6). The ISBT takes place between the energy levels labelled 2 and 1 in figure 0.6. The fast depopulation takes place between the energy level 1 and of the injector involving the phonon. This transition is named 'resonant' because the energy separation is exactly the LO-phonon energy. This resonant depopulation is very fast (∼1 ps), but at the detriment of the ISBT oscillator strength because of the lack of miniband. It allows to reduce the active region period nearly by a factor of two (Williams, 2007), which is a advantage to avoid stress relaxation from mismatched layers.

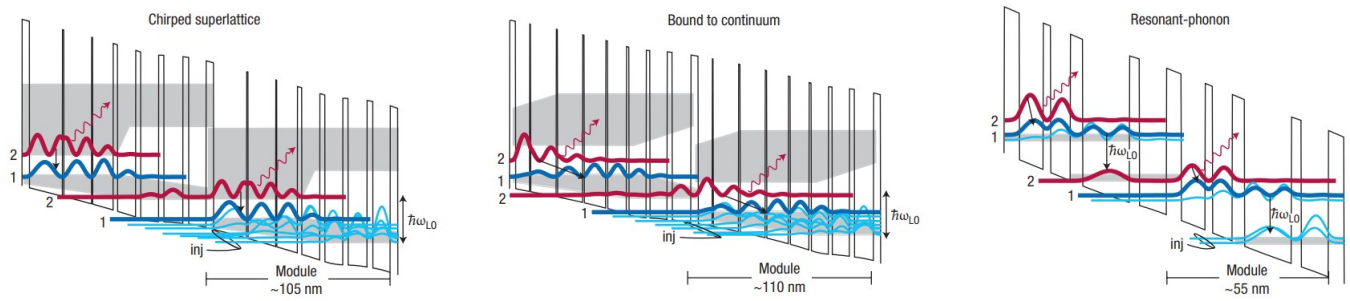

Figure 0.6.: Schematic of the the design approaches for the QCL active region. From right to left: chirped superlattice, bound to continuum and resonant phonon design. Large grey area show the minibands. *Reprinted by permission from Springer Nature Customer Service Centre GmbH: Springer Nature, Nature Photonics (Williams, 2007), Copyright (2007).*

Key material parameters

There are still some material parameters that should be considered for the QCL design. In the book (Paiella, 2006), the authors present a detailed argumentation about the influence of material parameters on different aspects of the QCL performances. The most influential material parameters are the electron effective mass m_e^* , the barrier bandoffset ΔE_c (or ΔE_v, if the relevant carriers are holes) and the interface roughness which all have an impact on the optical gain. The impact of the material parameters on the waveguide performances are also considered.

Theoretically, it has been found that the optical gain coefficient of a QCL is proportional to $(m_e^*)^{-3/2}$ (Paiella, 2006). To maximize the optical gain, we should think of a material system with the lower effective mass. This dependence of the optical gain with respect to the effective mass has

been validated experimentaly in (Benveniste *et al.*, 2008). In this paper, the authors have compared three quantum cascade electroluminescent devices, emitting at $30\,THz$, with similar designs in order to capture the influence of the material parameters on the lasers performances. The materials systems investigated were GaAs/AlGaAs, GaInAs/AlInAs and InAs/AlSb. They find that the optical quantum efficiency evolution deduced from light-current characteristics is in agreement with what was foreseen theoretically.

The influence of the barrier bandoffset is a key because an adequate band offset should be high enough to avoid the electron to thermally escape from the QWs to the continuum. On the other hand, it has a great impact on the injector transparency, meaning how easy it is for an electron to travel through the barriers. Typically a very high bandoffset reduces this barrier transparency as it can be understood from the equations 0.1 and 0.2.

$$k_B = \sqrt{\frac{2m_B^*(E)}{\hbar^2}(\Delta E_c - E)} \tag{0.1}$$

$$T_B \approx \exp(-2k_B t_B) \tag{0.2}$$

Where k_B represents how much the electron wavefunction is attenuated in the barrier for a given energy E. Note that here again, the electron effective mass plays a role. T_B is the transmission coefficient of the electron wavefunction throught a barrier of thickness t_B. It is worth noting that the barrier transparency scales with an exponential function which depends on the barrier bandoffset ΔE_c, which is far from being negligible.

To compensate this lack of transparency coming from the barrier height, the method consists in reducing the barrier thickness. Typically, barrier thicknesses of few monolayers are required. Depending on the material used, issues about alloy inhomogeneity can arise (most of the time barriers are made with ternary alloys). For instance, a shift of one ML thickness on a thin barrier has a larger impact on the intersubband position levels compared to a thicker barrier. Thus a slight thickness deviation can cause a large shift in the intersubband transition energy. If this thickness shift is not reproducible across the whole heterostructure, this leads to a broadening of the above-mentioned transitions.

Rough interfaces scatter electrons elastically when they encounter them. The reasons behind interface roughening are various, and are material and growth dependent (Paiella, 2006). It can be an alloy fluctuation during the growth, which is the case for In (Indium) that segregates (Offermans *et al.*, 2003). Interface roughness is known to broaden ISBT as well as optical gain curves (Flores & Albo, 2017; Leuliet *et al.*, 2006). Moreover, it can lead to a deep change of the electron dynamics. Indeed the electron scattering at rough interfaces changes the electron lifetime within the heterostructure. In (Flores & Albo, 2017), authors studied theoretically the impact of such roughness on performances of GaAs/AlGaAs THz QCLs and suggested that it becomes important when the GaAs QW thickness is less than 3 nm thick. The impact of interface roughness on the optical gain was experimentally proven in (Leuliet *et al.*, 2006), the authors used spectrocopy in a magnetic field

to decorrelate the impact of the inelastic scaterring due to LO-phonon and of the elastic scaterring due to interface roughness. They found that the latter mecanism is dominant at low temperature in the case of GaAs/AlGaAs QCL.

The last important parameter to consider in QCL performances is the waveguide confinement or the overlap factor Γ. This is not the only parameter to take into account to completely describe a waveguide performance (see (Williams, 2007; Paiella, 2006) for instance), but this is the one which is linked to the QCL active region, thus to the material which is used to build it. In fact to increase the waveguide performances through the confinement factor Γ, one should maximize it. One way is to increase the number of periods of the QCL active region to increase the overlap with the mode and the active region (Paiella, 2006). Depending on the material system, the increase of the total active region thickness due to the increased number of periods can lead to worsen the material structural quality. Indeed, growing stacks of crystal with slightly different lattice parameters leads to a lattice mismatch which is at the origin of a stress within the layers. When the total layer thickness increases, the stress accumulates, until a critical thickness at which the layers cannot accomodate it anymore. It ends up with a stress release which can take various forms according to the material and its orientation: appearance of cracks and dislocations for instance. They are highly detrimental to the QCL operation. Thus such mechanical parameters have to be taken into account in order to maximize the overlap between the waveguide modes and the active region without deteriorating the material quality.

0.2.2. Terahertz Quantum Cascade Lasers

In this part, we focus on the QCL in the THz range. In particular, I go through the main realizations in this field since the first demonstration in 2002. I point out what are the main differences that arise when working on THz QCL compared to its IR counterpart. This last review helps to understand what are the singular difficulties this field faces at the moment, which was not the case for IR QCL.

After the first demonstration of the THz QCL in 2002, both the wavelength range and the operating temperature were quickly extended. In 2005, (Worrall *et al.*, 2006) demonstrated an AlGaAs/GaAs QCL emitting at $2\,THz$, which represents a factor of two on the frequency compared to the first THz QCL ($4.5\,THz$). Great improvements on the operation temperature have been achieved during this year too, with a pulsed mode QCL emitting up to $164\,K$ (Williams *et al.*, 2005), and up to $117\,K$ in continuous mode. During the following years the operation temperature was extended in the range of $160 - 190\,K$, which enables devices to be cooled with liquid nitrogen (typically $77\,K$) (Belkin *et al.*, 2008; Kumar *et al.*, 2009, 2011). The present record for operation temperature is owned by Bosco *et al.* (2019), where the authors demonstrate a $4\,THz$ QCL working up to $210.5\,K$, which makes Peltier cooling possible. Figure 0.7 illustrates the difficulty faced by researchers to extend the operation temperature for QCL in the THz range whereas in the IR, continuous devices up to $350\,K$ are achieved. Here lies the first main difference between IR and THz QCL. Whereas for IR QCL, the extension of the operation temperature took only two years compared to the first demonstration of IR QCL in 1994, there is still no RT THz QCL after its first demonstration in 2002 (Belkin *et al.*, 2009).

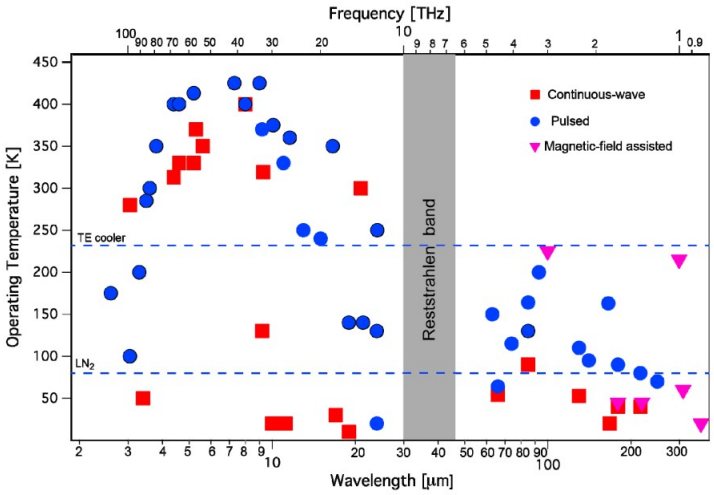

Figure 0.7.: Operation temperature of various QCL devices as a function of their emitting wavelength and frequency. *(Vitiello* et al.*, 2015), © figure used under the Creative Commons Attribution 4.0 International Licence. To view a copy of this licence, visit: URL*

We can observe that in the range between 1 to $12\,THz$, the operation temperature is stuck around $200\,K$, except for the devices assisted by a magnetic field, that can reach nearly $230\,K$.

The mecanism responsible for the lack of lasing action at RT is schematized in figure 0.8. When the temperature rises, the electrons in the high energy subband level have an additional energy given by the temperature k_BT, with k_B the Boltzman constant and T the temperature (ie $25\,meV$ at $300\,K$, to compare for instance to the LO-phonon energy of GaAs: $36\,meV$). Thus they are able to increase their energies within the higher subband. These electrons go from the high energy subband to the lower subband by emitting an LO-phonon. In that case, this transition involving the LO-phonon is in strong competition with the ISBT which is the essential for the QCL (Bellotti *et al.*, 2009; Vitiello *et al.*, 2015). In turn, the low energy subband has a large population of electrons that should be quickly evacuated to another energy level in order to keep the inversion of population. This depopulation process is not fast enough compared to the rate at which electrons come from the high energy subband by the LO-phonon assisted transition. Thus inversion population at RT cannot happen. The temperature at which the LO-phonon transition is activated depends both on the material used through the specific value of its LO-phonon energy, and on the energy separation between the two subbands which determines the wavelength at which the QCL lases. For IR QCL, the energy separation of the subband levels is larger than the typical LO-phonon energy, thus this non radiative path is not allowed. This explains why IR QCL encountered no problems to reach rapidly the RT operation, contrary to their THz counterparts (Belkin *et al.*, 2009).

Moreover, we can notice that no QCL was reported in the region between 6 to $10\,THz$ (grey region in figure 0.7). This lack has the same origin as the operation temperature limitation: the LO-phonon. Its frequency lies in the range of $25-40\,meV$, thus $6-10\,THz$, for the SC commonly used, where no QCL was reported. The reason for this lack is that the lifetime of an energy level which can be depopulated by an LO-phonon assisted transition is much lower than the lifetime of the same energy level if we consider an ISBT to happen (Faist *et al.*, 1994).

However a GaInAs/AlInAs QCL was recently reported at $11\,THz$, which corresponds to the Reststrahlen band of AlAs Ohtani *et al.* (2019). The authors take advantage of the coupling between light and phonons, which gives rise to quasi-particles named phonon polaritons. Contrary to electrons that are subject to strong interactions with LO-phonons in ionic crystals, called the Fröhlich interaction, phonon polaritons are free from this interaction, which enables light emission within the material Reststrahlen band.

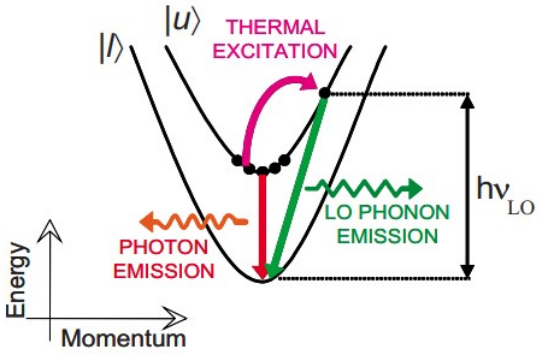

Figure 0.8.: Schematic showing the LO-phonon mecanism responsible for the lowering of the population inversion for RT QCLs. *Reprinted from (Bellotti* et al.*, 2009), with the permission of AIP Publishing.*

In order to tackle this problem, two main approaches are developed.

The first one aims at increasing the electron lifetime in the high energy subband by exploring different active region designs while keeping the same materials (Kumar *et al.*, 2009; Fathololoumi *et al.*, 2012; Franckié *et al.*, 2018). For instance, it can be designs where electrons are injected to the upper subband from a higher energy level using an LO-phonon assisted transition, rather than tunnel effect (Patimisco *et al.*, 2013). Despite a lot of efforts on design optimization, the operation temperature has been improved only a few Kelvin, which is still not enough for mainstream applications.

A promising approach relies on finding materials with either large LO-phonon energies (Vitiello *et al.*, 2015), or with weak electron/LO-phonon interactions. The different materials that can be candidates for this approach are compared in the next part.

0.2.3. A Zinc Oxide based Quantum Cascade Laser?

The materials that are commonly used to realize efficient QCLs are: InGaAs with either AlInAs, AlInGaAs, AlInAsSb or GaAsSb grown on InP substrates, GaAs/AlGaAs on GaAs or AlSb/InAs grown on InAs. They were chosen initially because for many reasons. From technological points of view like: the growth quality achievable and the process quality. From theoretical points of view considering the electron effective mass and the conduction band offset (Vitiello *et al.*, 2015). But THz QCLs made from these materials suffer from the operation temperature limitation due to their LO-phonon energies. An approach to tackle this issue is to search for materials with large LO-phonon energy so that at RT, the population inversion is preserved. In this sense, two SCs were proposed: GaN and ZnO. Their LO-phonon energies are $90\,meV$ and $72\,meV$ respectively, this is

nearly twice compared to GaAs. In the paper (Bellotti *et al.*, 2009), authors present a comparative theoretical study of THz QCL based on GaAs/AlGaAs, GaN/AlGaN and ZnO/ZnMgO. To make a meaningful comparison, the designs from the 3 material systems are very similar: they are based on a "resonant phonon" design. The targeted emission energy is set to $8.2\,meV$, or $2\,THz$ and Monte Carlo simulations are conducted to predict the inversion population evolution with the temperature. Figure 0.9 presents the simulated population inversion for the three material systems as a function of the temperature. We can observe that, contrary to GaAs, GaN and ZnO based QCLs show a nearly constant population inversion until $150\,K$, before the population inversion begins to drop. This ends with a population inversion of 25 and 30 % for ZnO and GaN respectively, whereas GaAs shows no more population inversion above $250\,K$.

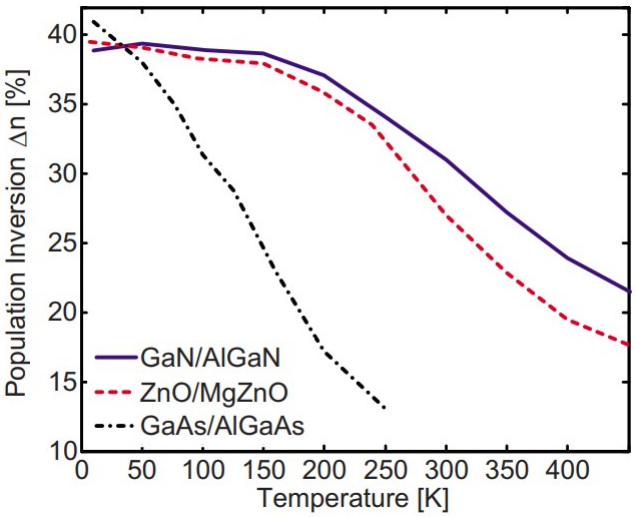

Figure 0.9.: Population inversion evolution as a function of the operating temperature for 3 QCLs made from GaAs/AlGaAs (black dashed curve), GaN/AlGaN (purple curve) and ZnO/ZnMgO (red dashed curve). The emission energy is identical for the 3 QCLs. *Reprinted from (Bellotti* et al.*, 2009), with the permission of AIP Publishing.*

Theoretically GaN and ZnO are shown to be able to lead THz QCL until RT operation. Another recent paper precisely compares ZnO and GaAs (Sirkeli *et al.*, 2017). The design is based on a "resonant phonon" scheme. The authors test the validity of their numerical simulation by comparing their results with the performance of the GaAs/AlGaAs QCL presented in (Fathololoumi *et al.*, 2012). They found out that ZnO based THz QCLs should present gain above RT. Moreover they highlight that the two QWs design allows the higher gain.

Gallium Nitride

Thanks to its high LO-phonon energy, GaN/AlGaN heterostructures show some potential for RT THz QCL operation. Among them, the first ISB absorption was observed experimentally in 1999 in the IR range (Suzuki & Iizuka, 1999) and was followed by others in the THz range, between 1.9 and $5.6\,THz$ (Machhadani *et al.*, 2010; Beeler *et al.*, 2014). The effect of crystalline orientation on the ISB absorption was studied in (Lim *et al.*, 2015). They demonstrate that the non-polar m-plane orientation can lead to efficient ISBT compared to c-plane without the issue of the internal electric

field which is typical for wurtzite heterostructures. In addition to the observation of ISBT in the THz range, the resonant tunnel effect has been observed reproducibly for a few years Bayram *et al.* (2010a,b); Encomendero *et al.* (2018). This late observation can be explained by the non-widespread use of GaN substrates. Indeed, growing on a foreign substrate gives rise to a high dislocation density ($10^8 - 10^9\,cm^{-2}$) and prevents the observation of the resonant tunnel effect because electrons were trapped by defects instead of tunneling. Switching to a GaN substrate helped to fix this issue. However, the use of GaN substrates is still nearly reduced to the c-plane orientation, which is known to create an electric field inside wurtzite heterostructures, adding another difficulty for QCL design.

One GaN based QCL was reported up to now (Terashima & Hirayama, 2015). However this demonstration is not well accepted by the QCL and GaN community. Another difficulty pointed out in (Terashima & Hirayama, 2011) concerns the waveguide fabrication: the double-metal waveguide, which is the most promissing waveguide configuration for high temperature THz QCL is still difficult to implement in GaN. Since this first controversial demonstration in 2015, no other GaN/AlGaN THz QCL was reported, indicating that this material is still not completely mature for the realization of RT THz QCL.

Zinc oxide

A few years ago, ZnO based heterostructures were primarily developed for UV light emitting diodes owing to the ZnO large band gap energy. But no competitive diodes were reported because of the difficulty to achieve reproducible p-doping in ZnO. Very recently, ZnO was considered to be a promissing candidate for unipolar devices like QCLs because only one type of doping is required. Thus the p-doping issue faced for light emitting diodes is not a drawback. Indeed, high quality heterostructures can be grown thanks to the availability of ZnO substrates in various orientations. It has allowed a drastic defect reduction inside ZnO epilayers, compared to ZnO grown on sapphire (Chauveau *et al.*, 2010). This high quality paves the way for the demonstrations of ISBT (Belmoubarik *et al.*, 2008; Ohtani *et al.*, 2009; Zhao *et al.*, 2014; Orphal *et al.*, 2017). However, they involve ISBT in the IR and up to now, none was reported in the THz range. Resonant tunnel transport at RT is not demonstrated in a repeated manner. (Krishnamoorthy *et al.*, 2002) reported such observation, but the negative differential resistance on I-V curves that they observed may be due to transport associated with defects within the (Zn, Mg)O barrier. The presence of defects might be explained by the use of sapphire as a substrate. Still, there is a huge gap between ZnO and GaN in terms of process that needs to be bridged if one wants to use ZnO for QCL because the related process it highly complex (Ozgur *et al.*, 2010). But due to the availability of ZnO substrates, and the good heterostructure quality demonstrated up to now, ZnO seems to be a very promissing candidate for RT THz QCLs

This is this challenge taken by the members of the european projet ZOTERAC, to demonstrate the first ZnO based THz QCL. And my thesis aims at taking a part in this challenge which is to grow and characterize ZnO/(Zn, Mg)O heterostructures grown on ZnO substrates so that they match the material quality required for a QCL to operate.

Silicon Germanium

During my thesis, a THz QCL using SiGe was predicted to be very robust against temperature increase, but for different reasons compared to its GaN and ZnO counterparts. Indeed, its LO-phonon energy is between 37 and 63 meV, depending on the proportion of Ge and Si (Levinshteĭn *et al.*, 2001). Its advantage is related to its atom bondings that are covalent rather than ionic. It is a non-polar crystal, and as a consequence, the Fröhlich interaction between LO-phonon and electrons is weakened compared to compounds like GaN and ZnO (Grange *et al.*, 2018). Even with a low LO-phonon energy, a SiGe based THz QCL presents theoretically gain at RT (Grange *et al.*, 2018). Among the advantages of this material is the use of Si, which cannot be circumvented in the SC industry. Moreover, ISB absorption in the THz range as well as tunnel transport have been experimentally demonstrated in this material (De Seta *et al.*, 2009; Busby *et al.*, 2010; Seta *et al.*, 2012; Grange *et al.*, 2018). However, a special care should be given to the strain relaxation within the heterostructure. The lattice mismatch between Si and Ge is of 4 % (Levinshteĭn *et al.*, 2001). Growing thick SiGe based heterostructures might be challenging depending on the composition range. Indeed, once the critical thickness is reached, the material relaxes and various defects are introduced which is very detrimental to the QCL operation. Up to now, there is no experimental SiGe based QCL reported, but it can be explained by its very recent developement for cascade devices.

0.3. Zinc Oxide and Zinc Magnesium Oxide

0.3.1. Properties of ZnO semiconductor

Crystalline structure

ZnO crystals can be encountered in three crystalline structures: rocksalt, zinc blende and wurtzite. The two first are cubic whereas the last one has a hexagonal symmetry around the c axis (see figures 0.11 and 0.10). The wurtzite phase is the most stable in ambient pressure and temperature conditions. The rocksalt crystal phase can be observed in high pressure conditions, typically greater than 10 GPa (Jaffe & Hess, 1993), and can not be obtained by epitaxy (Jagadish & Pearton, 2011). The zinc blende crystal phase can be grown by epitaxy on cubic substrates like Si or GaAs for instance (Kim *et al.*, 2003; Ashrafi *et al.*, 2000). Since the wurtzite phase is the most stable phase, it is easier to obtain good quality epitaxial layers, which is mandatory for the QCL growth. Thus the following description focuses on this particular phase.

From a crystallographic point of view, the wurtzite phase belongs to the space group $P6_3mc$ (or C_{6v}^4 in the Schonflies notation). As shown in figure 0.10, one Zn (or O) ion is surrounded by 4 O (or Zn) ions which build a tetraedron whose main axis is along the c axis. The ions are bound together by sp^3 bonds, which have a high ionic character. Indeed, wurtzite ZnO is at the very limit between covalent and ionic crystals, according to Phillips ionicity scale (Jagadish & Pearton, 2011).

In a hexagonal crystal, two lattice parameters are relevant: a and c. The a lattice parameter represents the distance which separates two adjacent Zn atoms (or O atoms) in a plane perpendicular to the c axis (named basal plane or (0001)), whereas the c axis is the distance which separates two adjacent basal planes. Moreover, the angles between the unit lattice vectors a_1, a_2 and a_3 are 120°

and the c axis is perpendicular to each of the above-mentioned vectors. The unit cell is limited by the parallelepiped defined by unit lattice vectors a_1, a_2 and c. They enable crystallographic planes and direction to be named according to Miller indices h, k, l (in parentheses for a plane and in square brackets for a direction). For crystals with the hexagonal symmetry, an alternative notation for crystallographic planes and directions can be used by adding an index with respect to the a_3 unit lattice vector. This has the advantage to let the hexagonal symmetry appear clearly. This latter notation - using h, k, i, l - is used in the rest of the manuscript.

For ZnO, the typical values for the lattice parameters are $a = 3.25\,\text{Å}$ and $c = 5.20\,\text{Å}$(Jagadish & Pearton, 2011; Özgür *et al.*, 2005). But most wurtzite crystals are slightly distorted with respect to the ideal wurtzite structure. To quantify this deviation, the parameter u can be calculated using the experimental lattice parameters (see equation 0.3).

$$u = \frac{a}{c}\sqrt{\frac{3}{8}} \tag{0.3}$$

In the ideal case, $\frac{a}{c} = \sqrt{\frac{3}{8}}$, which leads to an ideal parameter $u = \frac{3}{8} = 0.3750$. For ZnO, this parameter was found to range from 0.3817 to 0.3856 (Kisi & Elcombe, 1989; Jaffe & Hess, 1993; Gerward & Olsen, 1995).

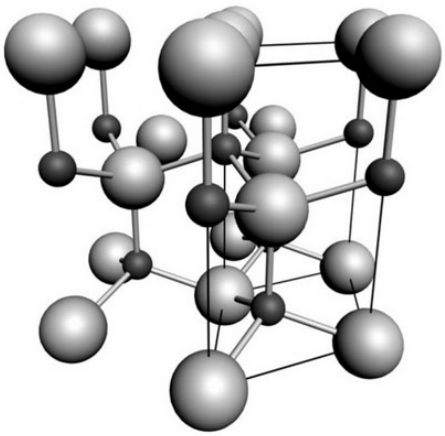

Figure 0.10.: Wurztite structure of ZnO. Zn atoms are represented by large gray spheres and O atoms by small black ones. *Reprinted from (Jagadish & Pearton, 2011), Copyright (2011), with permission from Elsevier.*

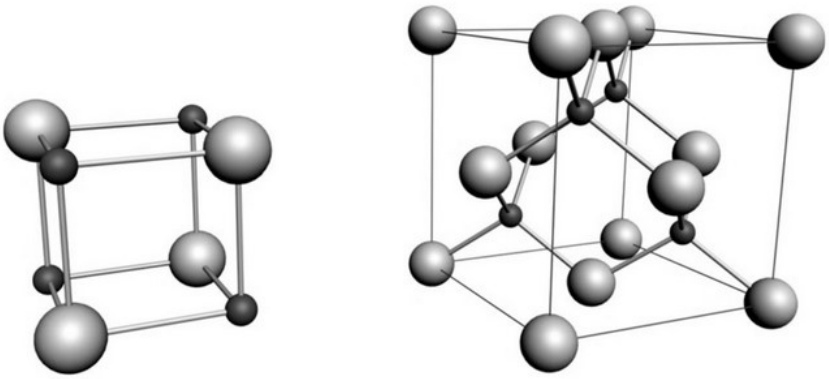

Figure 0.11.: Rocksalt and zinc blende unit cell structures (respectively left and right). *Reprinted from (Jagadish & Pearton, 2011), Copyright (2011), with permission from Elsevier.*

From a practical point of view, figure 0.12 shows the main orientations for the epitaxy. The most commonly used is the c plane - where growth occurs along the c direction (see figure 0.12). It is called the polar orientation. Then comes the non polar orientations: a and m planes which are both perpendicular to the polar orientation. The last orientation is the r plane, which is called semi-polar because it is neither parallel nor perpendicular to the c plane.

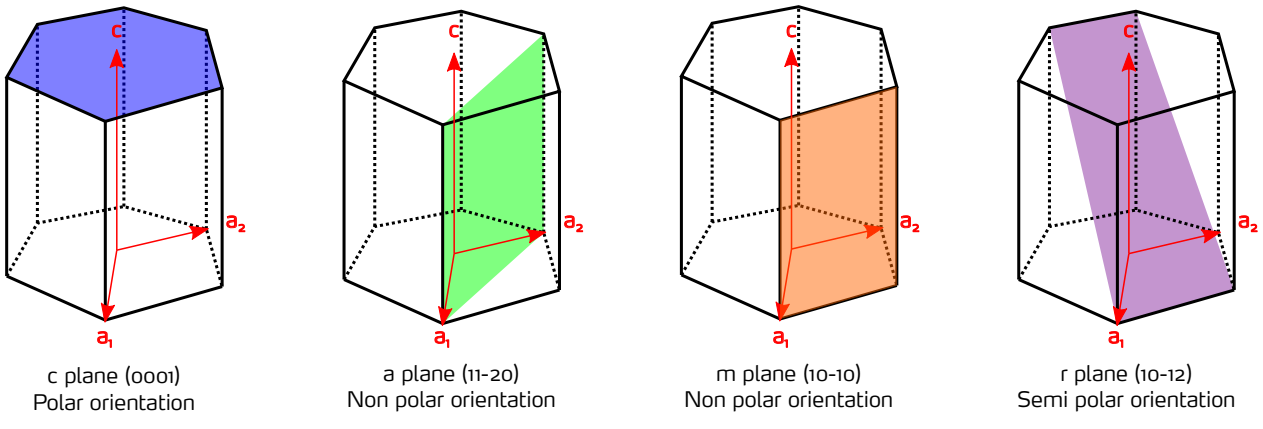

Figure 0.12.: Usual orientations for wurtzite ZnO epitaxial growth.

These 4 ZnO orientations have already been grown by epitaxy, mostly MBE. In my thesis I mainly focus on the m and r orientation. The reason for this choice is explained in the section 0.3.2.

Phonons and Reststrahlen band

When an optical excitation impinges a crystal lattice, it can trigger a collective motion of crystal lattice atoms. A unity of this collective motion is called a phonon. Depending on the atom number within the unit cell crystal, different kinds of collective motion patterns, or phonons, are possible. The unit wurtzite cell contains 4 atoms per unit cell: 2 Zn and 2 O atoms, giving 12 phonon modes. Among phonons, two families can be distinguished: the acoustic and the optical phonons. Acoustic phonons represent collective atom motions that are in phase: for wurtzite ZnO it means that Zn and O atoms nearest neighbours move in the same direction. This type of motion has low frequency and cannot be coupled to light. Optical phonons represent antiphase collective motions of atoms, meaning that the Zn and the O atoms move in an opposite way. Contrary to acoustic, optical phonons have high frequencies and can interact with an electromagnetic radiation such as light.

In the wurtzite crystals, among the 12 phonon modes possible, 3 are acoustic and 9 are optical modes (Loudon, 1964). Focusing on the optical modes, they can be classified according to the space group theory as shown is equation 0.4.

$$\Gamma_{opt} = 1A_1(1) + 2B_1(1) + 1E_1(2) + 2E_2(2) \tag{0.4}$$

The notation A_1, B_1, E_1 and E_2 indicates specific atom motion patterns. The number in parenthesis tells the number of variants existing within a given motion pattern: longitudinal or transverse, which are abreviated in the following by LO and TO for "Longitudinal Optic" and "Transverse Optic" respectively. An LO-phonon represents a configuration in which the atom motion is parallel to the phonon propagation, whereas for a TO-phonon, the atom motion is perpendicular to the phonon propagation. In order to investigate the phonon modes, IR and Raman spectroscopy are the experimental techniques classicaly used. They are complementary because some modes may be detected by one technique and not by the other. For instance, A_1 and E_1 modes are both IR and Raman active, whereas E_2 can only be seen using Raman spectroscopy. The phonon mode B_1 is called silent because it is both IR and Raman inactive (Bundesmann *et al.*, 2006). As the THz domain is known as 'far IR', we only focus on the modes that are IR active: A_1 and E_1, because they have chances to have an impact on the material properties in the THz domain in which we are interested.

Figure 0.13 shows the atom displacement for the A_1 and E_1 modes. Both are polar modes because the Zn and the O ions are moving in opposite direction, thus changing the dipole moment. In addition, we can observe that for the A_1 mode, the ion displacement is along the c direction, whereas for the E_1 mode, ions are moving perpendicular to the c direction. In the following, the phonon frequencies associated with the A_1 mode are noted $\parallel$, and $\perp$ for those associated with the B_1 mode.

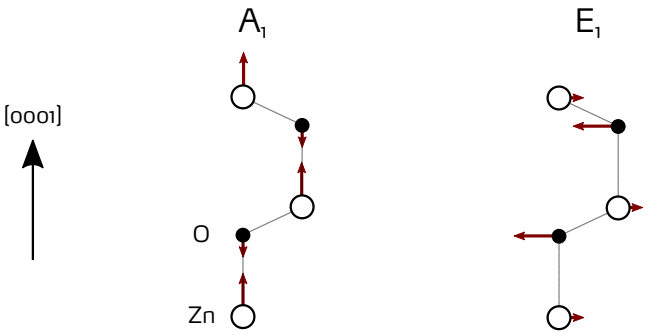

Figure 0.13.: Ion displacement in the case of A_1 and B_1 phonon modes.

Table 0.2 displays the typical frequencies for the optical phonons. Despite its structural anisotropy, wurtzite ZnO shows similar long wavelength phonon frequencies for ion motion parallel or perpendicular to the c axis. It justifies why only one single value is usually given for LO and TO phonons. This value is the average between the parallel and the perpendicular case. Thus for ZnO, we end up with $\omega_{LO} \approx 582\,cm^{-1}$ and $\omega_{TO} \approx 400\,cm^{-1}$, which corresponds respectively to $E = \hbar\omega_{LO} = 72\,meV$ and $E = \hbar\omega_{TO} = 50\,meV$.

Phonon	$\omega\ (cm^{-1})$	$E\ (meV)$	$\lambda\ (\mu m)$
$LO, \parallel$	576	71.4	17.4
$LO, \perp$	590	73.2	16.9
$TO, \parallel$	380	47.1	26.3
$TO, \perp$	409	50.7	24.5

Table 0.2.: Mean frequency, energy and wavelength values of $\lambda = \dfrac{hc}{E}$ LO and TO phonon for wurzite ZnO. These values are obtained from the following papers: (Ashkenov *et al.*, 2002; Damen *et al.*, 1966; Arguello *et al.*, 1969).

Light can be strongly absorbed by LO and TO phonons. This absorption happens in the frequency ranges delimited by $[\omega_{TO}; \omega_{LO}]$ and $[2\omega_{TO}; 2\omega_{LO}]$ and is called the Reststrahlen energy band. For ZnO, it lies in the THz range: between 12 and $17\,THz$ and 24 and $34\,THz$. A THz QCL in this frequency range is not feasible using ZnO. However, ZnO can be used to reach THz frequencies that are not reachable using GaAs or InGaAS based heterostructures. Due to its high LO-phonon energy, ZnO can achieve RT operation for THz QCLs. Since the phonon energies of ZnO are nearly twice compared to those of the SCs commonly implemented for QCLs, it allows ZnO to be used in order to emit light in the Reststrahlen band of GaAs, InAs and InSb for instance (Lockwood *et al.*, 2005). In the project, we focus on QCL emitting in the range of 5 to $10\,THz$.

Band structure

The knowledge of band structure of a SC is mandatory to fabricate an optoelectronic device. Indeed, knowing a SC band structure gives access to many crucial parameters as the electron and hole effective masses, energy levels as well as the selection rules for the electronic transitions and the related oscillator strength.

A SC band structure can be predicted by various calculation methods as ab-initio, quasi-particle or density functional calculation. These calculation methods have been applied to wurtzite ZnO (Schröer *et al.*, 1993; Lambrecht *et al.*, 2002; Schleife *et al.*, 2009). In parallel to these theoretical calculations, there are experimental means to measure a SC band diagram that have been applied to ZnO: X-ray absorption or emission spectroscopy (Dong *et al.*, 2004), resonant inelastic scattering (Preston *et al.*, 2008)or angle resolved photoemission spectroscopy (Kobayashi *et al.*, 2009). Figure 0.14 shows an experimental ZnO valence band diagram obtained by angle resolved photoemission spectroscopy on which the result of a hybrid density functional theory calculation has been superimposed. We can notice that they are in very good agreement, but this figure points out that determining a band diagram by experimental means is not precise enough. This highlights the importance of theoretical calculations to refine what is found experimentally.

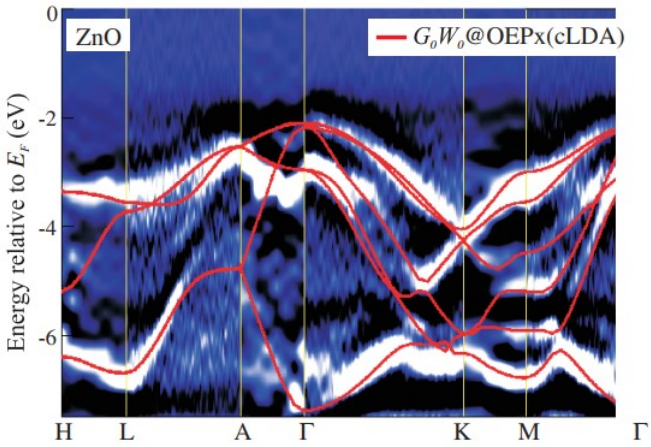

Figure 0.14.: Band Structure of wurtzite ZnO focused on the upper valence bands. The spectrocopic data represented in color graduations are taken from (Kobayashi *et al.*, 2009) and the theoretical calculation result is taken from (Yan *et al.*, 2010). *(Yan* et al., *2010), URL, © IOP Publishing. Reproduced with permission. All rights reserved. Reprinted figure with permission from (Kobayashi* et al., *2009), URL, Copyright (2009) by the American Physical Society.*

In wurtzite ZnO, there are 3 valence bands that originate from valence band splitting. Figure 0.15 summarizes splitting steps that the zinc blende ZnO band structure undergo to give the final ZnO wurtzite band structure (Mang *et al.*, 1995). The conduction band of zinc blende band structure has an s-like orbital character Γ_1, whereas the valence band has a p-like character Γ_5. Switching from a cubic to a hexagonal symmetry completely breaks the isotropy of the zinc blende band structure. As a consequence, the initial Γ_5 valence band is split into a Γ_5 band which is twice degenerate and a Γ_1 band according to wurtzite crystal anisotropy. Thus the Γ_5 band shows a $p_{x,y}$-like character whereas the Γ_1 a p_z-like character (with the z direction refering to the c axis of the wurtzite cell). The two bands are energetically separated by the crystal field energy Δ_{cr} of $41\,meV$ (Thomas, 1960). This anisotropy taken into account, the influence of the spins on the orbital induces another splitting of the Γ_5 valence band into two bands: Γ_9 and Γ_7 separated by a spin-orbit energy Δ_{so}, commonly named light hole and heavy hole bands repectively. In addition, this splitting occurs with a change of band symmetry from Γ_1 to Γ_7 in the conduction and in the valence band.

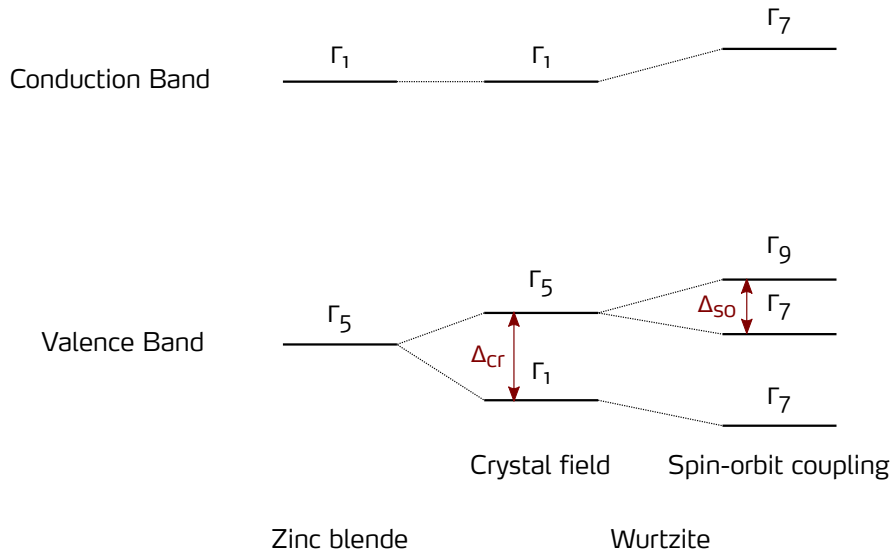

Figure 0.15.: Schematic explaining the valence band splitting in wurtzite ZnO.

0.3.2. Properties of ZnMgO and ZnO/ZnMgO heterostructures

Now that the main properties of ZnO have been reviewed, we can have a look at ZnO based heterostructures. A QW is created by the association of two SCs with different band gap energies. Figure 0.16 shows a generic example of such a QW: the SC 1 layers, with the larger band gap energy sandwich the SC 2 such that the carriers are confined in the SC 2 in order to minimize their energy. This is why the SC 1 is called the barrier, and the SC 2 the QW.

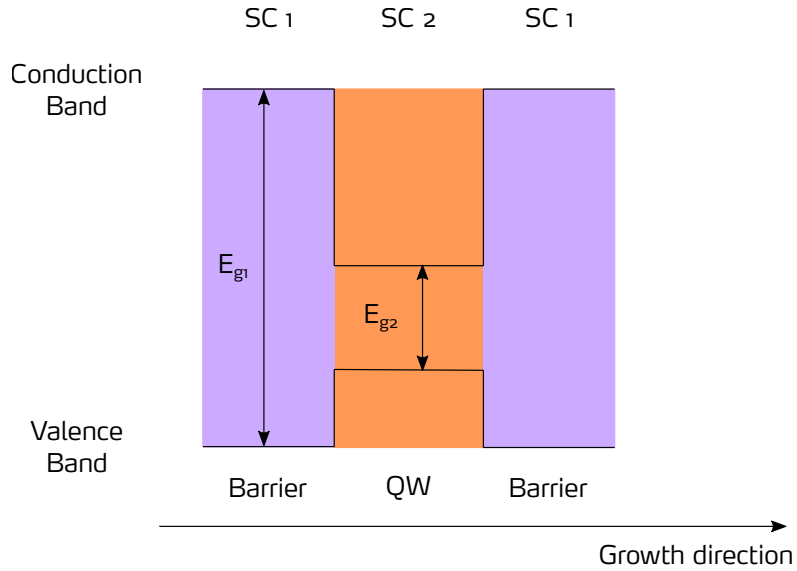

Figure 0.16.: QW schematic principle formed by the semiconductors 1 and 2 (respectively SC 1 and SC 2). E_{g1} and E_{g2} are the band gap of SC 1 and 2 respectively.

In ZnO QWs the barrier is (Zn, Mg)O (A. Ohtomo *et al.*, 1998). The Mg incorporation in ZnO is known to increase its bandgap. But (Zn, Mg)O is not the only SC that can be used for this purpose. There are studies dealing with (Zn, Cd)O (Makino *et al.*, 2001; Yang *et al.*, 2011) and (Zn, Be)O (Ryu *et al.*, 2006; Kim *et al.*, 2006; Chen *et al.*, 2013) as well but they have been less intensively studied compared to (Zn, Mg)O.

Crystal structure of MgO and (Zn, Mg)O

MgO crystallizes in the rocksalt structure at ambient conditions (see figure 0.11), a cubic structure (figure 0.17). Its lattice parameter is $a = 4.24\,\text{Å}$ and its band gap energy is nearly twice that of ZnO (ie $\sim 7.7\,eV$) (Özgür *et al.*, 2005). To form the (Zn, Mg)O alloy and to increase the band gap, Mg atoms are incorportated on Zn sites within the wurtzite lattice. This incorporation is facilitated by the fact that Mg and Zn have similar radii, thus the replacement of an Zn atom by a Mg one should not lead to a large distorsion of the wurtzite cell. Looking at the binary system ZnO/MgO, the MgO solubility limit in ZnO is only $4\,wt\,\%$ (Segnit & Holland, 1965). However, various growth techniques allow to push this limit, but since MgO and ZnO do not share the same crystalline symmetry, a phase transition is somehow expected. When alloying ZnO with Mg, the (Zn, Mg)O keeps its hexagonal phase until a certain Mg content, which depends on the growth method and parameters. For instance, it has been proved that a Mg content of $56\,\%$ can be reached in MBE while keeping the hexagonal phase (Redondo-Cubero *et al.*, 2012). Beyong this limit content, a phase transition occurs. To illustrate this phase change, the (Zn, Mg)O lattice parameter has been measured by X-rays (A. Ohtomo *et al.*, 1998). Figure 0.18 displays the variation of the lattice parameter of the (Zn, Mg)O alloy as a function of the Mg content. In this study, the Mg limit content for which the (Zn, Mg)O starts to become cubic is only $33\,\%$ because the growth technique used is pulsed laser deposition. In addition, when increasing the Mg content, the a and c parameters have opposite variations: whereas the a lattice parameter is increasing, the c one is decreasing. It can be explained because when increasing the Mg content, the (Zn, Mg)O lattice structure tends towards the cubic phase of the MgO (ie, $a = c$).

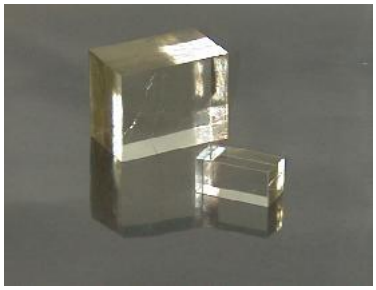

Figure 0.17.: Photo of a MgO single cristal (URL).

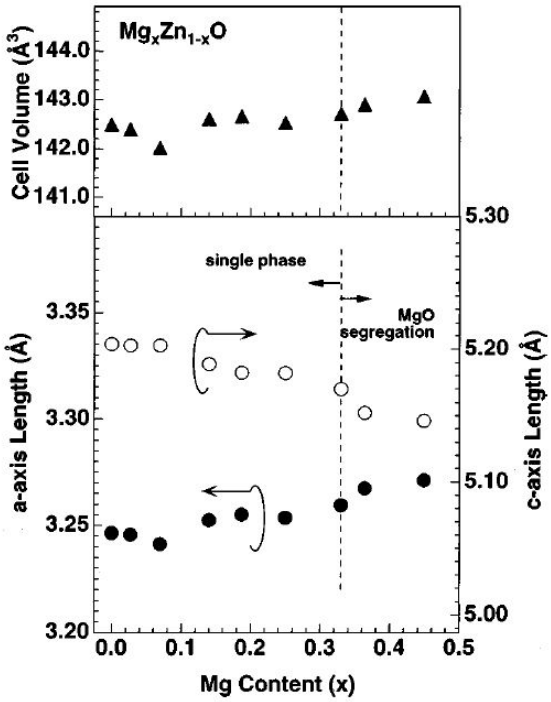

Figure 0.18.: Variation of lattice parameters of the (Zn, Mg)O alloy with the Mg content x measured by X-rays. *Reprinted from (A. Ohtomo* et al.*, 1998), with the permission of AIP Publishing.*

This latter evolution has important implications for the stress inside ZnO/(Zn, Mg)O heterostructures.

Mechanical properties

The QCL active region needed is at least $\sim 1\,\mu m$ thick for the waveguide confinement factor to be maximized. Since materials with different lattice parameters are associated to build the active region, mechanical properties of these materials should be taken into account. Indeed in the elastic limit, when deformations are reversible, the material stiffness coefficients C_{ij} are combined with the deformations ε_{kl} to give the material stress state σ_{ij} following Hooke's law (see equation 0.5).

$$\sigma_{ij} = C_{ijkl}\,\varepsilon_{kl} \tag{0.5}$$

This law is developed in the particular case of a wurtzite crystal in part III. Above a critical stress, the material enters the plastic domain. It undergoes irreversible changes in its structure to accomodate the imposed stress. These changes can be for instance creation and motion of dislocations or cracks. Knowing the epilayer deformation state together with the material stiffness coefficients is necessary to to estimate the stress state that the material can undergo without damage.

Growing materials with different lattice parameters leads to a strain state within the epilayer. This is the case when growing a material on a foreign substrate: the substrate imposes its lattice

parameters to the material grown on top of it. This is called lattice-mismatch. Two cases should be distinguished: the pseudomorphic and the metamorphic growth. Pseudomorphic growth is obtained when the epilayer takes perfectly the substrate lattice parameters. Another way to say it is that the epilayer accomodates completely the stress imposed by the lattice-mismatch with the substrate. Thus the epilayer behaves elastically. On the contrary, metamorphic growth is obtained when the epilayer is not able to accomodate elastically the stress imposed. Thus the epilayer accomodates it by changing its structure: dislocations and/or cracks appear.

As the metamorphic growth is not conceivable in our case, we only focus on the pseudomorphic growth. Figure 0.19 shows the 3 cases that can happen.

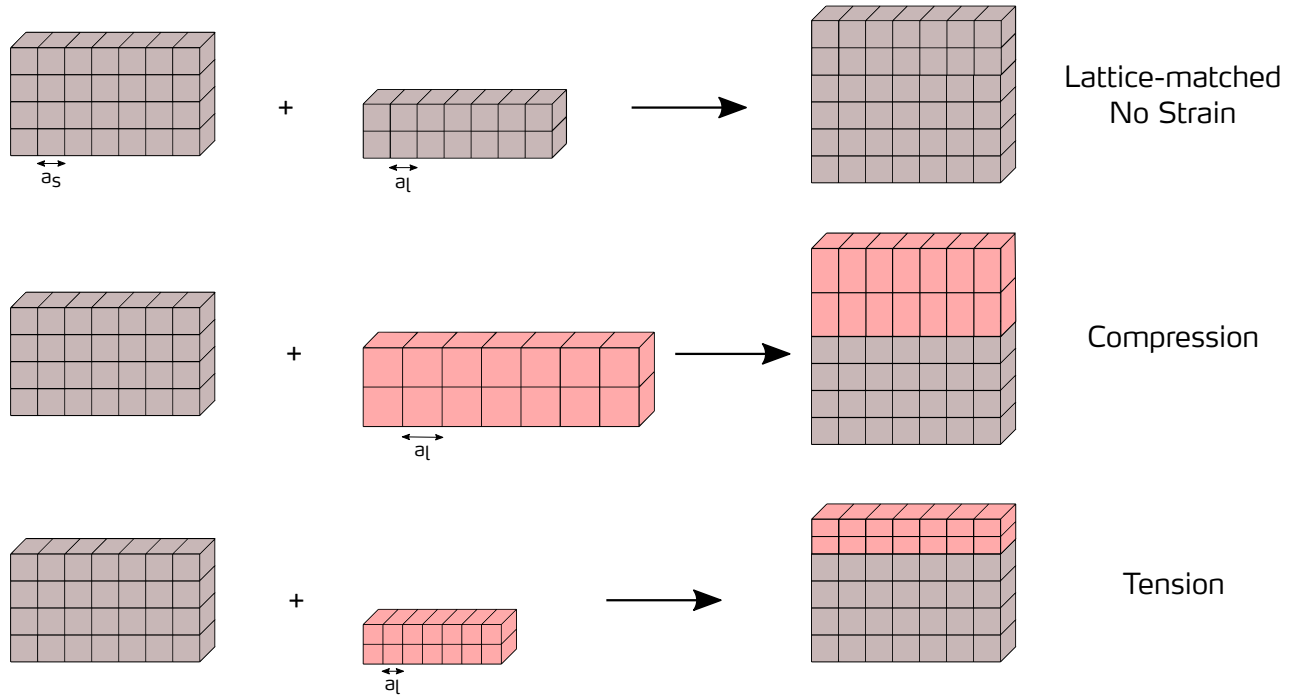

Figure 0.19.: Schematic explaining the epilayer strain state depending on the substrate and material lattice parameters.

The strain coming from the lattice mismatch can be defined as written in equation 0.6.

$$\frac{\Delta a}{a} = \frac{a_l - a_s}{a_s} \tag{0.6}$$

Where a_s and a_l stand for the lattice parameter of the substrate and the layer respectively. Coming back to figure 0.19, we can now make the link between the lattice mismatch value and the epilayer strain state. If the lattice mismatch is zero, the layer does not undergo strain: this is the case of homoepitaxial growth. Then if the lattice mismatch is positive, the epilayer is in compression on the substrate. In the reverse case, when the lattice mismatch is negative, then the epilayer is in tension. For sake of clarity, the lattice mismatch has been defined only in one direction. But in the case of in plane anisotropy, one needs to take into account the lattice mismatch in the two in-plane directions.

Moreover, for sake of simplicity, we reduce the deformation origin in the epilayer to a problem of lattice-mismatch with the substrate. Another case can happen: deformation due to the difference of thermal expansion coefficients between the epilayer and the substrate. In particular, it can happen

after the growth, when the sample is cooled down. We do not give a detailed description of it because this effect is low in (Zn, Mg)O grown on ZnO.

The lattice mismatch notion is useful when trying to understand epitaxy relations or to know what is qualitatively the epilayer stress state. However, this has to be clearly distinguished from the material deformation state in equation 0.5, which is useful to predict the epilayer stress. A material deformation is defined with respect to its lattice parameter when it is completely relaxed (see equation 0.7).

$$\varepsilon = \frac{a - a_0}{a_0} \tag{0.7}$$

With a_0 and a the lattice parameters of a material which is relaxed and strained respectively.

In the pseudomorphic case, and since we are dealing with ZnO homoepitaxy, the only deformation which exists, and which is meaningful, is the (Zn, Mg)O one. However, the lattice parameters of wurtzite (Zn, Mg)O are not known because this crystal does not exist in nature. Thus its deformation state, its stiffness coefficients and by turn the limit stress it can elastically cope with are not accessible. During my thesis, I propose a method to determine them: this is the object of part III. In particular, the sometimes called "deformation" especially for the X-Ray reciprocal space maps represents in fact the epilayer lattice mismatch with respect to the ZnO substrate.

Polarization and Quantum Stark Effect

A structure is polar when the barycentres of positive and negative charges do not match. This is the case of wurtzite crystals because there is no symmetry plane perpendicular to the c axis (see figure 0.10). Thus they have a spontaneous polarization parallel to this axis. This wurtzite structure can be strained. The latter deformation is responsible for a distorsion of the wurzite structure, which by turn, changes the negative and positive charge barycentre positions. As a consequence, a new polarization arises due to deformation: it is called the piezoelectric polarization. Figure 0.20 presents qualitatively the direction of the spontaneous polarization $\overrightarrow{P}_{sp}$ and the piezoelectric polarization $\overrightarrow{P}_{piez}$ with respect to a wurztite structure which is either relaxed, in compression, or in tension. This example is presented with ZnO, but it can be transposed to the case of (Zn, Mg)O.

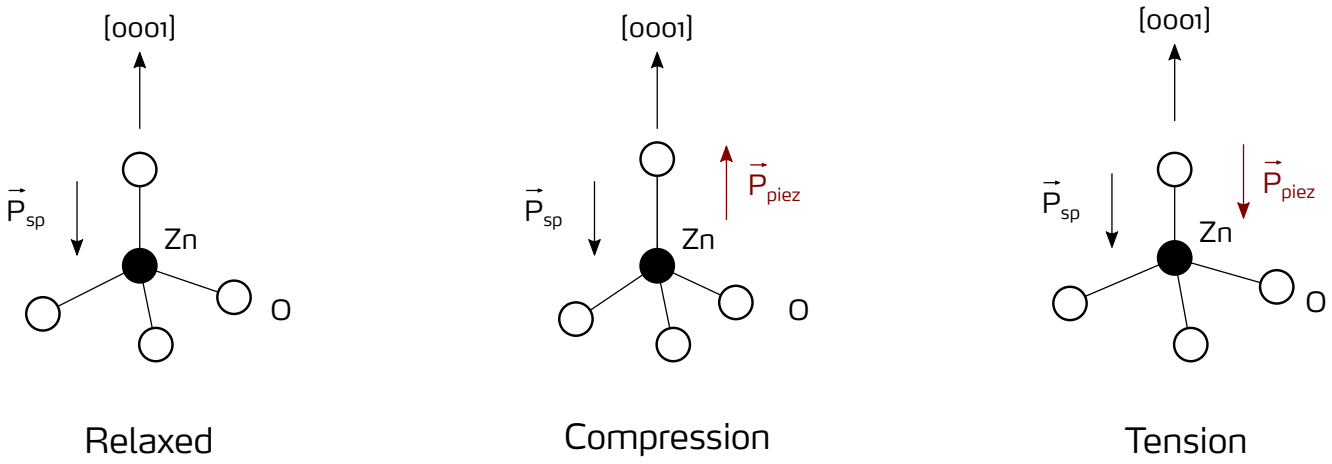

Figure 0.20.: Schematic showing qualitatively how a wurtzite structure can be deformed in case of compression and tension. $\vec{P}_{sp}$ stands for the spontaneous polarization which is not deformation dependent so that it is identical for the 3 cases represented. $\vec{P}_{piez}$ stands for the piezoelectric polarization which arises when the wurtzite structure is deformed due to either tension or compression.

In the case of heterostructures, each single layer can have its own total polarization (spontaneous and piezoelectric together). Thus at interfaces, a polarization discontinuity can arise and give birth to charges accumulation. In turn, accumulation of charges at the interfaces create an electric field within the heterostructure. Depending on the targeted application, this electric field can have either nice or detrimental consequences. One of them is the Quantum Confined Stark Effect (QSE), which is responsible for the asymmetry of QW energy profiles. Thereby, the distribution of charges - electrons and holes - inside the QW becomes asymmetric too, which induces a redshift of interband transitions (Im *et al.*, 1997; Leroux *et al.*, 1998). Even if a QCL is unipolar, this QW asymmetrization can really lead to complications when doing the active region design and the observation of ISBT. Such studies have already been done for the GaN/AlGaN system: in the paper of (Lim *et al.*, 2015), authors report the influence of the growth orientation, thus the presence of an internal electric field, on the ISBT energy for the same QW thicknesses. Our approach in the ZOTERAC project is to use non-polar orientations in which polarization vectors in each single layer are in the interface planes. A stack of layers with different polarization vectors does not lead to a polarization discontinuity. Thus, there is be no accumulation of charges at interfaces, no electric field and the QW profile remains symmetric. The fact that no QSE was observed in non-polar QWs has already been proved in ZnO/(Zn, Mg)O heterostructures (Chauveau *et al.*, 2009).

Intersubband transitions

This part aims at developing a simplified solution for the ISBT selection rule. We express the transition rate associated with an ISBT. Only the main steps are presented as well as the hypotheses that are made. Detailed resolution can be found in the following books (Bastard, 1988; Helm, 1999; Paiella, 2006). In particular, we stress the implication of equation terms from a material point of view when possible.

Let us consider a QW which is grown along the z axis in which different subbands exist. We are looking for the probability per second that a carrier - for instance an electron - goes from one

subband to another. Such an ISBT is triggered by an incident electromagnetic plane wave, linearly polarized, whose electric field is given by equation 0.8.

$$\overrightarrow{E} = \frac{E_0}{2}\overrightarrow{\varepsilon}\ \left(\exp\left(i\ \left(\omega t - \overrightarrow{q}.\overrightarrow{r}\right)\right) + \exp\left(-i\ \left(\omega t - \overrightarrow{q}.\overrightarrow{r}\right)\right)\right) \tag{0.8}$$

Where E_0 is the electric field amplitude, $\overrightarrow{\varepsilon}$ the polarization vector, ω the pulsation, $\overrightarrow{q}$ the propagation vector and $\overrightarrow{r}$ the position vector.

The hamiltonian associated with an electron can be divided in two parts (see equation 0.9).

$$\mathcal{H} = \mathcal{H}_0 + \mathcal{H}_{int} \tag{0.9}$$

Where $\mathcal{H}_0$ which stands for the electron energy associated with its momentum $\overrightarrow{p}$, and $\mathcal{H}_{int}$ the hamiltonian which represents the electron interaction with the incident electric field. They take the expressions given in equation 0.10 if we make the assumption of low intensity potential, which leads us to resonably neglect the A^2 terms.

$$\mathcal{H}_0 = \frac{p^2}{2m^*} \qquad \mathcal{H}_{int} = \frac{e}{2m^*}\left(\overrightarrow{p}.\overrightarrow{A} + \overrightarrow{A}.\overrightarrow{p}\right) \tag{0.10}$$

With m^* the electron effective mass in the QW material and $\overrightarrow{A}$ the potential vector associated with the electric field $\overrightarrow{E}$. The potential expression can be derived from the electric field thanks to equation 0.11.

$$\overrightarrow{E} = -\frac{\partial\overrightarrow{A}}{\partial t} \tag{0.11}$$

$$\overrightarrow{A} = \frac{iE_0}{2\omega}\overrightarrow{\varepsilon}\ \left(\exp\left(i\ \left(\omega t - \overrightarrow{q}.\overrightarrow{r}\right)\right) - \exp\left(-i\ \left(\omega t - \overrightarrow{q}.\overrightarrow{r}\right)\right)\right) \tag{0.12}$$

To simplify the potential vector expression given in equation 0.12, we use the dipolar approximation, which allows us to neglect the potential vector spatial variations. This approximation can be justified because the typical wavelength for the electromagnetic wave lies in the IR or THz domain. Thus its typical spatial variation is on the µm scale, whereas the electron is evolving in a nm thick QW, which means that the electron is not subject to the electromagnetic field spatial variation. We end with the simplifed expression for the potential vector given in equation 0.13.

$$\overrightarrow{A} \approx \frac{E_0 i}{2\omega}\overrightarrow{\varepsilon}\ \left(\exp\left(i\omega t\right) - \exp\left(-i\omega t\right)\right) \tag{0.13}$$

We use the Coulomb gauge that states that: $\nabla\overrightarrow{A} = \overrightarrow{0}$. As an important consequence, the $\overrightarrow{p}$ and $\overrightarrow{A}$ operators can commute, simplifying the interaction hamiltonian expression. The interaction potential independent of time V appears as (see equations 0.14 and 0.15).

$$\mathcal{H}_{int} = \frac{e}{m^*}\overrightarrow{A}.\overrightarrow{p} = V\ \left(\exp\left(i\omega t\right) - \exp\left(-i\omega t\right)\right) \tag{0.14}$$

$$V = \frac{e}{m^*}\frac{E_0 i}{2\omega}\overrightarrow{\varepsilon}.\overrightarrow{p} \tag{0.15}$$

Now we apply Fermi's Golden Rule, to express the transition rate for a single ISBT (equation 0.16).

$$W_{if}(\hbar\omega) = \frac{2\pi}{\hbar}\left|\langle\psi_f|V|\psi_i\rangle\right|^2 \delta\left(E_f - E_i \pm \hbar\omega\right) \tag{0.16}$$

i and f stands for the initial and final electron state respectively. $|\,\psi_i\,\rangle$ stands for the electron wavefunction in the state i. The function $\delta\left(E_f - E_i \pm \hbar\omega\right)$ represents the energy conservation during the transition from the state i to f. The "+" sign before the term $\hbar\omega$ in the δ function means a photon emission whereas the "−" sign stands for a photon absorption. By replacing V by its expression given in equation 0.15, the ISB transition rate can be written as (see equation 0.17):

$$W_{if}(\hbar\omega) = \frac{2\pi}{\hbar}\frac{e^2E_0^2}{4m^{*2}\omega^2}\left|\langle\psi_f|\overrightarrow{\varepsilon}.\overrightarrow{p}|\psi_i\rangle\right|^2 \delta\left(E_f - E_i \pm \hbar\omega\right) \tag{0.17}$$

The goal now is to develop the expression of the electron wavefunctions in order to end with the ISBT selection rule.

In such a heterostructure, we assume that we can separate the electron wavefunction in two contributions: Bloch and envelope function. This assumption is called the effective mass approximation. The Bloch function reflects the crystal periodicity effect on the electron behaviour, whereas the envelope function means the heterostructure periodicity effect on the electron behaviour. As both potentials - crystal and heterostructure - are periodic, Bloch and envelope functions are periodic too. They can be separated because their periodicities are not at the same scale: the Bloch function varies like the crystal lattice potential, typically on the Å scale, whereas the envelope function varies like the heterostructure periodicity, which is typically on a $\sim 10\,nm$ scale. According to this assumption, the electron wavefunction can be written as is shown in equation 0.18.

$$\begin{cases} \psi_j\left(\overrightarrow{r}\right) = u_{\nu_j}\left(\overrightarrow{r}\right)\, f_j\left(\overrightarrow{r}\right) \\ f_j\left(\overrightarrow{r}\right) = \dfrac{1}{\sqrt{S}}\exp\left(i\overrightarrow{k}_{\perp j}.\overrightarrow{r}_{\perp}\right)\, \chi_j\left(\overrightarrow{r}\right) \end{cases} \tag{0.18}$$

$u_{\nu_j}\left(\overrightarrow{r}\right)$ is the Bloch function of an electron in the band ν_j and $f_j\left(\overrightarrow{r}\right)$ is the envelope function with j indicates the relevant subband. The envelope function expression is cut in two pieces: $\dfrac{1}{\sqrt{S}}\exp\left(i\overrightarrow{k}_{\perp j}.\overrightarrow{r}_{\perp}\right)$ stands for the electron motion within the QW's plane, the x and y directions summarized by the sign $\perp$, whereas $\chi_j\left(\overrightarrow{r}\right)$ stands for the electron motion out of the QW's plane, ie the z direction. S is the in-plane sample surface which acts here as a normalization, $k_{\perp j}$ is the electron wavevector in the QW plane within the subband j. We keep identical electron wavefunctions within the QW and the barrier by assuming that the electron effective masses in both materials are identical.

Now we can develop the term $\langle\psi_f|\overrightarrow{\varepsilon}.\overrightarrow{p}|\psi_i\rangle$ according to the effective mass approximation (equation 0.19)

$$\begin{aligned}\langle\psi_f\,|\overrightarrow{\varepsilon}.\overrightarrow{p}|\,\psi_i\rangle &= \left\langle u_{\nu_f}\left(\overrightarrow{r}\right)\,f_f\left(\overrightarrow{r}\right)|\overrightarrow{\varepsilon}.\overrightarrow{p}|\,u_{\nu_i}\left(\overrightarrow{r}\right)\,f_i\left(\overrightarrow{r}\right)\right\rangle \\ &= \langle f_f\left(\overrightarrow{r}\right)\mid f_i\left(\overrightarrow{r}\right)\rangle\,\left\langle u_{\nu_f}\left(\overrightarrow{r}\right)|\overrightarrow{\varepsilon}.\overrightarrow{p}|\,u_{\nu_i}\left(\overrightarrow{r}\right)\right\rangle \\ &+ \left\langle u_{\nu_f}\left(\overrightarrow{r}\right)\mid u_{\nu_i}\left(\overrightarrow{r}\right)\right\rangle\,\langle f_f\left(\overrightarrow{r}\right)|\overrightarrow{\varepsilon}.\overrightarrow{p}|\,f_i\left(\overrightarrow{r}\right)\rangle \\ &= 0+\delta_{v_i,\nu_f}\,\langle f_f\left(\overrightarrow{r}\right)|\overrightarrow{\varepsilon}.\overrightarrow{p}|\,f_i\left(\overrightarrow{r}\right)\rangle \end{aligned} \tag{0.19}$$

The term $\langle f_f\left(\overrightarrow{r}\right)\mid f_i\left(\overrightarrow{r}\right)\rangle$ is zero because envelope functions from two distinct subbands are orthogonal. The δ_{v_i,ν_f} is equal to 1 because we are looking at transitions within the same band, so we have $\nu_i=\nu_f$. The next step is to develop the term with the envelope function using equation 0.18.

$$\begin{aligned}\langle f_f\left(\overrightarrow{r}\right)|\overrightarrow{\varepsilon}.\overrightarrow{p}|\,f_i\left(\overrightarrow{r}\right)\rangle &= \langle\chi_f\mid\chi_i\rangle\times\frac{1}{S}\iint dxdy\exp\left(-i\overrightarrow{k}_{\perp f}.\overrightarrow{r}\right)\,\left(\varepsilon_x p_x+\varepsilon_y p_y\right)\exp\left(-i\overrightarrow{k}_{\perp i}.\overrightarrow{r}\right) \\ &+ \delta_{k_{\perp f},k_{\perp i}}\,\varepsilon_z\,\langle\chi_f\,|p_z|\,\chi_i\rangle \\ &= \delta_{k_{\perp f},k_{\perp i}}\,\varepsilon_z\,\langle\chi_f\,|p_z|\,\chi_i\rangle \end{aligned} \tag{0.20}$$

Again, the term $\langle\chi_f\mid\chi_i\rangle$ is zero because of the envelope function orthogonality. The term $\delta_{k_{\perp f},k_{\perp i}}$ is non zero only if the in-plane initial and final wavevectors are identical, meaning that ISBT is vertical in the parabolic band approximation, which is also assumed here.

Thus we finally end with the following expression for the ISBT rate (equation 0.21).

$$W_{if}\left(\hbar\omega\right)=\frac{2\pi}{\hbar}\frac{e^2E_0^2}{4m^{*2}\omega^2}\varepsilon_z^2\left|\langle\chi_f\,|p_z|\,\chi_i\rangle\right|^2\delta_{k_{\perp f},k_{\perp i}}\delta\left(E_f-E_i\pm\hbar\omega\right) \tag{0.21}$$

In this final expression, the ISBT selection rule is visible: from the incident electric field, only the z polarization component is left. Thus the electric field should have a component in the z direction, also referred as the confinement direction, to trigger ISBT. Thus if we consider a incoming electromagnetic wave at normal incidence with respect to the sample surface - the plane defined by x and y - its polarization in the z direction is zero and no ISBT is happening.

Another interesting feature concerns the ISBT is the absorption coefficient α_{ISBT}. This coefficient is the proportion of the incoming light which is absorbed in the ISBT absoprtion process. Indeed, this coefficient is proportional to the ISB transition rate W_{if}, and thus to the term $\left|\langle\chi_f\,|p_z|\,\chi_i\rangle\right|^2$. In fact, this latter term varies as $\sin\left(\theta\right)^2$, with θ the incidence angle with respect to the QW's planes. In addition, we can see that it is consistent with the selection rule, because this term is zero at normal incidence ($\theta=0°$).

To conclude this part, we have derived in a simplified manner the ISBT rate, which makes the ISBT selection rule clearly appear. In addition, it depends strongly on the matrix element $\langle\chi_f\,|p_z|\,\chi_i\rangle$ in which only the component χ_j of the envelope function, related to the z direction, is involved and this term is precisely shaped by how the heretostructure is built. Thus it highlights that ISBTs are really strongly dependent on heterostructure architecture: controlled QW thickness, barrier composition as well as sharp interfaces to cite the most crucial parameters that are mandatory to observe ISBT.

This leads us to the next part, in which we will see how we have practically achieved these thorny requirements for ZnO/(Zn, Mg)O heterostructures.

Part II.

Growth of ZnO/(Zn, Mg)O heterostructures

This growth chapter is divided in two parts which follow a chronological order: from the growth to the thin film characterization. The growth method is presented in details as well as the substrate preparation. Then comes the search for suitable growth conditions in line with the growth requirements imposed by QCLs. The calibration procedure is established. Related to this part I would like to set the context.

At the beginning of my thesis, a new MBE system was installed in the frame of the european projet ZOTERAC. One reason was to achieve a low residual doping level which is mandatory for THz QCL realization. It implies to start the search for suitable growth conditions from scratch. That is the reason why it makes this part even more important.

Then we move to the structural and optical characterizations that are needed to achieve material quality suitable for cascade devices. C-V profiling was used to assess the residual doping level whereas SIMS (Secondary Ion Mass Spectroscopy) experiments give an insight on the Ga concentration in each single layer. AFM (Atomic Force Microscopy), XRR (X-Ray Reflectivity) and STEM-HAADF (Scanning Transmission Electron Microscopy High Angle Annular Dark Field) were performed in order to assess the quality of surface and burried interfaces.

PL (Photoluminescence) measurements as a function of the temperature were set in order to assess the quality of the (Zn, Mg)O barriers by investigating a the excitonic properties of heterostructures. All these characterization means were implemented for ZnO/(Zn, Mg)O heterostructures grown on m-plane and for few of them, on r-plane orientation.

0.4. Looking for suitable growth conditions for cascade structures

0.4.1. Growth technique: Molecular Beam Epitaxy

Epitaxial growth takes place when the film follows the same crystalline structure with respect to the substrate Arthur (2002).

The technique of choice for QCL growth is MBE because the grown layers gather all the characteristics required for a QCL structure. On one side, the high vacuum and ultra pure elements allow to prevent the film from contamination and, by turn, low residual doping can be achieved. On another side, the relatively low growth rate and temperature compared to vapor growth techniques makes it easier to control thicknesses at the monolayer scale and to have abrupt interfaces. Moreover, the specific temperature and pressure conditions place the growth far from the thermodynamic equilibrium, which means that MBE growth is mainly a kinetic driven growth process. This feature allows MBE to grow crystal phases that are thermodynamically forbidden. This is the case of wurtzite (Zn, Mg)O, for which the MgO solubility limit in ZnO is $4\,wt\,\%$ Segnit & Holland (1965), thus high Mg content (Zn, Mg)O alloy is not possible to grow at thermodynamic equilibrium.

In this section the MBE technique is prensented and then we move to the specificities of the MBE machine used to grow most of the samples during this thesis.

The MBE principle is to use atom beams that impinged the surface of a crystal substrate under ultra-high vaccum conditions (typically $10^{-6}\,T$ or $1.33 \times 10^{-4}\,Pa$ during the growth process). The

beam is produced by effusion cells and each one contains one atom specie in the solid form (9N for purity). The top and bottom are heated at two different temperatures so that the atom flux is directed toward the crystal substrate. As this phenomemon takes place in a ultra high vacuum chamber, the atoms mean free path is equivalent or larger than the distance between the cells and the substrate. In this configuration, no interaction takes place between atoms before reaching the substrate's surface. The chamber's walls are cooled by liquid nitrogen so that atoms that do not participate to the growth process are condensed to keep high vacuum condition. The high vaccum allows to add in situ characterisation tools as RHEED (Reflection High Energy Electron Diffraction). A few keV electron beam impinges the samples surface at grazing incidence ($\lesssim 2°$ typically). The beam is diffracted according to the sample's surface morphology toward a fluorescent screen where the RHEED pattern is visible (see figure 0.21). Depending on the observed patterns, information about the sample surface and thus the ongoing growth mode can be deduced. Moreover, following the time variation of RHEED intensity can be used to calculate de growth rate (see figure 0.22). The RHEED intensity is maximum when a complete ML is deposited. Between two complete MLs, the atoms do not cover the entire surface, which induces the electron beam to be scattered. As a consequence, an intensity decrease of the RHEED intensity is observed until the completion of the ML, for which the intensity is maximum again. The elapsed time between two RHEED intensity maxima thus corresponds to the growth time of a single ML, which by turn permit to deduce in real time the growth rate with a ML scale precision.

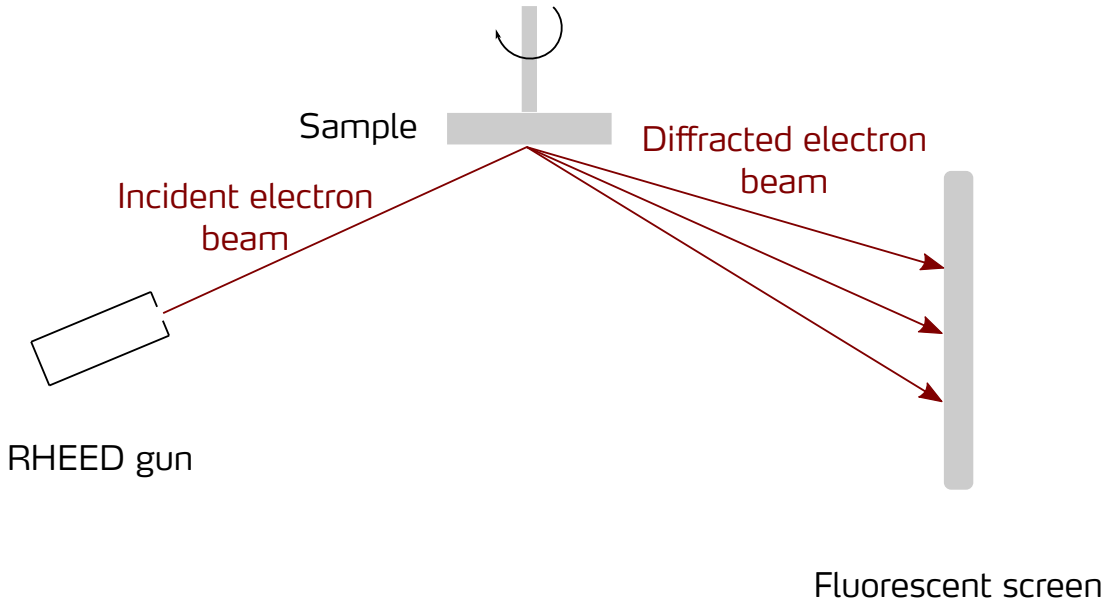

Figure 0.21.: Simple schematic describing the RHEED setup in the growth chamber.

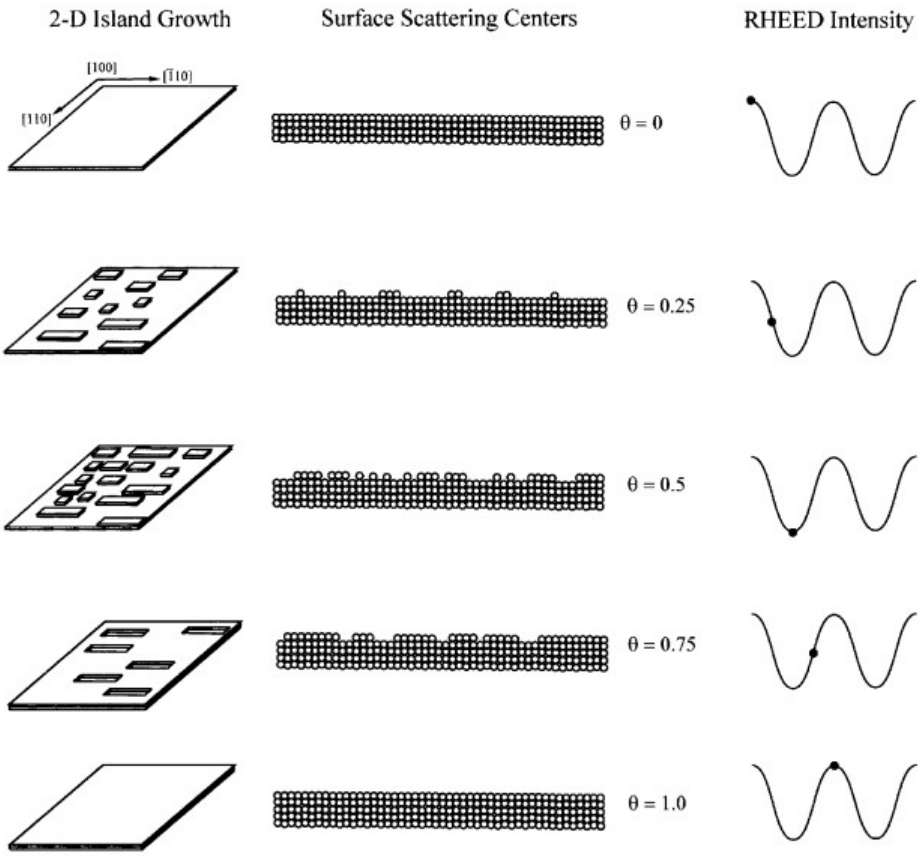

Figure 0.22.: Schematic showing the link between the surface coverage and the RHEED intensity. *Reprinted from Arthur (2002), Copyright (2002), with permission from Elsevier.*

The substrate is heated to allow incoming atoms to be diffused at its surface so that they can find lattice sites and create an atomic monolayer. Other various phenomena can takes place when an atom arrive on the surface. This surface processes depends on the growth conditions which affect the mobility of adatoms on the surface as well as the affinity of the coming atoms with the substrate, producing different growth modes (see figure 0.23).

- Layer by layer growth, called Frank-van der Merwe: the incoming atoms have a bigger affinity with the substrate's atoms, such that they prefer first to stick to the substrate compared to their counterparts. As a consequence, 2D layers are formed.

- Island growth, or Volmer-Weber: this is the reverse compared to layer by layer growth. The incoming atoms have a bigger affinity with themselves such that they prefer to stick together, which by turn form islands (3D growth mode).

- Layer and island growth, named Stranki-Krastanov growth. This is a mix between the last two growth modes: the growth begins to be 2D but after few ML, the atoms affinity change such that the 3D growth began.

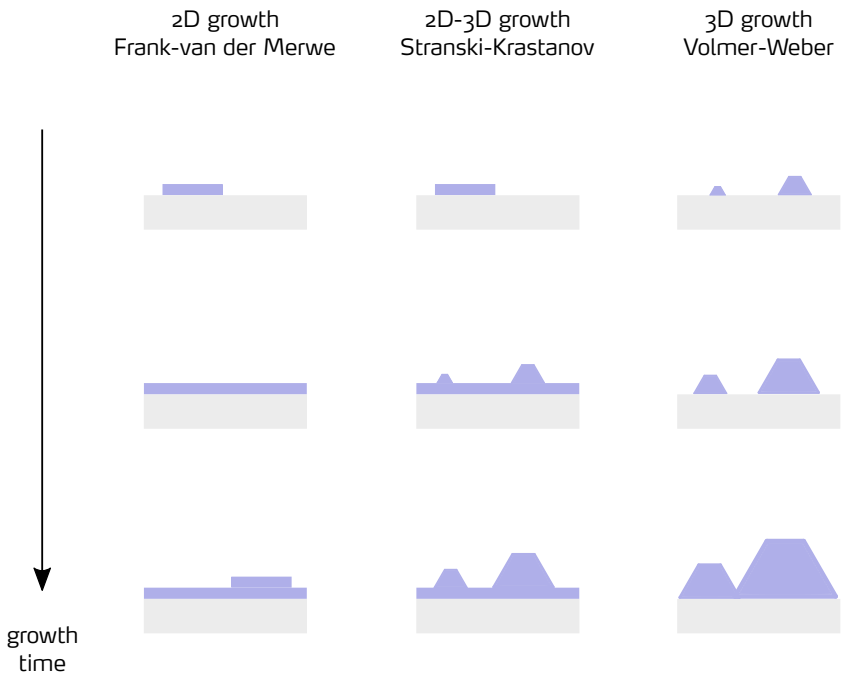

Figure 0.23.: Illustration of growth modes.

In our case, we want to favour the layer-by-layer growth mode which produce smooth interfaces and allows controllability at the monolayer scale.

Thicknesses are controlled by the opening and closing cell shutters. The closing/opening time is on the millisecond scale ($< 200\,ms$ verified on Riber C21). If we consider a mean growth rate of 200 nm/h and a thickness accuracy of one monolayer, it takes around 5 seconds to grow a monolayer of 3 angströms (nearly the monolayer on m-plane on ZnO). So the transient associated with the time to open and close shutters is negligible compared to the one needed to grow a monolayer. In addition, to ensure an homogeneous growth for alloys, the sample is rotated at a sufficient speed. "Sufficient speed" means that the time taken for the sample to do a complete revolution should be lower than the time to grow one monolayer. Otherwise, periodic alloy composition modulation occur when looking in the growth direction Alavi *et al.* (1983).

The MBE system used in this thesis is a RIBER Compact 21 (figure 0.24) equipped with 2 Zn cells, 2 Mg cells, 1 Ga cell for n-type doping. The oxygen is provided by a plasma cell. It is possible to grow one sample up to 3 inches at one time. This MBE system was installed at the beginning of the ZOTERAC project and is fully dedicated to it.

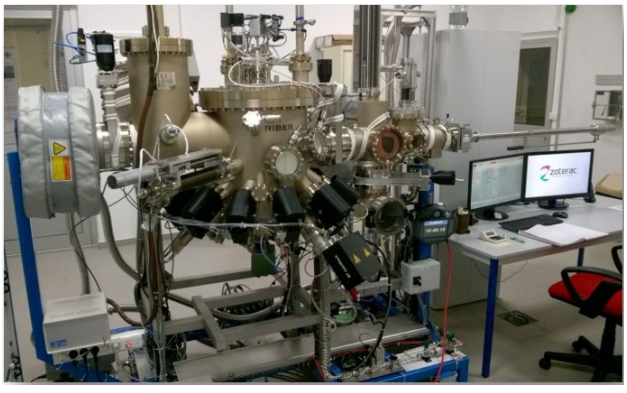

Figure 0.24.: Picture of the MBE system named ZOE for "Zinc Oxide Epitaxy" used for this work.

0.4.2. Substrate preparation

The substrates are $10 \times 20\,mm$ m-plane substrates from Crystec, one side polished. Prior to the growth, they are annealed in a Rapid Thermal Annealing (RTA) system at 1065°C under oxygen flux. This is known to clean the substrate from undesirable dusts and to reveal atomic steps (Ko *et al.*, 2004) (see figure 0.25). After this treatment, the RMS (Root Mean Square) roughness is typically in the range of $0.10 - 0.20\,nm$ (figure 0.26): the substrate is ready for the growth.

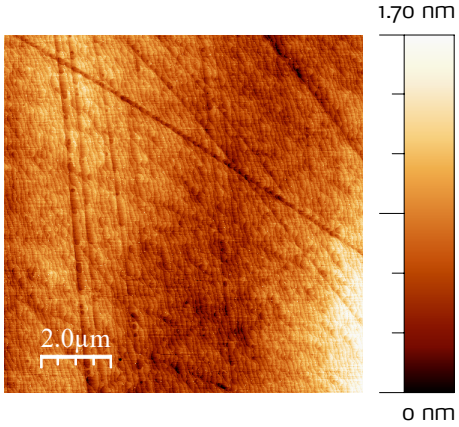

Figure 0.25.: AFM image of a ZnO m-plane substrate as received. The RMS roughness is $0.26\,nm$ and polishing scratches are clearly visible.

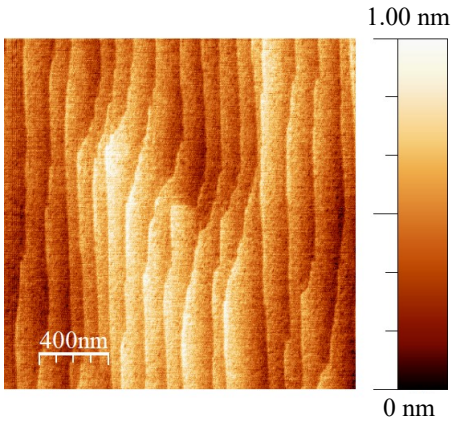

Figure 0.26.: AFM image after the RTA procedure. The RMS roughness is $0.17\,nm$ and atomic steps are clearly visible.

0.4.3. Variation of growth conditions

Growth temperature

A serie of samples was realized to study the effect of the growth temperature on the structural and optical properties of ZnO/(Zn, Mg)O single QWs. Two growth temperatures were tested: $240°C$ and $400°C$. Their influence on the QW and on the barrier was tested separately as shown in figure 0.27. Sample surfaces show no significant differences: the RMS roughness is in the range of 0.5 to $1.0\,nm$ on $10 \times 10\,\mu m^2$ AFM pictures. Then XRR was performed to assess the surface and interface quality. When surfaces are rough, it increases the rate at which the reflectivity intensity falls down with the angle 2θ (Gibaud, 1999). In the case of multilayers as QW or MQWs, there is periodic oscillations due to the constructive and destructive interferences inside the layer. In presence of interface roughness, these oscillations are dampen as well when 2θ increases. XRR spectra are presented in figure 0.28: periodic oscillations are visible, which comes from the two barrier layers. For samples A and B, the rate at which the specular reflectivity decrease is very similar because the two curves are nearly superimposed. As a consequence, the surface roughness for samples A and B are the similar. On the contrary, the spectrum of sample C exhibits a slower decrease of the intensity with the angle, so it is a proof of a lower surface roughness.

Sample	T QW (°C)	T B (°C)
A	400	240
B	240	240
C	400	400

Figure 0.27.: Growth temperature for the QW and the barrier.

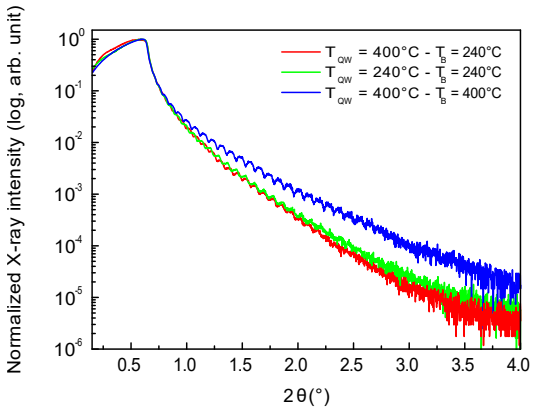

Figure 0.28.: XRR spectra of samples grown at various temperatures.

Regarding the growth temperature, we can conclude that changing the QW growth temperature has not a significant influence on the sample's surface or interface roughness. This is not the same behavior for the (Zn, Mg)O growth temperature: increasing it does not change the surface roughness but decreases the interface roughness. On the roughness point of view, it turns out that the growth temperature of the (Zn, Mg)O alloy is the driving parameter whereas the ZnO one has not a significant impact on the temperature range tested.

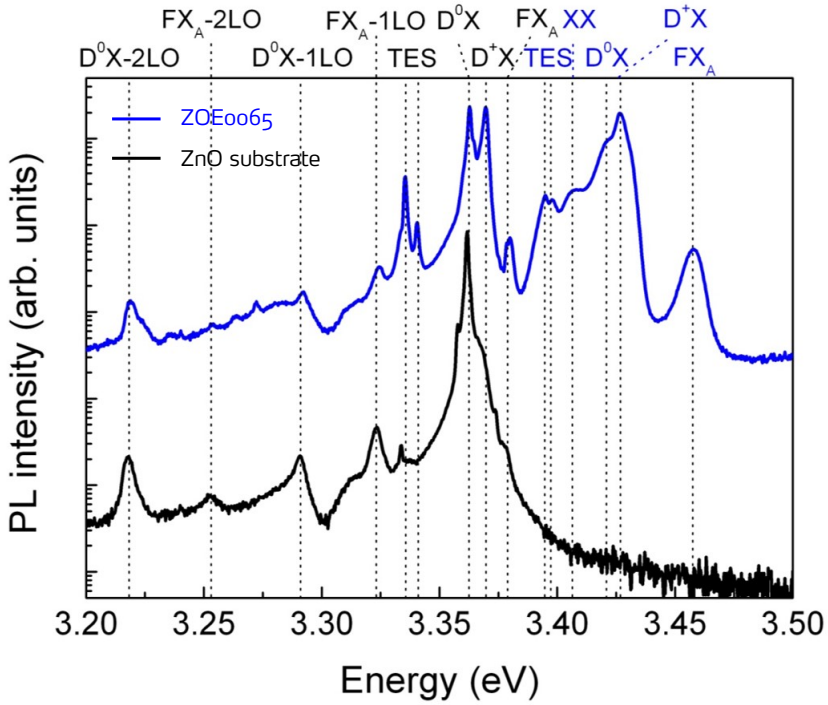

Figure 0.29.: PL spectra of a single QW sample and a m-plane ZnO substrate (respectively in blue and black curves) at 10 K. The QW is 2.9 nm thick, barriers are 80 nm wide and the Mg content is 26 %. The peaks attribution is shown is black for ZnO bulk related transitions and in blue for QW related transitions. The spectra have been shifted vertically in order to be easily compared.

Before describing the PL spectra related to this serie, let us examine typical PL spectra to see the common features observable. Figure 0.29 shows 10 K PL spectra for a ZnO m-plane substrate and a

ZnO/(Zn, Mg)O single QW grown on a m-plane ZnO substrate. By comparing the substrate and the QW spectra, we can easily distinguish two peaks families: one related to emissions from the bulk ZnO and another related to the QW emission. The emission lines related to the QW are at higher energy compared to those related to the ZnO bulk due to the quantum confinement. It is true here because there is no QSE, otherwise, QW emission lines at lower energies compared to the ZnO bulk ones can be observed Chauveau *et al.* (2009). Let us now focus on the emission lines related to the bulk ZnO. Wurtzite ZnO exhibits three valence bands: A, B and C, which have respectively the symmetries Γ_9, Γ_7 and Γ_7 Birman (1959); Reynolds *et al.* (1999) (see section 0.3.1). As a consequence, the excitonic transitions related to the A, B and C valence bands are possible. Due to the relative energy positions of the 3 valence bands, transitions related to the A valence bands have a higher probability to happen compared to the B and C related transitions because it involves lower energie. This explains partially why in the spectra presented in figure 0.29 does not show B and C related transitions.

Among the possible emission lines, there are intrinsic and extrinsic ones. Intrinsic transitions are related to the material itself if it was perfectly pure, whereas extrinsic are linked to the various impurities or crystal defects that create energy levels within the gap of the semiconductor Özgür *et al.* (2005). Looking at the intrinsic transitions, we can observe an intense emission line around $3.377\,eV$, noted FX_A, which is probably due to the the A free exciton emission of bulk ZnO Teke *et al.* (2004); Thonke *et al.* (2001); Boemare *et al.* (2001). Moreover, we can observe two phonon replicas associated to this free exciton emission, noted $FX_A - 1LO$ and $FX_A - 2LO$, separated to the FX_A peak by the LO phonon energy ($72\,meV$). The observation of such replica is a sign of a good crystalline quality. The first excited state associated to the free A exciton of bulk ZnO, normally at an energy of $3.422\,eV$ Teke *et al.* (2004), is not observed. At slightly lower energies than the A free excitons, two other intense emission lines can be observed around $3.36\,eV$. There are linked to the A exciton bound to a neutral donor. More precisely, the lower and the higher energy excitons are linked to the ground and first exited state, D^0X and D^+X, respectivelly Reynolds *et al.* (1998); Teke *et al.* (2004). We can note also two phonon replica, noted $D^0X - 1LO$ and $D^0X - 2LO$, related to the ground state of the donor bound exciton D^0X. Finally, we can observe a double Two Electron Satellites emission lines (TES) within the energy range $3.32 - 3.34\,eV$, they are associated to the donor bound excitons D^0X and D^+X Thonke *et al.* (2001); Alves *et al.* (2003). The observation of TES is quite useful for the determination of the associated donor binding energy: the energy difference between the ground donor bound exciton and the associated TES is equal to $^3/_4\,E_D$. Thus the presence of a TES line is really useful to analyse which donor is present within the sample Özgür *et al.* (2005).

Similar emission lines can be observed for the QW related emission - in blue in figure 0.29 : the more intense peaks are related to the gound state and first excited state of the donor bound exciton, around $3.425\,eV$, followed by the A free exciton at $3.45\,eV$. We can also observed a double TES lines in the energy range $3.39\,eV$ related to the donor bound exciton.

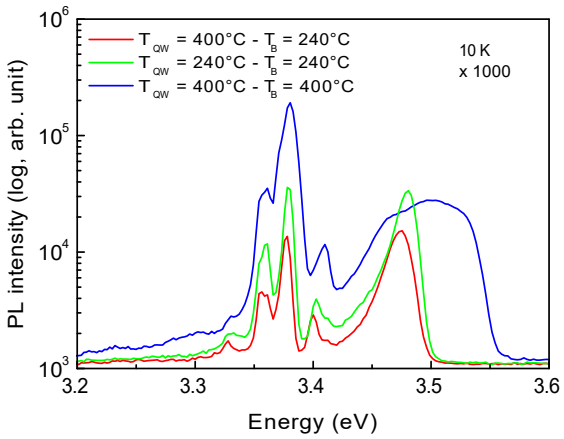

Figure 0.30.: PL spectra at $10\,K$. The intensities are 1000 times larger compared to the spectra shown in figure 0.31

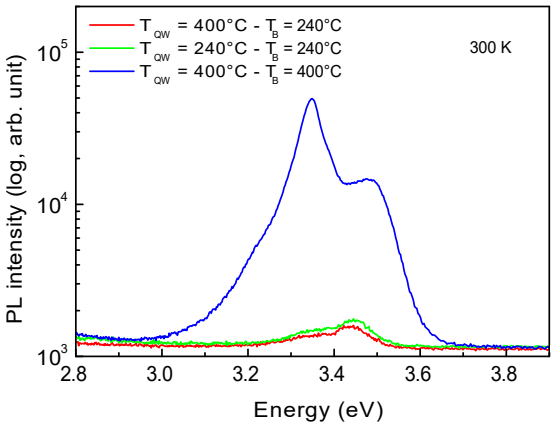

Figure 0.31.: PL spectra at RT.

PL experiments at $10\,K$ and $300\,K$ have been performed to evaluate the influence of the growth temperature on the optical properties. In figure 0.31, the PL spectra at $10\,K$ of samples A, B and C are presented. For all samples the main peak around $3.38\,eV$ is due to the emission of the bound exciton of the QW. At higher energy (above $3.45\,eV$), peaks around $3.4\,eV$ are attributed to the free exciton emission from the QW. The last peaks are related the barrier emission.We can see in figure that samples A and B are quite similar again in terms of intensity and shape of peaks. The sample C has a higher intensity: it is one order of magnitude higher in intensity compared to sample A. In addition, the barrier is much larger: the FWHM (Full Width at Half Maximum) is $83\,meV$ compared to $23\,meV$ for sample A. At $400°C$, the incorporation of Mg in the ZnO lattice is higher than at $240°C$, but a segregation in the alloy appears. At $300\,K$, the difference is striking: more than one order of magnitude between sample C and samples A and B. The ratio between the QW integrated intensity at $300\,K$ and at $10\,K$ is one order of magnitude higher in sample C conpared to the others. This ratio is commonly named IQE (Internal Quantum Efficiency). In this manuscript, it is not used as an absolute value, but as a relative one. Indeed we are not sure that all non-radiative paths are froozen at $10\,K$ in our samples. So it should be seen as a indicator to compare the radiative efficiencies.

Going back to this serie of samples, it seems a high growth temperature on the barrier reduces the non-radiative processes that can be activated with temperature, compared to the lower one, but by increasing the alloy fluctuation.

To conclude this paragraph, the barrier temperature is a key parameter in the growth of ZnO/(Zn, Mg)O heterostructures. We have seen that it lead to a reduction of the interface roughness as stated by XRR experiments. And with the PL analysis, it reduces the non-raditive recombinaisons that can be highly detrimental to the realisation of cascade devices. Thus this study is a good starting point to continue optimizing growth conditions.

II/VI flux ratio

To investigate the influence of the II/VI ratio on the structural and optical properties of ZnO/(Zn, Mg)O heterostructures, we have studied two samples for which the O flux was varied, keeping other growth parameters constants (growth temperature, Zn and Mg cells temperature). Sample A was grown with a O flux of 1 sccm, and sample B with 0.7 sccm. The structure of these samples is illustrated in figure 0.32. They consist of a single quantum well of $3\,nm$ embedded in thick (Zn, Mg)O barriers. XRR experiment was performed to measure thicknesses and we found for sample A: $2.8\,nm$ for the QW and $76.2\,nm$ for the barrier. For sample B we found $2.9\,nm$ and $79.0\,nm$ for the QW and the barrier respectively. Apart from the thicknesses difference, XRR spectra of the two samples are very similar in terms of interface roughness since the overall intensity decreases and the fringes damping are the same.

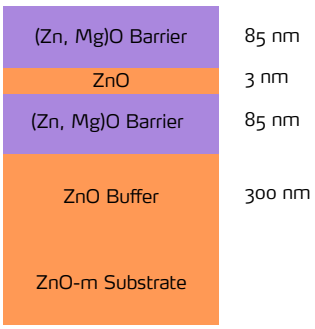

Figure 0.32.: Nominal samples' structures. The targeted value for the Mg content is 25 %.

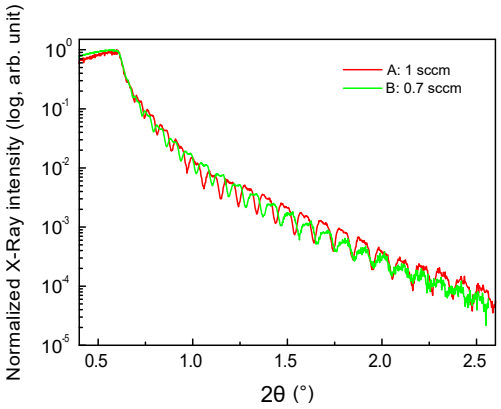

Figure 0.33.: XRR spectra of samples A and B.

On the surface, the two samples exhibit stripes oriented along the c-axis, a feature which is typical of m-plane ZnO surfaces (figures 0.34 and 0.35). This pattern comes from the difference of adatom diffusivity on the sample surface duiring the growth. The diffiusion is easier along the c-axis direction, than along the a-axis, giving rise to this typical stripes on the surface (Matsui & Tabata, 2006). From the roughness point of view, the sample B is nearly twice rougher compared to the sample A (figures 0.34 and 0.35). Looking at the mean stripe width, it varies between $29\,nm$ to $47\,nm$ when decreasing the O flux. From this observation, we can infer that the II/VI modifies the diffusivity of adatoms on the surface, which can be seen on the AFM pictures 0.34 and 0.35.

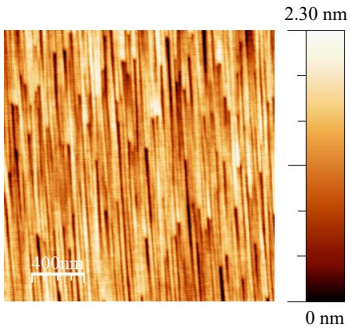

Figure 0.34.: AFM picture of sample A. The RMS roughness is 0.40 nm and the mean stripes width is 29 nm.

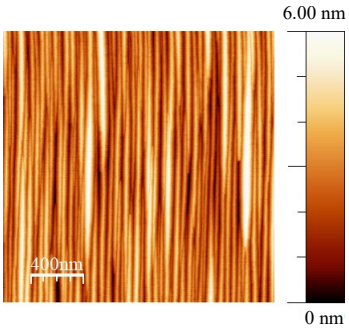

Figure 0.35.: AFM picture of sample B. The RMS roughness is 1.00 nm and the mean stripes width is 47 nm.

The optical properties were investigated by means of PL between 10 K and 300 K. The Mg contents are 22 % and 23 % for sample A and B respectively (see 0.4.4). From the temperature dependant measurement, we can calculate the integrated intensity for both the exciton linked to the QW and the one linked to the barrier. In figure 0.36, the normalized curves are presented. For both samples, the integrated intensity of the barrier decreases rapidly starting from a temperature of 100 K. In the barrier of sample B, we observe a slight increase of the integrated intensity around 30 K, indicating that additional carriers injected inside the barrier recombine radiatively. After this slight increase, the curve follows closely the trend of sample A. Focusing now on the evolution of the integrated intensity of the QW, the two samples exhibit maxima around 240 K. Here again, this can be explained by a possible increase of the injection of carriers inside the QW. As this maximum appears at the same temperature range when the barrier intensity begins to steeply fall down, we can suppose that additional carriers are provided by the barrier itself. But for sample A, the integrated intensity begins to decrease regularly from 30 K to 90 K and increases afterwards. On the contrary, sample B exhibits a regular increase of the integrated intensity from the lower temperature to the maximum at 240 K. So we can infer from these trends that sample A may have defects that are activated in the range of temperature $30 - 90\,K$. They may come from the fact that the oxygen flux was more important compared to sample B.

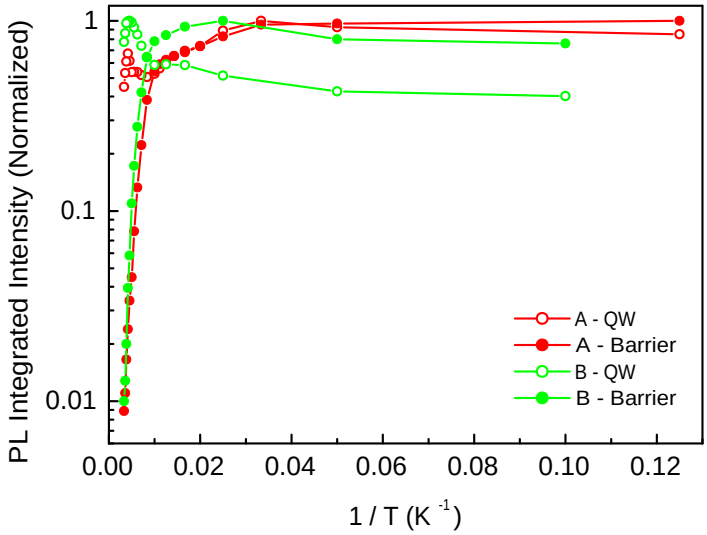

Figure 0.36.: Normalized PL integrated intensity as a function of $1/T$ for samples A (red) and B (green).

CL (Cathodoluminescence) at RT was perform to have get an insight about the non-radiative defects. We have seen with PL measurements that the ratio of integrated intensities between $10\,K$ and $300\,K$ depends on the non-radiative defects that are activated when the temperature raise. Sample A and B exhibit very different ratios: A has an IQE of 53% and B of 77%. Thus we can expect very different features from the CL measurements. In figures 0.37 and 0.38 are shown the CL pictures of the 2 samples on a scale of several tens of micrometers. We observe that for sample A a lot of dark points on the CL picture, which represents non-radiative recombinaison centers, whereas for sample B there is only few ones. We see on both CL pictures two kinds of non-radiative defects: one kind with a little section and another with a bigger one. For sample A most of defects are with the little section, whereas for sample B there are only few of them and the majority corresponds to defects with the larger section. So by reducing the O flux, defects with the little section are nearly suppressed. This piece of information may explain the differences seen in PL between the evolution of the integrated intensity for the QW (figure 0.36).

It is difficult to state about the influence of the O flux on the other defects. On sample A there is so many defects that we can not distingish between a defect with large section from an agregate of defects with a smaller one.

The exact nature of these defects is still unclear, but there are probably not related to dislocations because:

1. the m-plane orientation is not favourable to their nucleation (see section 0.7) and ZnO homoepitaxy has been shown to suppress these defects (Chauveau *et al.*, 2010).

2. on all the TEM (Transmission Electron Microscopy) cross-sections that have been prepared on various m-plane homoepitaxialy grown samples, no threading dislocation was detected.

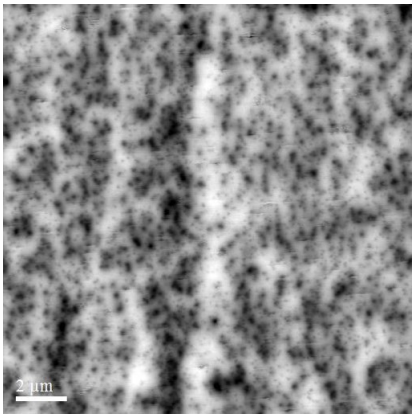

Figure 0.37.: CL picture of sample A at room temperature. The dark points represent non-radiative defects.

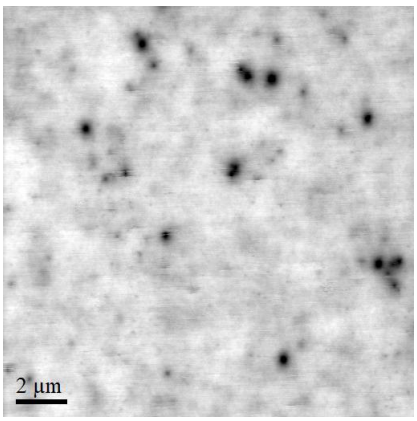

Figure 0.38.: CL picture of sample B at room temperature.

Our CL setup is coupled with a SEM (Scanning Electron Microscopy), so we can record the CL picture and the corresponding SEM one. In figure 0.39 we see a superposition of the CL and the SEM image. Images are treated using the software ImageJ. From the CL picture the dark points with the larger section are isolated and this image is superimposed to the SEM one. We observe that it exists a perfect match between the defects with the larger section and the surface morphology. At a larger scale, we can see that some stripes are more distinct that the ones shown on the AFM pictures (figures 0.34 and 0.35). This kind of defects are located at the tip of stripes, and only on the same extremity.

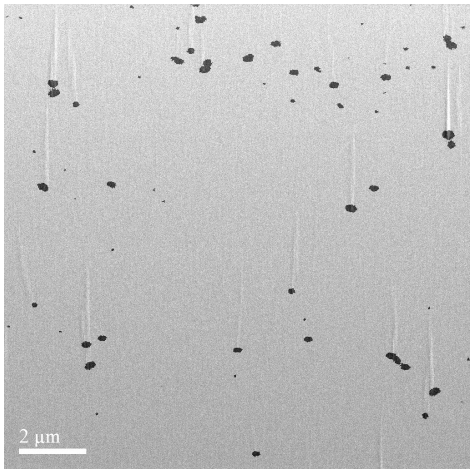

Figure 0.39.: Superposition of CL picture at room temperature with the SEM image. This images comes from another sample with similar defect density as sample B and was chosen for more clarity. The same phenomenon occurs for sample A and B.

SEM image of the surface of sample A and B are presented in figures 0.40 and 0.41 respectively. The number of enhanced stripes are nearly identical for the two samples. We can deduce that the O flux has no significant influence on the number of enhanced stripes, so no influence on the concentration of defects with the larger section. Since these defects are present with the same density in the two samples, they are not responsible for the large drop of the quantum efficiency observed in

PL. Moreover, since they are linked to surface morphology, we can hypothesise that they are present only on the surface. If it is the case, since the QW is 75 nm far from the interface, this could explain that this kind of defect do not play a major role in the QW radiative properties.

By opposition, the defects with the smaller cross-section probably play a non negligible role on the drop of IQE between the sample A and B.

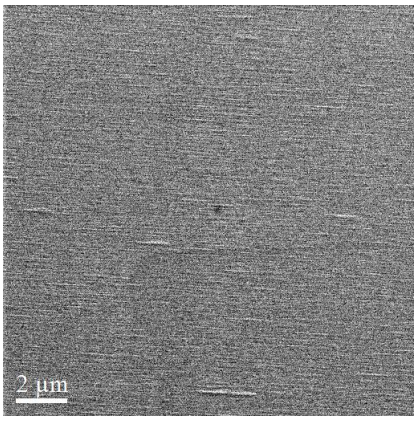

Figure 0.40.: SEM image in plane view of sample A.

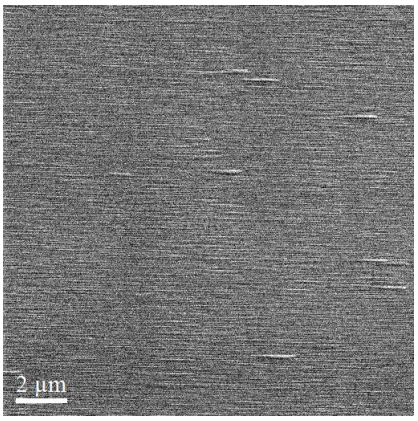

Figure 0.41.: SEM image in plane view of sample B.

To summarize, the diminution of the O flux gives rougher surfaces but still abrupt and coherent interfaces inside the layer. PL experiments reveal that it is favourable to the radiative efficiency by increassing the IQE ratio from few to 77 % when the O flux decreases from 1 to 0.7 sccm. This difference can be linked to the presence of less non-radiative defects with a small section as stated by CL experiments. The nature of defects are unknown, but they are unlikly related to dislocations.

Growth interruption

The effect of the growth interruption have to be adressed in view of complex device realisations. For instance, the Mg content or the doping may change from one layer of the cascade structure to another. Thus, growth interruptions are mandatory to stabilize cell temperature. Up to now, no articles report on the influence of growth interruption in ZnO-based heterostructures. But this topic is well documented for the GaAs material system, for which the growth is well known and controlled. Growth interruption in GaAs/AlGaAs QWs is known to leed to smoother interfaces by letting the surface adatoms diffuse and find there right place. As a consequence, an increase of the RHEED intensity can be observed during the growth interruption as well as a significant reduction of the PL peaks FWHM (Tanaka & Sakaki, 1987) (Tu *et al.*, 1987). Only few secondes are needed to see this effect. In our case, the growth interruption is much longer, so it can lead to the incorporation of indesirable atoms, thus creating defects.

We have grown two samples named A and B, whose structures are described in figures 0.42 and 0.43. They consist of single QW embedded in thick barriers. Sample A has been grown with growth interruptions of 10 minutes between each epilayer whereas sample B undergo no growth interruption steps.

The samples surface are identical: the typical stripes elongated toward the c-axis were visible and the RMS roughness on a $100\,\mu m^2$ is $0.5\,nm$ for both samples (not shown).

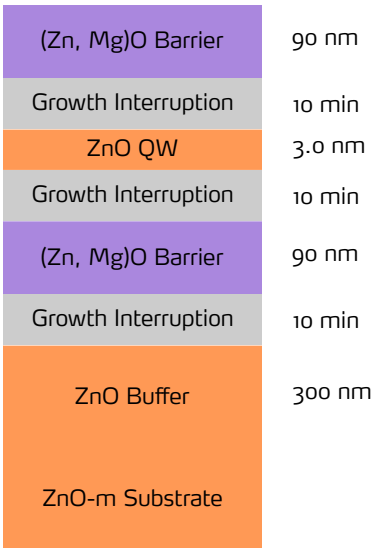

Figure 0.42.: Structure schematic of sample A. A growth interruption steps of 10 minutes was added between each epitaxial layer.

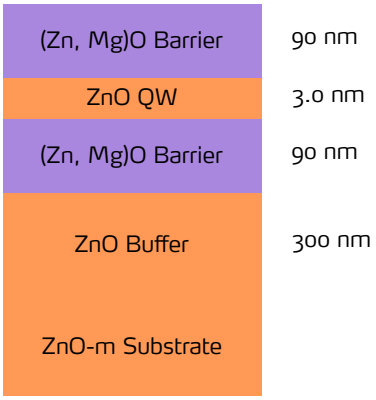

Figure 0.43.: Structure schematic of sample B. The same structure of sample A, without the growth interruption steps.

In order to investigate the influence of the 10 minutes of growth interruption steps led to an incorporation of non-radiative defects. PL measurement were performed. In figure 0.44, the spectra at $10\,K$ are presented. The most intense peak is linked to the emission of the bound exciton in the QW. At a lower and higher energy from this main peak, we can see respectively the exciton of the ZnO substrate and the free exciton of the QW. The large peaks at higher energy can be attributed to the exciton in the barrier. There is no noticeable intensity change in the spectra at low temperature. Going at RT, figure 0.45 shows two main peaks: the spectrum is dominated by the free exciton of the QW and at higher energy stands the exciton of the barrier. Contrary to the other PL spectra, the barrier is present both at low temperature and at RT because it is larger compared to the diffusion length of excitons. Here we see a slight intensity decrease for the sample A. But this difference is not strong enough to be clearly attributed to the growth interruptions steps.

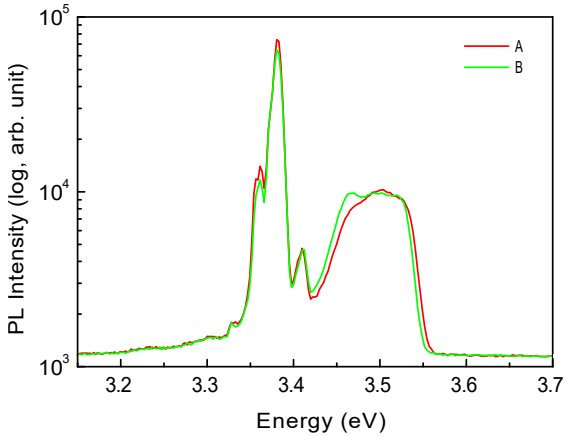

Figure 0.44.: PL spectra at $10\,K$ of samples A and B.

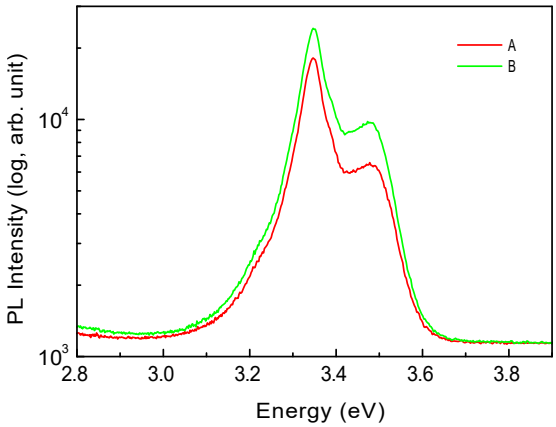

Figure 0.45.: PL spectra at $300\,K$ of samples A and B.

The normalized PL integrated intensity for the QW as a function of the temperature is shown in figure 0.46 for the two samples. Here again, no difference can be seen between the two curves. So we can conclude that the 10 minutes growth interruption steps does not lead to a significant augmentation of defect incorporation. We can infer that growth interruption steps during the growth of the device structure will not influence its performance.

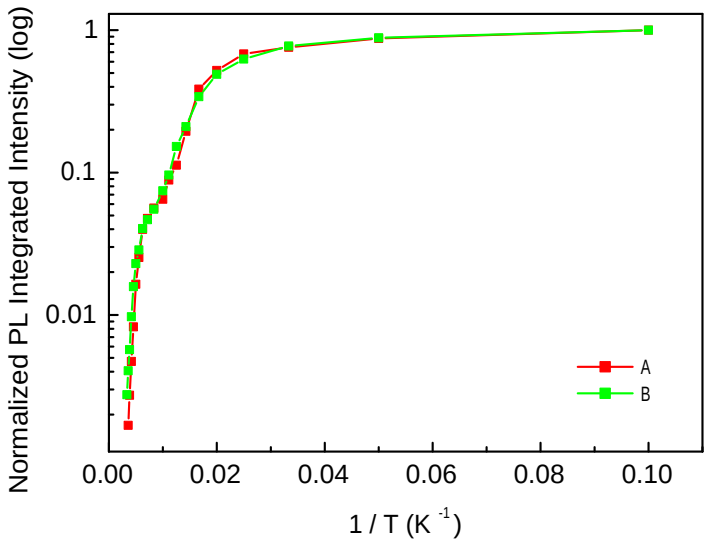

Figure 0.46.: Normalized PL Integrated Intensity from the QW for the two sample.

0.4.4. Calibration procedure

Calibration layers are essential to follow growth condition deviations of MBE. In our case, calibration focuses on several parameters: thicknesses, Mg content and n-type doping. We have designed a sample to make us able to determine precisely each of the former parameters. The structure is represented in figure 0.47. It consists of a (Zn, Mg)O tracer followed by a ZnO buffer followed by another one of (Zn,Mg)O and finally a 20 periods MQWs of ZnO:Ga/(Zn,Mg)O. The role of the

(Zn,Mg)O tracer is to be able to differenciate the ZnO from the substrate from the one of the buffer layer.

Thicknesses calibration

Thickness measurement is based on SEM measurement and on XRR. The sample is freshly cleaved and its cross-section is observed in SEM from which we measure the thick buffer of ZnO and the thickness of the MQW with the (Zn,Mg)O buffer (figure 0.48).

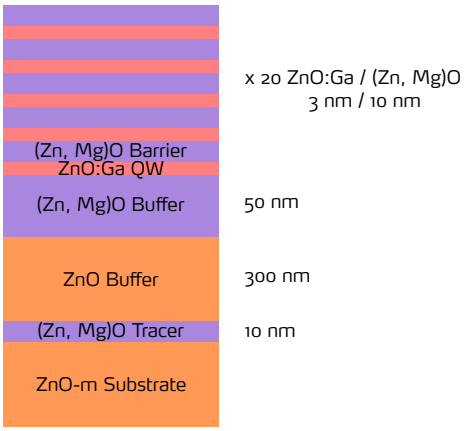

Figure 0.47.: Calibration layer structure.

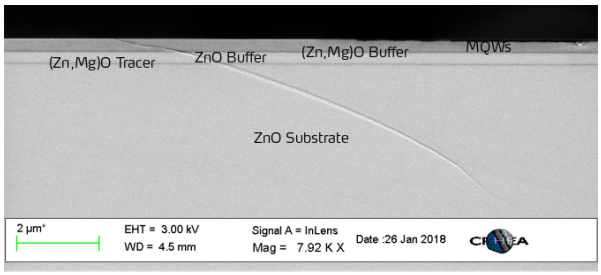

Figure 0.48.: SEM cross-section of a calibration layer.

Knowing the growth time of each layer, we can first have a good estimation of the ZnO growth rate. Growing a thick ZnO buffer reduces the error made on the thickness measurement. For the thickness of the MQW with the (Zn,Mg)O buffer layer: we can use the ZnO growth rate and the total growth time of ZnO and (Zn,Mg)O to determine the (Zn,Mg)O growth rate. The errors on the ZnO and (Zn,Mg)O growth rates are estimated through the error on the thicknesses (we assume that the error on the growth times are negligible compared to the thicknesses error). Thicknesses are measured on several images taken on different regions of the sample, from which a mean value and a dispersion are calculated according to equation 0.22. The typical error is in the range of ± 5 to $10\,nm/h$ for growth rates of $180 - 230\,nm/h$.

$$\Delta t = \sqrt{\frac{1}{n-1}\sum_{i=0}^{n}(t_i - < t >)^2} \tag{0.22}$$

With $< t >$ the mean value of thickness and t_i represents all thicknesses measured by SEM cross-section. The total number of thicknesses measured, n, is typically in the range of 5 to 10.

This is a reasonable error for thick layers, but is it not sufficient for the active region of the QCL, where layers are typically of few nanometers or less. In this frame, a precision on the monolayer scale is required, this is why XRR is used in a second time in the calibration procedure.

In figure 0.49, a XRR spectrum of a calibration layer is presented. The spectrum exhibit several sharp peaks regularly spaced with respect to the angle θ. The origin of these peaks comes from the periodic nature of the layer. This allows to observe constructive and destructive interferences. This is exactly what is evidenced in figure 0.49, where the sharp peaks corresponds to constructive interferences. It is possible to get to the root of the repeated thickness which triger these interferences by using a formula which came from this analogy with optics Moram & Vickers (2009):

$$\sin(\theta_{i+1})^2 + \sin(\theta_i)^2 = (2m_i + 1) \times \left(\frac{\lambda}{2t}\right)^2 \tag{0.23}$$

As for reflectivity, the incoming beam arrive at grazing incidence - from 0.1° to 4° - it is reasonnable to make the following approximation: $\sin(\theta_i) \approx \theta_i$. So 0.23 becomes:

$$(\theta_{i+1})^2 - (\theta_i)^2 \approx (2m_i + 1) \times \left(\frac{\lambda}{2t}\right)^2 \tag{0.24}$$

Where i points out the number of a peak, θ_i is the angle at which the peak i appears, and m_i is the order of the interference for the peak i. λ is the X-Ray wavelength and t is the thickness. In order to determine this thickness, one can plot $(\theta_{i+1})^2 + (\theta_i)^2$ as a function of $(2m_i + 1)$. Note that the knowledge of the order m_i is not required because the important parameter is the variation of $(\theta_{i+1})^2 + (\theta_i)^2$ when m_i increases. Thus this curve slope - $\left(\frac{\lambda}{2t}\right)^2$ - leads to the thickness t with the required precision. In this example, we found $18.0\,nm$, which represents the thickness of one QW and one barrier together.

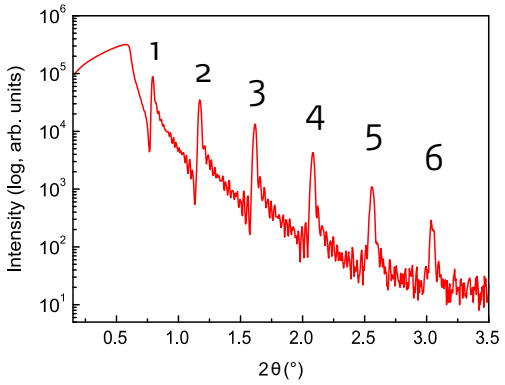

Figure 0.49.: Typical XRR spectrum of a calibration layer. The thickness related to the interference peaks is $t = 18.0\,nm$.

But we need to determine precisely the different contributions of the QW and barrier within t. We took into account the growth rates of ZnO and (Zn, Mg)O determined by SEM as well as the growth time.

By combining SEM and XRR experiments, we are able to measure the QW and the barrier thickness with a precision of one ML.

Mg content calibration

The Mg composition is routinely measured PL at RT. There is a linear relation between the band gap of the (Zn,Mg)O alloy and its Mg content (figure 0.50). From the litterature, the (Zn,Mg)O band gap raise by 25 meV per percent of Mg (Neumann *et al.*, 2016). Using EDX (Energy Dispersive X–ray spectroscopy) and PL, we found only a value of 20 meV. This discrepancy can be explained by the techniques used: in (Neumann *et al.*, 2016), ellipsometry has been carried out, which lead to the band gap determination. On the other side, PL gives access to the excitonic band gap which can be modulated by localization effects (figure 0.51). These localization effects arise when there is a potential fluctuation within the alloy, which can originates from composition fluctuations. It is known that localization effect becomes more important as the Mg content increases (Sun *et al.*, 2002) and increases the transition energy measured in PL experiment. In addition, the exciton binding energy exhibits a similar evolution with the Mg content, thus participates to the increase of the transition energy measured as well (Sun *et al.*, 2002). These two phenomena lead to the slower evolution of the excitonic band gap with the Mg content with respect to the bare band gap measured in (Neumann *et al.*, 2016).

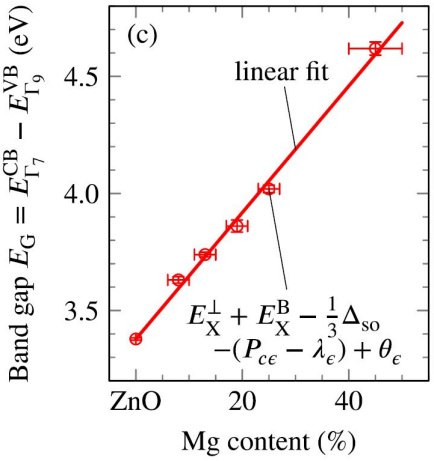

Figure 0.50.: Evolution of the (Zn,Mg)O band gap with the Mg content. *Reprinted from (Neumann* et al.*, 2016), with the permission of AIP Publishing.*

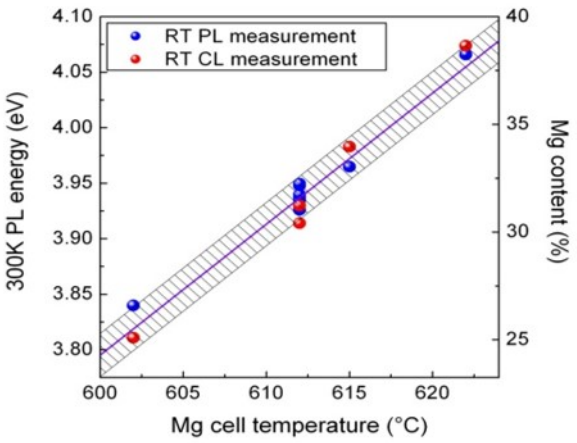

Figure 0.51.: Evolution of the (Zn,Mg)O excitonic band gap with Mg content measured in CRHEA by PL and CL experiments on various samples. The hatched region corresponds to an error bar of $\pm 1\,\%$ of Mg.

The Mg measurement is possible because of the (Zn, Mg)O buffer inside the calibration layer. Without it, the (Zn, Mg)O excitonic peak would not be visible because the diffusion length of excitons is larger than the typical barrier thickness. So we infer that most of the excitons recombine inside the QW.

However, an alternative determination for the Mg concentration has been setup during the project. It is based on reflectance spectroscopy in the IR range which is conducted by our partners at UPM. The physical principle is the Berreman effect Berreman (1963) which can be used to detect by optical means phonon absorption in a bulk material. Depending on the incidence angle of the probing light

and its polarization, either TO or LO-phonon frequencies can be accessed. In addition, it is known that the LO-phonon frequency of the hexagonal (Zn, Mg)O alloy is increasing with the Mg content Bundesmann *et al.* (2006). In this study, the alloy LO-phonon frequencies were determined by IR spectroscopic ellipsometry for c and a-plane orientation. For the non-polar orientations, a specific care should be given to the fact that the in-plane arrangements of atoms are not isotropic, thus leading to a change in the phonon modes frequencies. This is why reflectance spectroscopy experiments were conducted regarding the orientation of the incident electric field with respect to the crystal c-axis.

Coming back to the Berreman effect, (Zn, Mg)O LO-phonons can be detected using p-polarization (TM) at oblique incidence. The situation is more complicated in the case of MQWs in which the (Zn, Mg)O layer is thin (typically less than $15\,nm$). The Berreman effect is no more related to single phonons, but to IR interface phonon-polaritons that arise in polar semiconductor heterostructures Schubert *et al.* (2005).

Figure 0.52 shows typical spectra for MQW samples with different Mg compositions taken by our colleagues at UPM. Each sample presents a region below $600\,cm^{-1}$ where the reflectance is very high: this is the combinaison of the reststrahlen bands of both ZnO and (Zn, Mg)O. After $600\,cm^{-1}$, the samples exhibit two dips. The dip around $600\,cm^{-1}$ is related to the LO-phonon polariton of ZnO, which is at the same position for both samples. And around 650 and $675\,cm^{-1}$ they are related to the interface LO-phonon polariton. It can be seen clearly that these frequencies are shifted according to the nominal Mg content. Figure 0.53 shows a zoom in the region where the dip of the alloy LO-phonon polariton shows up for various Mg content going from 22 to 41 % by following the black arrow. We can observe that the wavenumber continously increases with the Mg content. Some dips are more pronounced due to different doping levels inside the QWs. The more the QW is doped, the better the dip is defined. This is an addtionnal proof of that this effect has not only a phonon contribution, but also an interface plasmonic one.

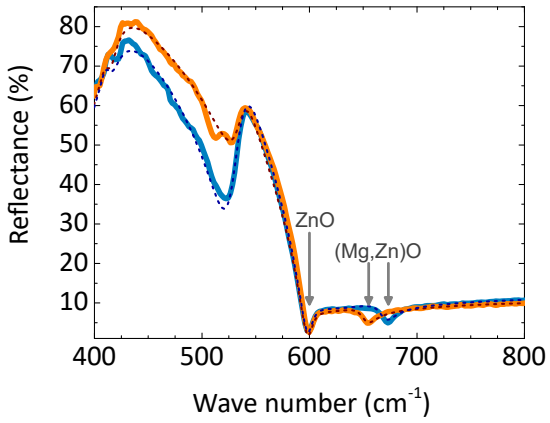

Figure 0.52.: Reflectance spectra taken in p-polarization at 30° of incidence of 2 MQWs based samples. The nominal Mg content for the sample described by the orange curve is 30 % and 34 % for the blue one. The thick lines are experimental curves and the dotted curves the fitted ones.

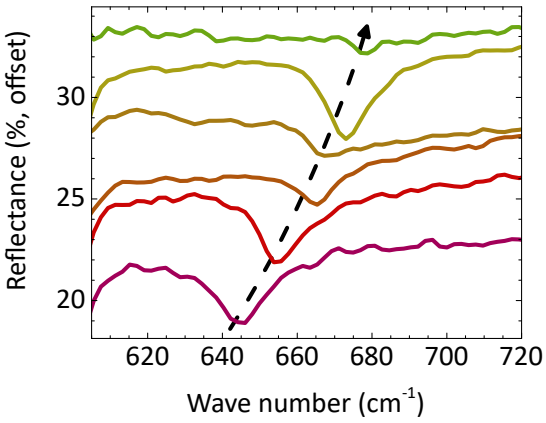

Figure 0.53.: Zoomed reflectance spectra taken in p-polarization at 30° of incidence of various MQWs with nominal Mg content ranging from 22 to 41 % according to the black arrow.

To extract the bare alloy LO-phonon frequency ω_{LO}, the dielectric function of the whole layer should be computed to fit the reflectance curve.

Compared to PL, this method has the advantage to give the Mg content in thin (Zn, Mg)O layers (less than $15\,nm$). This can be very useful for devices in which there is no (Zn, Mg)O buffer layer, while PL measurements on a calibration layer rely on this buffer layer. It has been experimentaly demonstrated for QWIPs (Quantum Well Infrared Photodetector) for which the Mg content determination would have required a destructive method as STEM-HAADF or SIMS.

Ga doping calibration

For the doping, two cases need to be consider depending on the targeted doping range:

- if the doping is in the range of 10^{15} to $10^{17}\,cm^3$, it is measured by C-V method on a thick ZnO:Ga layer (at least $1\,\mu m$ thick).
- if the doping is greater than $10^{18}\,cm^3$, it is measured by IR reflectance spectroscopy on the calibration layer presented in figure 0.47.

For the C-V profiling method, the layer is contacted in order to apply a voltage through it. The application of this voltage causes carriers to migrate from one point to another inside the sample. As a consequence, it creates a zone where there is no free carrier inside the sample: the space charge zone, or depletion zone. Then the voltage is varied in order to change the width of this zone and the capacitance of the depletion zone is measured for each applied voltage. In our case, the C-V measurements are performed by using a MIS structure (Metal - Insulator - Semiconductor). This technique allows to determine the ionised donors, which should be distinguished from the doping itself. However, these densities can be equal in specific cases. For instance, if the dopants are homogeneously spread and all activated and if the compensation is negligible. In the case of n-type doping in ZnO done by the introduction of Ga atoms the compensation of the n-type doping by p-type one is only $20\,\%$ for a doping levels as high as $1.7 \times 10^{20}\,cm^{-3}$ for layer grown by MBE Brochen *et al.* (2017).

For reflectance spectroscopy, as grown samples are used and oriented as shown in figure 0.54. Experiments were conducted at RT at UPM using a FTIR spectrometer and a wire grid in order to be able to select the incoming light's polarization (p or s-polarization). As wurtzite ZnO and (Zn, Mg)O are asymmetric crystals, they exhibit asymmetric optical properties known as birefringence. In this case the birefringence is uniaxial: there is an extraordinary refraction index n_e for polarizations states perpendicular to the c-axis, and an ordinary one n_o for polarization states parallel to the c-axis (Özgür *et al.* (2005)).

For reflectance experiments, the sample is oriented so that the c-axis always lies perpendicular to the incident electric field whatever the polarization state selected. As a consequence, the wurtzite crystal appears as optically isotropic for the two polarization states.

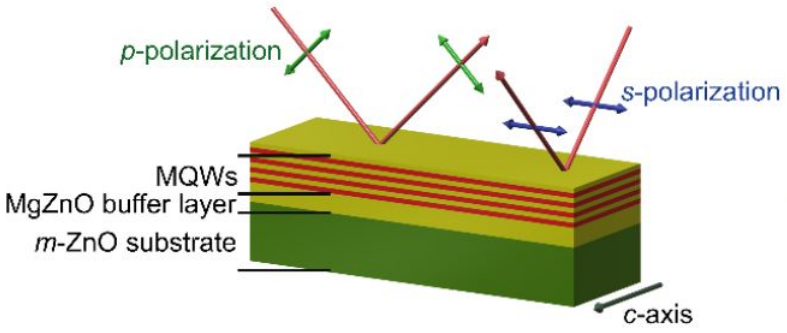

Figure 0.54.: Schematic of the reflectance experiment with the two polarization states used with respect to the sample's orientation. *Montes Bajo* et al. *(2018b), © figure used under the Creative Commons Attribution 4.0 International Licence. To view a copy of this licence, visit: URL*

The extraction of the doping level inside the QW rely on the observation of Multisubband Plasmons (MSP). In highly doped QWs - with doping higher than $10^{18}\,cm^{-3}$ - several ISBT can take place and coupled together to give rise to a single transition called MSP. This phenomenon is possible in particular in ZnO based heterostructure because of two features:

- effective masses are very high (in the range of 0.28 - 0.32 m_0) compared to other semiconductors like GaAs ($\sim 0.06\,m_0$), which allows to have flatter bands in k-space.

- doping as high as $5 \times 10^{21}\,cm^{-3}$can be achieved, as well as a low residual doping, which allows to have a large range of doping possible inside the QW.

These two features allow a high density of electrons in a relatively narrow energy range inside the same QW Montes Bajo *et al.* (2018b). As a consequence, several ISBT can take place as shown in figure 0.55 and can couple. Instead of measuring optically each single ISBT, only one single transition arises, which is shifted in energy compared to the bare ISBTs. This shift becomes more pronounced as the electron concentration inside the QW increases Delteil *et al.* (2012).

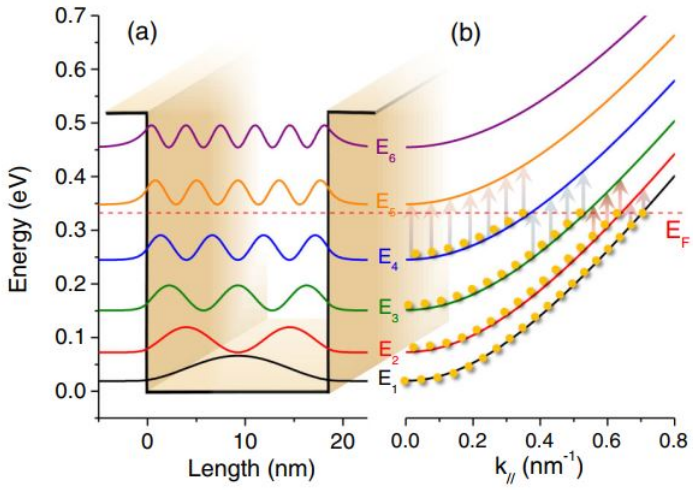

Figure 0.55.: Schematic showing the electron wave functions within a QW together with the Fermi level E_F. Dispersion for energy levels are shown in parallel to visualize the possible ISBT. *Reprinted figure with permission from Delteil* et al. *(2012), Copyright (2012) by the American Physical Society. URL*

Coming back to the determination of the electron concentration, the reflectance spectrum must be fitted using a dielectric model which takes into account all sample layers. Detailed expressions can be found in Montes Bajo *et al.* (2018b). Here, we only detail the different contributions in order to give an idea of the physics behind this model.

For the (Zn, Mg)O barrier, the dielectric constant is isotropic and takes only into account the interactions between the phonons and the incoming light. This contribution also appears in the case of the doped ZnO QW. For the ZnO QW, at least two other contributions to the dielectric function appear. One reports on the effect of the interaction between the incoming light and the electrons inside the QW. This part is described using the Drude's model and acts in the QW's plane only. The last contribution is the coupling between the incoming light with the ISBT that are allowed, which happens out of the QW's plane.

Depending on the doping level inside the QW, this last ISBT contribution can change to take into account the coupling that can arise between them (MSP contribution).

Thanks to these different contributions, the whole dielectric function of the sample can be computed and compared the reflectance spectra (figures 0.56 and 0.57). An undoped sample is taken as a reference in order to adjust the parameters related to the light-phonon interaction both in ZnO and in (Zn, Mg)O. Then these parameters are used in order to fit the reflectance spectrum of a doped sample for which the only free parameters are related to the electron concentration inside the QW.

Typical reflectance spectra taken under s and p-polarization are shown in figures 0.56 and 0.57. The main difference between the spectra taken under s and p-polarization lies in an absorption for the doped sample under p-polarization (see figure 0.57 around $2400\,cm^{-1}$). This absorption corresponds to MSP inside the QW since it is only seen under p-polarization (see 0.8.1 for explanations about the ISBT selection rule). The undoped sample show no absorption linked to MSP because its doping is not sufficient. The detection limit in terms of doping using this method is around $1.5 \times 10^{18} cm^{-3}$ and the error made on the doping determination is estimated at $\pm 7 \times 10^{17}\,cm^{-3}$.

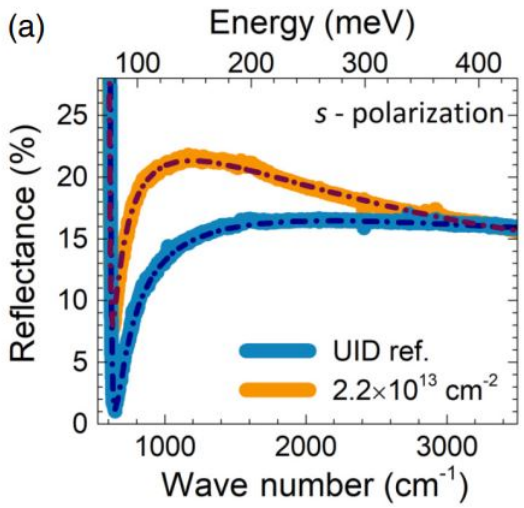

Figure 0.56.: IR Reflectance spectra of MQW samples doped at $6 \times 10^{19}\,cm^{-3}$ and undoped (respectively yellow and blue curves) taken under s-polarization. Both samples have the same QW and barrier thicknesses - $4.0\,nm$ and $15.0\,nm$. Dotted lines correspond to the fitting of the experimental spectra. *Montes Bajo* et al. *(2018b), © figure used under the Creative Commons Attribution 4.0 International Licence. To view a copy of this licence, visit: URL*

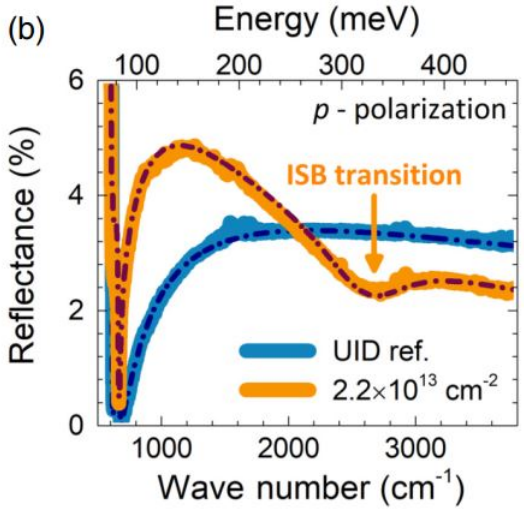

Figure 0.57.: IR Reflectance spectra of MQW samples doped at $6 \times 10^{19}\,cm^{-3}$ and undoped (respectively yellow and blue curves) taken under p-polarization. Both samples have the same QW and barrier thicknesses - $4.0\,nm$ and $15.0\,nm$. Dotted lines correspond to the fitting of the experimental spectra. *Montes Bajo* et al. *(2018b), © figure used under the Creative Commons Attribution 4.0 International Licence. To view a copy of this licence, visit: URL*

To summarize the advantages and disadvantages of the two methods presented above, they allows to measure the carrier density within ranges that are complementary. Thereby the C-V method is suitable for low carrier densities: from 10^{15} to $10^{17}\,cm^{-3}$ whereas the MSP method is suitable for higher carrier densities: from 10^{18} to $10^{21}\,cm^{-3}$. Thus a large range of carrier densities can be accessed by choosing one of these two methods. The main difference stands on the sample's design that should be used to carry the measurements. In the case of C-V, a dedicated µm thick sample should be grown and process needs to be done in order to contact the layer and apply a voltage and to avoid that the layer is fully depleted. By changing the applied voltage, the carrier density can be deduced as a function of the sample's depth. Thus carriers inhomogeneities can be detected. In the MSP method, carrier density is measured from heterostructures with thin layers (typically under $15\,nm$), which can be implemented directly on device's structures because it is non destructive (for instance QWIPs, see Montes Bajo *et al.* (2018b)). But in order to increase this method efficiency, it is better if the sample's structure is known in advance (layers stack and thicknesses) in order to fit the reflectance spectrum. In the dielectric function model, the carrier density in each single layer is assumed to be homogeneous. This hypothesis has been checked by SIMS analysis (see 0.5.1).

0.5. Structural and optical characterization

0.5.1. Doping

Residual doping

Low residual doping is mandatory when growing layers for realizing QCL: it helps limiting the detrimental impact of electron/electron scattering and free-carriers absorption on the device's operation. For that purpose, the MBE system used is new and fully dedicated to the project, so that memory effects due to shared activities involving other materials can be discarded. It is has already been reported that several parameters can influence the residual doping in ZnO thin films. This is the case of the growth method, the growth conditions, and other steps that can be added during or after the growth as annealing Brochen *et al.* (2014).

Looking at ZnO layers grown by MOVPE on ZnO O-polar substrates, the residual doping lies in the range of $10^{16}\,cm^{-3}$ Brochen *et al.* (2014), which is not compatible with QCL's growth. However, it has been reported that a residual doping of $10^{15}\,cm^{-3}$ can be achieved for (Zn, Mg)O layers grown on Zn-polar ZnO substrates Akasaka *et al.* (2010), which means that plasma MBE seems to be a good option to lower the residual doping in ZnO layers. Another parameter that can influence the residual doping is the orientation: in Taïnoff *et al.* (2011), authors demonstrate a residual doping of $10^{14}\,cm^{-3}$ using m-plane ZnO substrate and plasma MBE. Thus by using plasma MBE and m-plane orientation together, residual doping in line with QCL growth is possible.

We have grown thick nid ZnO m-plane layers on ZnO substrates, and we have checked the influences of the growth temperature and the II/VI flux ratio on the residual doping measured by C-V. The results of C-V measurements are shown in figure 0.58. When the growth temperature is decreased from $280°C$ to $240°C$, keeping the II/VI flux ratio constant, the residual doping is decreased by nearly one order of magnitude (see the green and blue curve in figure 0.58 respectively). It seems contradictory with what Taïnoff *et al.* (2011) observed. They varied the growth temperature from $370°C$ to $550°C$ and observed no change in the residual doping level. But in our case, the temperature range is nearly $100°C$ lower. Moreover, a special attention should be given to the fact that using different MBE machines can lead to a shift in temperature. This is what we observed at the beginning of the project when we transfered our activity from the old MBE machine to the new one. So the two results are not incompatible.

The other parameter which was varied during this experiment is the II/VI flux ratio: the O flux was kept constant and the Zn flux changed. We can observe that an increase of the Zn flux leads to a reduction of the residual doping (see the blue and the purple curves in figure 0.58 respectively). This evolution can appear as counter-intuitive because in ZnO, it is commonly accepted that the intrinsic n-type character comes from Zn intersticials and/or O vacancies. But this weird evolution has already been reported by Akasaka *et al.* (2010) in the case of (Zn, Mg)O grown on ZnO Zn-polar substrate. In their article, they made a parallel between what they observed in ZnO and what is known in GaN. In GaN, Ga-rich growth conditions are necessary to obtain the best GaN layers. It seems to favor the mobility of adatoms on the samples surface, which helps to reduce point defects like intersticials and vacancies. The authors propose the same interpretation for ZnO: going towards

Zn-rich conditions may trigger the reduction of point defects which by turn, leads to a lower residual doping. From what we have observed, this hypothesis can be a clue to explain this evolution, but we should be carefull because the growth window explored here is quite narrow, and other trends might be obtained by shifting it. The sample with the lowest residual doping (see the purple curve in figure 0.58) shows a bowing behaviour which is not observed in other samples. With a low carrier concentration, this sample is less conductive and can be subject to charging effects (called MIS-like effects). In order to verify this hypothesis, C-V measurements with a lower frequency can be carry out.

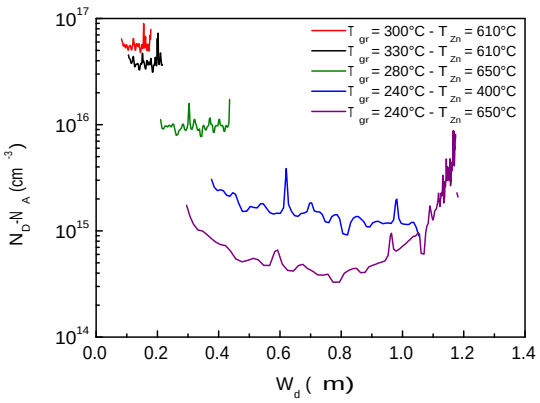

Figure 0.58.: C-V profile of several samples depending on the growth conditions.

In conclusion we achieve a low residual doping, which is a pre-requisite for the targeted application. To obtain it, we have seen that a "new-clean" MBE is not the magic solution to obtain a low residual doping: growth conditions need to be optimized, which enable us to start from $7 \times 10^{17}\,cm^{-3}$ and go down to $3 \times 10^{14}\,cm^{-3}$. This value is comparable to the one obtained by Taïnoff *et al.* (2011) for m-plane ZnO grown on ZnO substrates in plasma MBE. In particular, we have observed that on our growth window, the residual doping can be lowered by changing two parameters: either decreasing the growth temperature or increasing the Zn-flux. But for QCL, having a low residual doping is only the first step: a particular attention should be given to keep a low residual doping just after a doped layer.

n-type doping

To assess the possible range of doping, we have designed and grown the sample shown in figure 0.59. This is a MQW sample which consists of 17 ZnO layers intentionnaly doped with Ga separated with (Zn, Mg)O layers. The doping is increased gradually from $5 \times 10^{16}\,cm^{-3}$ to $5 \times 10^{20}\,cm^{-3}$ as presented in the table 0.3 and then decreased in the same manner. The thickness of the (Zn, Mg)O layers is chosen to let the temperature of the unique Ga cell stabilize between two ZnO doped layers.

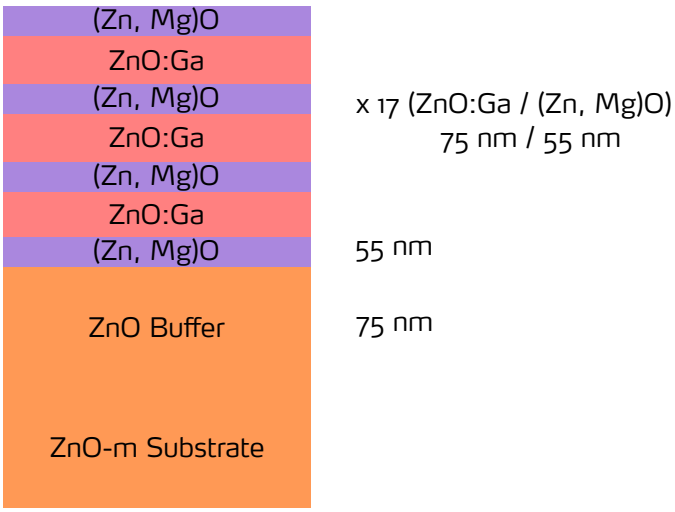

Figure 0.59.: Schematic of the gradually doped sample used for the SIMS measurement.

Layer number	Targeted doping (cm^{-3})
1	5×10^{16}
2	1×10^{17}
3	5×10^{17}
4	1×10^{18}
5	5×10^{18}
6	1×10^{19}
7	5×10^{19}
8	1×10^{20}
9	5×10^{20}

Table 0.3.: Targeted n-type doping of each layer ZnO layer. The layers 10 to 17 have a decreasing doping going from $1 \times 10^{20}\, cm^{-3}$ to $5 \times 10^{16}\, cm^{-3}$ respectively.

In figure 0.60, the SEM picture in cross-section is shown. The highly doped regions in the center of the layer can be very well distinguished from the less doped regions located near the substrate and the surface. In SEM, in image mode, the contrast is a function of the atomic number. The more the atomic number, the more the number of electrons that the incoming electron beam can interact with. As a consequence, (Zn, Mg)O regions appear darker than ZnO ones because the atomic number of Zn is higher than the Mg one. Then the sample was investigated by SIMS at the GEMAC to determine the Ga concentration inside the layers. Unlike C-V or IR spectroscopic measurements, SIMS determines an atom concentration (here Ga). It provides a chemical information rather than an electrical one. In particular, compensation effects are not probed, which can explain some discrepancies between SIMS and electrical measurements (see the paper of (Brochen *et al.*, 2017) for compensation effects in ZnO thin films).

SIMS is a destructive experiment which consists of a beam of primary ions that impinge on the samples' surface. From the various interactions taking place between the incident ions and the sample, atoms and ions can be sputtered out from the sample. They can be analysed by a mass spectrometer to assess qualitatively and quantitatively the atomical contituents of the sample. As atoms and ions are sputtered out from the sample, this technique allows to build a profile of the

sample composition as a function of depth. So at depth zero, the sample surface begins to be removed and the less doped layers are measured, whereas at depth 2.8 μm the entire epilayer has been "etched" and the substrate starts to be attacked. Figure 0.61 presents the variation of the Ga concentration as a function of the depth in the sample. The separation between the epilayer and the substrate is indicated by the dashed line on the SIMS profile (figure 0.61). The profile shows a staircase shape as expected, but which becomes asymmetric for doping values higher than $5 \times 10^{17} cm^{-3}$when the Ga cell temperature is decreasing (left side of the SIMS profile 0.61). As this asymmetric feature is not present when the Ga cell temperature is increased (right side of the SIMS profile 0.61), this can not be due to the measurement of Ga atoms coming from adjacent layers. Otherwise, it would have been displayed by the whole profile. One explanation could be that the Ga cell temperature takes more time to stabilize when the temperature is decreased. So the final doping can be sensibly different depending on how the Ga cell reach a given temperature. In addition, for doping levels between $1 \times 10^{18}\, cm^{-3}$ and $1 \times 10^{19}\, cm^{-3}$, when the doping increased gradually, we can observe that the doping is non homogeneous inside the layers number 3 and 4 from the surface because the Ga cell temperature is not stabilized. It can be noticed that the Ga concentration inside the ZnO substrate purchased from Crystec is in the range of $3 \times 10^{16}\, cm^{-3}$. In Brochen *et al.* (2017), they measured the donor concentration of a (0001) Crystec substrate and found $8,3 \times 10^{17}\, cm^{-3}$. This discrepancy may comes from the different orientations used: m-plane here and c-plane for Brochen *et al.* (2017). In Taïnoff *et al.* (2011) they measured by C-V method Ga concentrations in the low $10^{16}\, cm^{-3}$ for the same substrates (provider and orientation). Moreover it has been demonstrated that the orientation affects the residual doping of ZnO layers: in (Lautenschlaeger *et al.*, 2010), they have found that a-plane orientation can lead to a reduction of the residual doping in ZnO layers compared to c-plane.

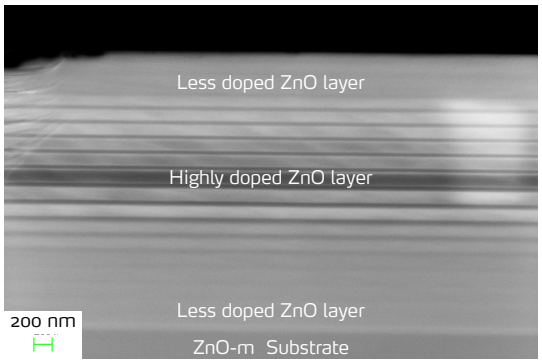

Figure 0.60.: SEM cross-section of the gradually doped sample.

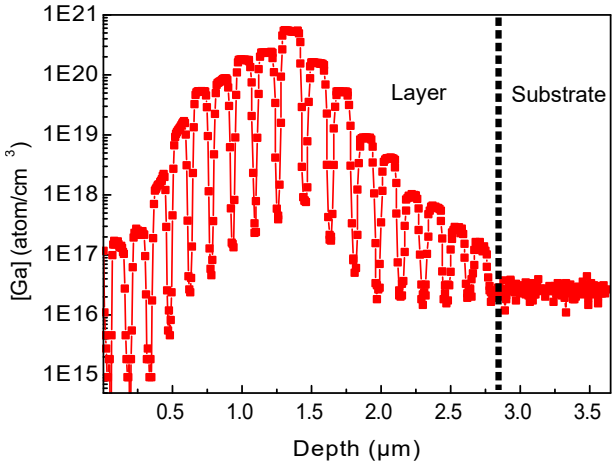

Figure 0.61.: SIMS profile of the Ga concentration.

Figure 0.62 displays the evolution of the donor ionization energy in ZnO thin films as a function of the donor concentration (Brochen *et al.*, 2017). All the points are experimental: the red ones comes from the study itself whereas other comes from the litterature. They are all consistent with the theoretical description (figure 0.62, solid line) which is described here by the hydrogenic Mott's law. The critical doping concentration at which the non-metal to metal transition takes place is

estimated to $4.2 \times 10^{18}\,cm^{-3}$. From the practical point of view, this curve shows that since the donor activation energy is higher when we go toward lower doping concentration, a higher energy is needed to ionise the donor so that it can release an electron in this concentration range. Thus, for low doping, its efficiency is minimized compared to higher doping due to this higher donor ionisation energy. Indeed it is fairly important in the case of QCL, because the targeted doping is in the range of $10^{17} - 10^{18}\,cm^{-3}$, for which the activation energy is between 20 and $40\,meV$ according to figure 0.62.

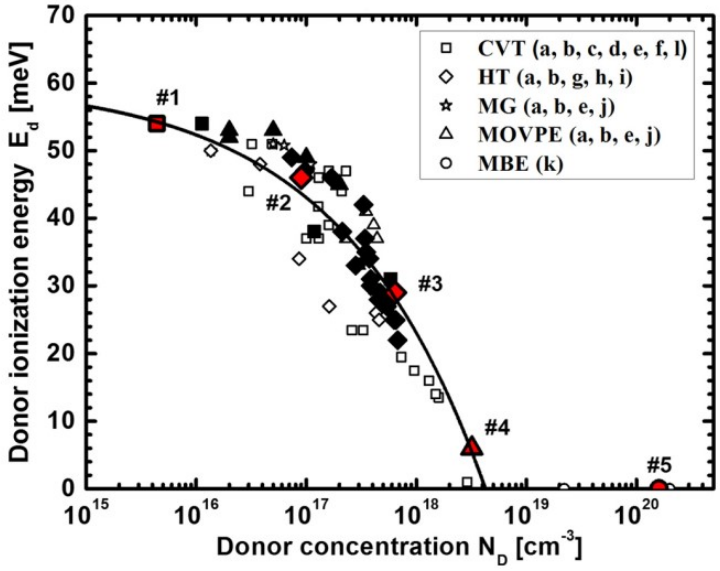

Figure 0.62.: Donor ionisation energy E_d as a function of the donnor concentration N_d in ZnO thin films grown by various growth methods (see figure legend). Samples #1, #2 and #3 are non-intentionnally doped whereas samples #4 and #5 are doped with Al and Ga respectively. *Reprinted from (Brochen* et al.*, 2017), with the permission of AIP Publishing.*

We have demonstrated that in addition to a very low residual doping (low $10^{14}\,cm^{-3}$), n-type doping using Ga is achievable in concentrations ranging from $10^{17}\,cm^{-3}$ to nearly $10^{21}\,cm^{-3}$. This range is suitable for the realization of QCL devices for which the doping needed is in the $10^{17} - 10^{18}\,cm^{-3}$ range, and for QCD (Quantum Cascade Detector) devices which need doping in the range of $10^{19}\,cm^{-3}$. Attention should be keeped if several doping levels are needed because of the non reproducibility of the doping in the range 10^{18} to $10^{19}\,cm^{-3}$ depending if the Ga cell temperature is increasing or decreasing.

0.5.2. Surface and interface probing: AFM, XRR and STEM-HAADF

This paragraph aims at showing how we can access the heterostructures surface and interface quality. The surface quality can be evaluated by the RMS roughness deduced from AFM or XRR, whereas the interface quality can be assessed from XRR and STEM-HAADF.

Figure 0.63 and 0.64 shows AFM images of two m-plane samples. The typical m-plane morphology, with stripes elongated toward the c-axis is present for both samples, but the period undulation is 10 times larger for the sample of figure 0.64 compared to the one of figure 0.63. This is the maximum range within which we can vary the period of undulations by modifying the growth conditions. The

two main parameters responsible for this change are the growth temperature and the II/VI flux ratio, as already discussed in the subsection 0.4.3. As a consequence of the undulation period increase, the RMS increases. In Matsui & Tabata (2005), authors reports a study on the surface morphology of homoepitaxially grown ZnO by laser-MBE. They shows similar surface morphology and demonstrate that when increasing the growth temperature from 420 to 600°C, the undulation period increases from 40 to 120 nm. This trend is fully consistent with our observations. Moreover, there is no significant change on the undulation period with the sample termination. It is also consistent with Matsui's results Matsui & Tabata (2005). However, as in Matsui & Tabata (2005), we observed that the stripes lengths are reduced on (Zn, Mg)O m-plane surfaces compared to ZnO. This reduction is even more noticeable when the Mg content is high, showing evidence that Mg atoms diffuse less in the c-axis direction compared to Zn atoms. As a consequence, (Zn, Mg)O surfaces are rougher than ZnO surfaces, and this roughening increases with the Mg content.

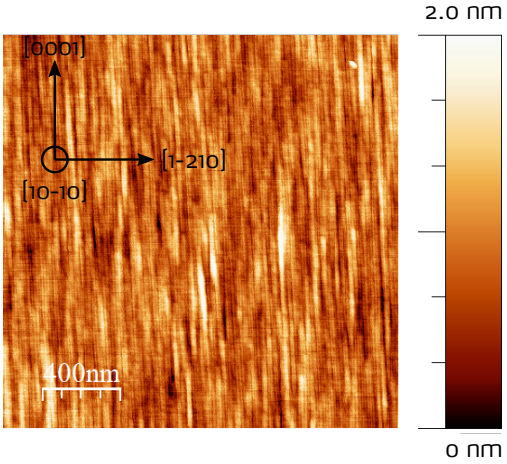

Figure 0.63.: $2 \times 2\,\mu m^2$ AFM image of an m-plane ZnO/(Zn, Mg)O MQW. The RMS is 3 Å. The lateral undulation period is around 10 nm.

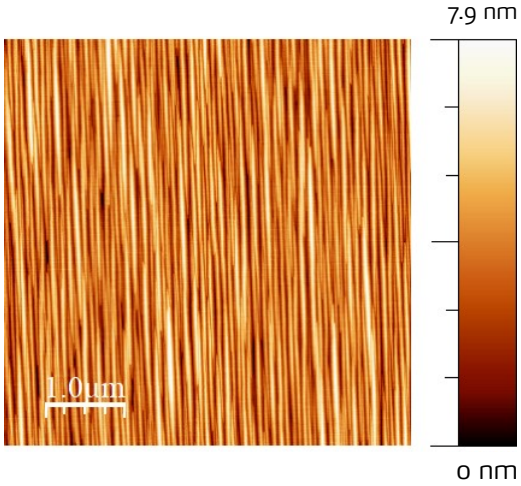

Figure 0.64.: $5 \times 5\,\mu m^2$ AFM image of an m-plane ZnO/(Zn, Mg)O MQW. The RMS is 1.4 nm. The lateral undulation period is around 100 nm.

Figure 0.65 shows XRR spectra of a ZnO/(Zn, Mg)O double barrier sample. The simulated spectrum was obtained by using the sofware GenX (Björck & Andersson, 2007). The main parameter to be imposed is the Mg composition. The output parameters are the ZnO and (Zn, Mg)O thicknesses and the RMS roughness. Thicknesses were adjusted so that the fringes can be well represented according to the experimental spectrum, whereas the RMS roughness was adjusted so that the overhall spectrum intensity decay follows well the trend of the experimental spectrum. It leads to a RMS roughness of 0.6 nm, which is very near to the one deduced from AFM experiment (0.7 nm). In this example, the agreement between the AFM roughness and XRR result is satisfying. This is in general not the case. Indeed, XRR is sensitive to 2 kinds of sample roughness: surface roughness, which can be also measured by AFM, and interface roughness, which can also be evaluated by STEM experiment. In the double barrier sample, the signature of surface roughness on XRR spectrum lies in the decay of the overhall intensity: the rougher the sample is, the faster the intensity decay is (this adjustment is done without taking into account a possible absorption process). The interface

roughness is seen on the evolution of fringes intensity: when interfaces are rough, a damping of the fringes is progressively observed when the incidence angle increases (Baumbach & Mikulik, 1999). For the double barrier sample, no interface roughness was needed to fit correctly the experimental spectrum. We can suppose that interfaces are very abrupt, or that they are not rough enough to detect a fringes damping with an incidence angle below 2.5°. In the general case, these 2 roughness parameters should be taken into account to entirely fit a XRR spectrum, and this process can be even more complicated if the interfaces are not identical (for instance, progressive interface roughening during the growth, but not limited to it). If this latter case occurs, a proper interface roughness can be defined for each single interface in the GenX software.

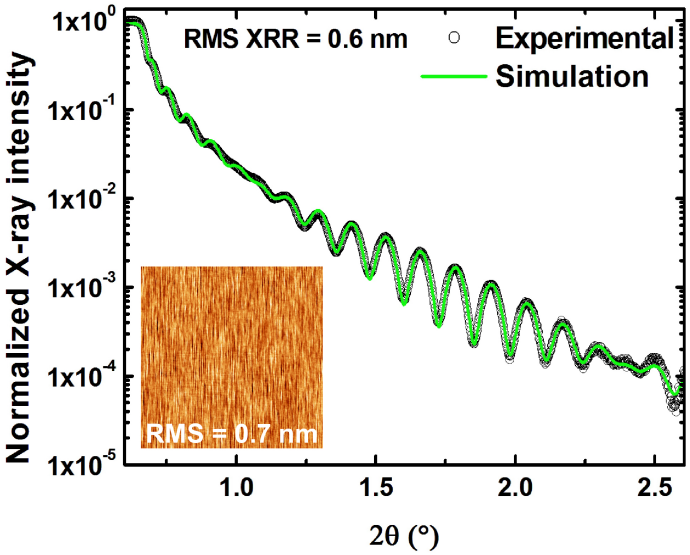

Figure 0.65.: Experimental and simulated XRR spectra for a (Zn, Mg)O double barrier. The barrier is 2.0 *nm* thick whereas the ZnO QW is 4.0 *nm* thick. The Mg composition implemented to fit the experimental spectrum was set to 30 %. The RMS roughness was used as an input parameter to adjust the fitted spectrum to the experimental one (here 0.6 *nm*). In inset is shown the corresponding AFM picture with a 0.7 *nm* RMS roughness. *Reprinted from (Le Biavan* et al.*, 2017), with the permission of AIP Publishing.*

We already know that the m-plane surface exhibits periodic stripes along the c-axis because of a diffusion anisotropy of adatoms during the growth process. In addition, the XRR spectra reveals that interfaces are coherent along the growth direction. This means that if we look at the interface number n, we can define the interface n+1 by a translation in the growth direction. With these two last statements we can wonder if the QW interfaces are still planar or if they are undulated according to the stripes that emerge on the surface. A cross-section was prepared on a similar MQW sample for STEM. Cross-sections were prepared along two directions: parallel and perpendicular to the c-axis (figure 0.66 and 0.67 respectively). They were observed in dark field mode using the High Angle Annular Dark Field detector (HAADF), which gives images with a chemical contrast. In figure 0.66 the cross-section is shown for the $[1\bar{2}10]$ zone axis. Flat interfaces are observed on a large scale, as we can expect from a 2D growth mode. Looking at the [0001] zone axis (figure 0.67) the interfaces are no more flat but presents periodic undulations. The period is of the order of 10 *nm* for this particular sample, which matches the stripes width measured in AFM (this statement has been verified on various samples) and is also consistent with the observations reported in Matsui & Tabata

(2005). Moreover, they are visible only along the [0001] zone axis, which is in aggreement stripes elongated along the c-axis. So we have the evidence that the stripes on the surface are the result of undulated interfaces inside the sample. In addition, these undulations are perfectly coherent along the growth direction, meaning that there is no change of thicknesses due the interface undulation. This coherence is in line with what is observed in XRR because it allows to observe constructive interferences (figure 0.49).

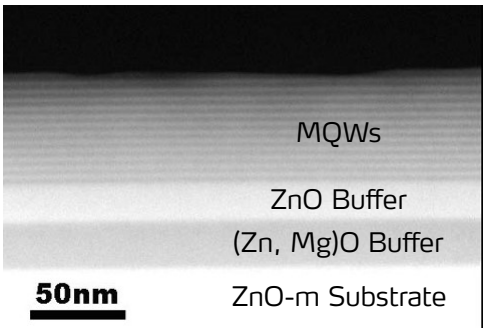

Figure 0.66.: STEM-HAADF image of a MQW sample in the $[1\bar{2}10]$ zone axis (meaning that the c-axis lies parallel to the QWs interfaces).

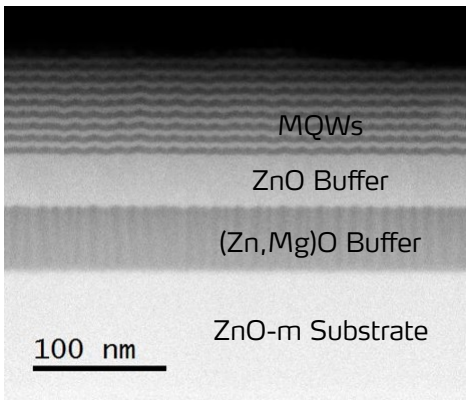

Figure 0.67.: STEM-HAADF image of a MQW sample in the [0001] zone axis (meaning that the c-axis is pointing out of the image).

Figure 0.68 aims at showing a further insight into the undulation coherence. In this sample, a (Zn, Mg)O tracer of few nanometers thick separates the ZnO substrate from the ZnO buffer. We can see that even at early growth times, the undulations start to form: even if the shape is not yet as homogeneous as in the MQWs, the mean periodicity is appearing and is reproduced at each interfaces. This is also consistent from the coherence observed in XRR spectra, but now we have the evidence that this undulated profile birth appear right after the substrate interface and that the periodicity is kept until the end of the growth. This statement is not in agreement to what is reported in Matsui & Tabata (2005), where authors measure a undulation period variation depending on the sample thickness in the range of 10 to $30\,nm$ thick samples. The authors explain this trend because of the presence of terrrases that limite the lateral diffusion of adatoms, leading to a saturation of the undulation period for a given critical thickness. Our experiments prove that we are not limited by such terrasses, and we rather think that the only relevant parameters are the growth conditions that set the undulation periodicity from the very first ML through preferential diffusion directions. Even if the undulation shape is not perfect at the beginning, it evolves quickly toward a long range periodic structure in the growth plane. In our case, this periodicity is kept on several hundreds of nanometers.

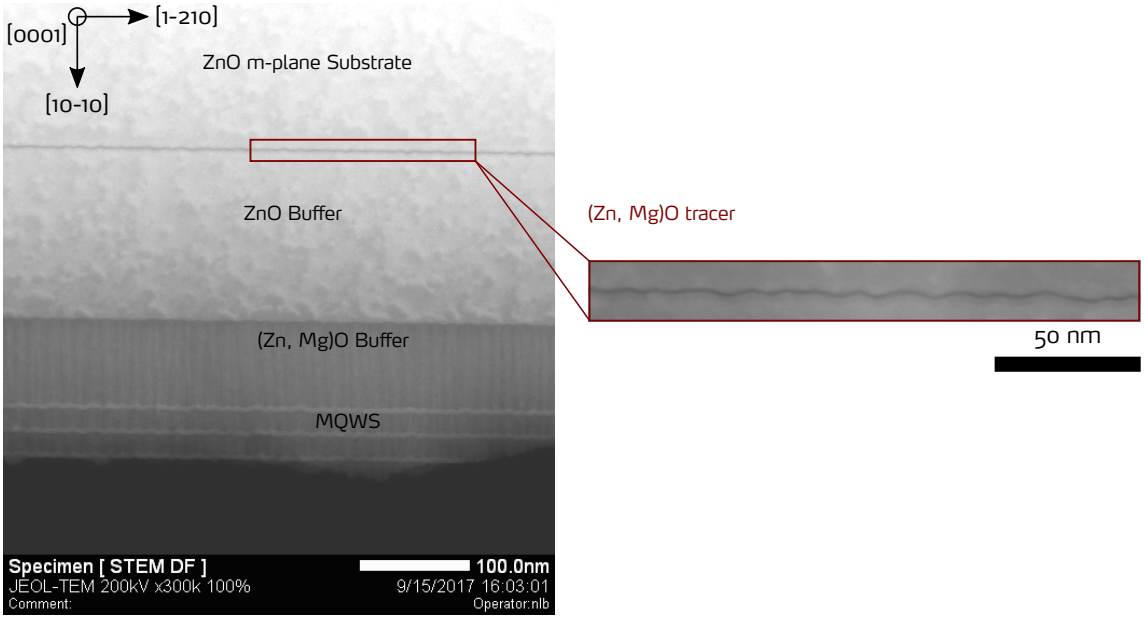

Figure 0.68.: STEM-HAADF image of a MQW sample in the [0001] zone axis. The zoomed part shows the (Zn, Mg)O tracer grown between the ZnO substrate and the ZnO buffer.

To conclude this part, we have seen that both AFM and XRR can give precious information concerning the samples surface quality whereas XRR and STEM-HAADF can gives an insight into the interface quality. They are complementary: both AFM and XRR can give de surface RMS roughness, but AFM captures also the surface morphology. XRR and STEM-HAADF allow to gather information about interfaces coherence and roughness at completely different scales: XRR is more averaged, whereas STEM-HAADF is rather local. Each of these techniques are thus totally relevant for the surface and interface probing of heterostructures in the scope of a QCL realization.

0.5.3. Magnesium content

The Mg content is an important parameter to investigate because it allows to control the quantum confinement through band-offset tailoring A. Ohtomo *et al.* (1998). A relevant aspect is its homogeneity when we consider an alloy in heterostructed materials. A non-homogeneous alloy creates potential fluctuations which can be responsible for carriers localization, as excitons localization for instance (see figure 0.69). In ZnO, the exciton Bohr radius is rather small - 18 Å A. Ohtomo *et al.* (1998) - leading to a high sensitivity to potential fluctuations Park *et al.* (2001). Alloy disorder is not the only cause of excitons localization in semiconductors: interface roughness of QW based heterostructures can induce thickness fluctuations at the ML scale, ending by exciton localization as well (see figure 0.69). In ISB devices, interface roughness and alloy disorder are responsible for an inhomogeneous braodening of transitions and its associated gain Paiella (2006). In addition, interface roughness can cause unwanted carriers scattering in the QW planes, which is detrimental from devices point of view.

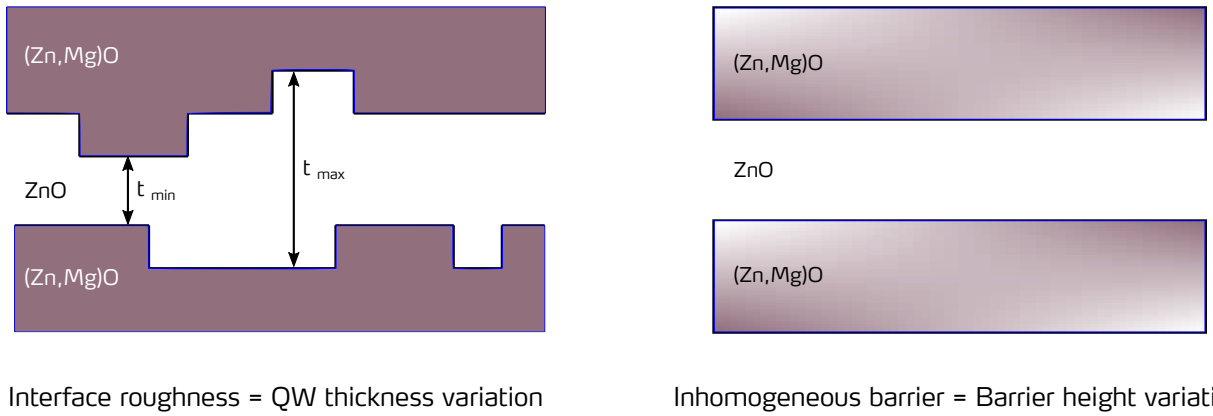

Figure 0.69.: Schematics showing two main causes for the carriers localization within QWs. Right: interface roughness which changes the QW thickness at the ML scale. Left: inhomogenous alloy composition which change locally the barrier height.

For these reasons, it is particularly relevant to investigate if there is carrier localization in our heterostructures. And if there is, to be able to determine where they come from.

To this purpose, PL was used on MQWs samples that have different Mg contents.

In previous studies, localization in ZnMgO thick layers has been experimentally observed Park *et al.* (2001); Shibata *et al.* (2007); Wassner *et al.* (2009). These layers were grown on various substrates and by different growth methods. In Park *et al.* (2001), ZnMgO thick layers on polar sapphire substrate were grown by MOVPE with Mg content up to 49 %. They found that the increase of Mg content leads to a broadening of the ZnMgO exciton line which is attributed to an increase of alloy fluctuations. The article Wassner *et al.* (2009) reports similar statements about the exciton line broadening for MBE grown ZnMgO on polar saphire. In addition they conduct temperature dependent PL experiment that shows that the energy of the ZnMgO exciton line as a "S-shape" behaviour with the temperature. This behaviour is commonly attributed to the localization: at low temperature, the excitons are trapped in local potential minima caused by interface roughness and/or alloy fluctuation (inside or outside the QW). When the temperature raises, they have enough energy to delocalize and reach lower energy state. Then the temperature continues to raise and excitons can reach local potential minima at higher energies, leading ot a blueshift (always due to interface roughness and/or alloy fluctuations). Finally at even higher temperatures the energy evolution follows the Varshni's law. Another evidence of the alloy localization in ZnMgO was reported in Shibata *et al.* (2007). They observe a tail of the ZnMgO exciton line towards the lower energies in PL spectra. This is attributed to the formation of tail states in the density of states that occurs in a disordered alloy. This tail is more pronounced as the Mg content increase, indicating that the localization due to alloy disorder increases when the Mg content increases as well.

Other studies deal with the localization in ZnO/ZnMgO heterostructures Al-Suleiman *et al.* (2007); Ashrafi (2010); Zhang *et al.* (2014). They focus on the effect of the localization on the emission properties of QWs. In Al-Suleiman *et al.* (2007); Zhang *et al.* (2014), QW and MQWs grown by MBE on c-plane saphire substrates show the typical "S-shape" in tempeture dependant PL experiments. In this case, both the interface roughness and the alloy disorder in the ZnMgO barrier can be the cause of the exciton localization in the QWs. In Al-Suleiman *et al.* (2007), the broadening of the

exciton peak is well modelized by taking into account an interface roughness of 1 ML. In Zhang *et al.* (2014), the QW thickness is fixed and two Mg content were tested (10 and 20 %). It turns out that the localization was only detected for the sample with the higher Mg content, proving that alloy fluctuation was the main cause of localization in their samples. As it can be seen from the two last references, the same growth methods and the same substrate can lead to different localization origins inside the QW.

We investigate our heterostructures with temperature dependent PL experiment if there is any trace of carrier localization inside. To that purpose MQW samples were grown with different Mg composition inside the barrier (15 %, 25 % and 35 %), keeping the QW and barrier thickness constant (see figure 0.70). Figure 0.71 shows the temperature dependant spectrum for the sample with 15 % of Mg. At 20 K, three main peaks are observed: the bound exciton and free exciton of the QW and the barrier when looking from the low energy side to the higher one. Both excitons exhibit several LO-phonon repliqua visible until 120 K. The observation of such phonon replica is usually assigned to a good crystalline quality of the material: here both the ZnO of the QW and the (Zn, Mg)O of the barrier.

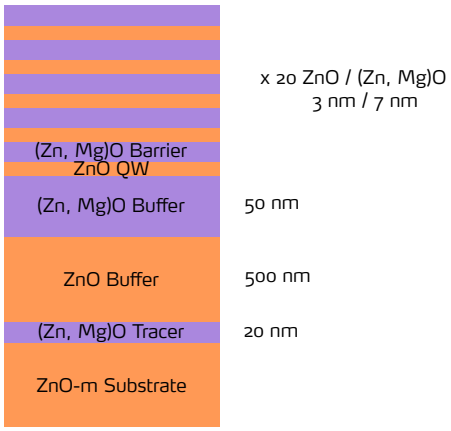

Figure 0.70.: Schematic of samples.

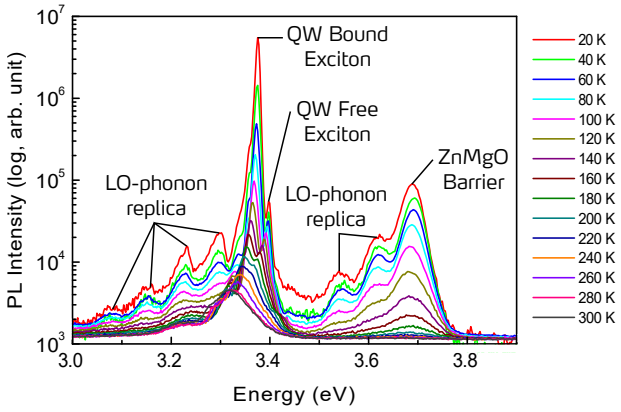

Figure 0.71.: PL spectra at different temperatures for the sample with 15 % of Mg.

Figures 0.72, 0.73 and 0.74 show the variation the exciton linked to the QW with the temperature. All samples follow the Varshni law, which describes how the band gap varie with the temperature. It can be noticed that at low temperature, the QW energy is higher when the Mg content. This is qualitatively in agreement with the fact that increasing the Mg content increase the quantum confinement and, by turn, the energy in the QW (at QW thickness constant, which is the case here). So contrary to Al-Suleiman *et al.* (2007); Zhang *et al.* (2014), our QWs do not show localisation, which is the proof that at the exciton scale, there is no interface roughness and that no effect of alloy disorder can be seen.

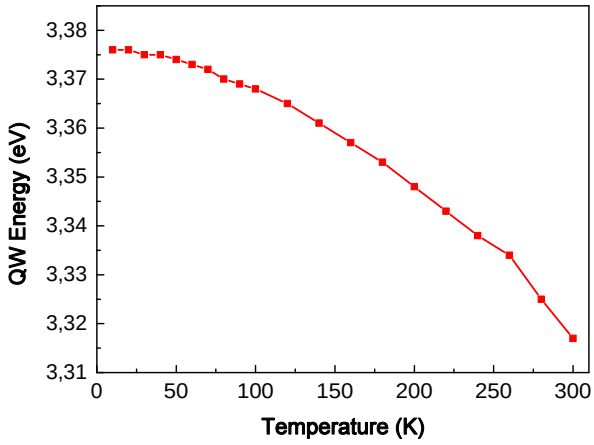

Figure 0.72.: Evolution of the exciton energy in the QW with the temperature. The Mg content in barriers is 15 %.

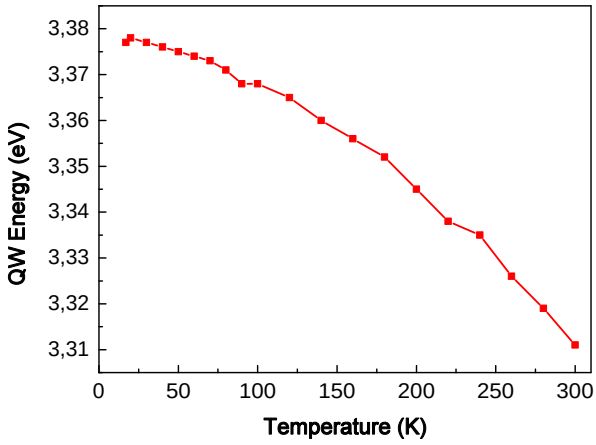

Figure 0.73.: Evolution of the exciton energy in the QW with the temperature. The Mg content in barriers is 25 %.

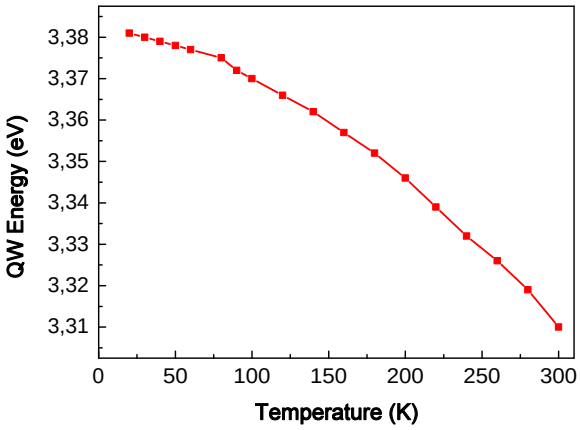

Figure 0.74.: Evolution of the exciton energy in the QW with the temperature. The Mg content in barriers is 35 %.

The energy evolution of the (Zn, Mg)O barriers is different (figure 0.75). For 15 and 25 % of Mg the energy increases of several meV before decreasing as predicted by Varshni's law. This is as we observe the second half of the "S-shape": excitons are already delocalized at $10\,K$ and when the temperature raise, they can reach high energy minima due to local potential fluctuation. For the sample with the higher Mg content (figure 0.75), the complete "S-shape" is observed, which confirms that there is localization due to alloy disorder in the barrier. This is important to note that even if there is alloy disorder, it does not induce exciton localization in the QW, which has never been reported in ZnO/(Zn, Mg)O heterostructures.

Moreover, the alloy disorder is more pronounced when the Mg content is high. We can estimate the localisation energy by the difference between the energy maximum and the energy at $10\,K$, and we found: $5\,meV$, $11\,meV$ and $43\,meV$ when increasisng the Mg content. If we assume that this energy

shift is only due to a fluctuation of Mg in the alloy, then we can use it to evaluate the fluctuation. Taking $20\,meV/\%$ of Mg, we can deduce a fluctuation in the alloy of $\pm 0,3\,\%$, $0,6\,\%$ and $2,2\,\%$ for $15\,\%$, $25\,\%$ and $35\,\%$ of Mg respectively.

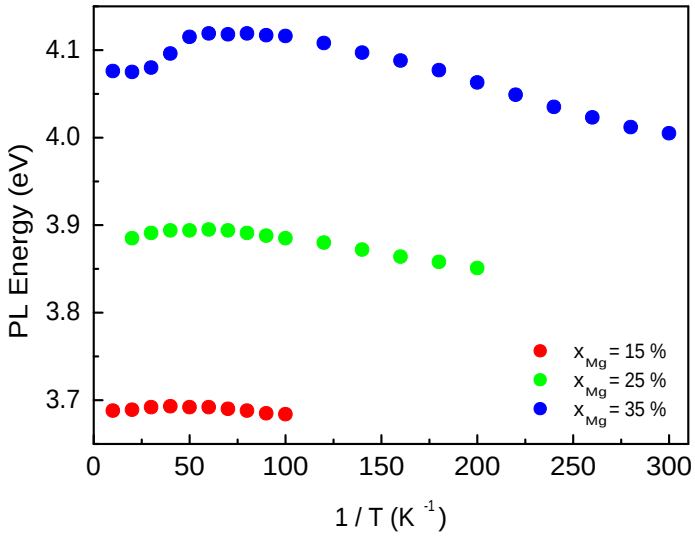

Figure 0.75.: Evolution of the exciton energy in the (Zn, Mg)O barrier with the temperature for various Mg content.

Figures 0.76, 0.77 and 0.78 represents the variation of the PL integrated intensity with the temperature for each sample. We can see that for the QW, the behaviour is qualitatively comparable. The decrease of the QW integrated intensity takes place at higher temperature when the Mg content is increased because the exciton confinement is stronger. From the barrier point of view, the trends are well distinguisable from one Mg content to another. The sample with $15\,\%$ of Mg (figure 0.76) begins at low temperature with a slow decrease before a steeper one. Then the sample with $25\,\%$ of Mg exhibit a plateau until $50-60\,K$ before decreasing sharply (figure 0.77). Finally, the sample with the higer concentration of Mg shows a plateau until $30\,K$ before a pronouced bump. This increase can be caused by an injection of excitons inside the barriers.

From the slopes of these Arrhenius plots, activation energies at high temperature can be deduced for the barriers (between 200 and $300\,K$). We find when increasing the Mg content that activation energies increase as well: $57\,meV$, $129\,meV$ and $140\,meV$.

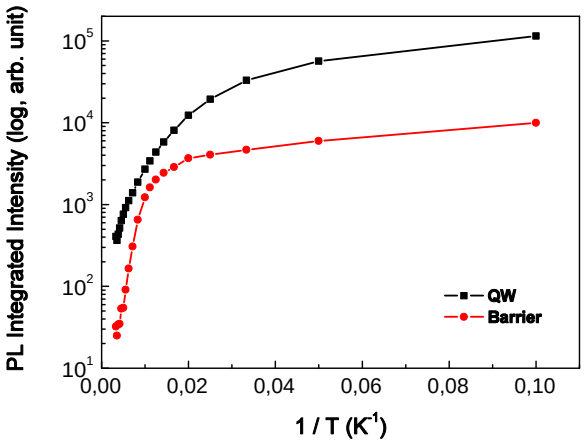

Figure 0.76.: Evolution of the PL integrated intensity with $1/T$ for the QW and the barrier. The Mg content is 15 %.

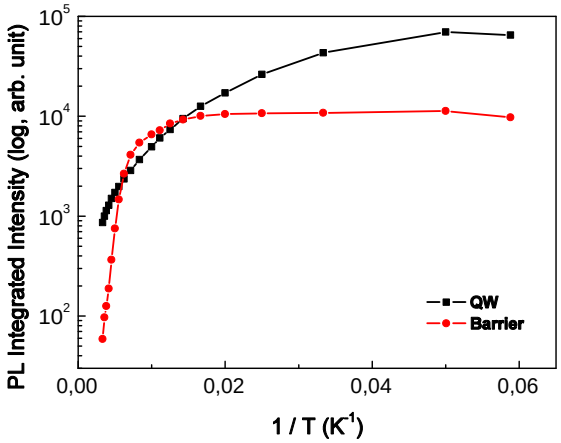

Figure 0.77.: Evolution of the PL integrated intensity with $1/T$ for the QW and the barrier. The Mg content is 25 %.

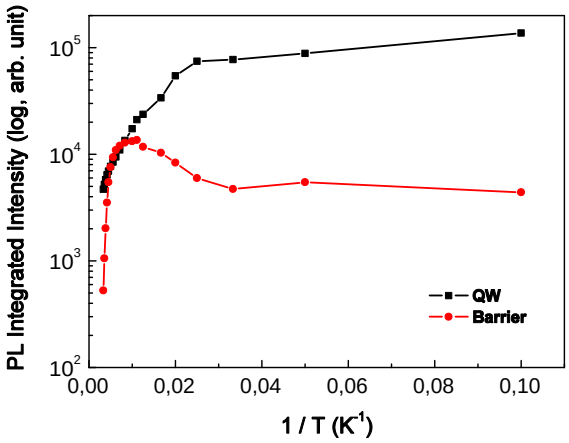

Figure 0.78.: Evolution of the PL integrated intensity with $1/T$ for the QW and the barrier. The Mg content is 35 %.

Regarding the Mg inhomogeneity of the alloy, PL experiments states a $\pm 2-3\,\%$ variation for 35 % of Mg, which is quite reasonnable since the error made when measuring the Mg content by PL is $\pm 2\,\%$. It represents the alloy disorder seen by excitons, and not an absolute value. Looking at STEM-HAADF images from various MQWs, we can see a periodic variation of contrast in the alloy. The periodicity scales exactly with the undulation (figure 0.79). Using the HAADF detector, images show intensities directly related to the chemical composition (proportional to Z^2, with Z the atomic number). The atomic numbers of Mg and Zn are respectively 12 and 30: more signal comes from the richer parts in Zn because incoming electrons have higher probability to interact with the heavier element (here Zn). In figure 0.79, we can thus conclude that the darker regions in the alloy are Mg rich and the lighter ones Zn rich. In addition, Mg rich regions are aligned with the top of undulations with respect to the $[1\,0\,\bar{1}\,0]$ growth direction. On the contrary, Zn rich regions are aligned with the bottom parts of undulations.

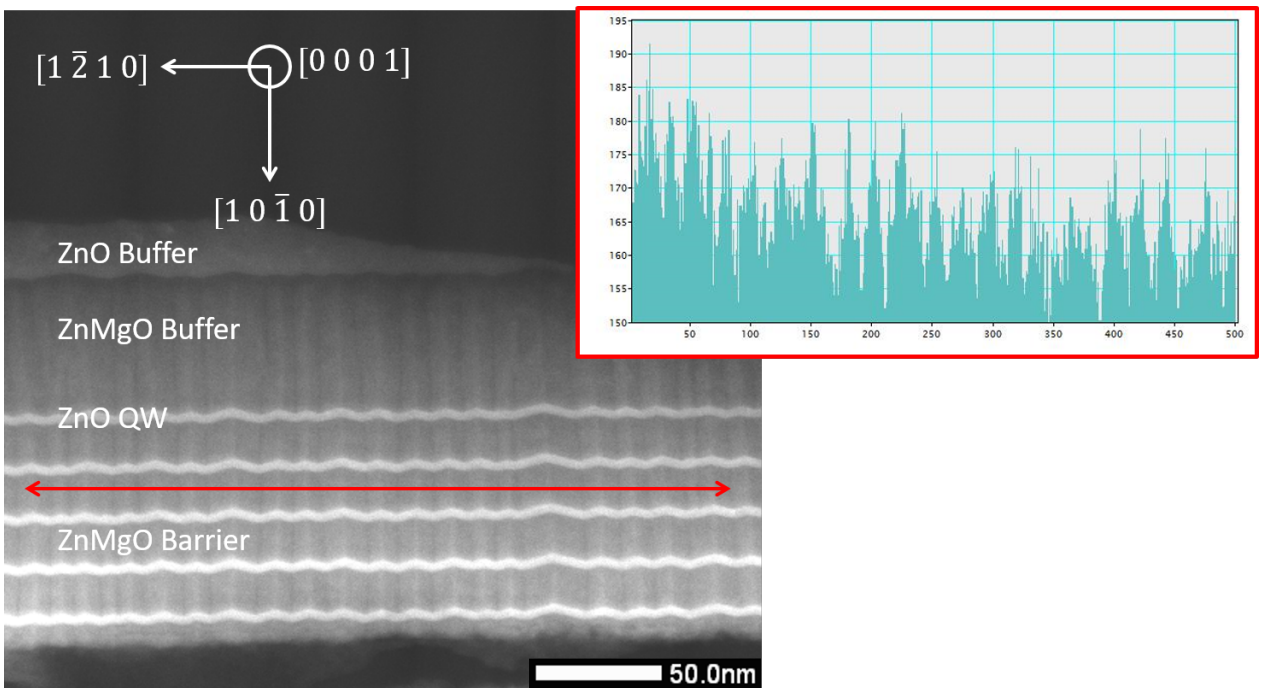

Figure 0.79.: STEM-HAADF image of a ZnO/(Zn, Mg)O MQWs in the [0001] zone axis. The inset highlights the periodic contrast variation along the red arrow.

The quantitative measurement of the variation of Mg composition within barriers has been assessed by STEM-HAADF and EDX in collaboration with GPM in Rouen. They observed MQWs samples grown in similar growth conditions and observed the same features: periodic undulations and periodic variation of contrast Di Russo *et al.* (2017). With EDX analysis, they measure a composition of 15 % of Mg in Zn rich regions, and 27.5 % in the Mg rich regions. Theses values have to be compared with the mean composition measured by PL experiments: 27 ± 2 %. In other materials systems, composition fluctuations can be either caused by strain gradients or anisotropy, either by a difference of diffusivity of the adatoms on the surface during the growth (see Lelarge *et al.* (1999)). In the case of our samples, strain gradients has been simulated along the V-groove interface in the a, m and c direction - respectively ε_{xx}, ε_{yy} and ε_{zz}. Simulations were performed using the Nextnano++ software, assuming that the layer is coherently strained on the substrate. In order to calculate them, the variation of the lattice parameters of the alloy were taken from Laumer *et al.* (2013). Figure 0.80 shows the variation of such strain states for an undulated barrier without and with the periodic variation of alloy composition. It can be seen that for each strain component that repartition of strain is not coherent along the growth direction. However, as observed in figure 0.79 and reported in Di Russo *et al.* (2017), the variation of the STEM contrast - and thus the alloy concentration is perfectly coherent along the growth direction. As a consequence of the Curie's principle, this pecular Mg content repartition cannot be due to the strain states inside the alloy layer alone, because of this symmetry breakage. Thus the hypothesis of the difference of diffusivity of adatoms on the surface seems to be more likely to explain the observed Mg segregation.

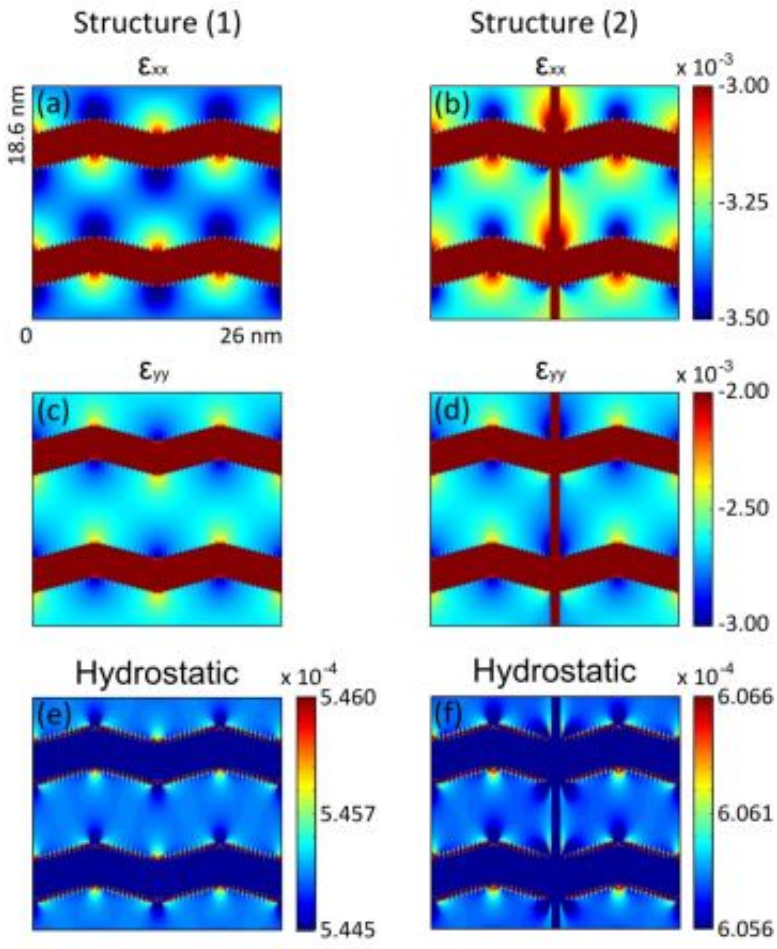

Figure 0.80.: Simulation of strains ε_{xx} and ε_{yy} for structures without and with periodic Mg content variation within the barrier - respectively structure (1) and (2). Strains are evaluated with respect to the unstrained lattice parameters of ZnO. The hydrostatic strain is represents the addition of $\varepsilon_{xx} + \varepsilon_{yy} + \varepsilon_{zz}$. *Reprinted from Di Russo* et al. *(2017), with the permission of AIP Publishing.*

From the band structure point of view, this phenomenon changes locally and periodically the band offset. In Di Russo *et al.* (2017), they investigated the effect on the electron and hole wavefunction of the periodic variation of Mg content. They compare a V-groove QW without and with the alloy fluctuations measured in EDX. Simulations reveal that even with such a high Mg fluctuation, it has only a little impact on the electron wavefunction (see figure 0.81). On the contrary, the simulations predict a large localization of the hole wavefunction in the Mg poor regions. For unipolar devices using only electrons, this effect should not be dramatic. Moreover, we can add from STEM observations on other QW samples that this Mg fluctuation is not present for alloy with 10 % of Mg (measured by PL) even if the undulation profile is present. Thus for THz intersubband devices with ~ 15 % of Mg, this effect should not compromise itself device operation.

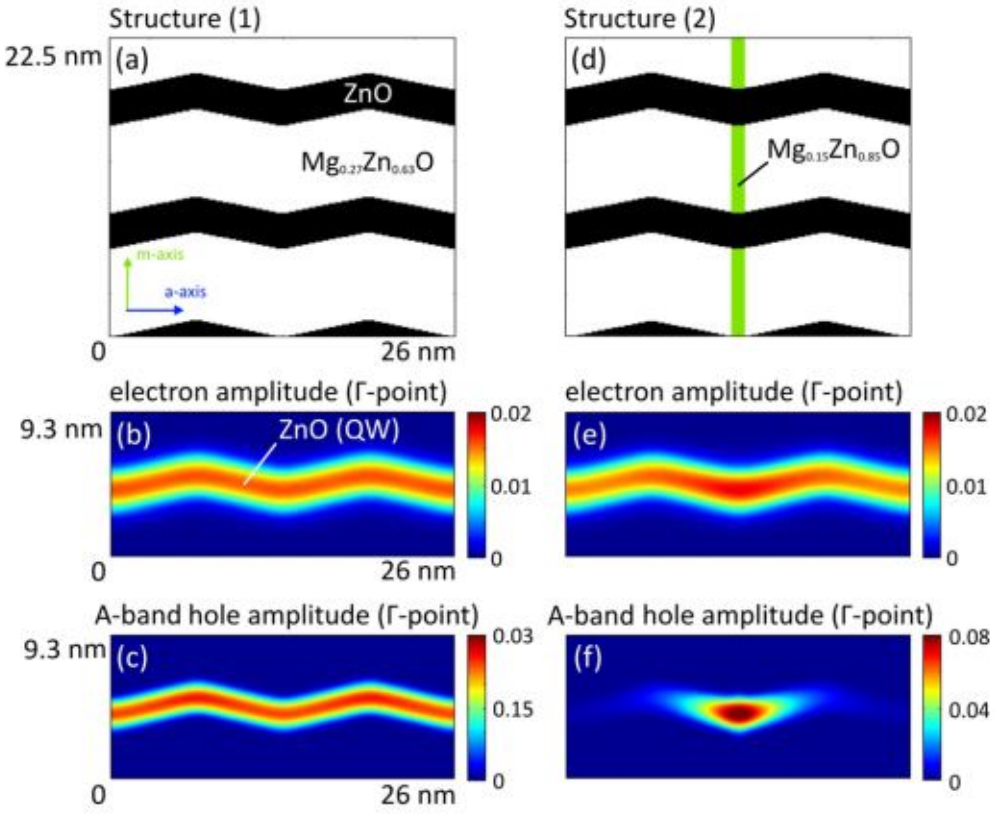

Figure 0.81.: (a) Structure of the ZnO QW in c zone axis. (b) Electron and (c) A-band hole amplitude wave-functions at the Γ point of the Brillouin zone for an undulated QW sandwiched in homogeneous (Zn, Mg)O barriers. (d) Structure of the QW in the case of periodic inhomogeneities of composition in the barrier and its effect on (e) the electron and (f) A-band hole wave-functions. *Reprinted from Di Russo* et al. *(2017), with the permission of AIP Publishing.*

0.5.4. First results on r-plane orientation

An alternative orientation to realize ZnO based QCL is to use the r-plane. This orientation is semi-polar, thus heterostructures shows a moderate QSE which has to be taken into account when designing the QCL structure (Chauveau *et al.*, 2013). But this orientation exhibit one main advantage comparing to m-plane: atomically flat surfaces can be achieved. Indeed interface roughness can be highly detrimental to the final performance of a QCL devices because it allows electrons to be scattered in the layers' planes. In particular, interface roughness scattering affects the intersubband transition lifetime so that it has been experimentally observed that it leads to:

- changes in the ISBT absorption
- ISBT broadening
- reduce the tunnel transport efficiency (Chiu *et al.*, 2012)

Now it is well established in the QCL community that scattering processes involving interface roughness can be as important as LO-phonon scattering, particularly for the IR range (Vitiello *et al.*, 2015). In figure 0.82 is shown a calculation that illustrates the influence of interface roughness on the

ISB absorption coefficient for a THz GaAs/AlGaAs QCL. According to this study, we see a dramatic decrease of the gain when realistic interface roughnesses are taken into account. For instance, a $0.25\,nm$ step height roughness reduce the gain by a factor of 4 compared to ideal (and non-realistic) interfaces.

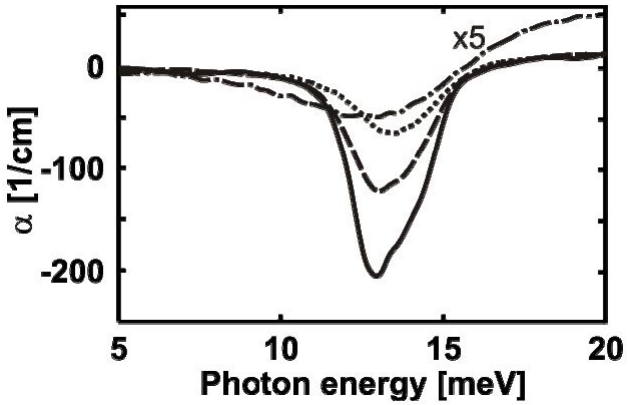

Figure 0.82.: Absorption coefficient as a function of the photon energy. The curves account for different step height interface roughness: 0 (straight line), $0.1\,nm$ (dashed line), $0.25\,nm$ (dotted line) and $1.0\,nm$ (dash-dotetd line). A factor 5 has been applied to the lastest curve. *Reprinted from (Kubis* et al.*, 2008), John Wiley and Sons, © 2008 WILEY-VCH Verlag GmbH & Co. KGaA, Weinheim.*

If we come back to our material system, we achieve routinely RMS roughness lower than $0.50\,nm$ on m-plane, compared to r-plane, where it is as low as $0.11\,nm$ for MQWs structures (Chauveau *et al.*, 2013).

Thus we have explored the growth conditions that are suitable for the r-plane orientation. Unfortunately, only few basic tests were conducted because of substrate shortage. So we grew MQWs samples described in figure 0.83 at different substrate temperatures T_{growth} (figure 0.84). The given thicknesses are nominal and may change with the variation of the growth rates induced by the growth temperature. Because the number of substrates were limited, our main concern here was to find what is the growth temperature range which gives the lower interface roughness, because flat surface and interfaces are a prerequisite for ISB devices. To that purpose samples were measured in AFM and XRR experiment respectively to assess the surface and the interface roughness.

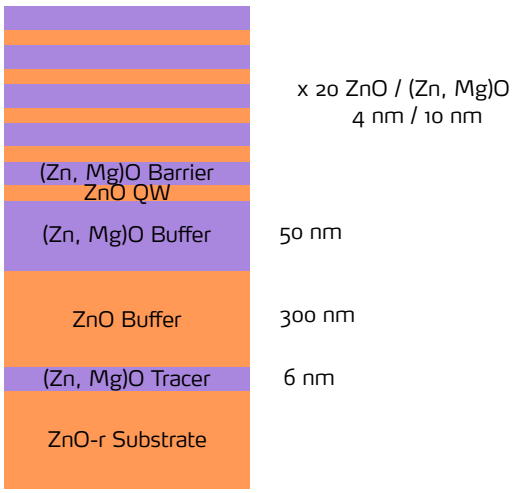

Figure 0.83.: Schematic showing the samples' structures.

Sample	$T_{growth}\,(°C)$
A	360
B	420
C	480

Figure 0.84.: Table which gives the growth temperature for each sample.

The AFM pictures of samples A, B and C are presented in figures 0.85, 0.86 and 0.87 respectively. From the RMS roughness point of view, the increase of growth temperature from $360°C$ to $480°C$ leads to a impressive reduction of the RMS roughness from $0.88\,nm$ to $0.15\,nm$ (see figure 0.88). Note that a RMS roughness of $0.15\,nm$ is a typical value of ZnO substrate's roughness. This the same order of magnitude that was obtained in the following publication (Chauveau *et al.*, 2013). This paper is the only one to date to report about homoepitaxy on r-plane orientation. They studied the structural and photoluminescence properties of various MQWs with different QW thicknesses and Mg content. In particular, they achieve a RMS roughness of $0.11\,nm$ for Mg contents up to $35\,\%$ and no relaxation of the (Zn, Mg)O alloy was observed for $17\,\%$ of Mg content, which are very promissing results for the use of r-plane for QCL. Moreover it is expected that this orientation corresponds to the smallest elastic energy stored for ZnO/(Zn, Mg)O heterostructures (Bigenwald *et al.*, 2012). This calculation is supported by experimental results showing that the out of plane lattice parameter varies slowly with the Mg content (Chauveau *et al.*, 2013).
In addition to the change of roughness, we can see an evolution of the surface morphology. Sample A exhibit a elongated islands of few nm hight (figure 0.85). Sample B shows a set of lines aligned in two directions, which can be an evidence of cross-hatch due to the nucleation and glide of disclocations during the growth (see section III). And sample C present a very flat surface, with no specific morphology measurable with AFM.

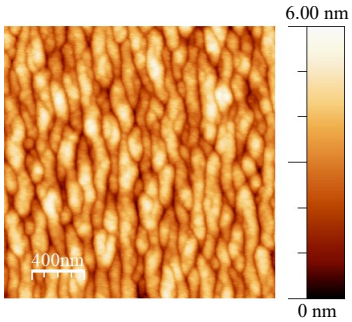

Figure 0.85.: AFM picture of sample A on a $4\,\mu m^2$ area. The RMS roughness is $0.88\,nm$.

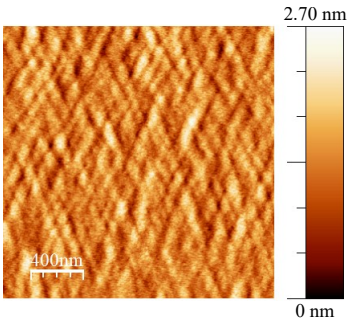

Figure 0.86.: AFM picture of sample B on a $4\,\mu m^2$ area. The RMS roughness is $0.35\,nm$.

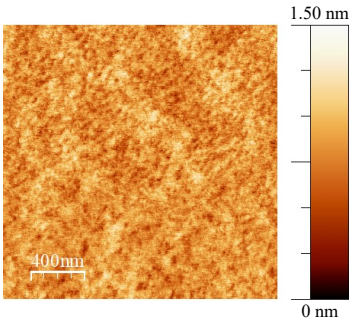

Figure 0.87.: AFM picture of sample C on a $4\,\mu m^2$ area. The RMS roughness is $0.15\,nm$.

XRR spectrum for samples A, B and C is presented in figure 0.89. We can see superlattice peaks which are linked to the thickness of one QW and one barrier together. When T_{growth} is increased, these peaks are shifted so that the mean growth rate of the superlattice decreased. In addition, the overall intensity exhibits a steeper decrease when the T_{growth} decreases. This is an evidence of an increase of the surface roughness when the T_{growth} decreases, which is consistent with the AFM results.

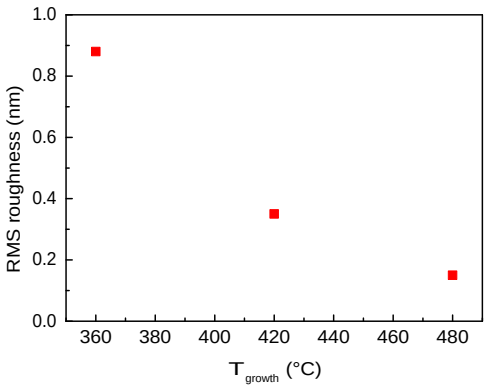

Figure 0.88.: Evolution of the RMS roughness with the growth temperature T_{growth} taken on $4\,\mu m^2$ images.

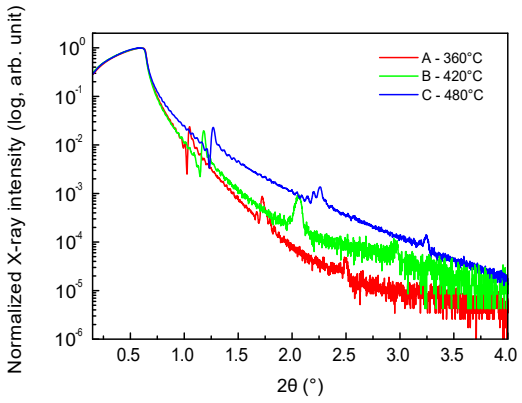

Figure 0.89.: XRR spectra of sample A, B and C.

From this preliminary work, we know that a growth temperature of $480°C$ is a good starting point because surface roughness is as low as $0.15\,nm$, which is comparable to what was demonstrated in a previous paper (Chauveau *et al.*, 2013). Moreover, the growth temperature used in this publication is $500°C$, which close to what was used there. From XRR experiment, we have seen that this growth temperature offers the lower surface roughness compared to others ones. So we have demonstrated the advantages of r-plane compared to m-plane from the surface point of view. The next step to this work is to assess how these parameters evolves with higher Mg content (only 5% here) as well as the

homogeneity of the ZnMgO alloy. STEM-HAADF is also useful to assess the interface roughness. As cascade devices are build from hundreds of periods, the final thickness can exceed the micrometer. Thus antother step is the way r-plane ZnO/(Zn, Mg)O heterostructures release the stress. This step is added in the following chapter that describes the mechanical properties of ZnO/(Zn, Mg)O heterostructures.

Part III.

Mechanical properties

This chapter proposes a review on the mechanical properties of ZnO and (Zn, Mg)O. In the first paragraph, mechanical properties are explored in the elastic limit, meaning when the deformation does not induce an irreversible change in the material behavior and / or structure. Theoretical model in the low deformation limit is developed to describe how a hexagonal crystal (ZnO, (Zn, Mg)O...) deform depending on the crystal orientation selected for the epitaxy. Then the models presented are compared to deformation measurements performed by X-Ray diffraction for the (Zn, Mg)O system.

In the second part, phenomena that arise above the elastic limit of the material are discussed. A comparison of the way ZnO/(Zn, Mg)O heterostructures grown on non-polar and semi-polar orientations relax stress are developed and compared to the theory.

0.6. Elastic limit

As stated in the introduction chapter, ZnO crystallizes in the hexagonal wurztite phase at ambient temperature and pressure conditions. From the mechanical point of view, the Hooke's law can be applied if we restrain the developement in the low deformation range. This law states the proportionality between the applied stress σ and the material response in terms of deformation ε (eq. 0.25). In a case of an isotropic material, the material response does not depend on the direction and the Hooke's law can be simply written:

$$\sigma = E\varepsilon \tag{0.25}$$

With E the Young's modulus, which describes how the material react to an applied stress (in Pa).

In hexagonal lattices, the anisotropy has to be taken into account. Instead of a single constant E, a 6 x 6 stiffness matrix C is needed. It describes the mechanical behaviour of the crystal in each direction (in the crystal lattice's coordinate system using the Voigt's notation). This compliance matrix is symmetric, *i.e.* $C_{ijkl} = C_{lkji}$, leading to a maximum of 21 independent coefficients. For a hexagonal crystal, this number can be reduced thanks to the orthotropy property (two symmetry planes perpendicular to each other). As a consequence, only 5 independent coefficients are needed to fully describe the mechanical response of a hexagonal crystal to an applied stress (eq. 0.26).

$$C = \begin{bmatrix} C_{1111} & C_{1122} & C_{1133} & 0 & 0 & 0 \\ C_{1122} & C_{1111} & C_{1133} & 0 & 0 & 0 \\ C_{1133} & C_{1133} & C_{3333} & 0 & 0 & 0 \\ 0 & 0 & 0 & C_{2323} & 0 & 0 \\ 0 & 0 & 0 & 0 & C_{2323} & 0 \\ 0 & 0 & 0 & 0 & 0 & \frac{1}{2}\left(C_{1111} - C_{1122}\right) \end{bmatrix} \tag{0.26}$$

Which gives formally this notation for the Hooke's law in the coordinate of the crystal lattice:

$$\sigma_{ij} = C_{ijkl}\,\varepsilon_{kl} \tag{0.27}$$

It is important to know each stiffness matrix component to anticipate the mechanical behaviour

of epitaxial layers. For ZnO, these values were determined experimentally in 1962 by an ultrasonic pulse technique (Bateman, 1962) (see table 0.4).

C_{1111}	C_{1122}	C_{1133}	C_{3333}	C_{2323}
209.7	121.1	105.1	210.9	42.5

Table 0.4.: Stiffness coefficients for ZnO in GPa (Bateman, 1962).

Unfortunately, (Zn, Mg)O crystal in the wurtzite phase cannot be found naturally. Most of the time, the authors use the Vegard's law to interpolate the Cij values between the ones of the ZnO and those of the MgO, that are established too. The problem with this approach, is that ZnO and MgO does not share the same crystal symetry: ZnO is a hexagonal cristal, whereas MgO is cubic. In this situation, it is not garanteed that the Vegard's law is still a good approximation for the determination of the (Zn, Mg)O stiffness coefficient. On the other side, the determination of (Zn, Mg)O stiffness coefficients can not be neglected in the scope of this project. Indeed the epitaxial layers grown for QCL are quite thick - typically 1 or 2 μm, so the risk of relaxation has to be considered. It can be seriously considered only if all the mechanical parameters of (Zn, Mg)O are known for each Mg content of the alloy.

It is necessary to think of another approach to overcome this material parameters issue.

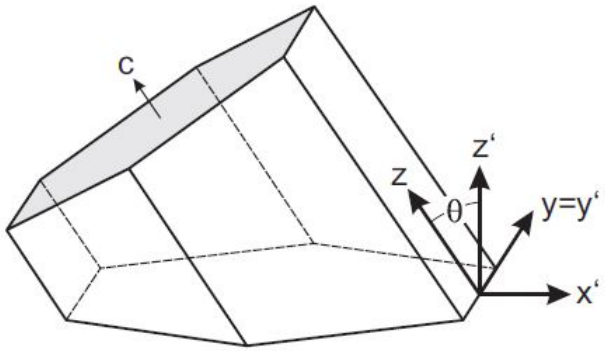

Figure 0.90.: Schematic of the hexagonal cell. The c axis is tilted by an angle θ with respect to the growth direction. *Reprinted from (Grundmann & Zúñiga-Pérez, 2016), John Wiley and Sons, © 2008 WILEY-VCH Verlag GmbH & Co. KGaA, Weinheim.*

We propose an alternative approach based on both theoretical and experimental elements. The idea comes from a paper which presents deformation calculations for a wurtzite crystal grown on a substrate, for various inclinaisons of the c-axis with respect to the growth plane (Grundmann & Zúñiga-Pérez, 2016). In the following paragraph, I shortly explain the main theoretical aspects developed in this paper, and how they can further be improved and coupled to experimental measurements.

The spirit of this paper is done in the limit of the reversible deformations, for which the Hooke's law can be applied. To distinguish the crystal system from the epitaxial layers' one, we define a coordinate system for each of these two systems (see figure 0.90).

We define the vectors associated to the crystal lattice:

$$\begin{cases} \overrightarrow{e_x} \\ \overrightarrow{e_y} \\ \overrightarrow{e_z} \end{cases} \tag{0.28}$$

and those associated to the epitaxial layer:

$$\begin{cases} \overrightarrow{e_x}' = \cos\theta \overrightarrow{e_x} - \sin\theta \overrightarrow{e_z} \\ \overrightarrow{e_y}' = \overrightarrow{e_y} \\ \overrightarrow{e_z}' = +\sin\theta \overrightarrow{e_x} + \cos\theta \overrightarrow{e_z} \end{cases} \tag{0.29}$$

We can pass from the crystal lattice to the epitaxial layer coordinate by applying the following rotation matrix $R(\theta)$:

$$R(\theta) = \begin{bmatrix} \cos\theta & 0 & \sin\theta \\ 0 & 1 & 0 \\ -\sin\theta & 0 & \cos\theta \end{bmatrix}_{(\overrightarrow{e_x}', \overrightarrow{e_y}', \overrightarrow{e_z}')} \tag{0.30}$$

By using this description, all the parameters that can be measured experimentally - as deformations for instance - are expressed in the epitaxial layer coordinate. In particular, we need to express the Hooke's law in this coordinate system. Each component of the stiffness matrix in the epitaxial layer coordinate C'_{pqrs} can be written as followed:

$$C'_{pqrs} = R_{pi}(\theta)\ R_{qj}(\theta)\ R_{rk}(\theta)\ R_{sl}(\theta)\ C_{ijkl} \tag{0.31}$$

The Einstein summation convention must be applied in the former expression, meaning that repeated indexes should be summed. For each component, a maximum addition of 12 terms should be done, which gives this general expression for the stiffness matrix in the epilayer coordinate as a function of the tilted angle θ:

$$C' = \begin{bmatrix} C'_{1111} & C'_{1122} & C'_{1133} & 0 & C'_{1131} & 0 \\ C'_{1122} & C'_{2222} & C'_{2233} & 0 & C'_{2231} & 0 \\ C'_{1122} & C'_{2233} & C'_{3333} & 0 & C'_{3331} & 0 \\ 0 & 0 & 0 & C'_{2323} & 0 & 0 \\ C'_{1131} & C'_{2231} & C'_{3331} & 0 & C'_{3131} & 0 \\ 0 & 0 & 0 & 0 & 0 & C'_{1212} \end{bmatrix} \tag{0.32}$$

Now we can apply the Hooke's law in the epilayer coordinate: $\sigma' = C'\,\varepsilon'$

$$\begin{pmatrix} \sigma'_{xx} \\ \sigma'_{yy} \\ \sigma'_{zz} \\ \sigma'_{yz} \\ \sigma'_{xz} \\ \sigma'_{xy} \end{pmatrix} = \begin{bmatrix} C'_{1111} & C'_{1122} & C'_{1133} & 0 & C'_{1131} & 0 \\ C'_{1122} & C'_{2222} & C'_{2233} & 0 & C'_{2231} & 0 \\ C'_{1133} & C'_{2233} & C'_{3333} & 0 & C'_{3331} & 0 \\ 0 & 0 & 0 & C'_{2323} & 0 & 0 \\ C'_{1131} & C'_{2231} & C'_{3331} & 0 & C'_{3131} & 0 \\ 0 & 0 & 0 & 0 & 0 & C'_{1212} \end{bmatrix} \begin{pmatrix} \varepsilon'_{xx} \\ \varepsilon'_{yy} \\ \varepsilon'_{zz} \\ \varepsilon'_{yz} \\ \varepsilon'_{xz} \\ \varepsilon'_{xy} \end{pmatrix} \tag{0.33}$$

$$\sigma'_{xx} = C'_{1111}\varepsilon'_{xx} + C'_{1122}\varepsilon'_{yy} + C'_{1133}\varepsilon'_{zz} + C'_{1131}\varepsilon'_{xz} \tag{0.34}$$

$$\sigma'_{yy} = C'_{1122}\varepsilon'_{xx} + C'_{1111}\varepsilon'_{yy} + C'_{1133}\varepsilon'_{zz} + C'_{2231}\varepsilon'_{xz} \tag{0.35}$$

$$\sigma'_{zz} = C'_{1133}\varepsilon'_{xx} + C'_{2233}\varepsilon'_{yy} + C'_{3333}\varepsilon'_{zz} + C'_{3331}\varepsilon'_{xz} \tag{0.36}$$

$$\sigma'_{yz} = C'_{2323}\varepsilon'_{yz} \tag{0.37}$$

$$\sigma'_{xz} = C'_{1131}\varepsilon'_{xx} + C'_{2231}\varepsilon'_{yy} + C'_{3331}\varepsilon'_{zz} + C'_{3131}\varepsilon'_{xz} \tag{0.38}$$

$$\sigma'_{xy} = C'_{1212}\varepsilon'_{xy} \tag{0.39}$$

Considering that the epitaxial layer surface is strain free, we can assume that $\sigma'_{zz} = \sigma'_{xz} = \sigma'_{yz} = 0$. These last condition leads to $\varepsilon'_{yz} = 0$ according to equation 0.37. In particular, the most interesting equation is 0.36, because the deformation ε'_{zz} can be measured experimentally. This equation depends on 4 deformations components: ε'_{xx}, ε'_{yy}, ε'_{zz} and ε'_{xz}. We can deduce the expression of ε'_{xz} by using the equation 0.38 as:

$$\varepsilon'_{xz} = -\frac{1}{C'_{3131}}\left(C'_{1131}\varepsilon'_{xx} + C'_{2231}\varepsilon'_{yy} + C'_{3331}\varepsilon'_{zz}\right) \tag{0.40}$$

Then we can remplace the expression of ε'_{xz} found in equation 0.40 in the equation 0.36 to give an expression of the deformation ε'_{zz}:

$$\varepsilon'_{zz} = \frac{\left[C'_{3131}C'_{1133} - C'_{1131}C'_{3331}\right]\varepsilon'_{xx} + \left[C'_{3131}C'_{2233} - C'_{2231}C'_{3331}\right]\varepsilon'_{yy}}{(C'_{3331})^2 - C'_{3131}C'_{3333}} \tag{0.41}$$

Now we have the expression of ε'_{zz} as a function of the C component matrix that we want to determine, of the tilt angle θ that we know, and of the deformations ε'_{xx} and ε_{yy}' that are unknown. To express them we need to define the lattice mismatch between the layers and the substrate:

$$\varepsilon_a = \frac{a_S}{a_L} - 1 \qquad \varepsilon_c = \frac{c_S}{c_L} - 1 \tag{0.42}$$

Where a_S and a_L are the a lattice parameter of the substrate and the layer (c_S and c_L are the same but for the c lattice parameter). As for the matrices C and C' that are linked by the rotation matrix $R(\theta)$, we need to find the link between the lattice mismatches in the crystal lattice coordinate ε_a and ε_c and the lattice mismatches in the epilayer coordinate ε'_{xx} and ε'_{yy}. For ε'_{yy}, it is straightforward since the rotation by the tilt angle θ is realized around the y axis, so axis y and y' are identical. Thus in any way $\varepsilon'_{yy} = \varepsilon_a$ whatever is the value of θ (see figure 0.90). For the deformation ε'_{xx} we have the following geometric relation:

$$\cos\theta = \frac{d_{hkl}}{c/l} \tag{0.43}$$

With d_{hkl} which is the reticular distance between two consecutive crystal's planes in the growth direction $[hkl]$ (h, k and l are the Miller indices). The expression of d_{hkl} is well known for a hexagonal crystal and is expressed as followed:

$$d_{hkl} = \left(\frac{^{3}/_{4}}{\frac{3}{4c^2}\left(l^2 + \frac{4c^2}{3a^2}(h^2 + hk + k^2)\right)} \right)^{1/2} \tag{0.44}$$

Which gives the final expression for the angle θ:

$$\theta = \arccos\left(\frac{l}{\sqrt{l^2 + \frac{4c^2}{3a^2}(h^2 + hk + k^2)}} \right) \tag{0.45}$$

On the other hand, we have for ε'_{xx}:

$$\varepsilon'_{xx} = \frac{a_S}{\cos\theta_S}\frac{\cos\theta_L}{a_L} - 1 \tag{0.46}$$

Then let's replace θ_S and θ_L by their expressions (equation 0.45) in the equation 0.46.

$$\varepsilon'_{xx} = \left(\frac{4c_S^2(h^2 + hk + k^2) + 3a_S^2 l^2}{4c_L^2(h^2 + hk + k^2) + 3a_L^2 l^2} \right)^{1/2} - 1 \tag{0.47}$$

In equation 0.47, it is assumed that the substrate is a hexagonal crystal and that it has the same orientation as the epilayer ($\theta_S = \theta_L = \theta$). With a little transformation, we ended with the expression of ε'_{xx} as a function of θ, ε_a and ε_c:

$$\varepsilon'_{xx} = \left(\left(\frac{\cos\theta}{1 + \varepsilon_a} \right)^2 + \left(\frac{\sin\theta}{1 + \varepsilon_c} \right)^2 \right)^{-1/2} - 1 \tag{0.48}$$

We can further simplify it if we assume that we treate only little deformations, which is the case when we apply Hooke's law:

$$\varepsilon'_{xx} \approx \varepsilon_a(\cos\theta)^2 + \varepsilon_c(\sin\theta)^2 \tag{0.49}$$

The final expression for the deformation in the growth direction ε'_{zz} can be computed by replacing ε'_{xx} and ε'_{yy} by their expression.

$$\varepsilon'_{zz} = \frac{\left[C'_{3131}C'_{1133} - C'_{1131}C'_{3331}\right]\left(\varepsilon_a(\cos\theta)^2 + \varepsilon_c(\sin\theta)^2\right) + \left[C'_{3131}C'_{2233} - C'_{2231}C'_{3331}\right]\varepsilon_a}{(C'_{3331})^2 - C'_{3131}C'_{3333}} \tag{0.50}$$

By simplicity it was chosen not by replacing the stiffness component C' by their expression as a function of C and θ. Their expressions are detailed in the appendix (see V). In particular, we can look at two specific cases: polar orientation ($\theta = 0°$) and the non-polar orientation ($\theta = 90°$). For the polar orientation, the two stiffness matrices C' and C are equal.

$$\varepsilon'_{zz}(0) = -\frac{2C_{1133}}{C_{3333}}\varepsilon_a \tag{0.51}$$

For the non-polar orientation, we end with the following expression for the deformation $\varepsilon'_{zz}(90)$:

$$\varepsilon'_{zz}(90) = -\frac{C_{1122}\varepsilon_a + C_{1133}\varepsilon_c}{C_{1111}} \tag{0.52}$$

As shown in the equation 0.50, the deformation in the growth direction depends on 7 stiffness parameters C'_{pqrs}, on the crystal orientation described by the tilted angle θ and on the lattice mismatches ε_a and ε_c. In fact, these 7 stiffness parameters depends on only 5 stiffness parameters C_{ijkl} (in the crystal lattice coordinate). At the end, we have 7 unknown material parameters (5 C_{ijkl}, ε_a and ε_c), and one variable θ. To determine them, we can grow (Zn, Mg)O layers on ZnO substrates for 7 orientations θ and measure the out-of-plane lattice mismatch $\frac{\Delta d_\perp}{d_\perp}$ by X-Ray. The out-of-plane lattice mismatch can be expressed as followed:

$$\frac{\Delta d_\perp}{d_\perp} = -\frac{d^S_{ZnMgO} - d_{ZnO}}{d_{ZnO}} = -\frac{d^R_{ZnMgO}(1 + \varepsilon'_{zz}) - d_{ZnO}}{d_{ZnO}} \tag{0.53}$$

$$\varepsilon'_{zz} = \frac{d^S_{ZnMgO} - d^R_{ZnMgO}}{d^R_{ZnMgO}} \tag{0.54}$$

With d_{ZnO} which represents the out-of plane lattice constant of the bulk ZnO substrate.

d^S_{ZnMgO} and d^R_{ZnMgO} which are the strained and the relaxed out-of-plane lattice mismatch of the wurtzite (Zn, Mg)O layers respectively.

ε'_{zz} is the (Zn, Mg)O out-of-plane deformation in the lattice coordinate system.

So we are able to determine the parameters for a given Mg composition. To know completly what the mechanical behaviour of the alloy is, a serie of at least 3 samples with different Mg content should be grown for each orientation θ. For each sample it is important to adjust the (Zn, Mg)O thickness so that the layer does not relax.

The samples have been grown and the corresponding lattice mismatch $\frac{\Delta d_\perp}{d_\perp}$ have been measured for the following orientations: a-plane, c-plane, m-plane, r-plane and y-plane (table 0.5). Figures 0.91, 0.92, 0.93, 0.94 and 0.95 show the evolution of the out-of plane lattice mismatch $\frac{\Delta d_\perp}{d_\perp}$ as a function of the Mg composition. We can notice that the out-of-plane deformation grows linearly

with the Mg content for a, m, c and r planes. For y plane, the out-of plane lattice mismatch is very low. The lattice mismatches are nearly one order of magnitude lower compared to the other orientations. The experimental errors are still large, which explains that it is difficult to comment its trend.

Orientation name	Miller index	Tilt angle θ (°)
a	$(11\bar{2}0)$	90
c	(0001)	0
m	$(10\bar{1}0)$	90
r	$(10\bar{1}2)$	43
y	$(20\bar{2}1)$	75

Table 0.5.: Correspondance between the different orientations tested, the Miller indices and the tilt angles θ.

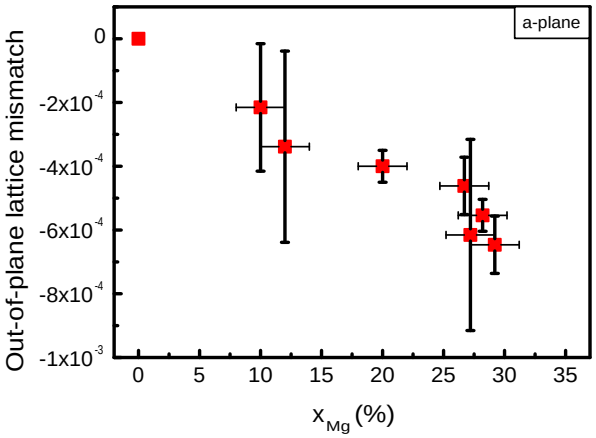

Figure 0.91.: Evolution of the out-of plane lattice mismatch direction $\frac{\Delta d_\perp}{d_\perp}$ for a-plane oriented (Zn, Mg)O with the Mg composition x_{Mg}.

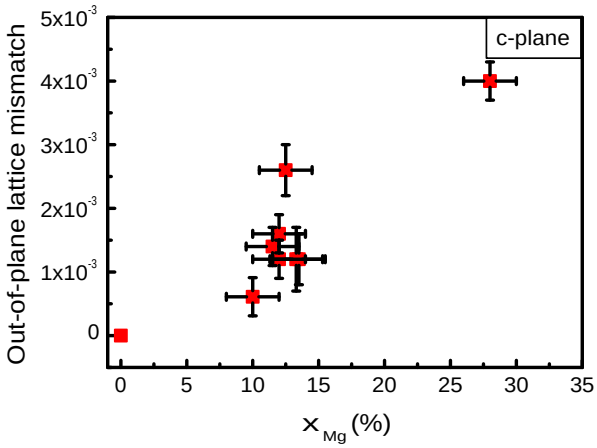

Figure 0.92.: Evolution of the out-of plane lattice mismatch $\frac{\Delta d_\perp}{d_\perp}$ for c-plane oriented (Zn, Mg)O with the Mg composition x_{Mg}.

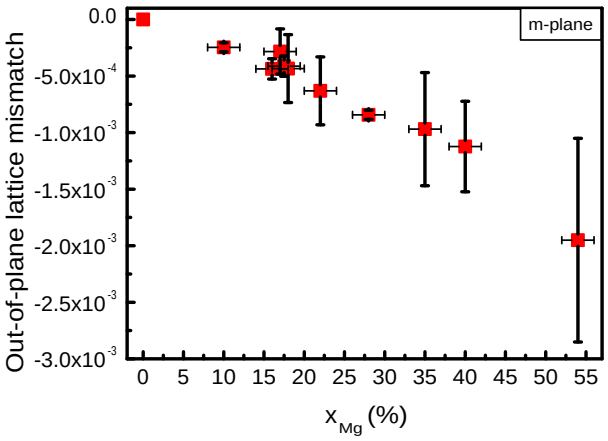

Figure 0.93.: Evolution of the deformation in the growth direction $\frac{\Delta d_\perp}{d_\perp}$ for m-plane oriented (Zn, Mg)O with the Mg composition x_{Mg}.

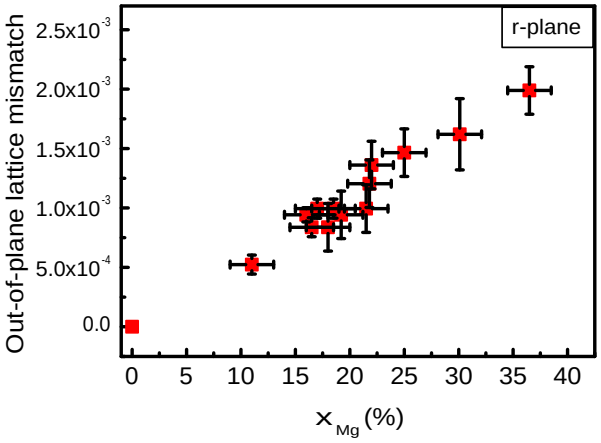

Figure 0.94.: Evolution of the deformation in the growth direction $\frac{\Delta d_\perp}{d_\perp}$ for r-plane oriented (Zn, Mg)O with the Mg composition x_{Mg}.

Figure 0.96 shows the strain variation as a function of the tilted angle θ. The variation of $\frac{\Delta d_\perp}{d_\perp}$ with the tilted angle θ is symmetric with respect to $\theta = 90°$ (ie non-polar orientation). From $\theta = 0°$ to 90°, according to the XRD, we observe a decrease of $\frac{\Delta d_\perp}{d_\perp}$ in which two domains can be distinguished:

- a domain from $\theta = 0°$ to $\theta \approx 75°$ where $\frac{\Delta d_\perp}{d_\perp}$ is positive.
- a domain from $\theta \approx 75°$ to $\theta = 90°$ where $\frac{\Delta d_\perp}{d_\perp}$ is negative.

The angle for which the out-of plane lattice mismatch is zero is at the vicinity of an orientation with $\theta \approx 75°$, i.e. close to y-plane.

In addition, we measure experimentally distinct out-of-plane lattice mismatch values for the two non-polar orientations tested (a-plane and m-plane). This explain why we will propose in the following a model with two rotation angles to be able to make a distinction between the two non-polar orientations.

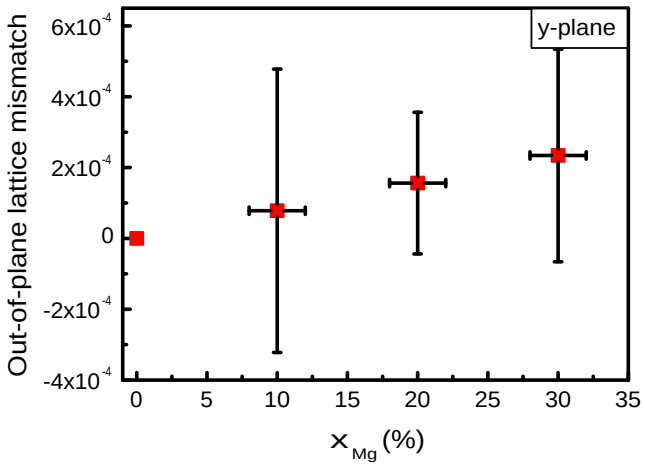

Figure 0.95.: Evolution of the out-of-plane lattice mismatch $\frac{\Delta d_\perp}{d_\perp}$ for y-plane oriented (Zn, Mg)O with the Mg composition x_{Mg}.

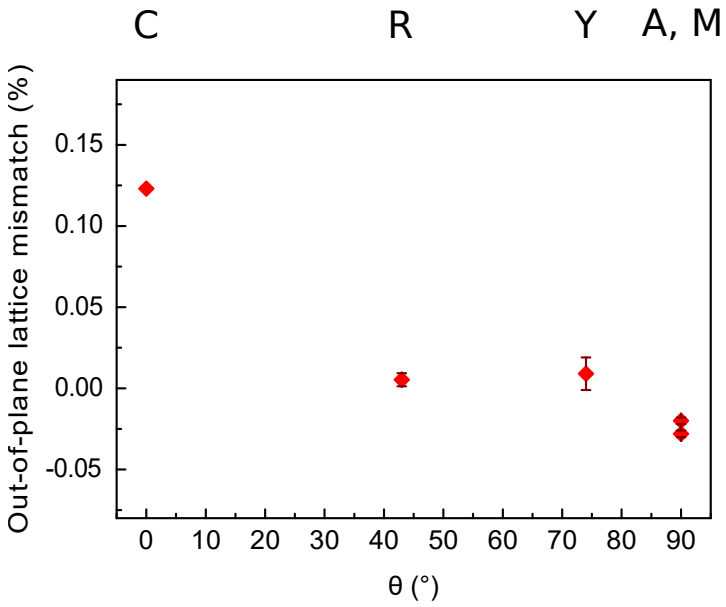

Figure 0.96.: Out-of plane lattice mismatch obtained by XRD in the case of (Zn, Mg)O with 10 % of Mg. The letters above the graph help to identify the crystallographic planes.

We push the model developed in Grundmann & Zúñiga-Pérez (2016) forward by adding another degree of freedom for the rotation around the z' axis (see figure 0.97). The method is identical as previously but with two tilted angles θ and ψ. To describe the stiffness matrix in the epitaxial coordinate $(\overrightarrow{e_x}'', \overrightarrow{e_y}'', \overrightarrow{e_z}'')$, the following notation is used: C''.

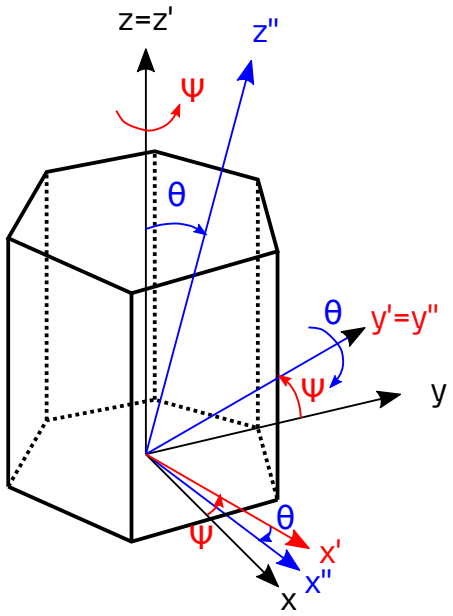

Figure 0.97.: Schematic showing the two rotations involved in the model.

Only meaningful results are shown and details on the calculation can be found in the appendix (see V). As the C'' matrix does not have coefficients equal to zero, the system to resolve is a bit more complex than is the case of a single tilt angle (see equtaions 0.55 to 0.60).

$$\sigma''_{xx} = C''_{1111}\varepsilon''_{xx} + C''_{1122}\varepsilon''_{yy} + C''_{1133}\varepsilon''_{zz} + C''_{1123}\varepsilon''_{xz} + C''_{1131}\varepsilon''_{yz} + C''_{1112}\varepsilon''_{xy} \tag{0.55}$$

$$\sigma''_{yy} = C''_{1122}\varepsilon''_{xx} + C''_{2222}\varepsilon''_{yy} + C''_{2233}\varepsilon''_{zz} + C''_{2223}\varepsilon''_{xz} + C''_{2231}\varepsilon''_{yz} + C''_{2212}\varepsilon''_{xy} \tag{0.56}$$

$$\sigma''_{zz} = C''_{1133}\varepsilon''_{xx} + C''_{2233}\varepsilon''_{yy} + C''_{3333}\varepsilon''_{zz} + C''_{3323}\varepsilon''_{xz} + C''_{3331}\varepsilon''_{yz} + C''_{3312}\varepsilon''_{xy} \tag{0.57}$$

$$\sigma''_{xz} = C''_{1123}\varepsilon''_{xx} + C''_{2223}\varepsilon''_{yy} + C''_{3323}\varepsilon''_{zz} + C''_{2323}\varepsilon''_{xz} + C''_{2331}\varepsilon''_{yz} + C''_{2312}\varepsilon''_{xy} \tag{0.58}$$

$$\sigma''_{yz} = C''_{1131}\varepsilon''_{xx} + C''_{2231}\varepsilon''_{yy} + C''_{3331}\varepsilon''_{zz} + C''_{2331}\varepsilon''_{xz} + C''_{3131}\varepsilon''_{yz} + C''_{3112}\varepsilon''_{xy} \tag{0.59}$$

$$\sigma''_{xy} = C''_{1112}\varepsilon''_{xx} + C''_{2212}\varepsilon''_{yy} + C''_{3312}\varepsilon''_{zz} + C''_{2312}\varepsilon''_{xz} + C''_{3112}\varepsilon''_{yz} + C''_{1212}\varepsilon''_{xy} \tag{0.60}$$

The free surface condition is still valid and give $\sigma''_{zz} = \sigma''_{xz} = \sigma''_{yz} = 0$. From equation 0.57 we see that the out-of-plane deformation ε''_{zz} is now a function of the deformations: ε''_{xx}, ε''_{yy}, ε''_{xz}, ε''_{yz} and ε''_{xy}. ε''_{xx} and ε''_{yy} can be expressed using the lattice mismatch between the (Zn, Mg)O layer and the ZnO substrate. We should express ε''_{xz}, ε''_{yz} and ε''_{xy} as a function of ε''_{xx}, ε''_{yy}, ε''_{zz} and C''_{ijkl}. To do so we do the following hypothesis: $\sigma''_{xy} = 0$. As a consequence, equations 0.58, 0.59 and 0.60 form a system that we can resolve to have the expressions of ε''_{xz}, ε''_{yz} and ε''_{xy}.

We end with the final expressions for ε''_{xz}, ε''_{yz} and ε''_{xy} (see equations 0.61, 0.62 and 0.63).

$$\varepsilon''_{xz} = C_3 C_\lambda \varepsilon''_{xx} + C_3 C_\mu \varepsilon''_{yy} + C_3 C_o \varepsilon''_{zz} \tag{0.61}$$

$$\varepsilon''_{yz} = (f_1 C_\alpha + C_1 C_3 C_\lambda)\, \varepsilon''_{xx} + (f_1 C_\beta + C_1 C_3 C_\mu)\, \varepsilon''_{yy} + (f_1 C_\gamma + C_1 C_3 C_o)\, \varepsilon''_{zz} \tag{0.62}$$

$$\varepsilon''_{xy} = (f_1 C_\delta + C_1 C_3 C_\lambda)\, \varepsilon''_{xx} + (f_1 C_\varepsilon + C_1 C_3 C_\mu)\, \varepsilon''_{yy} + (f_1 C_\eta + C_1 C_3 C_o)\, \varepsilon''_{zz} \tag{0.63}$$

Where f_1, and C_i are constants whose expressions can be found in the appendix (see section V). Here is the final expression for the deformation ε''_{zz} as a function of ε''_{xx} and ε''_{yy}:

$$\varepsilon''_{zz} = -\frac{C_x \varepsilon''_{xx} + C_y \varepsilon''_{yy}}{C_z}$$

With ε''_{xx} and ε''_{yy} that now depend on both angles θ and ψ (see section V for detail).

In this paragraph we have set the theoretical environment which allows to describe how the out-of-plane deformation of an epitaxial layer varies for different orientations using one tilt angle Grundmann & Zúñiga-Pérez (2016). This model coupled with out-of plane-lattice mismatch measurements for several tilt angles and Mg content can help us to determine (Zn, Mg)O alloy's stiffness parameters. More precisely, the out-of-plane deformation ε''_{zz} is found to be a function of 7 unknown parameters: the deformations ε_a and ε_c and the 5 independent stiffness components C_{1111}, C_{3333}, C_{1122}, C_{1133} and C_{2323}. Thus to determine them without any isotropy approximation, 7 different crystal orientations (θ, ψ) should be grown with various Mg content, and then their out-of-plane lattice mismatch should be determined by XRD. Up to now, 5 of them has been grown and measured: y, m, c, a and r. So 2 other crystal orientations are needed to complete this work to determine all the stiffness component and lattice parameters of the wurtzite (Zn,Mg)O alloy.

Out-of-plane lattice mismatch measurements were performed by XRD. The values measured for two non-polar orientations - a-plane and m-plane - are not equal, as suggested by the model. To take this discrepancy into account, we refined the theoretical model by adding an other tilt angle ψ to enable distinguish non-polar orientations.

This theoretical environment is valid in the elastic limit, or with relatively little deformation. As in this project we are focused on micrometer-thick layers, the validity limit of the latter hypothesis can be easily reach. In the next paragraph we discuss what happens beyond the elasticity limit.

0.7. Plasticity and damaging

When we begin to apply strain on a material, for instance during a traction test, most of them exhibit a region where the stress is proportional to the strain Yonenaga *et al.* (2008). This corresponds to the linear elasticity regime described by the Hooke's law, which was treated in the previous paragraph for ZnO. In this region, the strains are completly reversible. When increasing further the strain, we enter another regime where strain is no more proportional to stress, and no more reversible. This is the plastic regime where the material set its own strategy to accomodate the resulting stress. These strategies are various. For crystals one very common is the nucleation and/or the displacement of

dislocations Hull & Bacon (2011). We discuss how ZnO and (Zn, Mg)O accomodate the stress in this plastic domain for two orientations: m-plane and r-plane. But this strategy has its limit: when the dislocation concentration becomes high, they begin to interact and to slow each other, leading to a less efficient stress accomodation. At this point the material encourter the maximum stress that he can hold without any damage.

When the stress accomodation mechanism is out, the hold stress becomes to decrease: the material enters the part of the plastic regime where damage starts occuring. This region extends until the complete breackage of the material.

Figure 0.98 represents the stress versus strain curve of ZnO wurtzite bulk crystal. The experiment was realized in compression, with the compression direction at 45° with respect to the c-axis Yonenaga *et al.* (2008). For all tested temperatures, curves show two regions: a first one with a linear dependency which corresponds to the elasticity region. A a second domain, at higher strain, which own to the plasticity region (damaging region not represented).

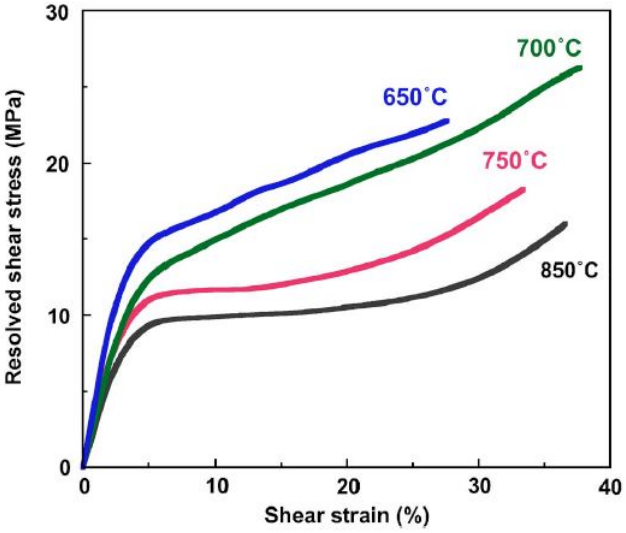

Figure 0.98.: Resolved shear stress as a function of the shear strain for ZnO at different temperatures during a compression test at a strain rate of $4.2 \times 10^{-4}\, s^{-1}$. Damaging is not reach during this test. Reprinted from *Yonenaga* et al. *(2008), with the permission of AIP Publishing.*

Now we review how our ZnO/(Zn, Mg)O heterostructures - typically MQWs - behave in the plastic and damage region. For each orientation that were investigated, m-plane and r-plane, we try to discuss the following points:

- How does the strain state look like?
- What are the possible strategies for the epilayer to accomodate the strain?
- How do damages look like? Can we predict and avoid them?

0.7.1. On m-plane orientation

As we are growing directly on ZnO substrates, strains are mainly concentrated in (Zn, Mg)O layers. On a m-plane surface, we can consider the two following in-plane directions: [0001] and $\left[11\bar{2}0\right]$ (figure 0.100). MgO crystallizes in a cubic system with its lattice parameter bounds between the a and c lattice parameter of hexagonal ZnO. So for hexagonal (Zn, Mg)O we have:

- $a_{(Zn,Mg)O} > a_{ZnO}$: leading to an alloy in compression in the $\left[1\bar{2}10\right]$ direction
- $c_{(Zn,Mg)O} < c_{ZnO}$: leading to an alloy in tension in the [0001] direction

For dislocation, we should look if m-plane is a favorable to dislocation displacement. To go back to the basics, it means to look if the m-plane has slip systems that can be activated. Here we consider only glide as a displacement because climb is very unlikely to occur. Dislocation glide is completly described if we know the slip plane and the so-called Burgers vector. Most of the time, it happens in atomically dense planes, with a Burgers vector with the shortest lattice translation vector possible included in the slip plane. In hexagonal structures, it corresponds to basal and prismatic planes $\{0001\}$ and $\left\{10\bar{1}0\right\}$ and to Burgers vectors $\frac{1}{3}\left\langle 11\bar{2}0\right\rangle$ Hull & Bacon (2011).

To trigger dislocation glide in a given plane and direction, a shear stress in this plane is required. It is triggered by a force $\overrightarrow{F}$. The piece of material considered has a section S whose normal is paralell to $\overrightarrow{F}$.The shear stress resolved in the glide plane and along the glide direction is a product of the projection of $\overrightarrow{F}$ in the glide direction and of the projection of the section S on the glide plane. Using the projection angles in figure 0.99 it gives:

$$\tau = \frac{F}{A}\cos\alpha\,\cos\beta \tag{0.64}$$

From the equation 0.64, we can infer that the dislocation glide is only possible if the factor $\cos\alpha\,\cos\beta$ is non zero. This factor is known as the Schmid factor and gives an idea of how easy it is for a dislocation to glide on a given slip system, keeping the force and the section constant Hull & Bacon (2011).

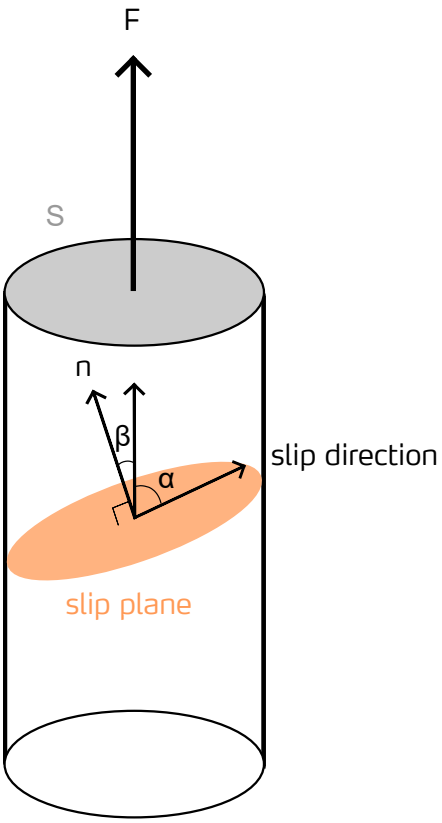

Figure 0.99.: Schematic for the understanding of the resoled shear stress needed to make a dislocation glide in a given glide plane and direction.

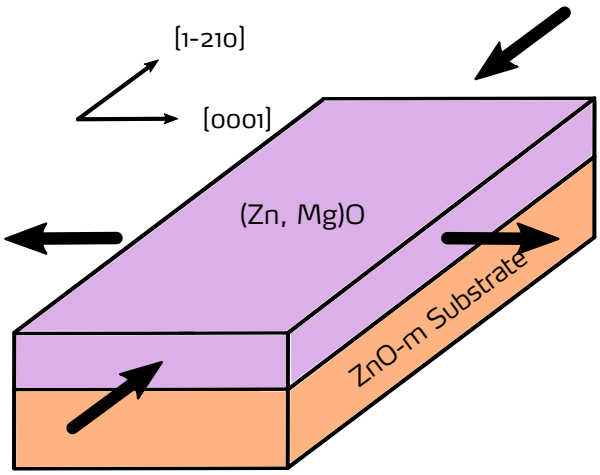

Figure 0.100.: Schematic representation of the stress states of m-plane (Zn, Mg)O grown on ZnO. The alloy is in tension in the [0001] direction, whereas it undergoes compression in the $[1\bar{2}10]$ direction.

In the paper Chauveau *et al.* (2008), authors calculate Schmid factors for m-plane for two in-plane directions supporting strain: $\langle 0001 \rangle$ and $\langle 11\bar{2}0 \rangle$. It turns out that for basal planes, Schmid factor is zero, so it cannot be activated. For pyramidal planes, Schmid factors are non zero, so dislocations using such planes can be activated. But corresponding Burgers vectors are large. It leads to a high activation energy, making glide on these planes unlikely to occur. The last option is prismatic planes $\{1\bar{1}00\}$. In this case Schmid factors are non zero for strain along $\langle 11\bar{2}0 \rangle$, which corresponds to the compression direction. Moreover, from the Brugers vectors possibles - $\langle 11\bar{2}0 \rangle$ and $\langle 11\bar{2}3 \rangle$ - $\langle 11\bar{2}0 \rangle$ is short, giving rise to a little activation energy.

It seems that the most promissing glide system to relax the strain in the $[1\bar{2}10]$ direction is prismatic planes $\{1\bar{1}00\}$ with Burgers vector in the $\langle 11\bar{2}0 \rangle$ direction. This conclusion is drawn in the light of Schmid factor and activation energy. This analysis holds in the static regime.

These opposite strain states on the sample surface can induce two kinds of relaxation: cracking due to the tension or dislocation nucleation and/or displacement due to the compression. We can wonder which strain state leads to the first relaxation. Figure 0.101 shows a SEM picture in cross-section of a MQW sample. We can observe that there is a crack whose line is perpendicular to the c-axis, which is the proof that there was a tension strain state in the [0001] that have been relaxed. Other SEM

images on the same sample shows that cracks are regularly spaced (between $6-7\,\mu m$, not shown).

The figure 0.102 shows a plane view of a single QW. This image shows very well that when the epilayer relax, it creates regularly spaced cracks. In this case, they are separated at least by $8-9\,\mu m$. Cracks spacing is governed by the amount of stress to relax, so it depends on various factors as:

- the Mg content
- the total thickness of (Zn, Mg)O
- the growth parameters used

If we compare the samples presented, the MQW sample (figure 0.101) contains 40 % of Mg and a total (Zn, Mg)O thickness of $160\,nm$ whereas the single QW sample (figure 0.102) has 32 % and $154\,nm$. We can notice that the total (Zn, Mg)O thickness is nearly identical, whereas the Mg content is higher for the MQW sample. As a consequence, the amount of stress to relax is higher, which explains the higher density of cracks observed in SEM.

About the other possible stress relaxation mechanism, TEM experiments realized in cross-section on various MQWs samples never shown dislocations on this orientation.

So it seems that the relaxation of (Zn, Mg)O occurs preferentially by crack formation along the $[1\bar{2}10]$. This relaxation arises because the lattice mismatch between (Zn, Mg)O and ZnO create a tension stress along the [0001]. It turns out it is the predominant relaxation mode of (Zn, Mg)O in this orientation.

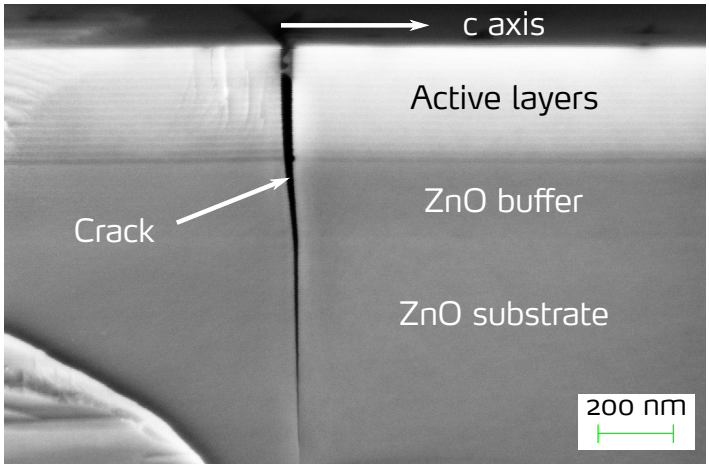

Figure 0.101.: SEM image in cross-section of a MQW with $x_{Mg} = 40\%$. The total (Zn, Mg)O thickness is $160\,nm$. A crack is starting from the surface and end in the substrate.

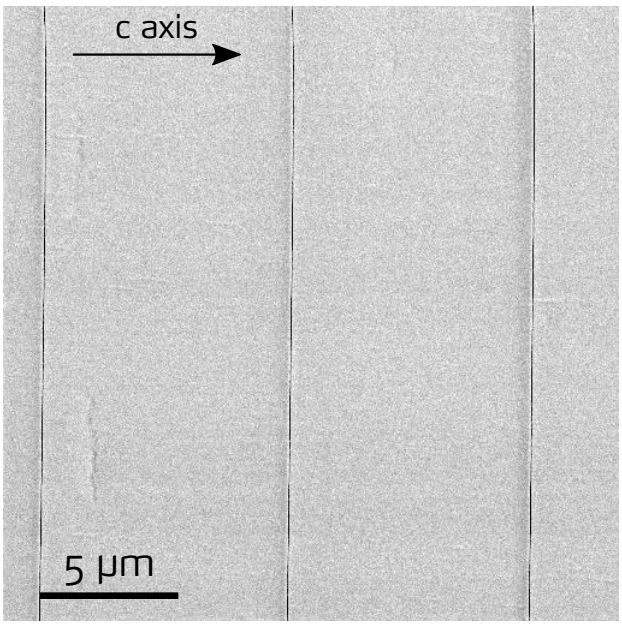

Figure 0.102.: SEM image in plane-view of a single QW with $x_{Mg} = 32\%$. The total (Zn, Mg)O thickness is $154\,nm$.

We investigate the misfit of (Zn, Mg)O on ZnO in the two in plane directions by X-Ray reciprocal space maps (RSM). The misfit in the $[1\bar{2}10]$ direction is noted ε_a and the one in the [0001] direction, ε_c. ε_a and ε_c are deduced respectively with the RSMs around the (220) and the (302) nodes. Two additional symmetric RSMs were recorded for two different angles φ to verifiy that no tilt was present in the sample. Figure 0.103 is showing how the sample is oriented with respect to the incoming beam depending on the rotation angle φ. The sample studied here is a single ZnO QW embeded in two (Zn, Mg)O barriers with 35 % of Mg and a total (Zn, Mg)O thickness of $226\,nm$ which is cracked. The density of cracks measured in SEM across the sample is $145\,mm^{-1}$.

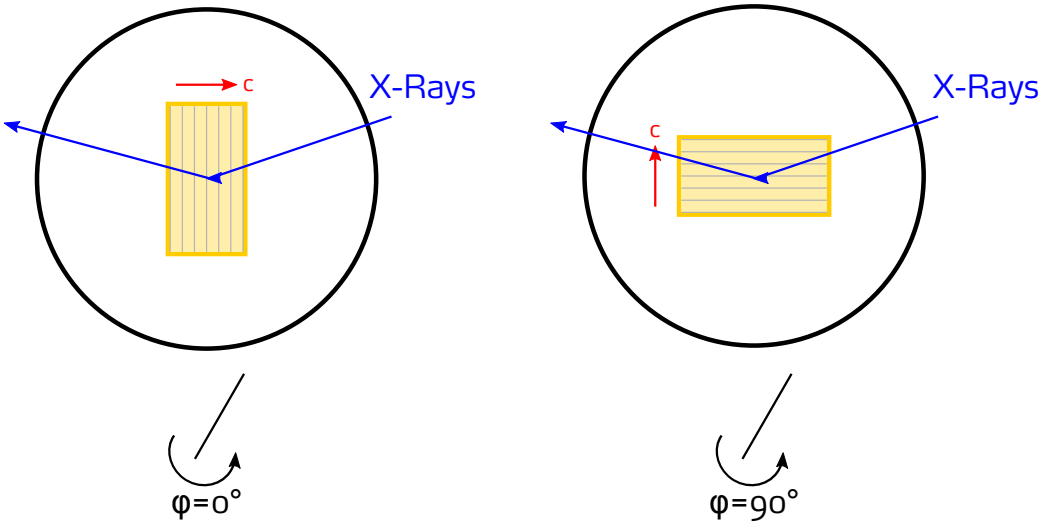

Figure 0.103.: Schematic of the X-ray experiment which precise how the sample is oriented with respect to the incoming X-ray beam for the rotation angles $\varphi = 0°$ and $\varphi = 90°$. Gray lines indicate cracks direction.

Figures 0.104 and 0.105 show RSM around the (220) and the (302) node of ZnO respectively. For

the RSM around the (220), no (Zn, Mg)O diffraction peak is observed. It confirms that the alloy does not relax along the $[1\bar{2}10]$ direction. As a consequence, $\varepsilon_a = 0$. The RSM around the (302) node shows a well defined diffraction peak which can be attributed to the alloy. Along the Q_x axis, the peak is misaligned with respect to the ZnO substrate. This is an evidence that the alloy has relaxed along the [0001] direction. We can deduce the misfit of the alloy compared to the ZnO from this shift : $\varepsilon_c = 3,4 \times 10^{-3}$. Note that this value is positive, which is in agreement with the prediction that stated tension in the c-axis direction and with the observation of cracks perpendicular to the c-axis.

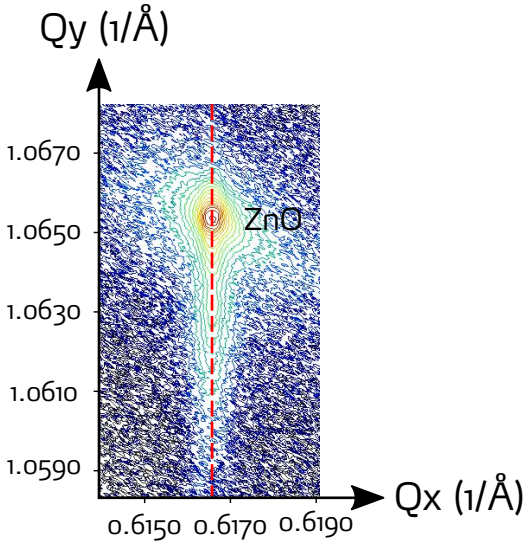

Figure 0.104.: RSM around the node (220), with $\varphi = 90°$.

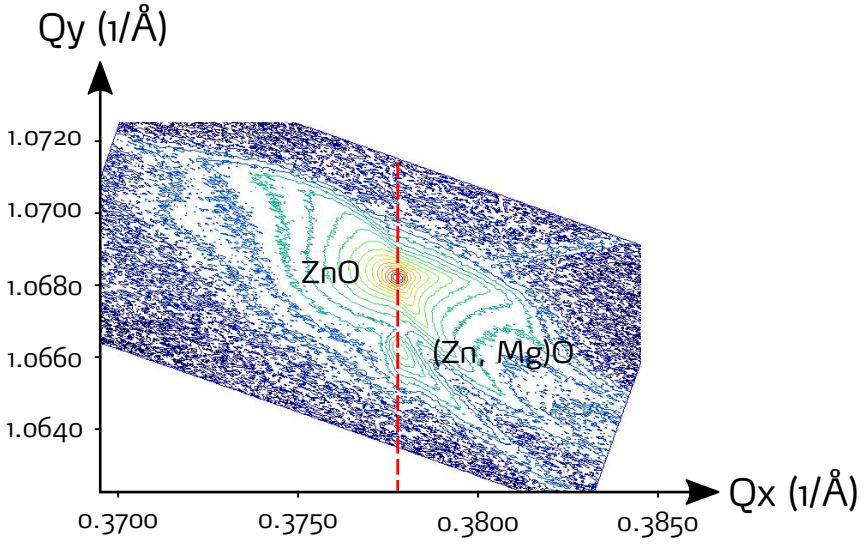

Figure 0.105.: RSM around the node (302), with $\varphi = 0°$.

Now it seems that the dominant relaxation mode of (Zn, Mg)O grown on ZnO on m-plane is well defined. As stated before, symmetric RSM with 2 different angles φ were recorded too. They are presented in figures 0.106 and 0.107. What is stricking is that their shapes look totally different.

When $\varphi = 0°$ - incoming beam parallel to the c-axis - the RSM presents an additional diffuse pattern around the ZnO and (Zn, Mg)O nodes, which is symmetric with respect to the $\left[1\bar{1}00\right]^*$ direction. For $\varphi = 90°$ - incoming beam perpendicular to the c-axis - the RSM does not present this diffuse pattern at all. So according to Curie's principle Curie (1894), there should be a phenomenon which is asymmetric with respect to the rotation φ. Moreover, on symmetric RSM, this phenomenon should preserve the symmetry with respect to the $\left[1\bar{1}00\right]^*$ direction (or in the real space, the normal to the m-plane). One possible candidate is the presence of cracks perpendicular to the c-axis.

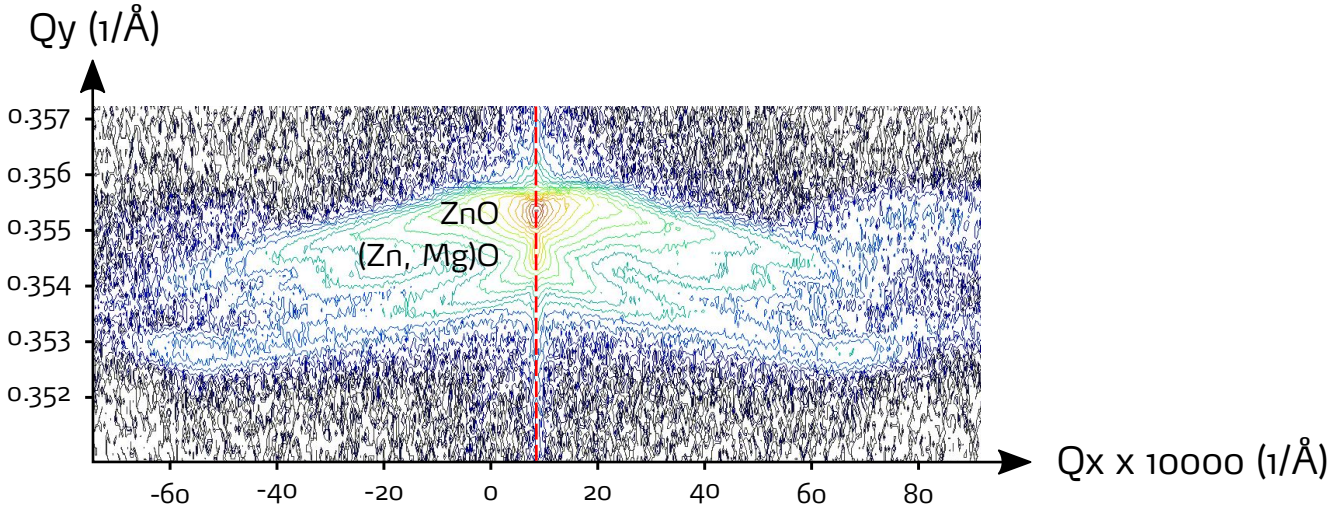

Figure 0.106.: RSM around the node (100), with $\varphi = 0°$.

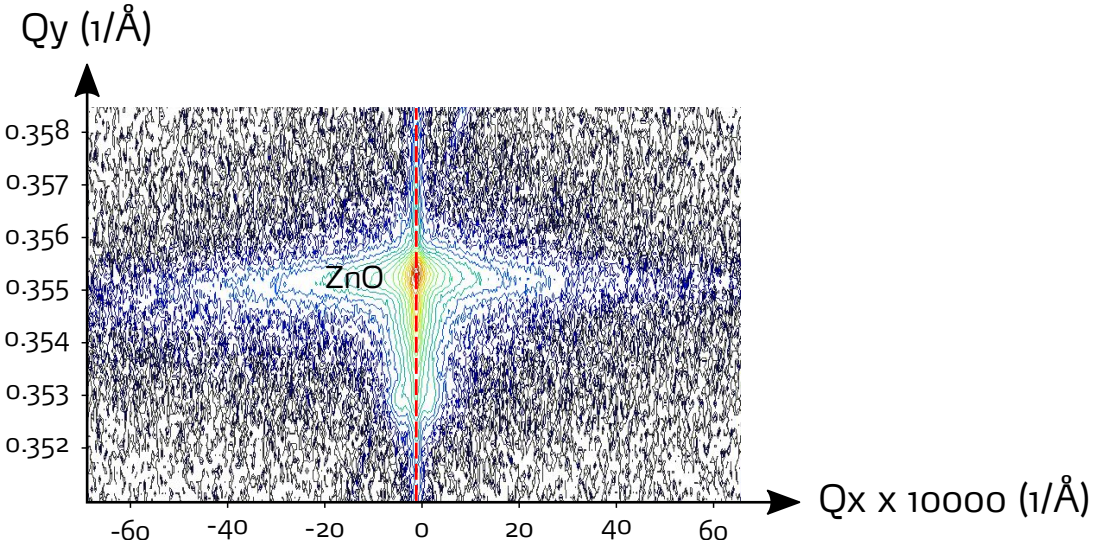

Figure 0.107.: RSM around the node (100), with $\varphi = 90°$.

To verify this hypothesis, when have performed two experiments. The first experiment was to check if this feature was present in a sample without cracks. And the second experiment was to take a sample with cracks, and to investigate the asymmetric nodes (220) and (302) in oblique and asymmetric configurations. When moving from oblique to asymmetric, the angle φ is changing by

90°. At the end, we should be able to distinguish in every RSM what the contribution of cracks and diffraction is.

The first experiment was performed on a single QW sample with 14 % of Mg and a total (Zn ,Mg)O thickness of 200 nm. No cracks was detected in this sample (AFM, optical microscope). Figures 0.108 and 0.109 represent the RSM around the node (100) of ZnO for $\varphi = 0°$ and $\varphi = 90°$ respectively. They are very similar: no diffuse pattern can be observed in the RSM with $\varphi = 0°$. In addition, they are quite similar to the RSM shown in figure 0.107. This confirmes there is no significant influence of cracks on the RSM for the rotation angle $\varphi = 90°$,. Thus we can conclude that cracks are responsible for the diffuse pattern on symmetric RSM with $\varphi = 0°$.

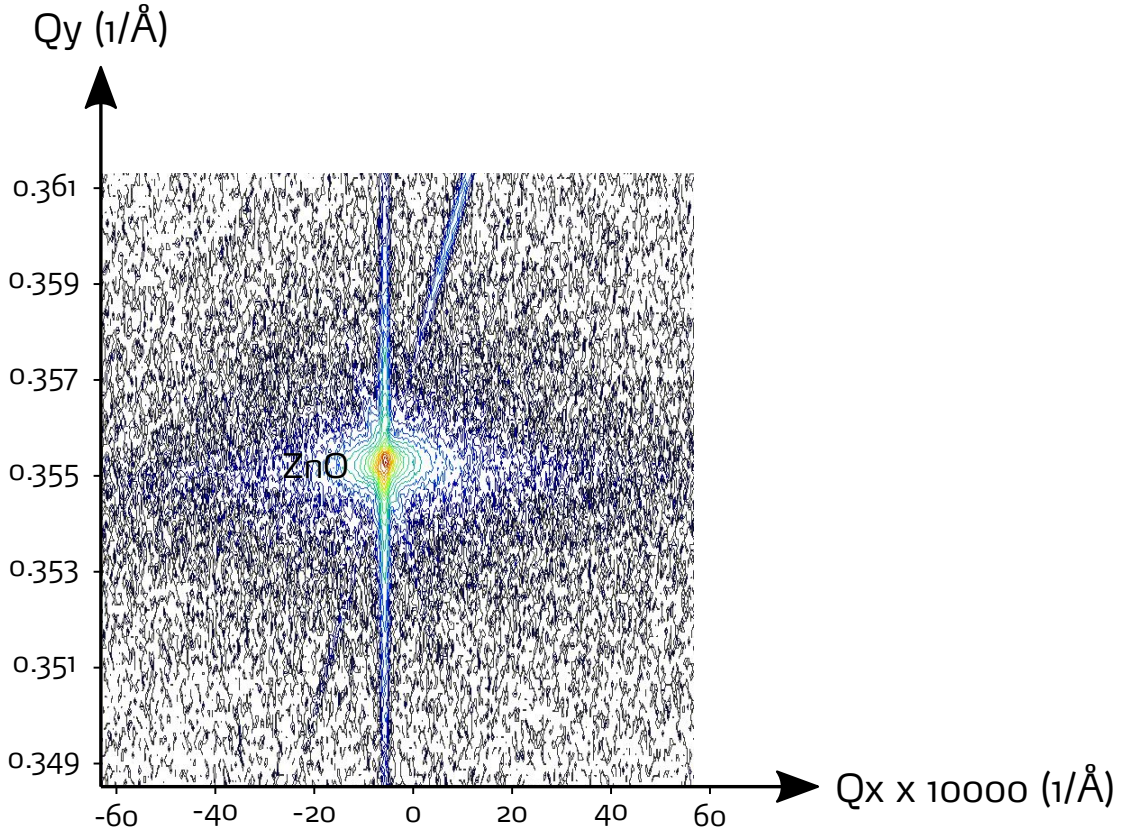

Figure 0.108.: RSM around the node (100), with $\varphi = 0°$ for a sample without cracks.

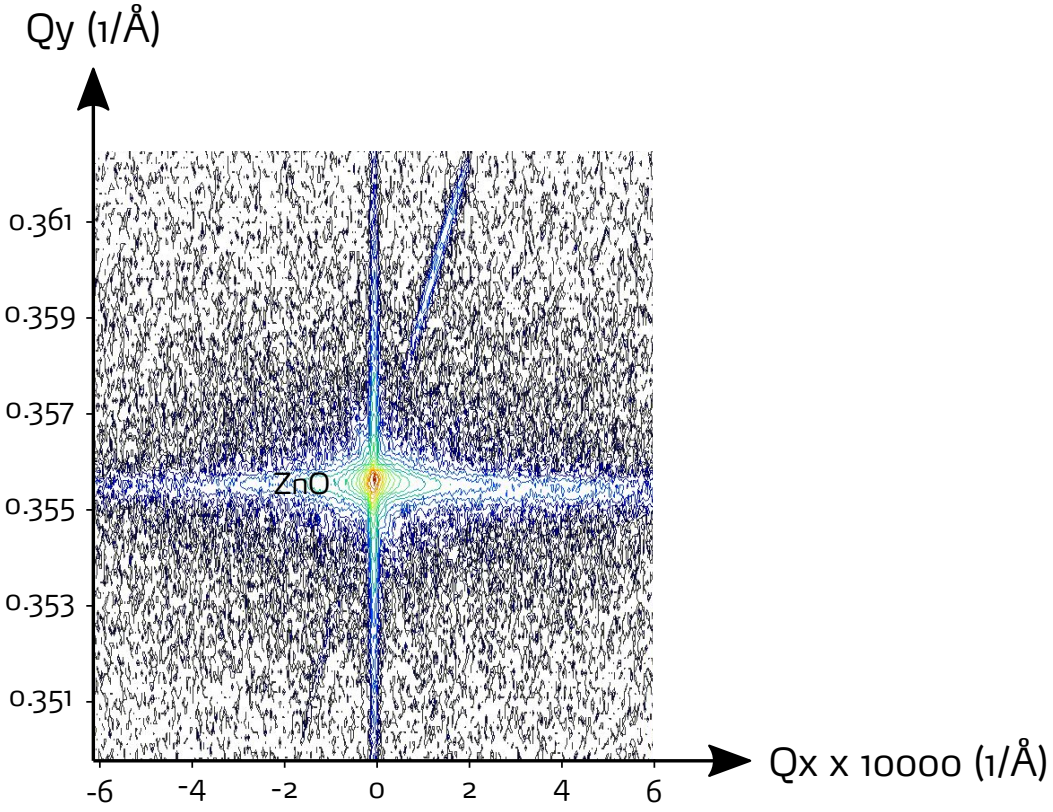

Figure 0.109.: RSM around the node (100), with $\varphi = 90°$ for a sample without cracks.

For the second experiment, the sample used is a MQW with 28 % of Mg and a total (Zn, Mg)O thickness of 28 %. In figures 0.110 and 0.111, we can once more observed a strong diffuse pattern on the RSM taken in the oblique configuration, ie for $\varphi = 0°$. The same goes for the (302) node where the diffuse pattern due to cracks is only visible in the asymmetric configuration with $\varphi = 90°$ (not shown).

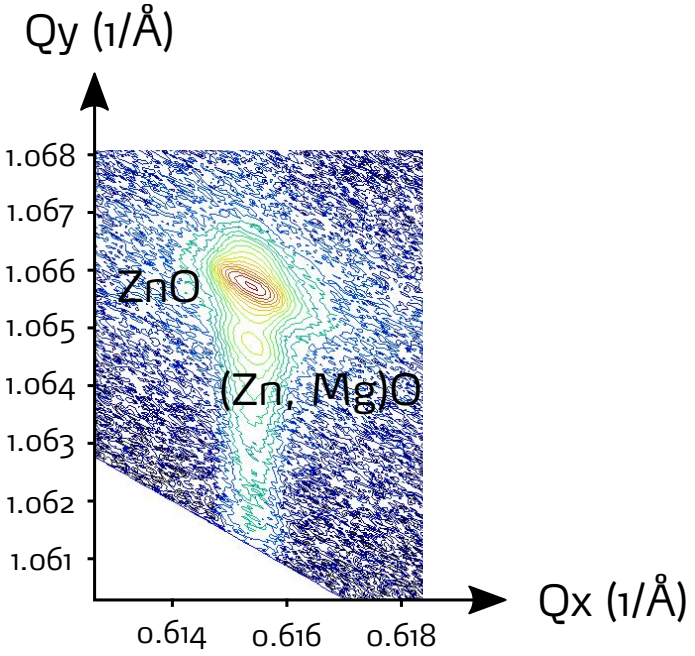

Figure 0.110.: RSM around the node (220), with $\varphi = 90°$, for a sample with cracks in asymmetric configuration.

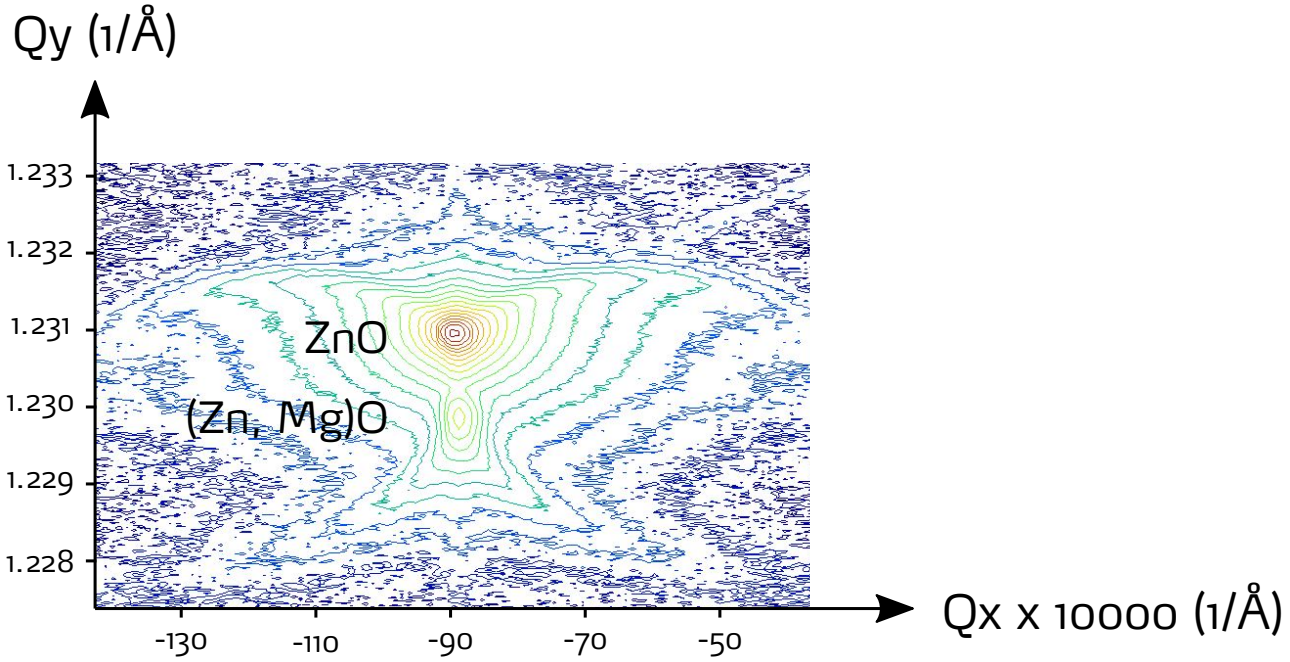

Figure 0.111.: RSM around the node (220), with $\varphi = 0°$ for a sample with cracks in oblique configuration.

In addition, Taboada *et al.* (2014) have investigated the relaxation of GaAs on a Si/Ge substrate. They have observed symmetric RSM very similar to ours when $\varphi = 0°$ (ie, when we see an influence of cracks). In this layer, cracks are aligned with the offcut direction with a density of $8\,mm^{-1}$, which is less than in our case. The RSM is shown in figure 0.112. Around the diffraction nodes related to the GaAs and the Ge, symmetric wings are evidenced. Authors propose that the wings are related to the part of the material which is relaxed at the vicinity of cracks. Another paper on the same

material system shows by µ-PL experiment and finite element calculation that cracks only partially relax the stress accumulated in the layer Colombo *et al.* (2007). Thich is in agreement with the observation of the wings in RSM. As similar wings are observed for ZnO and (Zn, Mg)O, cracks can only relax partially the stress in the epilayer. Additional experiments, as µ-PL, can be conducted to estimate at which distance of the crack the layer is fully strained.

The observation of crack effect on RSM is not detectable in our case for layer with such a low crack density. We can estimate that the limit lies between 20 and 90 $cracks/mm^{-1}$. To refine it, RSM around the (200) or (300) nodes can be performed to be able to see easiliy slight changes in the RSM shapes. This is the first time that the signature of relaxed material around cracks is detected on RSM for ZnO and (Zn, Mg)O.

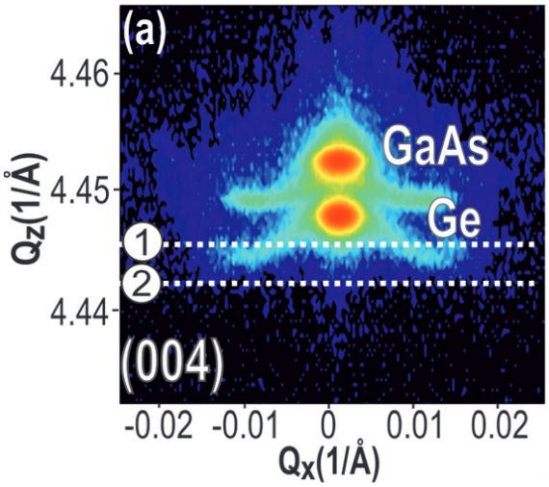

Figure 0.112.: RSM around the node (004) of a GaAs layer grown on a Ge/Si miscut substrate. *Reprinted from Taboada* et al. *(2014), with the permission of AIP Publishing.*

The appearance of cracks in an epitaxial layer grown on a mismatched substrate - as (Zn, Mg)O on ZnO - can be predicted using the critical thickness criteria. The critical thickness corresponds to the maximun thickness that can be grown before the nucleation of the first crack in the layer. It can be defined as followed for an isotropic material (Hutchinson & Suo (1992)):

$$h_c = \frac{\Gamma E_f}{Z\sigma^2}$$

Where Γ is the fracture resistance, E_f the Young modulus of the film, σ the applied stress responsible for cracking and Z is a dimensionless factor which depends on the geometry of cracks. Unfortunately, this formula cannot be used in the case of wurtzite (Zn, Mg)O because of the unknown material parameters such as stiffness matrix components.

Therefore, we have determined the critical thickness experimentally. Figure 0.113 shows the total (Zn, Mg)O thickness as a function of the Mg content for various sample structures as thick (Zn, Mg)O layers, single and MQWs, THz QCDs and QCLs, QWIPs and QCDs in the IR range.

- At 40%: the critical thickness lies between 100 and 155 nm.
- At 30%: the situation is not so clear. A sample without cracks is present for a total (Zn, Mg)O

thickness of 220 nm, whereas cracked samples were found for lower thicknesses down to 100 nm. This phenomenon can be explained by the different growth conditions and substrates used. For the majority of samples that shows "early cracking", the growth temperature used was several tens of degree Celsius lower compared to a sample without cracks, with the same Mg content.

From the device point of view, two cases should be distinguished. The high Mg content range - from 30 to 40 % - which corresponds to cascade devices in the IR range, and the low Mg content range - from 5 to 15 % - which corresponds to cascade devices in the THz range.

In the high Mg content range, a (Zn, Mg)O total thickness of 220 nm can be grown without cracks, which is not sufficient for cascade devices with a high number of periods. However, a solution exists for growing thick (Zn, Mg)O layers with a high Mg content: growing on patterned ZnO substrates. The substrate can be textured with micrometer large stripes along the c-axis so that the (Zn, Mg)O can relax on the free surfaces created on the sides of the stripes. The stripe widths should be tailored so that it is lower that the minimum distance between two adjacent cracks appearing on a layer grown on a unpatterned substrate (for the same Mg content).

In the low Mg content range, which corresponds to THz cascade devices. Samples with no crack were observed. Layers with total (Zn, Mg)O thicknesses as high as 1 μm for 15 % of Mg and 2 μm for 5 % can be grown, which allows technically to grow THz cascade devices made from m-plane ZnO and (Zn, Mg)O without defects.

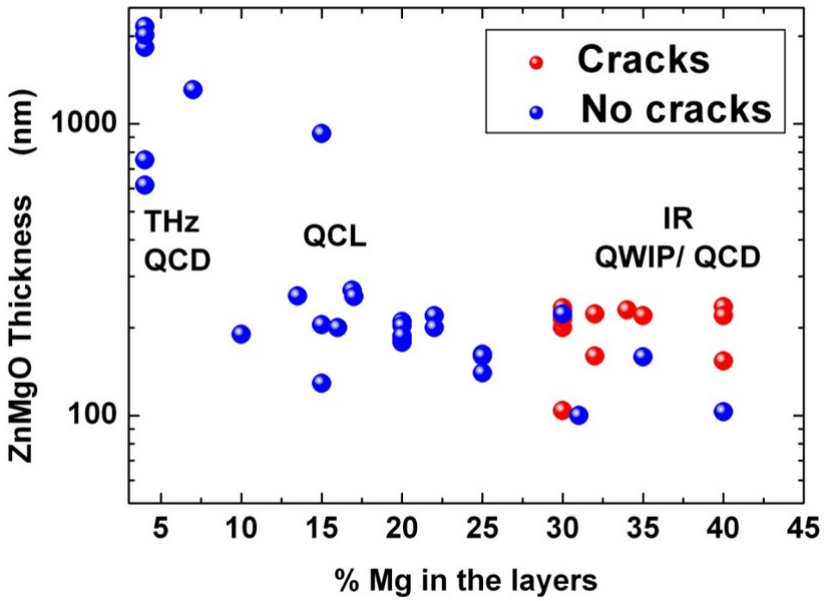

Figure 0.113.: (Zn, Mg)O total thinckness in various samples as a function of the Mg content. The red dots represent layers that have cracks.

0.7.2. On r-plane orientation

The stress state of the (Zn, Mg)O alloy grown on a r-plane ZnO substrate is quite different from m-plane. On a r-plane surface, we can define two in-plane directions: $[1\bar{2}10]$ et $[\bar{1}011]$ for which we can calculate the lattice mismatch. The lattice parameters used for this calculation are experimental and comes from this paper: A. Ohtomo *et al.* (1998). For the $[1\bar{2}10]$ direction, the lattice mismatch

is 0.62 % and 0.32 % for $[\bar{1}011]$ for 35 % of Mg. In addition, this compressive state stays whatever the Mg content, while keeping the wurtzite phase. If we compare to the mismatches on m-plane for 35 % of Mg, we find -0.63 % for the [0001] direction and 0.62 % for the $[1\bar{2}10]$ direction. So on r-plane (Zn, Mg)O, we have values for the lattice mismatch which are equivalent or lower compared to m-plane. Indeed, it has been assessed that r-plane is the orientation which provides the minimum lattice-mismatch for the wurtzite ZnO/(Zn, Mg)O Chauveau *et al.* (2013). So r-plane should lead allow a higher critical thickness before relaxation, compared to m-plane, which is beneficial for cascade devices. In addition, a theoretical study discusses the evolution of the elastic energy stored in wurtzite (Zn, Mg)O grown on ZnO depending on the orientation Bigenwald *et al.* (2012). The orientation with a minimum elastic energy is tilted by an angle of 41.3° with respect to the c-axis (see figure 0.114). As a comparison, r-plane is tilted by an angle of 42.77°, which is very close to the value of the minimum elastic energy. On the other side, non-polar orientations - as m-plane - gives a value nearly 4 times higher than the minimum for an alloy with a Mg content of 27 %.

However, the stiffness coefficients of (Zn, Mg)O used for this prediction comes from the Vegard's law between wurtzite ZnO and rocksalt MgO, which is discussed in the beginning of this chapter, may not be correct due to the different crystal structures used for the linear interpolation. Due to this uncertainty, authors emphazise that these predictions may be changed.

As a result, r-plane may be a good orientation to tackle the plastic relaxation in thick (Zn, Mg)O layers. This feature seems to extend even at high Mg content, which is the weak point of m-plane.

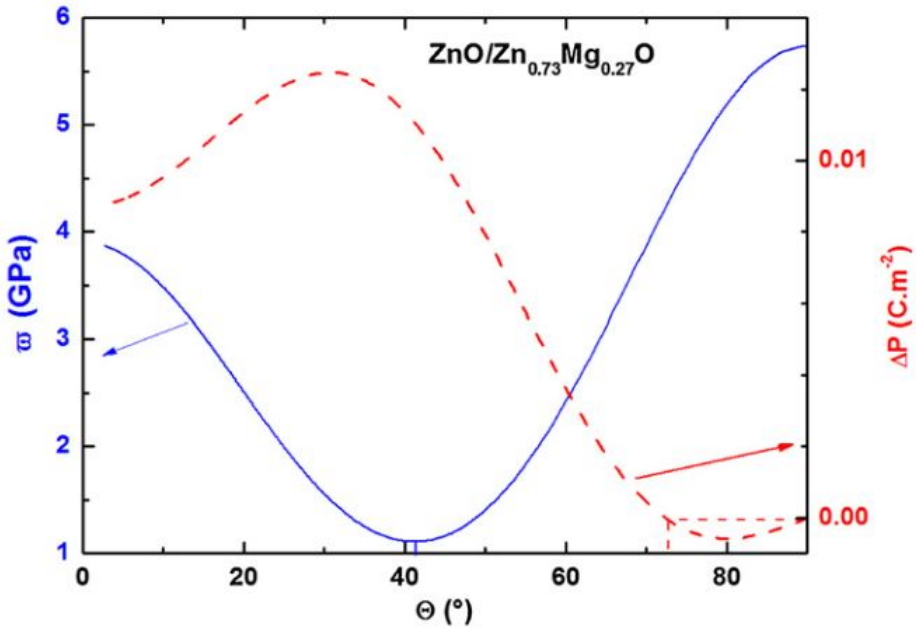

Figure 0.114.: Evolution of the elastic energy density stored as a function of the tilt angle Θ with respect to the c-axis (blue curve). The red curve represents the evolution of the polarization shift at the interface between ZnO and (Zn, Mg)O. It is assumed that the (Zn, Mg)O is lattice matched on the ZnO. *Bigenwald* et al. *(2012), URL, © IOP Publishing. Reproduced with permission. All rights reserved.*

As the two in-plane directions of (Zn, Mg)O are in compression, relaxation by dislocation glide can occur. Two relaxation models can be used to describe thin film relaxation on a lattice mismatched substrate. For low mismatch values ($< 7\%$), the Lattice Matching Epitaxy (LME) prevails. The

thin film is grown pseudomorphically on the substrate until the critical thickness Narayan & Larson (2002). These dislocations nucleate from the surface and glide toward the thin film / substrate interface before bending to create an half loop to end at the surface. For large mismatch values ($> 7\%$), the so-called Domain Matching Epitaxy (DME) occur Narayan & Larson (2002); Narayan *et al.* (1992). In particular, this approach is valid for crystals with different structures between the film and the substrate. Its principle stands on the matching of lattice constants at the thin film / substrate interface. Contrary to LME, the stress produced by the lattice mismatch is relaxed within the first ML , leaving the upper material strain-free.

In the case of ZnO/(Zn, Mg)O grown on ZnO substrates, we have seen that the lattice mismatch does not exceed the percent, both for m and r-plane. As a consequence, we foresee that LME should occur in our layers.

Dislocation glide using basal planes - $< 11\bar{2}0 >$ (0001) are very likely to occur in hexagonal crystals Fitzgerald (1991); Romanov *et al.* (2011). The angle between the $[10\bar{1}2]$ and the [0001] directions is close to 45°. Therefore the Schmid factors for slip systems using these planes are maximized. However, other slip systems can be activated: it has been found that it depends on the value of the ratio $\frac{c}{a}$. If this ratio is low ($\frac{c}{a} \leq 1.59$), glide on prismatic planes can also be observed Romanov *et al.* (2011). In the case of ZnO, this ratio is greater that 1.59, thus glide on basal planes should be still favoured according to this last statement.

Figure 0.115 shows an AFM picture of an r-plane MQW structure with 18 % of Mg. The sample is very smooth with a RSM roughness under 2 Å. In addition to the smooth surface, we can observe two families of lines that cross each other with an angle of 51°. They may be atomic steps originated from a dislocation glide during the early stage of plastic relaxation. In order to localize these dislocations, CL experiments at various accelerated tensions were performed (2, 6, 8, 12, 15 and $20\,kV$). Figure 0.116 shows the CL picture taken at $20\,kV$, where we can see two features. First, we see the same dark dots as for m-plane samples. The second is the presence of dark lines crossing each other at an angle of 51°. Thus these dark lines are the dislocation network that produces the atomic steps visible on the AFM picture (figure 0.115). Moreover, we have observed that this network appear on CL images at for a tension in the range of 6 to $8\,kV$. The more the electron are accelerated, the more they penetrate into the sample. Using the Casino software Drouin *et al.* (1997) and the sample structure, we were able to estimate the electrons penetration depth for a given applied tension. It turns out that the dislocation network lies at the interface between the (Zn, Mg)O buffer and the substrate.

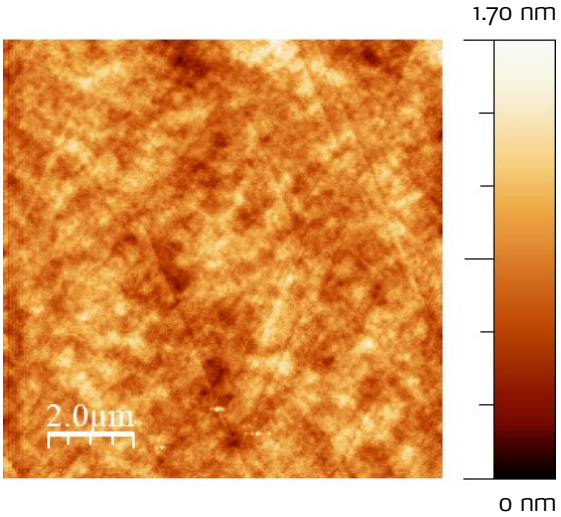

Figure 0.115.: AFM picture of r-plane MQW sample with $x_{Mg} = 18\,\%$.

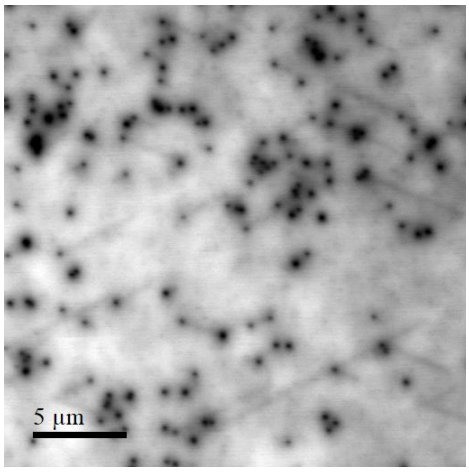

Figure 0.116.: CL image of a r-plane MQW sample with $x_{Mg} = 18\,\%$. The applied tension for electrons is $20\,kV$. This image is rotating by 90° with respect to the AFM picture 0.115.

Giving the trace shape of the dislocation at the r-plane surface, they are not linked to a glide on the basal plane (0001). Otherwise the atomic steps at the sample surface would have been parallel to each other. We have calculated the angle at which two planes are crossing each other in projection on a r-plane surface. We found out that $(\bar{1}104)$ & $(0\bar{1}14)$ are crossing each other at an angle of 50°, and that $(11\bar{2}0)$ & $(1\bar{2}10)$ as well as $(1\bar{2}10)$ & $(\bar{2}110)$ are making an angle of 52° when crossing an r-plane surface. Other high index planes might also lead to a crossing angle near 50°, but we have restricted our search to low index planes. Indeed they are more dense, and thus more likely to host dislocations. In order to determine unambiguousliy the slip systems, TEM experiment in dark field configuration might be helpfull.

In order to quantifiy the strain, this sample was investigated by XRD. Several RSM were recorded: symmetric RSMs around the (102) node and asymmetric RSMs around the nodes (103) and (113) (presented respectively in figures 0.117, 0.118, 0.119 and 0.120). For each of these RSMs, the more intense peak can be assigned the the ZnO diffraction spot. On (102) RSM, a tail can be seen when going toward higher values of Q_y (in yellow color in figures 0.117 and 0.118). This tail corresponds to the (Zn, Mg)O diffraction node. It is impossible to distinguish it precisely because it is too close to the ZnO diffraction spot. This is why we have recorded the asymmetric RSM.

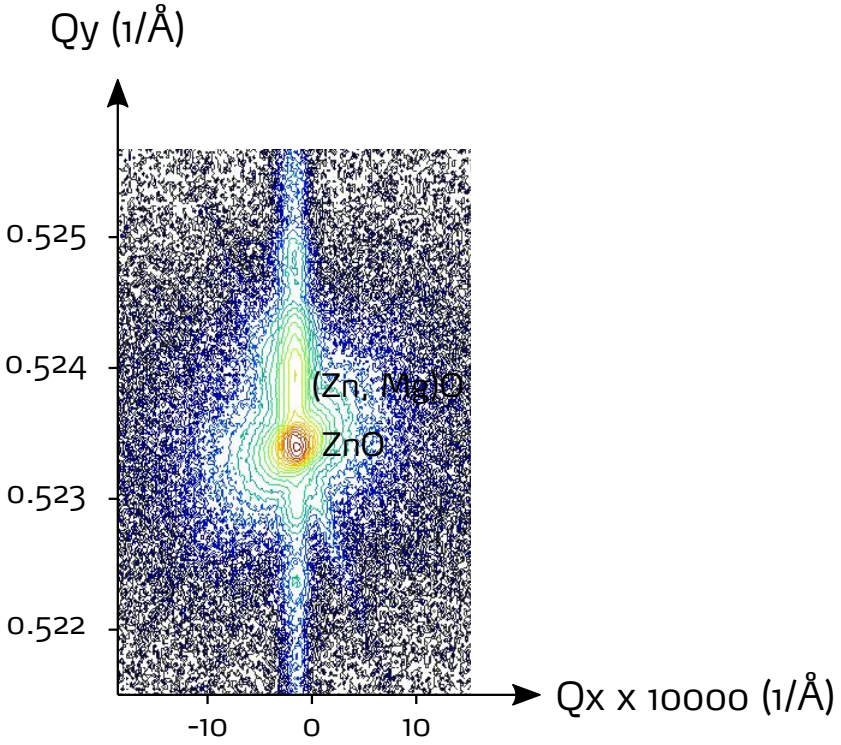

Figure 0.117.: RSM around the (102) node for $\varphi = 0°$.

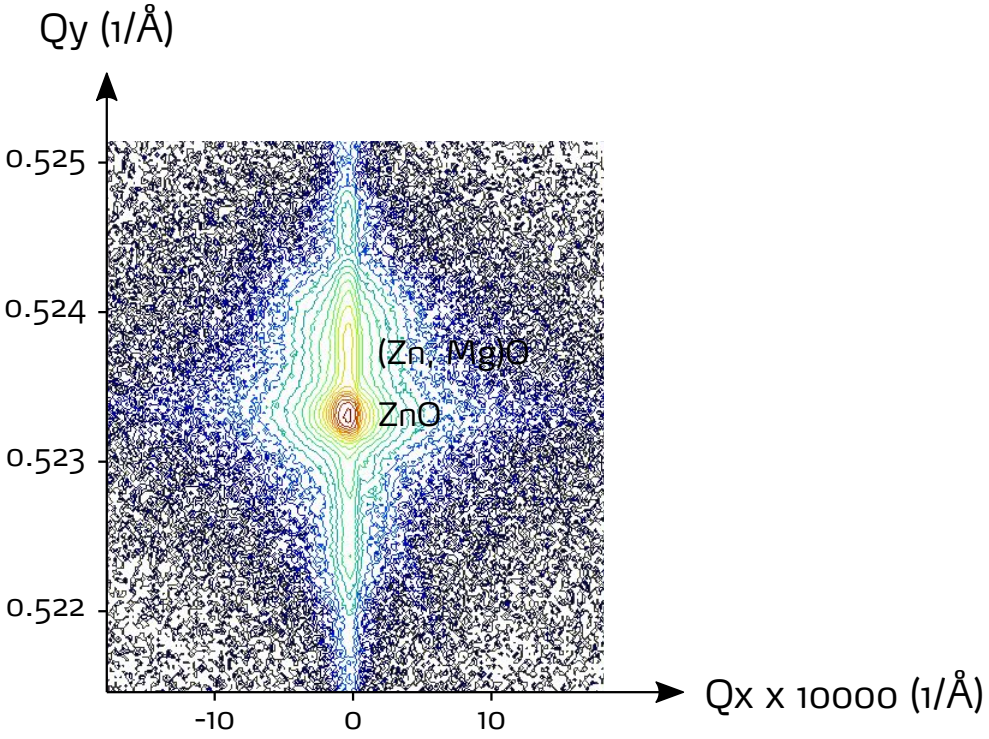

Figure 0.118.: RSM around the (102) node for $\varphi = 90°$.

Indeed on the RSM for the (103) and (113) reflection, the (Zn, Mg)O diffraction spot can be clearly observed (figures 0.119 and 0.120). In addition we can see the (103) map that other spots less intense than the ZnO and (Zn, Mg)O ones that are aligned: they show the sample periodicity.

On both (103) and (113) maps, we can see that the (Zn, Mg)O diffraction spot is aligned with the ZnO peak - thus having identical Q_x coordinates. This indicates that the (Zn, Mg)O is still

pseudomorphic with respect to the ZnO substrate, *i.e.* no evidence of plastic relaxation, despite the presence of dislocations.

From the two asymmetric maps, we can record the (Q_x, Q_y) coordinates for both ZnO and (Zn, Mg)O diffraction spots and deduce the lattice parameters a and c for both the ZnO and the (Zn, Mg)O in order to compute the out-of-plane strain ε'_{zz} (see equations 0.65 and 0.66).

$$\varepsilon'_{zz} = \varepsilon_{102} = -\left[\frac{d_{102}^{ZnMgO} - d_{102}^{ZnO}}{d_{102}^{ZnO}}\right] \tag{0.65}$$

$$d_{102}^{X} = \frac{1}{\sqrt{\frac{4}{3a_X^2} + \frac{4}{c_X^2}}} \tag{0.66}$$

d_{102}^{X} stands for the interreticular distance for the reflection (102) for the material X, which can be here either ZnO or (Zn, Mg)O.

Following this method we found out that the out-of-plane strain ε'_{zz} is 1.4×10^{-3}. If we compare this value with the ones which represent the evolution of ε'_{zz} with the Mg content for r-plane (figure 0.94), we found out that this strain is consistent with the other experimental points. So despite the presence of dislocations that aim at relaxing plastically the strain, the overhall sample is not relaxed: it is still elastically strained. The dislocation density is probably too low to have a significant influence on the overall relaxation. This confirms that it is the observation of the early stage for plastic relaxation.

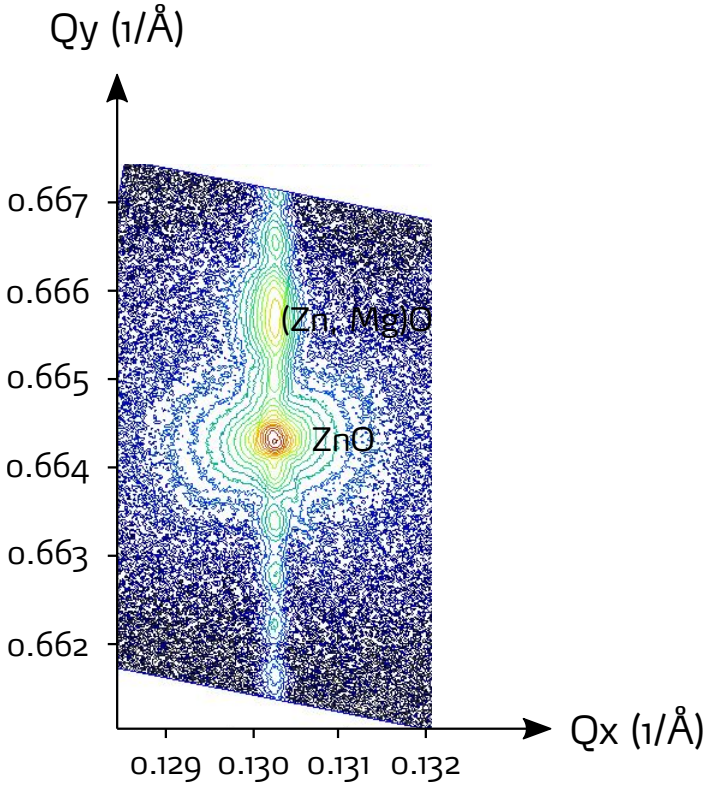

Figure 0.119.: RSM around the (103) node for $\varphi = 0°$.

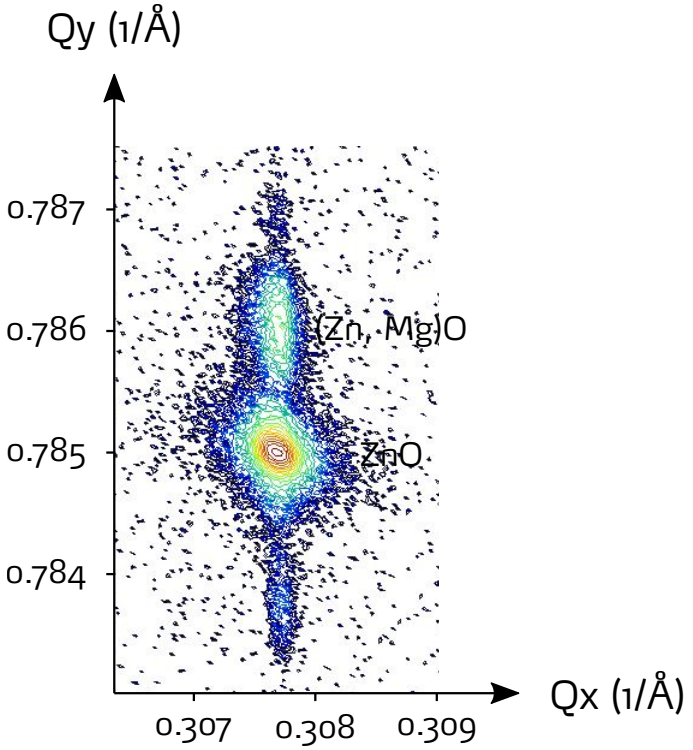

Figure 0.120.: RSM around the (113) node for $\varphi = 90°$.

This difficulty to release stress that originates from layers with low lattice mismatch ($< 7\%$), can be explained by the "domain matching paradigm". It is more difficult to release layer stress when the lattice mismatch is low, compared to a large lattice mismatch. Even if this explaination seems reasonable to describe our experimental results, TEM experiment would be useful in order to find to confirm or infirm our hypothesis on the dislocation glide planes that are effective in homoepitaxially grown r-plane ZnO/(Zn, Mg)O layers.

However, from the AFM and CL experiments, the approach using Schmid factor for predicting the dislocation glide system cannot be applied to r-plane ZnO. Other slip systems than basal systems need to be considered to match the CL and AFM experiments. It is possible that Peierls stress have to be taken into account in order to foresee which glide system is the prefered one. This Peierls stress represents required the stress to move a dislocation considering the friction coming from the crystal lattice Hull & Bacon (2011). It is a function mainly of the mechanical parameters, the dislocation width as well as the Burger vector of the glide system considered. Thus this stress depends both on the material and on a the glide system. In Wu *et al.* (2011), authors reports observation of non-basal dislocation glide in semipolar InGaN/GaN in addition to basal glide. They explain this observation by saying that "slip on pyramidal planes is not typically observed in the case of other materials with hexagonal close packed crystal structure (hcp), *i.e.* hcp metals, because of higher Peierls stress for these planes in comparison to the basal c-plane" Wu *et al.* (2011). Then their observation is due to the less important Peierls stress for pyramidal glide systems compared to basal ones for semiconductors. Thus this Peierls stress approach can be a reasonnable track to predict the glide systems that are activated in r-plane ZnO and (Zn, Mg)O.

To conclude this mechanical study of m and r-plane ZnO/(Zn, Mg)O heterostructures, we have seen that the relaxation mecanisms at play for m or r-plane are completely different. On the m-plane

orientation, stress is relaxed by formation of an crack array perpendicular to the c-axis, whereas on r-plane, dislocation glide prevails. From the device point of view, the m-plane orientation have a critical thickness sufficiently high to allow the conception of THz QCL, because the required Mg content is not high. However, the conception of QCL in the IR range using m-plane is not possible because the Mg content is higher and by turn, the critical thickness is greatly reduced. For r-plane, dislocations appear for low critical thicknesses. They are located in the (Zn, Mg)O buffer, and not in the MQWs region. TEM experiments will be conducted in order to confirm, as well to assess the interfaces quality on this orientation. To date, we have checked all the material aspects to say that m-plane is a suitable orientation for THz QCL growth: thus is the following part dealing with intersubband devices, all the studied samples are grown on m-plane.

Part IV.

Intersubband devices

0.8. Evidence of ISBT and tunnel effect

0.8.1. Observation of ISBT

At the beginnig of the ZOTERAC projet in 2015, only two papers were dealing with the observation of ISBT in ZnO based heterostructures (Belmoubarik *et al.*, 2008; Zhao *et al.*, 2014). In both papers, they used the polar orientation, thus having a strong polarization discontinuity at ZnO/(Zn, Mg)O interfaces because of the wurtzite structure of the crystal. The first objective was to assess that our heterostructures quality was sufficient to observe clearly ISBT.

To that purpose samples were designed to exhibit ISBT in the MIR by our colleagues of UPM. They consists of MQWs for which only the QW thickness varies between 2.2 nm and 3.7 nm as shown in figure 0.121. Other parameters are kept constant: the Mg composition (30 %), the barrier thickness (15 nm) and the QW doping ($1 \times 10^{19}\, cm^{-3}$). The QW doping is adjusted to set the Fermi level between the first and the second ISB energy levels. The first level is populated whereas the second one is empty. By doing so, ISBTs between the first and the second level in the QW are expected. The number of periods was chosen to avoid the strain relaxation so that the total thickness of (Zn, Mg)O is kept under the critical thickness for this particular Mg content (see section 0.7). The (Zn, Mg)O buffer layer is used to assess the Mg content as explained in section 0.4.4.

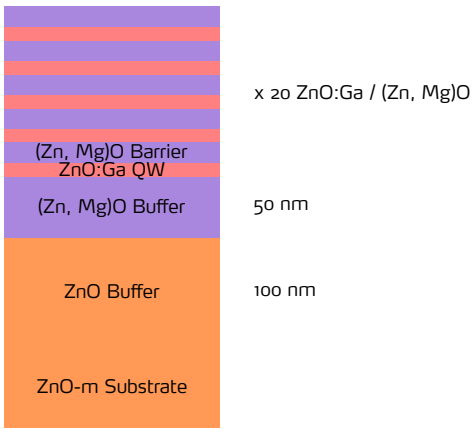

Figure 0.121.: Samples schematic. The QW thickness varies between 2.2 and 3.7 nm and the barrier one is kept constant. QWs are doped to $10^{19}\, cm^{-3}$.

For all samples the surface in smooth as stated by the AFM image 0.63. The RMS roughness for all samples of this serie is in the range of 0.3 nm.

Abruptness and coherence are both checked by XRR by looking at the shape of the interference peaks (figure 0.122). Observing interference peaks garanty that interfaces are coherent along the growth direction because the thickness profile along this direction is periodic. The sharpness assesses for the interface abruptness and the degree of interface coherence. If interfaces were not abrupt because of interdiffusion for instance, interference peaks are enlarged. In figure 0.122, we can see very sharp peaks, which ensure that interfaces are coherent and abrupt. Moreover, they are shifted from one sample to another according to the QW thickness, so we can use their position to determine precisely thicknesses as explained in section 0.4.4.

PL experiement at RT were carried out to check for the Mg content (section 0.4.4) and to verify if

excitons energies for QW are coherent with thicknesses found previously in XRR. PL spectra at RT are presented in figure 0.123 is presented PL spectra at RT. For each samples, two peaks are visibles: the most intense is related to the QW emission and the less intense one to the barrier. The barrier peak is at the same energy for all samples, meaning the Mg content is identical for each samples. The QW peak, we is shifted from one sample to another according to the QW well thickness. This is due to the variation of quantum confinement which affects the energy levels of the excitons in the QW. The expected trend is observed: the thinnest the QW, the higher the exciton energy. Calculation for the QW exciton energy using the thicknesses determined in XRR were performed. The change of the exciton binding energy with the quantum confinement is taken into account by using the approximation of the Leavitt-Little model (Leavitt & Little, 1990). The material parameters used are the following:

- electron effective mass: $m_{e^-} = 0.24\, m_0$
- hole effective mass: $m_{h^+} = 0.78\, m_0$
- ratio between the conduction band offset and the valence one: $\dfrac{\Delta E_C}{\Delta E_V} = 0.675$

As a result, calculations are in agreement with the experimental data (see red squares and circles, figure 0.123). We can conclude that there is no QSE in our samples, and that thicknesses determined in XRR are correct.

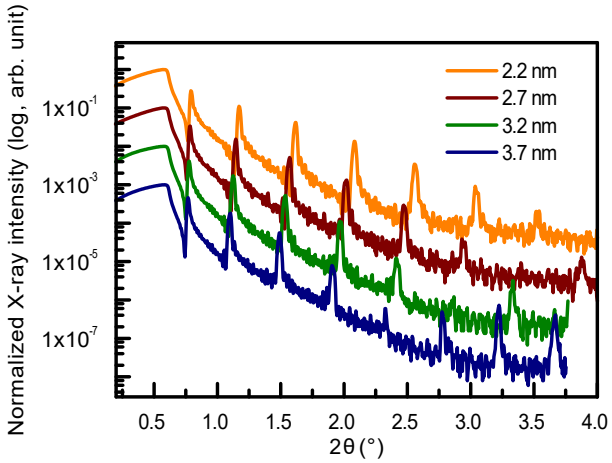

Figure 0.122.: XRR spectra of the MQWs samples. Interference peaks are shifted from one sample to another according to the QW thickness.

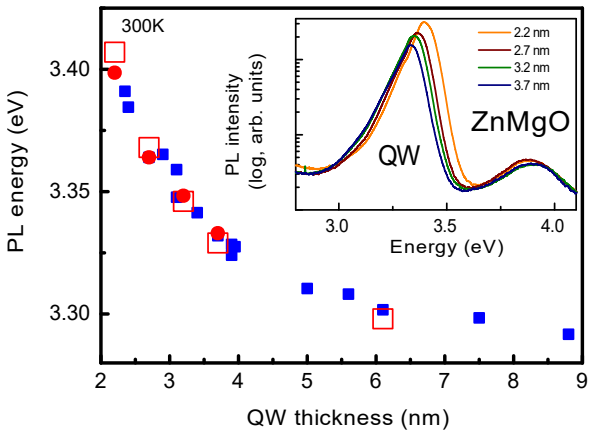

Figure 0.123.: Exciton energy of the QW as a function of the QW thickness. The red symbols correspond to the samples of this study. Red circles are experimental points whereas red squares repersents the calculation. Blue squares are other various samples measured in CRHEA. Insert: PL spectra at RT for the samples of the serie.

The ISBT measurements are done by absorption experiment by our colleagues at UPM. Samples are cut, beveled and polished as 45° multipass waveguides of $5\,mm$ for several internal reflections.

To observe ISBTs, the selection rule should be fulfilled: only light with a component with the electric filed perpendicular to QWs can trigger ISB. This polarization is referred as p-polarized or TM. The s-polarization or TE cannot trigger these transitions. Absorption was then measured for the two polarizations. Figure 0.124 represents the p-spectrum normalized by the s-polarization to enhance the signal from the ISBT. We can see peaks which is the proof that ISBT are present in these samples. In addition, the transition energy is shifted according to the QW thickness: the thinnest the QW, the higher the energy. This trend is expected for ISBT. The energies are between 250 and $300\,meV$, which corresponds to MIR . We can note that there is no absorption spectrum for the thinnest QW ($2.2\,nm$) because the higher energy level is lying in the continuum, so no ISB absorption was detectable in this case. The FMHM is around $100\,meV$, which is less than what was reported by (Zhao *et al.*, 2014) ($150 - 180\,meV$) at RT too. However, even if the ISBT FWHM is improved compared to previous reports available on ZnO, a linewidth of $100\,meV$ is far too large for THz ISBT. Indeed the linewidth is larger than the targeted emission energy ($1.25 - 125\,meV$ in the THz).

The main causes for ISBT broadening are: interface roughness, alloy disorder, LO or LA phonons (Longitudinal Acoustic) or ionized impurities scattering (Unuma *et al.*, 2003). They have been adressed experimentally and/or theoretically in other material systems as GaAs/AlGaAs, InGaAs/AlGaAs and GaN/AlGaN for instance (Unuma *et al.*, 2001, 2003; Campman *et al.*, 1996; Machhadani *et al.*, 2011), where the ISBT FWHM can be only of few meV. In (Campman *et al.*, 1996), authors studied the influence of the QW thickness on the ISBT FWHM for GaAs/AlGaAs and InGaAs/AlGaAs material systems. They found that the FWHM increased when the QW was thin: from 2.3 to $4.4\,meV$ for 10.0 and $7.5\,nm$ QWs respectively at cryogenic temperature. Since interface roughness is in general more important for thin QWs than for large QWs, authors concluded that interface roughness was the dominant scattering mecanism responsible from the transition broadening. The same conclusion can be drawn from the paper (Machhadani *et al.*, 2011), in which this effect is more obvious: the ISBT FWHM goes from 180 to $9\,meV$ when varying the QW thickness from 3 to $15\,nm$. In our case, no variation of the transition FWHM was observed by varying the QW thickness from 2.7 to $3.7\,nm$, maybe because this variation range is too small. So one idea could be to grow an additional MQW sample with thick QWs, and to measure the resulting ISBT FWHM. It will determine if the interface roughness scattering is the main scaterring mechanism responsible for the enlargements of ISBT in ZnO/(Zn, Mg)O.

In figure 0.125 we observe that there is a redshift of $60\,meV$ between the calculation using Schrödinger-Poisson equation and the experimental values because of the depolarization shift Allen *et al.* (1976). It occurs when there is a coupling between the incident wave and the electrons inside the QW. The electrons are excited by the incoming wave and becomes to oscillate as a plasma. As a consequence, the ISBT energy is redshifted. A model that take into account this phenomenon was developed by our colleagues at UPM and is represented in green squares in figure 0.125. Error bars take into account the experimental error of +/- 1ML on thicknesses. As a result, experimental points lie in the confidence interval of the model with the depolarization shift.

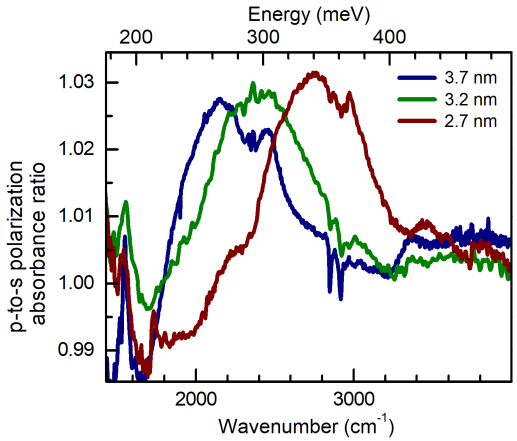

Figure 0.124.: p to s polarization absorption spectra at RT.

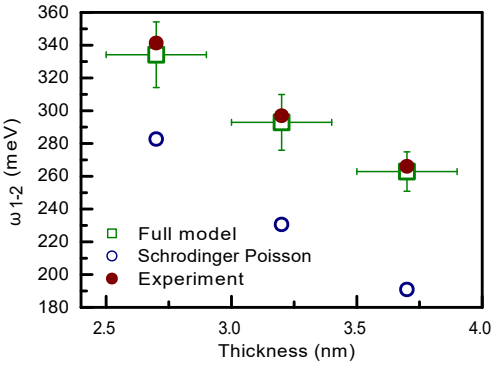

Figure 0.125.: ISBT energy as a function of the QW thickness.

Now I would like to focus on another unexpected physical phenomenon involved in ISB physics in non-polar ZnO. Does the undulated interface profile of QWs (see figure 0.67) affect the ISBT? To recall the ISB selection rule, the way the QW interfaces are oriented with respect to the incident electric field is essential. So is the ISBT selection rules change due to these undulated interfaces? For perfectly flat QW interfaces, it is known that the ISBT absorption coefficient α_{ISBT} is proportional to $\frac{sin^2(\theta)}{cos\,(\theta)}$, where the angle θ is the angle of incidence of the incoming wave. It is straightforward that for $\theta = 0°$ - at normal incidence - ISBT is strictly forbidden because the incident electric field has no component perpendicular to QWs interfaces. Considering our undulated interfaces, we can distinguish two cases for the normal incidence case. If the incident electric field is parallel to the c-axis, it has no component perpendicular to the QW interfaces (figure 0.126). In this case, ISBT can not take place as for flat QWs. But if the incident electric field is perpendicular to the c-axis, it has a component perpendicular to the QWs interfaces because there are undulated (figure 0.127). As a consequence, ISBT at normal incidence becomes allowed.

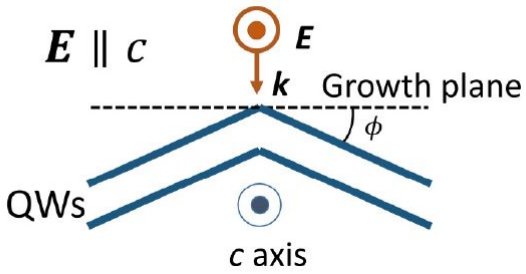

Figure 0.126.: Schematic of the incident case for undulated interfaces when the electric field is parallel to the c-axis. *(Montes Bajo et al., 2018a), © figure used under the Creative Commons Attribution 4.0 International Licence. To view a copy of this licence, visit: URL*

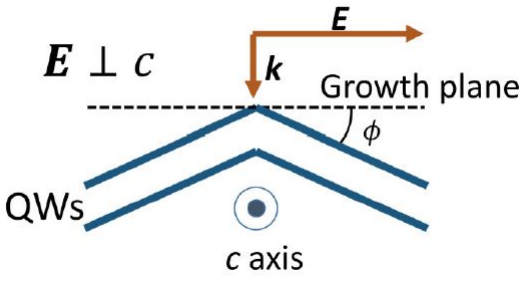

Figure 0.127.: Schematic of the incident case for undulated interfaces when the electric field is perpendicular to the c-axis. *(Montes Bajo et al., 2018a), © figure used under the Creative Commons Attribution 4.0 International Licence. To view a copy of this licence, visit: URL*

Our colleagues at UPM have developed a model of the absorption coefficient taking into account interfaces tilted with respect to the growth plane. The approach is purely geometric: for the same incoming wave, two cases can be considered. They are represented in figure 0.128: for a given incidence angle θ, the incident wave interacts with two kinds of interface. One is tilted with the angle $\theta + \phi$ with respect to the normal of the tilted interface, and the other one is tilted with the angle $\theta - \phi$. So the absorption should account for these two effective incidence angles as follow:

$$\alpha_{ISBT} = A \left(\frac{sin^2(\theta + \phi)}{cos(\theta + \phi)} + \frac{sin^2(\theta - \phi)}{cos(\theta - \phi)} \right) \tag{0.67}$$

In the equation 0.67, A is a constant which does not depends on the angles θ and ϕ. It can be noticed that for $\phi = 0°$, the classical proportionality relationship for the absorption coefficient is obtained. This expression is only valid when the incident electric field is perpendicular to the c axis (figure 0.127). To verify experimentally the validity of this geometric model, we have determined experimentally the absorption coefficient of MQWs samples. The idea is to measure the integrated intensity of the ISBT, which is linked to the ISBT absorption coefficient, when varying the incident angle θ. First the absorption spectra in the configuration when $E \parallel c$, at different angles θ. Here, the angle of tilt ϕ does not influence the ISBT (we have seen earlier that when $E \parallel c$, it is like the flat QWs configuration). So $\phi = 0°$, and constant A can be determined by adjusting the model with the experimental data. The result is shown in figure 0.129. The experimental data are represented in brown dots and the geometric model by the blue line. It can be noticed that as expected for normal incidence, the ISBT absorption is zero because of the selection rule.

The second step is to repeat the same experiment, but for the configuration where $E \perp c$. Now the tilted angle ϕ influences the integrated ISB absorption. The geometric model is feed with the value of A found in the configuration $E \parallel c$ and several tilted angles ϕ are tested. Results are shown in figure 0.129: the blue dots represents the experimetal data and the yellow, green and red curves the

geometric model for values of ϕ equal to 10°, 12° and 14° respectively. We obtain a good agreement between the geometric model and the experimental data. This model described qualitatively the the influence of tilted interfaces.

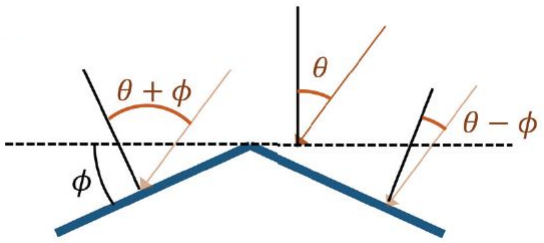

Figure 0.128.: Schematic of the angles used in the geometric model for the absorption coefficient. Angle θ is referred as the incident angle between the incident wave and the growth plane (dotted line). Angle ϕ described the inclinaison of the undulated interfaces with respect to the growth plane. *(Montes Bajo* et al., *2018a), © figure used under the Creative Commons Attribution 4.0 International Licence. To view a copy of this licence, visit: URL*

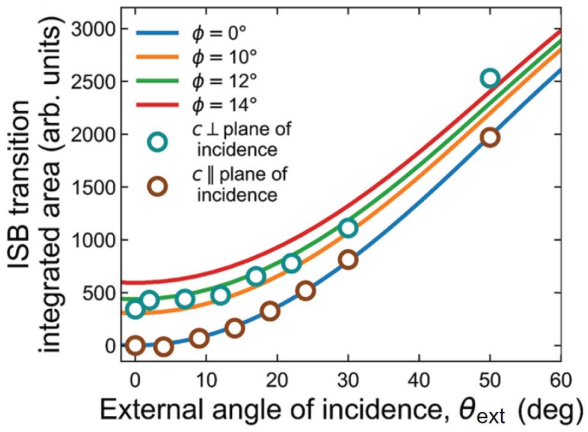

Figure 0.129.: Evolution of the ISBT intergrated area when the angle of incidence varies. Dots represents the experimental data and the lines the geometric model for various tilted angles ϕ. *(Montes Bajo* et al., *2018a), © figure used under the Creative Commons Attribution 4.0 International Licence. To view a copy of this licence, visit: URL*

The last step of this study is to verify if the model can predict quantitatively the tilted angle ϕ. In figure 0.129, the experimental data are well fitted when ϕ lies between 12 and 14°. In parallel of these absorption experiments, the tilted angle was measured directly by TEM on the same sample. Figure 0.130 shows one ZnO QW which exhibits tilted interfaces. The tilted angle ϕ is deduced from the Fourier transform taken from different zones. The figure 0.131 is a typical Fourier transform of a TEM image. The white spots are arranged in a hexagonal pattern. But 2 couples of additionnal spots are present, which are highlighted in red (figure 0.131). There is another period in the system. If we select only these spots and calculate the reverse Fourier transform, we get an image in the real space in which the undulated interfaces are highlited. By selecting only one couple of spots, interfaces with the same inclinaison are highlighted in the real space image. Moreover, applying this image treatment on image without undulations does not give additional spots (for instance in the buffer region). Thus these red spots are due to the undulated shape of interfaces. We can use them to measure the tilt angle ϕ, by measuring the angle between one diffraction spot and the reciprocal growth direction [10-10]*. The accuracy on the angle determination is evaluated by the width of the diffraction spots. The value of the tilted angle ϕ is found to be 14 ± 3°, which covers the values

determined by the geometric absorption model. So we obtain a good agreement between the angle values determined by TEM and by the absorption model. Moreover, the TEM method gives a very local information on the tens of nm scale while the aborption method probe the sample on the millimeter scale. So absorption is faster and gives a more realistic picture the interface tilt inside a sample. Thus it can be used in the future to predict the tilt angle.

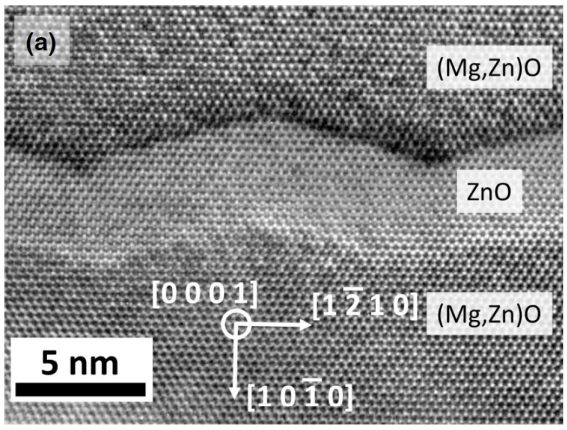

Figure 0.130.: HRTEM image of a cross-section in the [0001] zone axis. *(Montes Bajo* et al., *2018a), © figure used under the Creative Commons Attribution 4.0 International Licence. To view a copy of this licence, visit: URL*

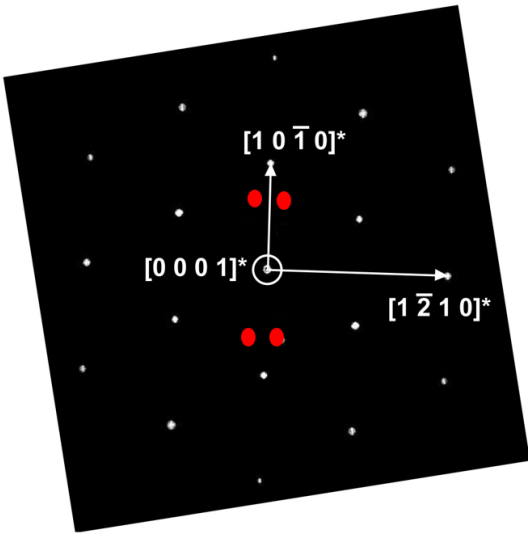

Figure 0.131.: Fourier transform of a TEM image in the [0001] zone axis. The hexagonal pattern comes from the crystal symmetry. Additionnal diffraction spots are highlighted in red.

This paragraph demonstrates the observation of ISBT at RT in the MIR for m-plane ZnO/(Zn, Mg)O heterostructure. It reprensents a huge step forward because ISBT is one of the two key physical phenomena essential to the realization of QCL. In addition, we have a clear understanding of the impact of the periodic and undulated interfaces on the ISBT absorption.

0.8.2. Asymmetric QWs

The demonstration of ISBT in ZnO represents half of the key physical components for QCL. Tunnel effect is still needed to be demonstrated in our heterostructures. A serie of samples were designed as sketched in figure 0.132. They are QWs samples with one thick (Zn, Mg)O barrier, a thick ZnO QW, a thin (Zn, Mg)O barrier and a thin ZnO QW respectively. The thin barrier was varied between 0.5 to 4.0 nm to probe the coupling between the two QWs. Table 0.6 gathers nominal values of thicknesses, doping and period. We can distinguish two categories: undoped and doped samples because two different optical measurements are carried on. Undoped samples are investigated by PL to probe the excitonic transitions in both thin and thick ZnO QW. Whereas for doped samples, transmittance measurements are performed to investigate the ISBT. Most of the elements of this

study are explained in detail in the following article: Meng *et al.* (2019).

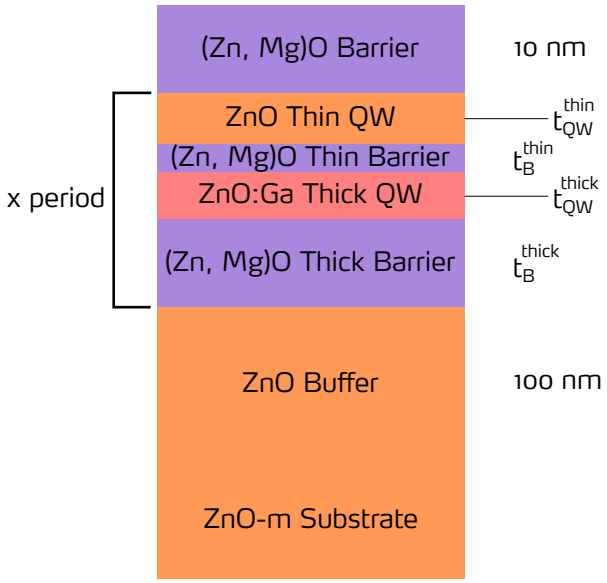

Figure 0.132.: Schema of the samples. The nominal Mg content is 30 % .

Sample	t_B^{thick} (nm)	t_{QW}^{thick} (nm)	t_B^{thin} (nm)	t_{QW}^{thin} (nm)	n (cm^{-3})	period
ZOE0120	10.0	2.5	0.5	1.2	5×10^{19}	20
ZOE0121	10.0	2.5	1.0	1.2	5×10^{19}	20
ZOE0122	10.0	2.5	1.5	1.2	5×10^{19}	20
ZOE0123	10.0	2.5	1.0	1.2	nid	20
ZOE0124	80.0	2.5	1.0	1.2	nid	1
ZOE0125	80.0	2.5	4.0	1.2	nid	1

Table 0.6.: Nominal thicknesses doping and number of period. nid stands for "non intentionaly doped".

In addition, thicknesses, Mg content and doping were measured as described in the subsection 0.4.4.

For thicknesses, SEM and XRR experiments are coupled to obtain a complete and precise information on each layer thickness (see 0.4.4). This procedure has been followed to deduce the real thicknesses that are gathered in table 0.7. Except for the thick (Zn, Mg)O barriers, the measured thicknesses correspond to the nominal values if we take into account the error of $\pm 1\,ML$ ($0.28\,nm$ on m-plane).

Samples	t_B^{thick} (nm)	t_{QW}^{thick} (nm)	t_B^{thin} (nm)	t_{QW}^{thin} (nm)
ZOE0120	10.0	2.7	0.5	1.3
ZOE0121	9.9	2.7	1.0	1.3
ZOE0122	9.9	2.7	1.5	1.3
ZOE0123	8.8	2.6	1.0	1.2
ZOE0124	79.4	2.6	1.0	1.3
ZOE0125	79.5	2.4	4.0	1.2

Table 0.7.: Thicknesses measured by the coupling of SEM and XRR techniques.

Some samples exhibit unexpected features on their XRR spectrum. Figure 0.133 shows one of them (sample ZOE0120, thinnest barrier). The 5 sharp peaks here correspond to the constructive interferences due to the repetition of the thick barrier, the thick QW, the thin barrier and the thin QW together. But the one around 2° is nearly completely suppressed (extinction in figure 0.133). This extinction is due to the interferences which raise from the periodic nature of the sample. It is a destructive interference.

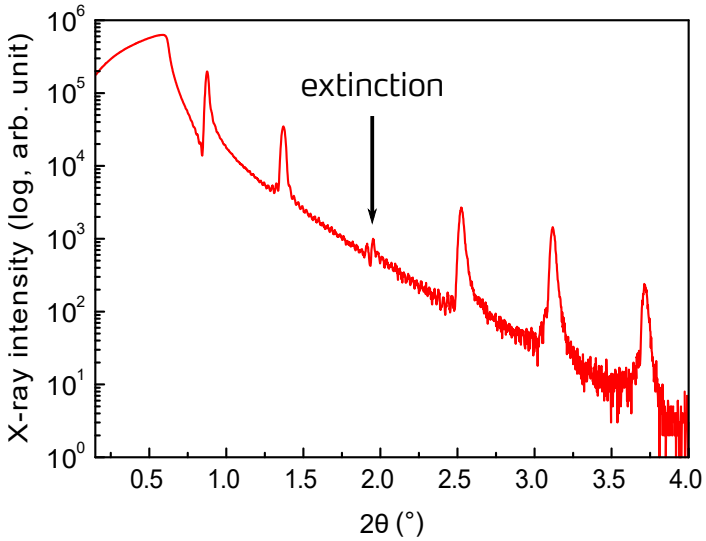

Figure 0.133.: XRR spectra of the asymmetrical QW with the thinner barrier - 0.5 nm.

In order to analyse this extinction, we can use an analogy to optics and adapt it in the case of destructive interferences. We end up with the following relation:

$$\theta_i = \arcsin\left(\sqrt{(\sin\theta_c)^2 + \left(\frac{\lambda\ (2m_i+1)}{4\,t}\right)^2}\right) \tag{0.68}$$

Where θ_i is the angle of the extinction, θ_c is the critical angle - and t is the unknown thickness at the origin of the extinction. We calculate where the extinction should be. In this particular case, we find only one possible solution for $m_i = 0$, $t = 2.4\,nm$, which gives an extinction at $\theta_0 = 1.81°$. This is in good agreement with the XRR spectrum and with the nominal structure because $t = t_{QW}^{thick} \pm 1ML$. As a consequence, the availability of both constructive and destructive interferences allow us to determine completely and independently the thicknesses inside the sample without the need of the growth rates coming from the SEM while keeping the precision of 1 ML.

Then, our partners at UPM determined by optical means the Mg content and the n-type doping using fitting of reflectance spectra (see susbsections 0.4.4 and 0.4.4). The Mg content was found to be 27 %. For the doping, a large difference is detected (see table 0.8) with respect to the nominal value, probably due to the instability of the Ga cell. However, the real doping level is still compatible with the absorption experiments that has been planned.

Samples	$n\,(cm^{-3})$
ZOE0120	7.5×10^{19}
ZOE0121	8.2×10^{19}
ZOE0122	8.8×10^{19}

Table 0.8.: Doping values measured using the reflectance spectroscopy method with MSP.

Figure 0.134 shows the PL spectra taken at RT for the undoped samples. In this spectra, we can see 4 main peaks. The peak labeled "4" at high energy, which is seen for ZOE0124 and ZOE0125 only is related to the excitonic emission of the (Zn, Mg)O barrier. Sample ZOE0123 does not show such a peak because its barriers are thinner compared to ZOE0124 and ZOE0125. So we can suppose that the diffusion length of carriers is greater than this thickness so that they all recombine radiatively in the QWs. This is not the case for ZOE0124 and ZOE0125 which have nearly 10 times larger barriers so that all the carriers are not able to diffuse across through the entire thickness.

The peak labeled "1", which lies at the lowest energy, is only observed in samples ZOE0124 and ZOE0125. This peak may be related to structural defects in the substrate or in the layer. However, the observation of this peak is not systematic on our samples: ZOE0123 does not show such a peak. Further work should be done in order to clarify the growth parameters which cause this defect line to appear in some samples.

Then peaks labeled "2" can be attributed to the free exciton recombinaison inside the larger QW. For samples with the thinner coupling barrier (ZOE0123 and ZOE0125), this transition arise at the same energy, whereas for the sample with the thick barrier (ZOE0125), this transition is slightly shifted toward higher energies (respectively $3.396\,eV$ and $3.403\,eV$). This blue-shift can have two origins. The fact that ZOE0125 has a thick QW of $2.4\,nm$ instead of $2.6\,nm$, can lead to a higher exciton energy recombinaison. Or this shift can be due to the thick barrier: the two adjacent QWs are not coupled anymore. As a consequence, the energy of transition is higher. Such shifts of few meV due to coupling were reported in similar structures grown on m-plane ZnO substrates Stachowicz *et al.* (2017).

Finally the peak labeled "3" is observed only on the sample ZOE0125, which exhibits the thicker coupling barrier. Its energy matches very well the free excitonic emission of the thinnest QW Béaur (2011). As this emission is not observed for the samples with the thinnest coupling barrier, this indicates that the two QWs are not coupled with the barrier of $4.0\,nm$ thick and the excitonic ground state of the thin QW is detected. This strenghens the origin of the blue shift, *i.e.*: two uncoupled QWs.

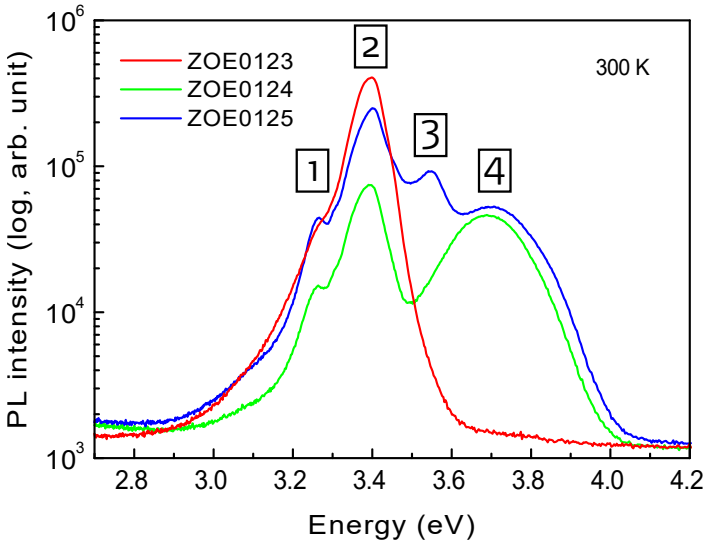

Figure 0.134.: PL spectra of samples ZOE0123, ZOE0124 and ZOE0125 taken at RT.

In Stachowicz *et al.* (2017), authors report a PL study of two asymmetrical QWs samples grown by plasma MBE on m-plane ZnO substrates. The QWs are 2.0 and 5.0 nm thick and are eather separeted by a (Zn, Mg)O barrier of 7.0 or 20.0 nm. The Mg content of each sample was determined by Rutherford Back-Scattering (RBS) to be 21 and 27 % for the sample with the thick and thin coupling barrier respectively. They evidence an inter-well coupling in the case of the 7.0 nm thick barrier by studying the evolution of QWs excitonic emmision with the temperature. When the temperature raises, they observe a decrease of the intensity of the 2.0 nm QW while the 5.0 nm increases. This evolution highlights the exciton transfert from the thinner well to the thicker one, which by turn, increases the intensity of the thicker QW at RT. Such an evolution is not observed for the sample in the 20.0 nm barrier. This suggests that the two QWs are completely uncoupled. In our case, the intensity increase of the thicker QW in the case of coupling is observed for sample ZOE0123, but not for the sample ZOE0124 at RT (see figure 0.134). However, for the sample ZOE0123, this increase can come from the better injection of exciton from the barrier inside the QWs, because asymmetrical QWs are sandwiched between thinner barriers in this sample, thus enabling a more efficient diffusion of excitons directly in the QWs (see figure 0.132). By recording the different excitonic contributions intensities, the authors ended at RT with qualitatively the same results as us. Indeed, for the thin coupling barrier, the RT spectrum exhibits only the emission line related to the free exciton of the thick QW, whereas for the thick coupling barrier, they see the emission lines of free excitons of both QWs. This similar observation is quite puzzling because the coupling barriers thicknesses involved in the two experiments are completely different: 20.0 and 7.0 nm in Stachowicz *et al.* (2017) and 4.0 and 1.0 nm in our case. To explain this phenomenon, we can hypothezise that it exists - in one serie of samples - at least one mechanism which favors the transfert of excitons across the coupling barrier. One of them could be the presence of composition fluctuations inside the barrier which can locally increase the barrier height and lead to a less efficient transfert of excitons. But in the case of Stachowicz *et al.* (2017), no composition fluctuation was detected using RBS. In our case, we will see that STEM-HAADF images does not show such decomposition as well. So this hypothesis should definitely be sidelined. Another one can be the presence of defects inside the coupling barrier which can help tunnel effect to occur because of the assistance of these defects. But

to comfirm or not this hypothesis, further experiments needs to be done as TEM for instance.
Before going to the absorption experiment, let's have a look at what can be expected from this experiment. Figure 0.135 is a schematic representing the energy levels and the possible ISBT for coupled and uncoupled QWs. In the case of uncoupled QWs, i.e. with a infinitely large barrier between the thick and thin QWs, we will find two energy levels in the thick QW and only one in the thin QW. In this case, we will expect to see in the absorption spectrum a peak likned to the ISBT between the ground state and the first excited state of the thick QW. An ISBT between the ground state of the thin QW and the continuum is also possible, but will be very large. We will only consider the ISBT between bound states, even if transitions with the continuum exist. In the case of a thin barrier, QWs are coupled and it leads to a three energy levels system with one ground state and two excited states. Two ISBT are expected to be observed in absorption: one between the ground state and the first excited state and the other between the ground state and the second excited state. To illustrate practically these two cases, absorption spectra have been simulated for a $0.5\,nm$ and a $4.0\,nm$ thick coupling barriers (see figure 0.136). For the $0.5\,nm$ thick barrier, two aborption peaks are present, which means that the two QWs are coupled. On the contrary, for the $4.0\,nm$ thick barrier, only the higher energy peak remains (higher wave number), which correspond to the ISBT within the thick QW.

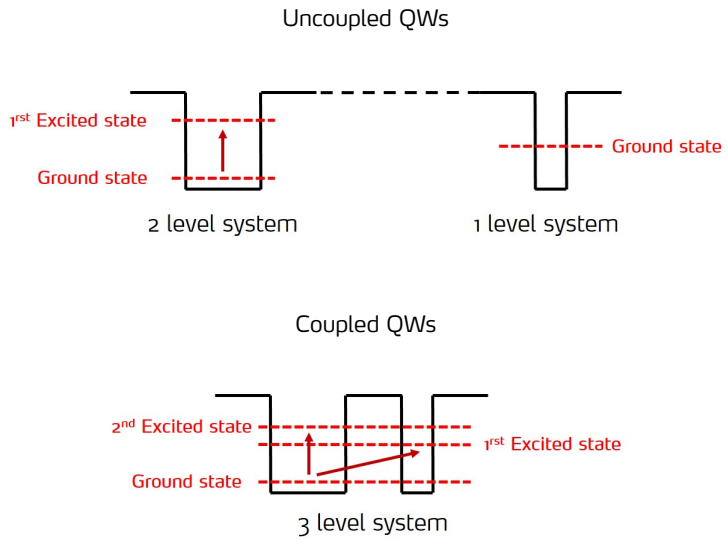

Figure 0.135.: Schematics showing the energy levels and the expected ISBTs in the case of uncoupled and coupled QWs (top and bottom respectively). The Fermi level lies between the ground states of the thick and thin QWs (not represented).

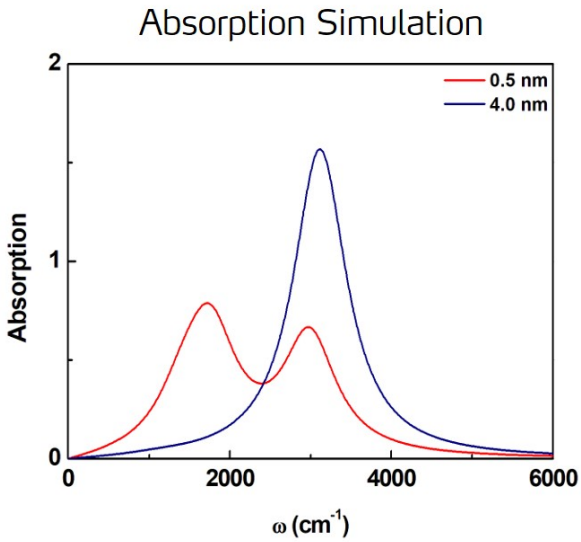

Figure 0.136.: Simultation of the absorption spectra for a $0.5\,nm$ and $4.0\,nm$ coupling barrier (red and blue curve respectively). The absorption unit is arbitrary.

Our colleagues at UPM and ETHZ performed the transmittance experiments on the doped samples in the IR range in order to probe the intersubband transitions. Experiments have been done at Brewster angle to avoid optical distorsion of the transmittance spectra Wong & Yen (1988). Spectra are presented in figure 0.137. All three samples show two peaks around $3500\,cm^{-1}$ and $2000\,cm^{-1}$.

The low energy peak can be attributed to the ISBT between the ground state of the thick QW and the first energy level coming from the thin QW across the coupling barrier. The oscillator strength of this transition is strongly affected by the barrier width. When the barrier width is increased, the oscillator strength diminishes, which by turn leads to a less intense absorption peak. This trend is clearly observed in this sample serie. This coupling effect is observed even for the sample which exhibits the thicker coupling barrier: $1.5\,nm$. Moreover, as for PL spectra, there is a continuous blueshift of the of the thick QW ISBT energy when the tunnel barrier becomes thicker. When the barrier thickness is increased by $0.5\,nm$, the ISBT is blueshifted by nearly $70\,cm^{-1}$ or $9\,meV$. This blueshift is a proof that the coupling between the two QWs is changing significantly when the coupling barrier lies in the range $0.5 - 1.5\,nm$.

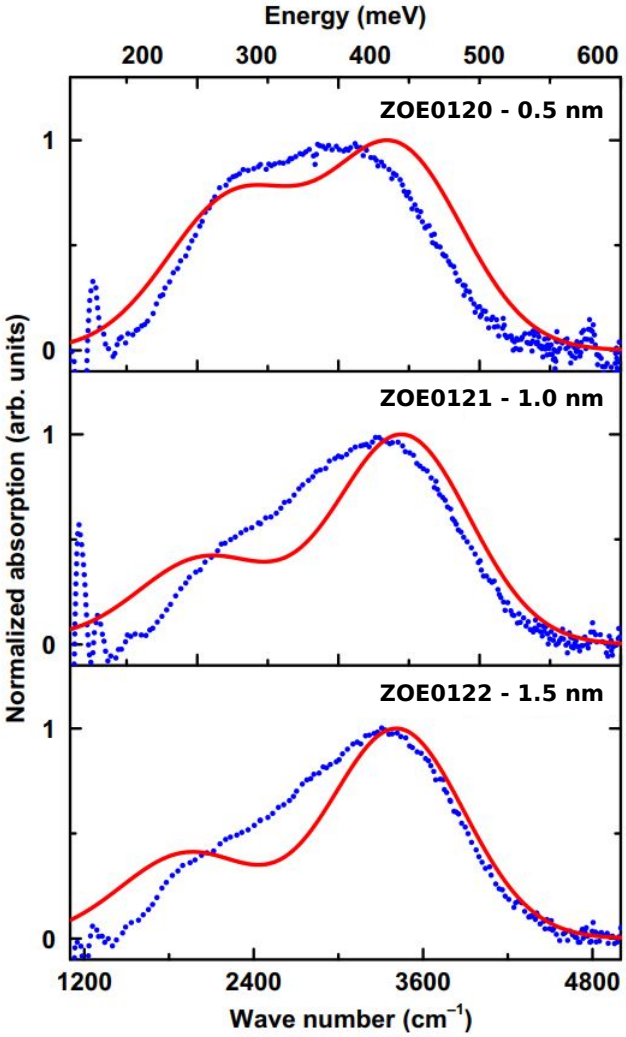

Figure 0.137.: Normalized s to p transmittance spectra taken at Brewster angle for samples ZOE0120, ZOE0121 and ZOE0122. The blue dots shows the experimental data and the red line the simulation using the thicknesses deduced by XRR. The nominal thickness values for the coupling barriers are in inset.

ISBT absorption simulations were performed by ETHZ. A good agreement is found between the simulated spectrum and the experimental values while using the thicknesses deduced by XRR (see figure 0.137). Simulations are done using the MSP picture (details can be found in the supplementary

materials of the article Meng *et al.* (2019)).

With such a thin barrier, it is very important to measure precisely the thickness, the fluctuations at an atomic scale. We have prepared two samples for STEM observations. First the right zone axis must be chosen because of the presence of the undulations in the [0001] direction. The $[1\bar{2}10]$ zone axis shows a contrast which is averaged across several undulations (see figure 0.138). In other words, for each single column of atoms near an interface, its contrast is a sum of contrast coming on both sides of the interface. As a consequence, images that are not taken in the undulation zone axis appear as blurry. This phenomenon is shown in figure 0.139, which is taken on the zone $\left[1\bar{2}10\right]$, perpendicular to the [0001] one on the sample ZOE0123. Interfaces are so blurry that this image is not usable for accurate thickness determination, that is why the [0001] - where undulations can be clearly seen - is the prefered zone axis for this purpose.

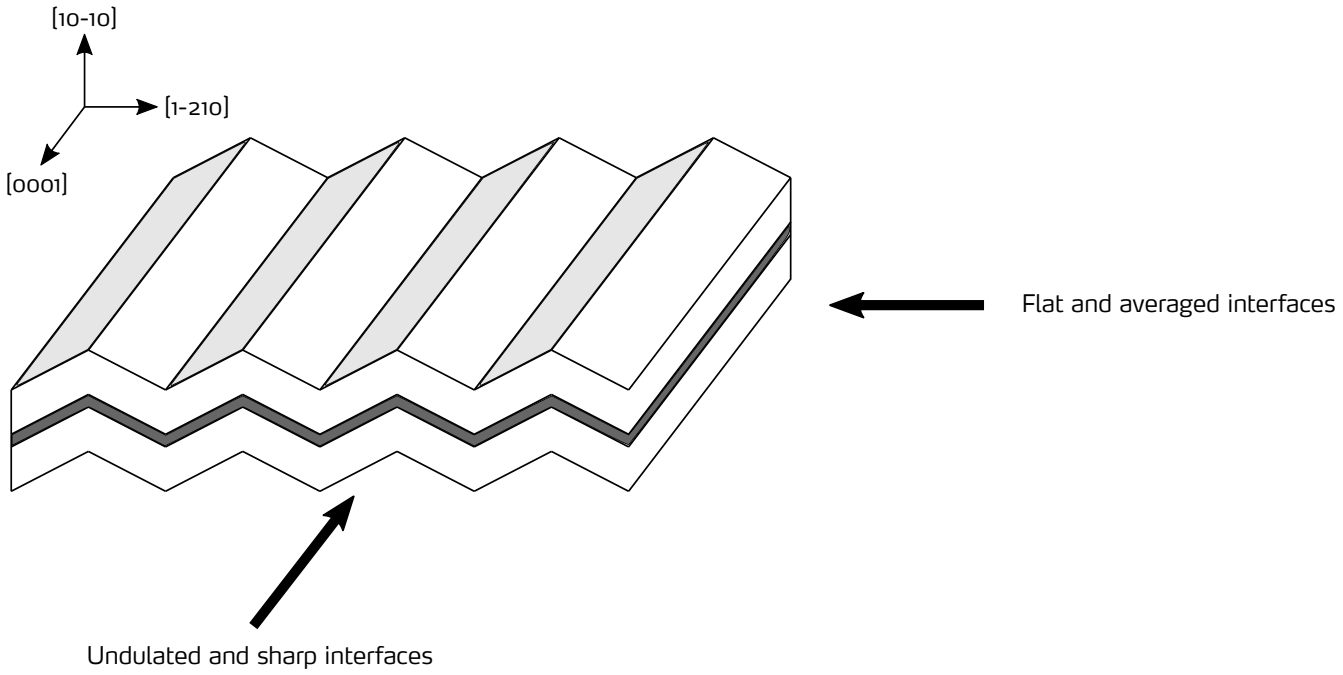

Figure 0.138.: Illustration of the effect of undulations on thickness determination.

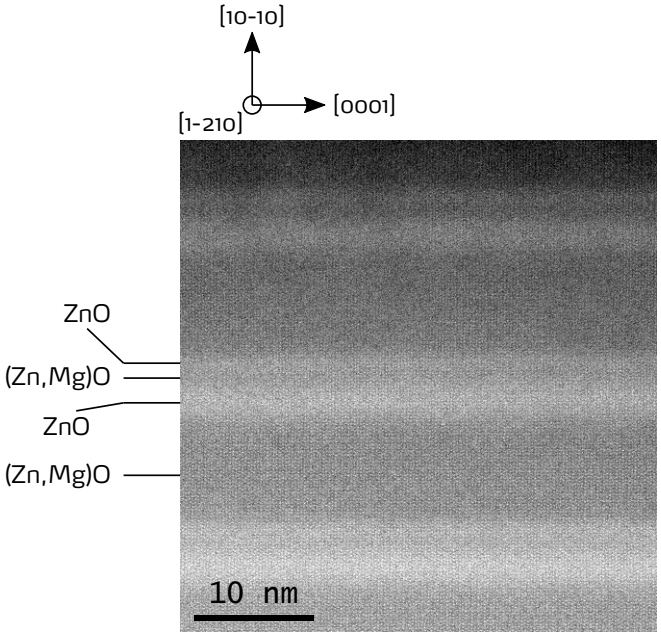

Figure 0.139.: STEM-HAADF image of sample ZOE0123 taken on the $[1\bar{2}10]$ zone axis (perpendicular to the undulation's zone axis).

Figure 0.140 shows an STEM-HAADF image on which the whole structure can be seen from the ZnO buffer to the last (Zn, Mg)O barrier on top. The layers are regular in the QW planes and the growth was clearly coherent along the growth direction. Figure 0.141 presents an insight of few periods: the undulations are observed as well as the thin barrier sandwiched between the two QWs. From all the sample areas observed, this thin barrier is always continuous, regular and with sharp interfaces, even if it is only 2 ML thick. No interdiffusion of Mg inside the adjacent QWs has been detected. From the growth point of view, the control at the ML scale of our heterostructures is achieved.

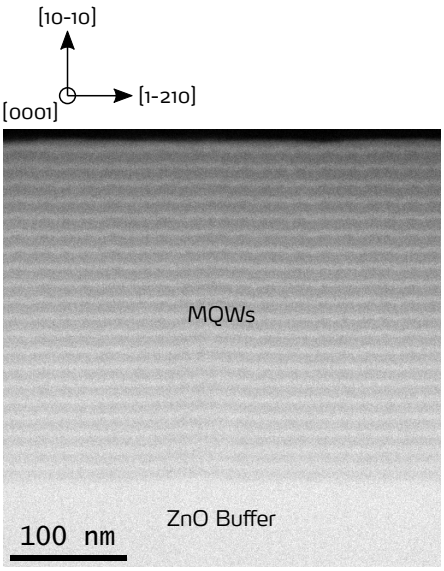

Figure 0.140.: STEM-HAADF image of sample ZOE0120. The whole structure can be seen from bottom to top.

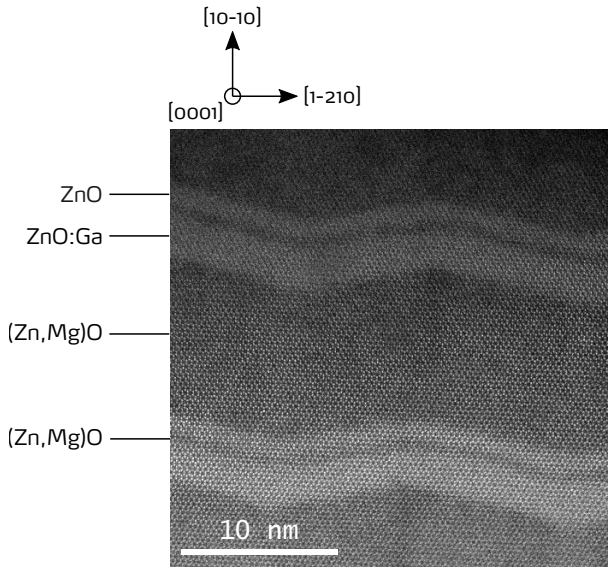

Figure 0.141.: STEM-HAADF image of sample ZOE0120. The thin coupling barrier is continous and of regular thickness.

Figures 0.142 displays a high resolution STEM image zoomed on one single period. Atoms colums can be clearly seen and their hexagonal arrangement is typical from the [0001] zone axis. Such high resolution images need to be used in order to determine low thicknesses with accuracy. The method is used a profile (blue rectangle in figure 0.142) in which the intensity variations is recorded. Figure 0.143 shows such an intensity profile taken for the area of figure 0.142. Each peak represents intensity summed over all the atoms inside the same column. Since Mg atoms are lighter than Zn atoms, the interaction between the electron beam and Zn atoms is stronger, inducing a brigther signal the ZnO layers. This intensity variation can be used to can measure thicknesses with a precision under the ML scale.

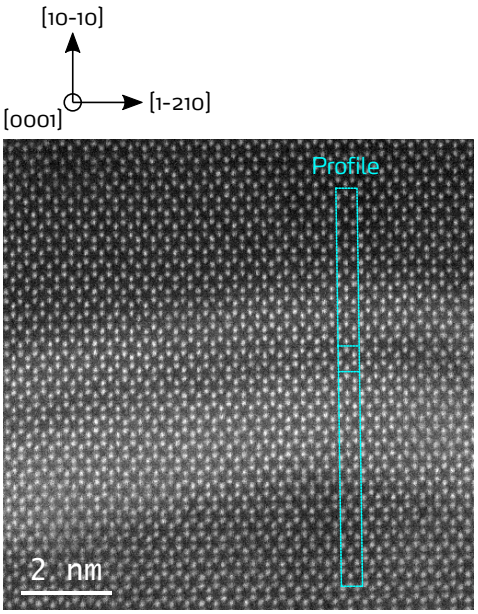

Figure 0.142.: HRSTEM-HAADF image of sample ZOE0120. The blue rectangle shows the area used to measure the thin barrier thickness using the intensity profile method (see figure 0.143).

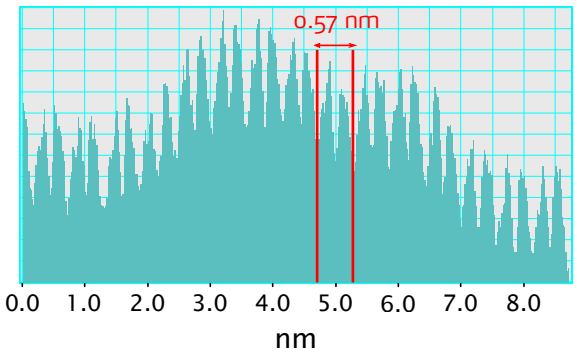

Figure 0.143.: Intensity profile of the area shown in figure 0.142. The thin barrier thickness on this image is $0.57\,nm$.

Thickesses are determined using this intensity method. For each thickness, we typically average the results over 10 different images taken in various zones in the sample. The error is calculated by taking into account the dispersion square of the results with respect to the average (see 0.22). Results are gathered in table 0.9 by following this procedure. The thicknesses measured by STEM-HAADF agrees very well with the nominal ones if the error on thickness measurement is considered. The same goes between the STEM-HAADF measurements and the one using SEM and XRR (see table **??**). Further work - as simulation of QWs with an undulated profile - can be performed in order to get a better insight on the influence of undulations on the electron behaviour.

Thickness	t_B^{thick} (nm)	t_{QW}^{thick} (nm)	t_B^{thin} (nm)	t_{QW}^{thin} (nm)
Nominal	10.0	2.5	0.5	1.2
STEM-HAADF	9.9 ± 0.5	2.4 ± 0.3	0.57 ± 0.08	1.2 ± 0.1

Table 0.9.: Comparison between nominal and STEM-HAADF thicknesses for ZOE0120.

0.9. Quantum Cascade Detector

After the demonstration of ISBT in the IR, we have grown and processed a detector based on these transitions. Two types of superlattices detectors can be considered: either a Quantum Well Infrared Detector (QWIP) or a Quantum Cascade Detector (QCD). The main difference between these two approaches is that no electric field is needed in the case of the QCD, contrary to the QWIP (Hofstetter *et al.*, 2010). In the latter, the electron undergo a transition between the fundamental level of a QW

and a higher level by absorbing a photon (see figure 0.144). The particularity is that the higher energy level of the QW is located at the top of the barrier so that the electron can be collected as a photocurrent after the absorption of one single photon (Levine *et al.*, 1987). For the QCD, the electron goes from the ground state to the higher energy state inside the active QW (see figure 0.145). After this transition, the electron is transfered to the other active QW through a serie coupled QWs called the extractor. The transfert is done by a serie of transitions assisted by LO-phonons. If we call N the number of QCD periods, one collected photoelectron means that N photons have been detected. This is fundamentaly different from QWIP where one photoelectron corresponds to one photon detected.

One advantage of QCD over QWIP is that since no bias is needed, a higher doping level can be used and thus enhance the overhall structure's quantum efficiency (Gomez *et al.*, 2008). Moreover, the electron is ultimately transfered to the next active QW, which gives to this device a lower noise (Graf *et al.*, 2004).

The critical point for the efficient QCD operation is explained in (Gendron *et al.*, 2004; Gomez *et al.*, 2008). In order to enhance the detectivity, the noise level should be as low as possible. In photovoltaic devices, this noise is called the Johnson noise: it points the noise created by the thermal agitation of carriers (here electrons). This Jonhson noise is proportional to $1/R_0$, with R_0 the device resistance at zero bias. Thus to reduce it and achieve a high detectivity, one should find a way to maximise the device resistance R_0. On the other side, one would like to trigger fast and efficient electron transfert from one active QW to another through an efficient electron/phonon coupling, as well as a fast ISBT in the active QW through a high oscillator force between energy levels. The efficiency of these two phenomena together is called the device quantum efficiency. But a high quantum efficiency ends with a low resistance R_0. A QCD with good performances thus requires a balance between a high quantum efficiency and a low noise.

But still: is there any interest of using ZnO for such a device? From the quantum efficiency point of view the answer is yes. As the electron/LO-phonon interactions - known as Fröhlich interactions - are strong in ZnO, an efficient electron transfert from one active QW to another is expected to happen. From the growth point of view, a high level of controlability of ZnO/(Zn, Mg)O heterostructures has been proved in the asymmetrical QW part (see subsection 0.8.2). So it seems that nothing can prevent from the realization of a ZnO based QCD.

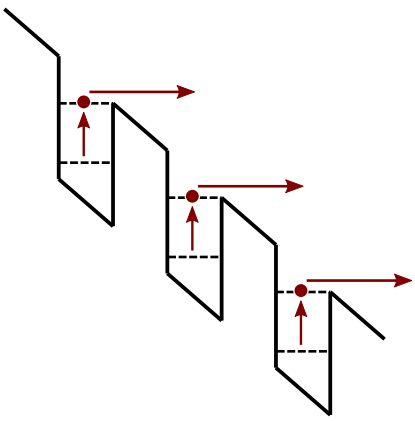

Figure 0.144.: QWIP schematic principle.

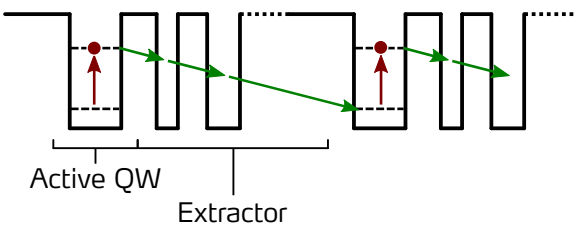

Figure 0.145.: QCD schematic principle.

A QCD design based on ZnO/(Zn, Mg)O heterostructures was proposed by our colleagues in C2N (figure 0.146). The targeted detection wavelength lies in the MIR, at 3.7 µm. The operation is not different compared to existing QCDs. After absorbing the photon energy, the electron undergoes an ISBT and reaches the higher active QW's energy level (red arrows in figure 0.146). Then it is tranfered to the next period by 4 transitions assisted by LO-phonons (green arrows in figure 0.146). As the photon energy is high compared to the THz domain, barriers should be higher. This is why a Mg rich alloy is used for this energy domain (40% of Mg content). The active QW is doped at a nominal value of $2 \times 10^{19}\, cm^{-3}$. The period - active QW and extractor - was repeated 30 times. The active region is sandwiched between to two contacts made of ZnO:Ga at the same doping level as the active QW. The bottom contact is 1 µm thick and the top one 100 nm thick. The structure is grown on the m-plane orientation.

One immediate issue after growing the first QCD sample was the material relaxation. Cracks perpendicular appeared as shown in figure 0.147 because the critical thickness for a (Zn, Mg)O alloy with 40 % of Mg is reached (see subsection 0.7.1). As for the QCL, these defects are highly detrimental to the device because electrons use cracks as a more efficient way to cross the entire heterostructure (leakage currents). So we lower the number of periods to 20 and no cracks were observed. From this information we can infer that the critical thickness for an alloy with 40 % of Mg lies between 110 and 165 nm based upon the thickness nominal values.

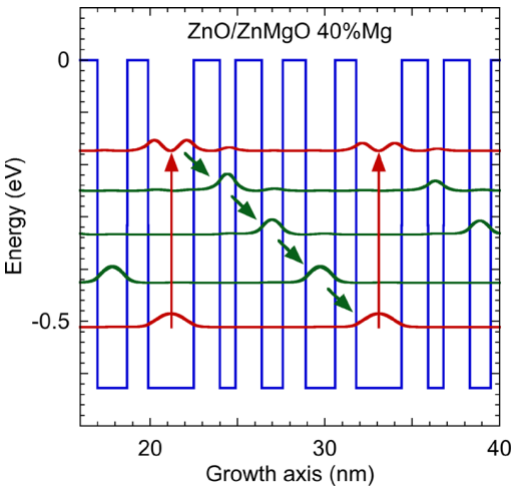

Figure 0.146.: MIR QCD design of a single period. The targeted wavelength is $3.7\,\mu m$. The thicknesses are $2.6/\mathbf{1.5}/0.9/\mathbf{1.5}/1.2/\mathbf{1.3}/1.7/\mathbf{1.2}$ nm starting from the active QW. Bold values correspond to (Zn, Mg)O layers. The nominal Mg content is 40 %. The only layer doped is the active QW with a nominal value of $2 \times 10^{19}\,cm^{-3}$. *Reprinted from (Jollivet* et al.*, 2018), with the permission of AIP Publishing.*

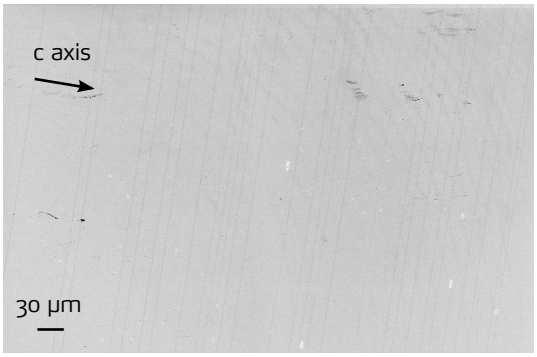

Figure 0.147.: SEM plane-view of a QCD sample with 30 periods. Cracks perpendicular to the c-axis can be seen with a density of $30\,mm^{-1}$.

Figure 0.148 shows the AFM image of the 20 period QCD. The surface is smooth with a RMS roughness of $0.72\,nm$. However this value is two times larger than the typical ones we obtain for regular 20 periods MQWs. This roughening is probably due to the high Mg content. Such surface roughening of (Zn, Mg)O has already been reported in several articles (Asahara *et al.*, 2010; El-Shaer *et al.*, 2007). Figure 0.149 presents the XRR spectra obtained for the sample with 20 periods. Intense and periodic peaks are observed which correpond to the repetition of an active QW and the extractor together. This extracted thickness for one period is $11.8 \pm 0.3\,nm$, which agrees with the nominal value: $11.9\,nm$. If we combine this result with the growth rates extracted from SEM measurements performed on the same sample, thicknesses of each single layer agree with the nominal values.

Note that the Mg content was not checked by PL because the top contact layer prevent us to see the signal from the barrier.

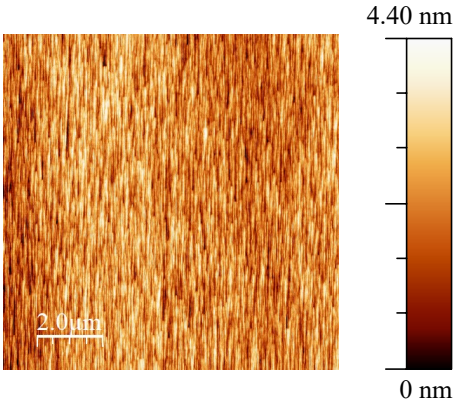

Figure 0.148.: AFM image $10 \times 10\,\mu m^2$ of the 20 periods QCD. The RMS roughness is $0.72\,nm$.

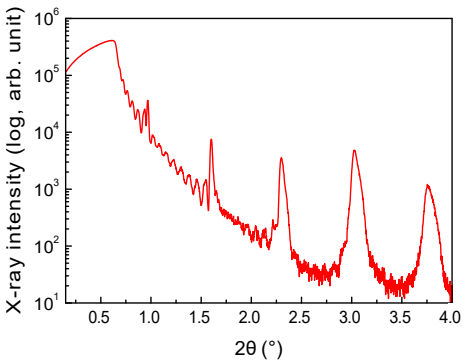

Figure 0.149.: XRR spectrum of the 20 period QCD.

Absorption experiments were performed at C2N by using a multipass waveguide configuration as explained in the subsection 0.8.1. The normalized p/s (or TM/TE) transmittance spectrum shown in figure 0.151. Both experimental spectra fulfill the ISB selection rule, so we can conclude that ISB aborption are observed at 2.98 µm, or $416\,meV$.

This experimental values are blue-shifted compared to the targeted wavelength, even if the sample structure itself matches the design requirements. This blueshift may be due to the depolarization shift (Montes Bajo *et al.*, 2018b; Jollivet *et al.*, 2018). Absorption simulations with this depolarization shift ends with an absorption peak at 3.00 µm, which is in good agreement with experimental spectra. Moreover, it allows to estimate the doping within the active QW: $1.8 \times 10^{19}\,cm^{-3}$, which is close to the targeted one: $2.0 \times 10^{19}\,cm^{-3}$. In addition, the ISBT FWHM is found to be $112\,meV$, which is 10 times larger than what was found in the samples used to prove the ISBT in our structures (see subsection 0.8.1). For the IR range, it is not a limitation because the ISB transition energy is several times larger (here nearly 4 times larger). The two ISB energy levels are still be energetically separated. This is a completly different story for the THz where the ISBT energy is in the range of 1 to $100\,meV$. In this case, this ISBT enlargement is equivalent or larger than the ISBT energy and thus the transition does not happen at all because the two energy levels are not separated anymore.

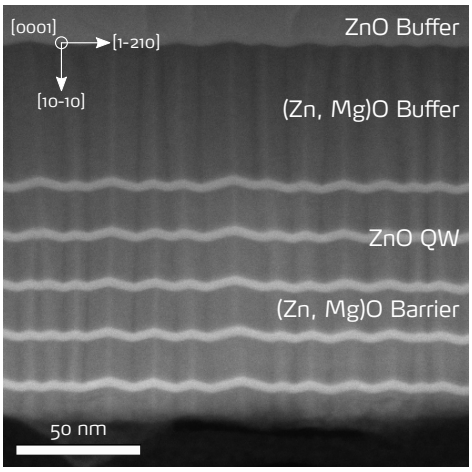

Figure 0.150.: STEM-HAADF image of a 5 period MQW with a Mg content of 40 %.

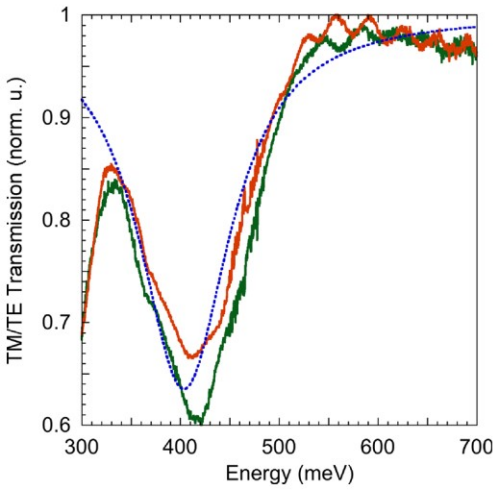

Figure 0.151.: Absorption à RT et à 77K. The green and red curves are recorded at $77\,K$ and $300\,K$ respectively. The blue dotted curve shows the simulated spectrum. *Reprinted from (Jollivet* et al.*, 2018), with the permission of AIP Publishing.*

The sample was then processed at TU in Vienna in the form of 260 mesas with different areas from $10 \times 10\,\mu m^2$ to $100 \times 100\,\mu m^2$. Details about the process can be found in (Jollivet *et al.*, 2018), but a special care was given to the sidewalls passivation with H_2O_2 at $95°C$ in order to avoid leakage currents. Indeed, the application of this treatment is known to produce a highly insulating layer, which helps avoiding surface leakage (Schifano *et al.*, 2009). The Brewster configuration was chosen in order to couple the incoming light to the intersubband resonance. A picture of one final device can be seen in figure 0.152 inset: only the perimeter was metalized for carrying the top contact in order to keep the central square fro the photocurrent measurement at Brewster angle. On the 260 devices processed, 86 % show the same I-V caracteristic whose asymmetric behaviour comes from the conduction band profile one. This is a very nice result because all the process steps had to be optimized from scratch for this material. In addition, the I-V curves for other mesas sizes were recorded and computed in order to plot the current density evolution with the applied voltage. Results are summarized in figure 0.153: at RT all the curves are well superimposed, which means that there is no leakage through the sidewalls at RT. In inset, the figure shows the current normalized by the mesa perimeter at $77\,K$. The curves are again quite well superimpozed, which is here an evidence of sidewalls leakage at low temperature. An evidence of this low temperature leakage is found with the measurement of the resistance at zero bias, R_0, which is found to vary with the mesas area (Jollivet *et al.*, 2018).

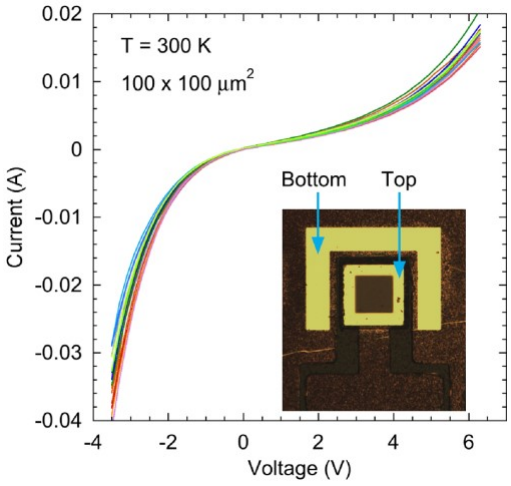

Figure 0.152.: I-V caracteristic of the QCD at RT. Each curve represents the caracteristic of one single mesa. Inset: a photo of a mesa with the top and bottom contacts. *Reprinted from (Jollivet* et al.*, 2018), with the permission of AIP Publishing.*

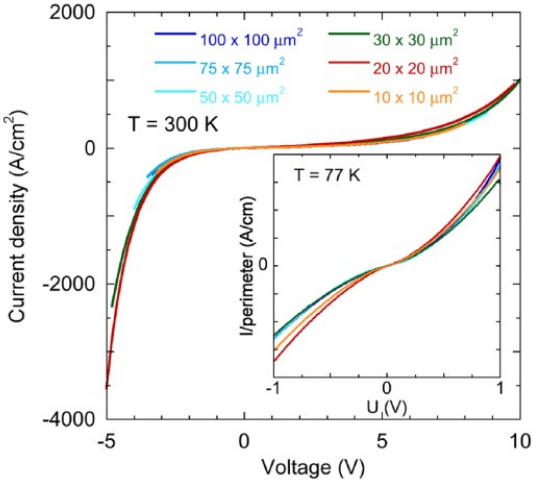

Figure 0.153.: J-V (Current density - Voltage) caracteristic of QCD at RT. Inset: current normalized by the mesa permimeter at $77\,K$. *Reprinted from (Jollivet* et al.*, 2018), with the permission of AIP Publishing.*

The detectivity, R_0A, with A the mesa area, is commonly used as a figure of merit to compare QCD devices performance (Gomez *et al.*, 2008). In our case, R_0A is found to vary from 0.1 to $20.0\,\Omega.cm^2$ between room and low temperature respectively. This is far from what is obtained for InGaAs/InAlAs QCDs at 4.7 µm: the product R_0A is found to be $10^6\,\Omega.cm^2$ at low temperature (Hofstetter *et al.*, 2010), or in (Gendron *et al.*, 2004) where they show a GaAs/AlGaAs at 9.2 µm with a R_0A of $100\,\Omega.cm^2$. Similar values are obtained for GaN/AlGaN QCDs at 1 µm(Sakr *et al.*, 2012). So compared to these devices, our QCD exhibits a high dark current level, even at low temperature. As explained in (Gomez *et al.*, 2008), the radiative transition is not the only one allowing the electron to travel across the entire structure: here, diagonal transitions take place too. They can have as well a contribution to the R_0A value. This is why authors propose to set magnetotransport experiment to know each transition contribution to the overhall R_0A. This type of experiment can be thought to be conducted in the future in order to understand better which QCD design is the more adapted to ZnO. The same goes for the responsivity, which respresents the collected current with respect to the input power. In our case, a value of $0.15\,mA/W$ was deduced (Jollivet *et al.*, 2018). Typical values for QCD responsivities are ranging from 0.32 up to $35\,mA/W$, for various material systems as GaAs/AlGaAs, GaN/AlGaN or InGaS/AlAsSb (Hofstetter *et al.*, 2010; Giorgetta *et al.*, 2007; Graf *et al.*, 2004; Sakr *et al.*, 2012). So the first ZnO based QCD presents a responsivity with the same magnitude order of the one presented in (Giorgetta *et al.*, 2007), made in InGaS/AlAsSb and working around 2 µm, which is quite encouraging.

To improve the performance of ZnO QCD, particular efforts should be put on the design as well as on the process in order to adapt it to the particularity of ZnO and to reduce the sidewalls leakage respectively. However, the realization of ZnO QCD in the IR, which involve high Mg contents, is

not the best option because the heterostructure quality might not be good enough. And, of course, GaAs based QCDs are already satisfyingly working in this energy domain.

Another good point with this realization is that tunnel transport occur in our heterostructures (Jollivet *et al.*, 2018). So with ISBT, the two physical phenomena on which the QCL is based has been evidenced, so it paves the way for the realization of ZnO/(Zn, Mg)O QCLs, which is the next topic.

0.10. Quantum Cascade Laser

In this last part we present our first attempt to realize THz QCL structures based on ZnO/(Zn, Mg)O heterostructures. Figure 0.154 shows a band diagram example for a ZnO based QCL working in the THz range. All the design optimization was done by our colleagues of ETH in Zurich. Due to the fast LO-phonon scattering rates (Chen *et al.*, 2004; Stroscio *et al.*, 1999), typically in the range of $10^{-1} - 10^{-2}\, ps^{-1}$, QCL designs based on wurtzite crystals usually take this intrinsic property as an advantage to fastly depopulate the lower laser state (Sun *et al.*, 2005; Terashima & Hirayama, 2011). Thus a resonant phonon design was chosen for a ZnO based QCL. As a consequence, the bandoffset needed to confine the electron is mainly driven by the LO-phonon energy for a resonant phonon THz QCL (see figure 0.154). And since the LO-phonon energy in ZnO is high: $72\, meV$ (Bundesmann *et al.*, 2006; Özgür *et al.*, 2005), a bandoffset of nearly $200\, meV$ is required even if the ISBT is only ten times lower for this specific design. This feature explains also the high typical values of applied electric field, $83\, kV.cm^{-1}$, compared to GaAs based THz QCL (1 to $50\, kV.cm^{-1}$ (Page *et al.*, 2001; Sirtori *et al.*, 1998; Scalari *et al.*, 2009; Fathololoumi *et al.*, 2012; Barbieri *et al.*, 2004)). The same applies to GaN based THz QCL, for which the LO-phonon energie is even higher: $90\, meV$ (Azuhata *et al.*, 1996; Barker & Ilegems, 1973; Sobotta *et al.*, 1992). So typical electric field values are in the range of $60 - 70\, kV.cm^{-1}$(Sun *et al.*, 2005; Terashima & Hirayama, 2011).

The design takes into account several constraints from the growth. The first limitations are the uncertainties on the thicknesses and the Mg content. An error of $\pm 1\, ML$ on thicknesses and $\pm 2\,\%$ on the Mg content is achievable on a every day basis. So the design should be robust enough to such deviations. The second part comes from the n-type doping: the MBE machine was equipped with only one Ga cell (at the beginning of the project). SIMS measurements show that it is difficult to achieve reproducible doping when several doping levels are incorporated in the structure (see the paragraph 0.5.1 and the figure 0.61). This is why the structures have only one doping level. In february 2019, a second Ga cell was set on the reactor. The idea is to use one Ga cell for high doping levels and the other one for lower ones in order to be able in the future to switch in a reproducible way between a low and a high doping level.

The physical parameters used to build these design adapted to ZnO comes either from the litterature or from specific measurement done by our partners in ISOM (for instance for the effective masses of ZnO and (Zn, Mg)O). But since ZnO is a completly new material system in the field of QCL, some specific material parameters are lacking. This is the case for the coherence length which is taken from GaAs. The realization of QCL devices are needed in order to refine these parameters to the ZnO material system.

Coming back to figure 0.154, the electron in the upper subband of the active QW first undergo an ISBT and arrive in the lower subband. Then it goes from the lower subband to the ground state by a LO-phonon assisted transition. The next step is to transport the electron throught a serie of coupled QWs by tunnel transport so that the electron reaches on the upper subband of the next active QW.

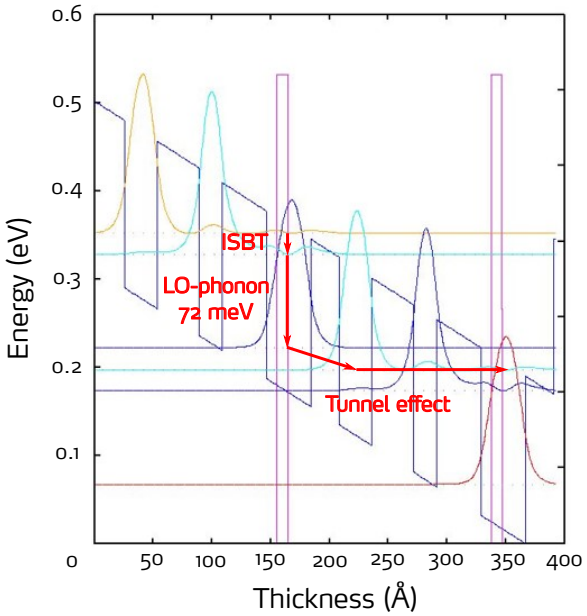

Figure 0.154.: Example of THz QCL active region design for ZnO/(Zn, Mg)O targeted a $5\,THz$ emission. The applied electric field needed is $83\,kV.cm^{-1}$ and the band offset is $190\,meV$.

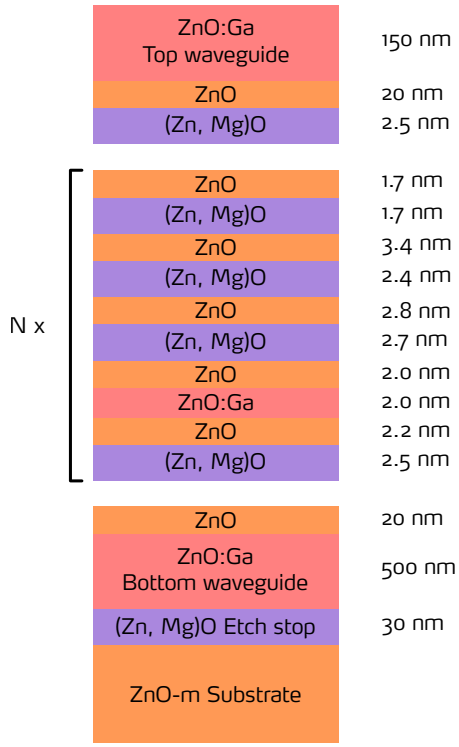

Figure 0.155.: Structure of QCL samples for THz. The number of active region period varies from one sample to another.

A serie of THz QCL samples has been grown. Each of them are grown on a m-plane ZnO substrate annealed at 800°C during 20 minutes prior to the growth inside the growth chamber. The structure consists of a $30.0\,nm$ (Zn, Mg)O layer as a etch stop for the process followed by a $500\,nm$ bottom wave-guide made by Ga doped ZnO (nominal doping level $3 \times 10^{18}\,cm^{-3}$). A $20.0\,nm$ ZnO layer was added between the doped wave-guide and the active region in order to avoid interdiffusion of Ga atoms inside the active layers. The active region is a repetition of N times the single period which is $25.2\,nm$ thick. All the layers inside the active region can be seen in detail in figure 0.155.The last ZnO QW is followed by a $2.5\,nm$ thick (Zn, Mg)O barrier in order to keep the electron confined within the QW. The structure is ended by the $20.0\,nm$ ZnO layer and by the top wave-guide. Only one doping level is used in the structure and the Mg content is set to $12\,\%$.

The first sample of this serie has a number N of period of 100, and accumulate nearly 15 hours of total growth duration. This is huge compared to the duration of MQWs we are used to grow ($2-4$ hours). For this first sample, 'dusts' appear on the surface as it can be seen from optical microscope picture (see figure 0.156). We can see a lot of defects which are at a distance of around few µm.

These kind of surface defects are detrimental to the process and the device. Thus such a surface exclude the possibility to process a device out of this layer because the mesas are several micrometer wide. Up to now, these defects have appeared on the surface for growth longer than 8 hours. One hypothesis is to consider that due to this long time growth, the Mg and Ga cells shutters stop and accumulate atoms that are released when shutters open. Thus we can not simply grow a QCL as we grow a 15 periods MQW sample.

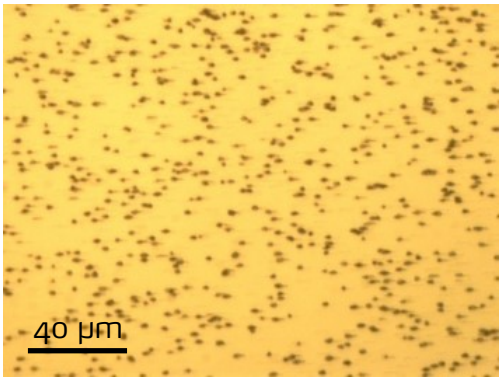

Figure 0.156.: Optical microscope image of the surface of sample ZOE0218.

Figure 0.157 shows the diffraction spectra of the serie taken around the (100) node (symmetric node). All the spectra show one intense peak which correspond to the diffraction of the ZnO substrate. Around this main peak, several ones can be observed which are regularly spaced: they are called Pendellösung fringes and comes from interferences between layers with different thicknesses (Moram & Vickers, 2009). As these Pendellösung fringes arise from a diffraction phenomenon, their intensity is closely related to the contrast of out-of-plane lattice parameters between materials. So in addition to the active region thickness which can be obtained using the fringes spacing, a high intensity means that there is a sharp and reproducible out-of-plane lattice parameters across all the active region. Thus high intensity Pendellösung fringes are reminiscent from coherent layers out-of-plane, or in the growth direction, with sharp composition variations, meaning that interfaces are well defined. In particular high intensity Pendellösung fringes allow to exclude strain gradient or relaxation processes in the growth direction. Between these peaks, very rapid periodic intensity variations can be seen clearly for samples ZOE0224, ZOE0230 and ZOE0227. They are Pendellösing fringes coming from a thick layer, *i.e.* the top wave-guide and the nid ZnO layer on top of the structure (it is not possible to distinguish a ZnO from a ZnO doped layer because the lattice parameter chage is not sharp enough).

With the presence of these two kind of Pendellösung fringes, we are able to determine experimentally the thicknesses of each single layer of this complex structure. Indeed the quick Pendellösung fringes gives the information about the ZnO growth rate (it is assumed that the growth rate of ZnO and ZnO Ga doped is the same). And the high intensity Pendellösung fringes gives the information about the overhall active region thickness, which is a mix between ZnO and (Zn, Mg)O layers with distinct growth rates. Thus if we use the ZnO growth rate coming from the quick fringes and the overhall active region thickness, one can deduce the (Zn, Mg)O growth rate. And if the growth rates of both ZnO and (Zn, Mg)O are known independently, it is possible to calculate the thickness of each single layer within the layer. Of course, it assumes that the growth rates are stable during the all growth process. This hypothesis is checked separately by STEM cross-section observation.

Coming back to the first sample, ZOE0218, we can observe from its diffraction spectra, see figure 0.157, that Pendellösung fringes are not so well defined, which indicates that the interface quality and the period reproducibility might be possible to improve.

For the second sample of this serie, named ZOE0221, we choose to reduce the growth time in order to improve the surface quality. The period number is reduced to 30 and grown the sample in 3 steps. The procedure is the following: after the growth of the bottom wave-guide at day 1, the growth is stopped. The sample stays in the growth chamber until day 2 and the sample is annealed at $800°C$ during 20 minutes in order to smooth the surface. During this annealing step, an thinning of the RHEED stripes can be seen, which is a proof that the surface quality is improved. Then the active region is grown and after that the growth is stopped another time. It begins again at day 3 with the same annealing step as day 2, and the top wave-guide is grown. By doing so, the each growth steps is limited to 3.5 hours, which is typically what is needed to grow a MQW for which the surface is clean. As a result, we suppressed the 'dusts' which were seen on the previous sample (*i.e.* ZOE0218). But in the diffraction spectrum, the periodic peaks are not very intense compared to ZOE0218. A possible interpretation is that the interfaces are not so well defined compared to the sample ZOE0218. It can come from the annealing step which was added after the active region growth which favoured the interdiffusion of atoms between different layers at the interfaces vicinity. In order to reduce this interdiffusion process, the active region annealing temperature was divided by two (*i.e.* $400°C$) for the next sample, keeping other steps unchanged (ie ZOE0227). On its XRD spectrum, we can see a clear intensity increase of Pendellösing fringes related to the active region. This confirm that the loose of peak intensity for the sample ZOE0221, whose active region was annealed at 800°C undergo a strong interdiffusion process. The RMS roughness deduced from AFM is $0.85\,nm$ for a $2 \times 2\,\mu m^2$ picture.

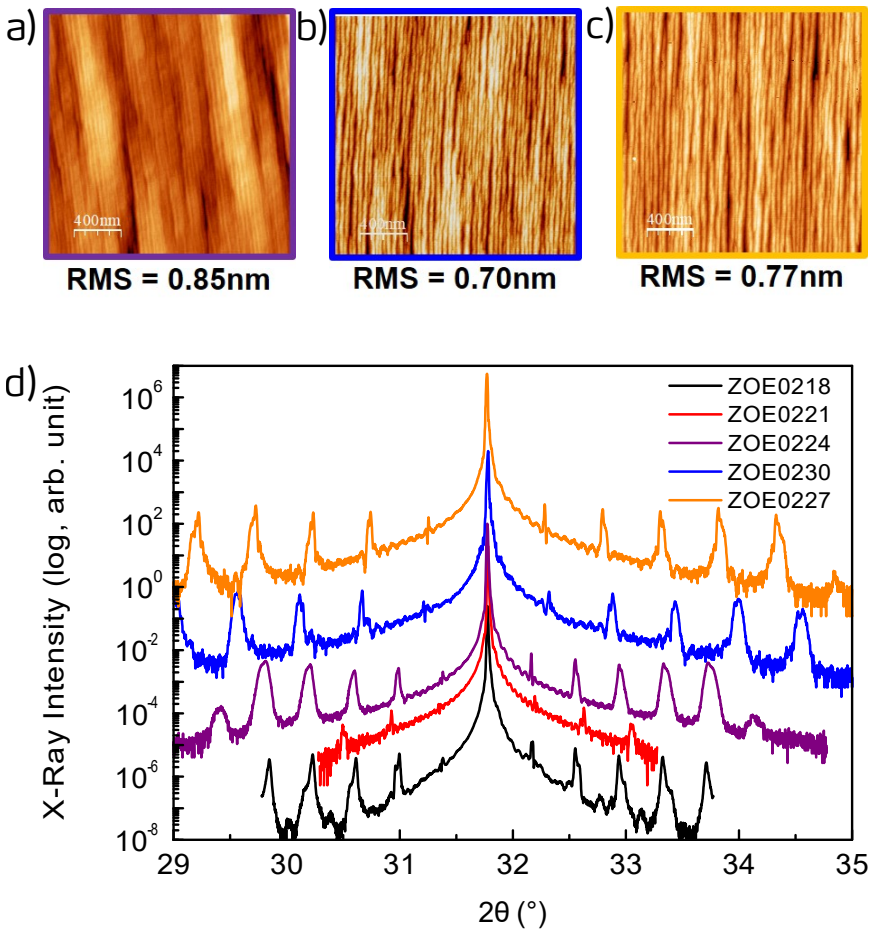

Figure 0.157.: a), b) and c) AFM picture of the QCL sample ZOE0224, ZOE0230 and ZOE0227 respectively. d) XRD spectra of several QCL samples around the (100) node. The intensity is normalized by the experiment time so that intensities are comparable from one sample to another.

Sample ZOE0230 was grown as ZOE0224, but even with reduced annealing temperatures in order to investigate the influence of the in-situ annealing ($200°C$ after the active region). Looking at the diffraction spectrum, there is no qualitative changes for the intensity of Pendellösung fringes, meaning that interfaces are of similar quality as the sample ZOE0224. However, the AFM image shows a slight improvement of the surface roughness.

The last sample of this serie was grown as ZOE0227, but with an increased period number of the active region: 100 instead of 30. Again, the XRD spectra of samples ZOE0227 and ZOE0230 are very similar despite the increase of the period number. On the AFM image, we can notice a little increase of the RMS roughness from 0.70 to $0.77\,nm$ by increasing the number of period by a factor of nearly 3.

Looking at the spacing between Pendellösung fringes, we can see that it varies a lot from one sample to another. This variation implies thicknesses variations that can be explained by the fact that O cell was poorly reproducible because of a technical issue. The requirements are not fulfilled. However, the samples ZOE0218 and ZOE0224 have thicknesses in agreement with the nominal values within a error bar of $\pm 1ML$ (see table 0.10).

Layer name	Nominal thickness (Å)	ZOE0218 (Å)	ZOE0221 (Å)	ZOE0224 (Å)	ZOE0227 (Å)	ZOE0230 (Å)
ZnO:Ga Top wave-guide	1500	1414	1089	1387	1065	1000
ZnO	200	188	145	185	142	133
(Zn, Mg)O	25	24	18	23	18	17
ZnO	36	34	26	33	26	24
(Zn, Mg)O	17	16	12	16	12	11
ZnO	34	32	25	31	24	23
(Zn, Mg)O	24	23	17	22	17	16
ZnO	27.5	26	20	25	20	18
(Zn, Mg)O	27	25	20	25	19	18
ZnO	20	19	15	18	14	13
ZnO:Ga	20	19	15	18	14	13
ZnO	21.5	20	16	20	15	14
(Zn, Mg)O	25	24	18	23	18	17
ZnO	200	188	145	185	142	133
ZnO:Ga Bottom wave-guide	5000	4710	3630	4620	3550	3330
(Zn, Mg)O etch stop	300	283	218	277	213	200

Table 0.10.: Thicknesses measured by XRD for the QCL samples of the serie. The layers are going from the samples surface down to the substrate when going from the top to the bottom part of the table.

The sample ZOE0230 was prepared for STEM-HAADF cross-section observation. 0.158 shows a large view of the active region stack, with nearly 15 periods visible that are very homogeneous on this large scale.

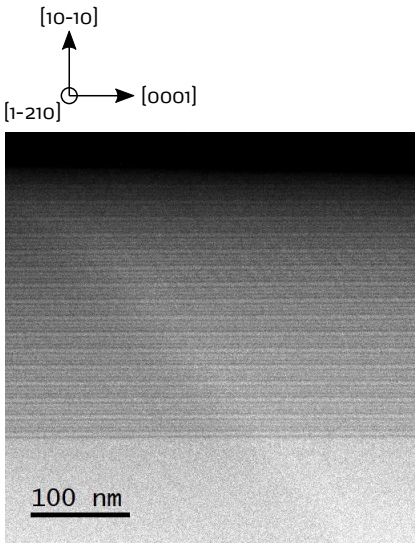

Figure 0.158.: STEM HAADF image in the zone axis $[1\bar{2}10]$ of the sample ZOE0230.

Looking at the atomic scale, the stability of the growth process can be investigated. So we took images on three zones as it is shown in figure 0.159 reparted as follow: first active region period (near the bottom contact), an period in the middle of the active region and the last active region period (near the top contact). The three images have different intensities if we compare the (Zn, Mg)O regions (in dark on the images). It cannot be interpreted as variation of the Mg composition because the sample thickness varies between the top and bottom of the active region, modifying the collected signal. Layers thicknesses in the 3 zones were measured and they are all identical within an error bar of $\pm 0.1\,nm$, which is the typical error obtained for thickness measurements on atomical resolution images. Thus the growth process is completely reproducible on a time scale up to 4 hours.

As the sample was grown in 3 steps with an annealing procedure between two of them, we wanted also to check for the impact of these growth interruptions and annealings on the active region (figure 0.159, images a) an c)). Near the bottom contact, we can see that there is no visible trace of the re-growth near the first (Zn, Mg)O layer. Moreover, layers interfaces are as sharp and abrupt as layers located on the middle of the active region. Thus no detrimental impact of this growth interruption and annealing is seen near the first active region period.

However, this is different for the last active region period: we can notice that interfaces are very diffuse such that a (Zn, Mg)O layer nearly vanished (figure 0.159 c)). This can be reasonably attributed to the $200°C$ annealing step between the active region end and the top contact. To avoid it, we can think about two options: either reduce the annealing temperature and/or duration (respectively $200°C$ and $15\,minutes$), or protect the last active region period by a ZnO capping layer. Indeed, since the second to last period does not show diffuse interfaces, a ZnO capping layer as thick as one period should be sufficient to protect the last period from diffusion (in our case, between 20 and $25\,nm$).

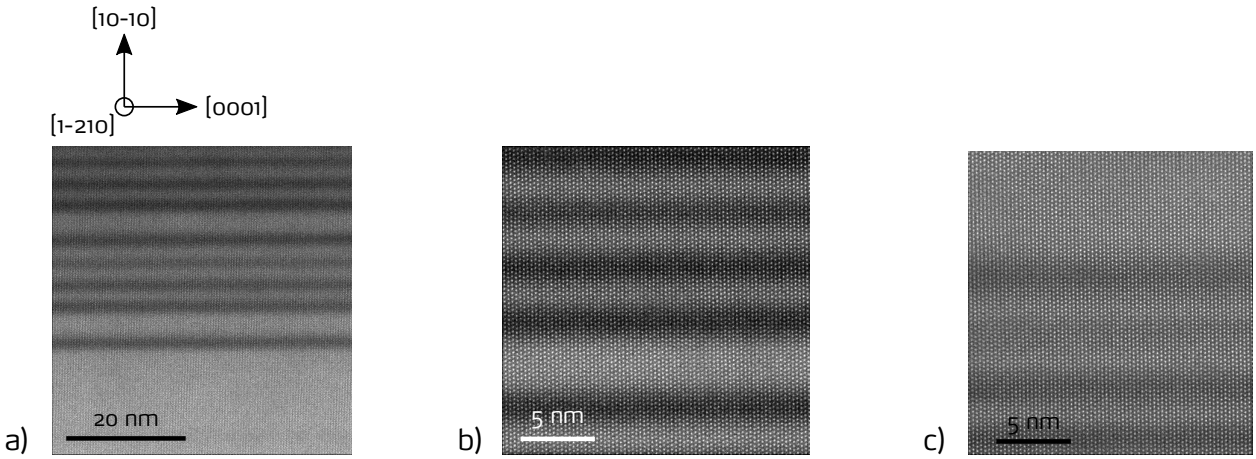

Figure 0.159.: STEM HAADF images in the zone axis $[1\bar{2}10]$ of the sample ZOE0230 a) near the bottom contact, b) in the middle of the structure and c) near the top contact. Note that the contrast difference between the 3 images is not linked to a variation of Mg content between them.

For QCL, two families of waveguides are used: dielectric or metal waveguides. In the case of dielectric waveguides, the dielectric thickness required to confine the modes scales roughly like the emission wavelength (Scalari *et al.*, 2009). For the THz, where the emission wavelength spans from 10 to 1000 µm, this option is not suitable because the thickness is huge to be grown reasonnably by MBE. This explains why most of the THz QCL employ metal waveguide. Among this family, two approaches are possible: the single plasmon or the double metal waveguide. In the case of the single plasmon waveguide, a thick - several hundred nanometers - doped semiconductor layer is grown between the substrate and the active region and a metal layer is added on top of the structure after the growth. As a result, the modes - called surface plasmons - are confined between the two conductive layers: the doped semiconductor at the bottom part of the sample, and the top metallic layer. For the double metal waveguide, a metal layers are deposited after the growth at the bottom and on top of the active layer by a waferbonding process. This approach has the advantage confine nearly perfectly the modes (Unterrainer *et al.*, 2002; Williams *et al.*, 2003), and to show the best performances when the operating temperature is increased (Belkin *et al.*, 2009; Scalari *et al.*, 2009; Williams, 2007; Yu & Capasso, 2010). This last argument explains why this double waveguide approach has been favoured in the scope of making a RT THz QCL.

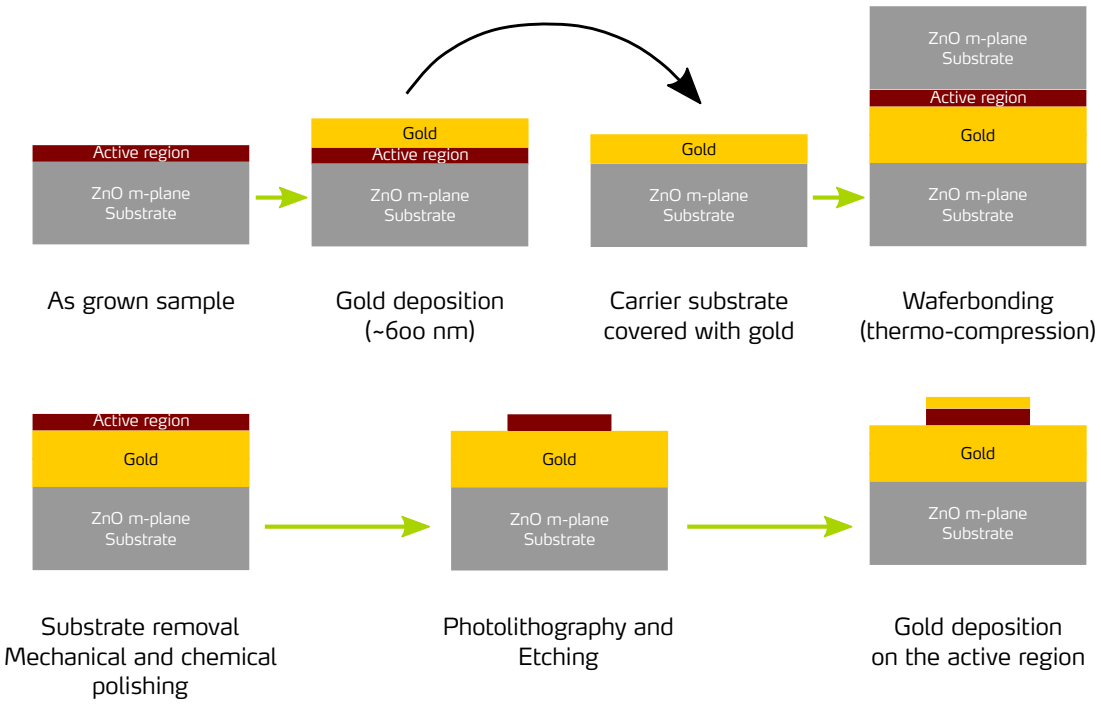

Figure 0.160.: Schematic showing waferbonding steps chronologically from right to left.

The process of the QCL is performed at TU Wien using the double waveguide approach. The main process steps are sketched in figure 0.160. A ZnO susbtrate covered with gold is used as a carrier wafer for the waferbonding process. Then the substrate is removed mainly by mechanical polishing using diamond compounds - sandpaper and then paste - until the optical quality is achieved. The next step consists to process the active region in the form of ridges and cover them with the top metal contact. Devices has been successfully proceessed and have been send to our colleagues at ETH Zurich for measurement.

However, we have some preliminary results on a previous QCL serie. At this time the waferbonding process for ZnO was not fully optimized, so these QCL does not contain the waveguides. They have been processed and contacted as it can be shown in figure 0.161. One of them has been investigated at ETH in Zurich by THz spectroscopy. Figure 0.162 prensents spectra taken at temperatures ranging from $10\,K$ to $150\,K$: a signal can be seen for each temperature in the range of $10-20\,meV$, which lies in the THz range. We can observe that at $10\,K$, the signal is peaked at $11\,meV$, or $2.7\,THz$, which was very close to the targeted energy: $2.5\,THz$. Since there are no waveguides, this signal is a spontaneous emission. Further investigations are underway in order to clarify if these peaks comes from ISBT within the QCL active region and why there is an energy shift with the temperature.

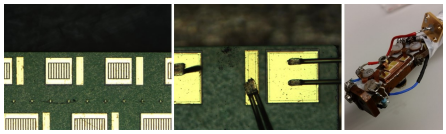

Figure 0.161.: Photos of processed QCLs that have been lapped, cleaved and mounted for spectroscopic measurements. Squares are top contacts whereas rectangles are the bottom ones.

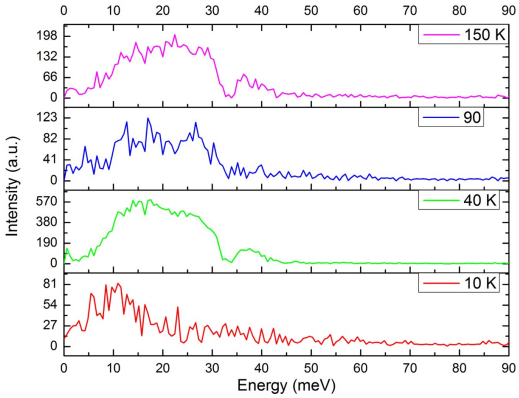

Figure 0.162.: THz spectrum of one ZnO/(Zn, Mg)O QCL at different temperatures.

Finally a new series of QCL structures has been grown following a new design from ETH Zurich. This series has been grown after a modification of the O-plasma cell. The full QCL structures can be grown in less than 8 hours without any growth interruption. The obtained structure are only 0.6% off the nominal values, *i.e.* 1 ML error on 22 nm thick period (see table 0.11) after calibration. The full process is being performed in TU Wien.

Sample	x_{Mg} (%)	T_{Ga} ($°C$)	Number of periods	Measured period (Å)	Deviation
ZOE0261	11.8	495	40	208	5 %*
ZOE0264	11.8	490	50	191	13 %*
ZOE0265	11.8	500	50	188	15 %*
ZOE0266	11.8	500	50	225	2 %
ZOE0267	11.8	490	50	218	0.6 %
ZOE0268	11.8	480	50	218	0.6 %
Nominal	11.85	-	-	220.5	-

Table 0.11.: Thickness of the QCL period measured by XRR. *: calibration layers. The Ga temperature is modified to ensure the right range of doping in the active layer.

Part V.

Summary

This thesis aims was to demonstrate that a THz QCL working at RT was achievable using ZnO based heterostructures. The advantage of ZnO compared to other semiconductors commonly used for QCL is its large LO-phonon energy which can enable it to achieve RT population inversion in the THz. ZnO has never been used to realise quantum cascade devices, which are based on quantum engineering. Indeeed the device operation stands completly on the architecture of its building blocs, and not on the nature of its building blocks. To suceed, the heterostructures should be controlled at the monolayer scale, with abrupt interfaces. Within the european project ZOTERAC, a new MBE system was set up at the beginning of my thesis: a part of my work was to participate to the transfert of non-polar ZnO knowledge from the old MBE system to the new one. In only few months we were able to come back to similar material quality compared to the old MBE system, with for instance roughness under 0.5 nm for ZnO/(Zn, Mg)O MQWs as well as a residual doping under $10^{15}\,cm^{-3}$.

Naturally, the first part of this thesis is related to the growth and material characterization of ZnO/(Zn, Mg)O MQWs, since QW is the building block for cascade devices. I was using AFM, XRD, XRR, SEM and PL regularly in order to select a growth window for which the layers quality were compatible with the realization of cascade devices. The temperature and the II/VI flux ratio were varied independently and changes in surface roughness as well as internal quantum efficiency were observed using XRR and temperature dependant PL measurements. In addition, I developed a reliable calibration procedure for thicknesses using a single MQW sample: the coupling of SEM thickness measurements on thick ZnO and (Zn, Mg)O buffer with XRR spectrum gives a thickness precision on the QW and barrier thickness at the ML scale. Our colleagues at ISOM in Madrid found out optical methods in order to assess the Mg content and the n-type doping using IR reflectance spectroscopy. The Mg content is assessed by looking at the position of the LO-phonon absorption within the (Zn, Mg)O barrier in the reflectance spectrum. For the n-type doping, they demonstrate the existence of MSP inside the ZnO QWs and use their signature to extract the doping value from reflectance spectrum. The main advantage of these two last methods is that they don't need the presence of buffer layers, parameters are directly extracted from the ZnO QW and the (Zn, Mg)O barrier. Thus it can directly be applied on device layers without any damage.

Apart from these daily basis developments I conducted material studies focused on the (Zn, Mg)O alloy. One of them started from an observation of a MQW sample with 40 % of Mg by STEM-HAADF: there is a variation of the Mg content within the barrier which follows the undulated profiles of the QWs. Such composition variation can lead to electrons localization which is detrimental to cascade devices. So I studied the localization of excitons be photoluminescence and it turns out that they are not localized for Mg composition under 25 %, which is much higher compared to the Mg content required THz for cascade devices: $\sim 15\,\%$. The other study on the (Zn, Mg)O alloy focused on its mechanical properties: since cascade devices needs thicknesses on the micrometer range, the risk of layers relaxation due to the lattice mismatch between ZnO and (Zn, Mg)O should be considered. But the (Zn, Mg)O alloy in its wutzite phase does not exist in nature, which have forbidden the determination of its mechanical properties by classical means like traction tests. I developed a mechanical model based on linear elasticity in order to determine the expression of the out-of-plane deformation as a function of the alloy mechanical parameters, when it is grown on a lattice matched ZnO susbtrate. The idea was to use the epitaxial growth as a system for mechanical testing in order

to be able to vary the out-of-plane deformation as a function of the crystalline orientation and Mg content. The out-of-plane deformation was measured using XRD and can be compared to the theory. This projet have required a lot of effort because 7 orientations are needed with various Mg content to have a complete picture of how this alloy behaves. It is not finished because 2 crystalline orientations are missing.

After the elastic limit came the plastic domain: on m-plane ZnO/(Zn, Mg)O heterostructures, cracks perpendicular to the c axis appear when the total thickness of alloy is beyong the critical thickness, which can be evaluated using the mechanical parameters of (Zn, Mg)O which are still unknown. Since cascade devices require a total layer thickness in the micrometer range, I estimated empirically the critical thickness as a function of the Mg content. It turns out that for the THz range, relaxation on m-plane is not an issue because the critical thickness for 15 % of Mg is above 1 µm. In addition, I was able to observe the signature of cracks in RSM because of the out-of-plane lattice parameter gradient at the crack vicinity.

On r-plane, the plastic behaviour is completly different: observations by AFM and CL reveals that the strain relaxation occurs thanks to a dislocation network. These dislocations cross each other with an angle of 51° on the r-plane surface. So it cannot be dislocation from basal plane, which are predicted to be the favoured ones according to the Schmid factor values. In this case, the static approach of Schmid factor is not sufficient to describe the reality, so a dynamical one may be prefered as a description using Peierls forces.

The last chapter focuses on the ISBT physics and on cascade devices. The good layer quality enables us to observe clearly ISBT in the IR at RT within MQWs samples, and to get an insight about the physics of ISBT in ZnO. We have shown that the undulated profile of QWs has an impact on the ISBT selection rule. For flat QWs, the normal incidence absorption is forbidden, but for an undulated one, it is shifted to the angle value of the undulation with respect to the QW plane. In addition, a strong depolarization shift was found to be the clue for the large energy shift of ISBT in doped QWs.

Asymmetrical QWs with various barrier thicknesses has been grown to look at the coupling between QWs, which is very important in the QCL injector region. STEM-HAADF experiments give the evidence that we are able to grow reproducibly 2 ML (Zn, Mg)O barriers with sharp interfaces. This is an undubitable proof that we have reach state-of-the art of growth controlability which is mandatory for cascade devices. PL and absorption experiments have shown that there is exciton and electron tranfered from one QW to another through the tunneling barrier respectively.

QCD in the IR range are demonstrated at RT: this is the first one made of ZnO/(Zn, Mg)O. The sample was processed as 260 square mesas and it turns out that 86% of them exhibit the same asymmetric trend in I-V measurements, showing a good process reproducibility despite the fact that the process steps used were not optimized before the beginning of the project. Then QCL samples has been grown and a growth protocole has been set up in order to improve the layer quality for long growth. It consists of cutting the growth in 3 parts in order to reduce each growth step to 4-5 hours. By doing so and by adjusting the annealing temperature between each step, we have improve the surface and reduced a lot the interdiffusion process, which is detrimental to the interface quality. All the process steps needed, including waferbonding are optimized. A first serie of sample

processed without the waveguides have been measured by THz spectroscopy and a THz signal is detected at $2.7 THz$, which is close to the targeted value. The second serie of QCL structures have been successfully processed in TU Wien and will be characterized by ETH Zurich soon.

Appendix

Calculation details on deformation

Expression of the stiffness components C'_{pqrs} in the epitaxial layer's coordinate as a function of the stiffness components C_{ijkl} in the crystal lattice coordinate with the tilt angle θ.

$$\begin{aligned} C'_{1133}(\theta) &= (\cos\theta\sin\theta)^2 C_{1111} + (\cos\theta)^4 C_{1133} + (\sin\theta)^4 C_{3311} + (\sin\theta\cos\theta)^2 C_{3333} \\ &\quad - (\sin\theta\cos\theta)^2 C_{3131} \\ &= (\cos\theta\sin\theta)^2 C_{1111} + \left[(\cos\theta)^4 + (\sin\theta)^4\right] C_{1133} + (\sin\theta\cos\theta)^2 C_{3333} \\ &\quad - (\sin\theta\cos\theta)^2 C_{2323} \end{aligned}$$

$$\begin{aligned} C'_{3131}(\theta) &= (\cos\theta\sin\theta)^2 C_{1111} - (\sin\theta\cos\theta)^2 C_{1133} - (\sin\theta\cos\theta)^2 C_{3311} + (\cos\theta\sin\theta)^2 C_{3333} \\ &\quad + (\cos\theta)^4 C_{3131} \\ &= (\cos\theta\sin\theta)^2 C_{1111} - 2(\sin\theta\cos\theta)^2 C_{1133} + (\cos\theta\sin\theta)^2 C_{3333} + (\cos\theta)^4 C_{2323} \end{aligned}$$

$$\begin{aligned} C'_{1131}(\theta) &= (\cos\theta)^3(\sin\theta) C_{1111} - (\cos\theta)^3(\sin\theta) C_{1133} + (\sin\theta)^3(\cos\theta) C_{3311} - (\sin\theta)^3(\cos\theta) C_{3333} \\ &\quad - (\cos\theta)^3(\sin\theta) C_{3131} \\ &= (\cos\theta)^3(\sin\theta) C_{1111} + (\cos\theta\sin\theta)\left[(\sin\theta)^2 - (\cos\theta)^2\right] C_{1133} - (\sin\theta)^3(\cos\theta) C_{3333} \\ &\quad - (\cos\theta)^3(\sin\theta) C_{2323} \end{aligned}$$

$$\begin{aligned} C'_{3331}(\theta) &= (\sin\theta)^3(\cos\theta) C_{1111} - (\sin\theta)^3(\cos\theta) C_{1133} + (\cos\theta)^3(\sin\theta) C_{3311} - (\cos\theta)^3(\sin\theta) C_{3333} \\ &\quad + (\cos\theta)^3(\sin\theta) C_{3131} \\ &= (\sin\theta)^3(\cos\theta) C_{1111} + (\cos\theta\sin\theta)\left[(\sin\theta)^2 - (\cos\theta)^2\right] C_{1133} - (\cos\theta)^3(\sin\theta) C_{3333} \\ &\quad + (\cos\theta)^3(\sin\theta) C_{2323} \end{aligned}$$

$$\begin{aligned} C'_{2233}(\theta) &= (\sin\theta)^2 C_{2211} + (\cos\theta)^2 C_{2233} \\ &= (\sin\theta)^2 C_{1122} + (\cos\theta)^2 C_{1133} \end{aligned}$$

$$\begin{aligned} C'_{2231}(\theta) &= (\cos\theta\sin\theta) C_{2211} - (\cos\theta\sin\theta) C_{2233} \\ &= (\cos\theta\sin\theta) C_{1122} - (\cos\theta\sin\theta) C_{1133} \end{aligned}$$

$$\begin{aligned} C'_{3333}(\theta) &= (\sin\theta)^4 C_{1111} + (\cos\theta\sin\theta)^2 C_{1133} + (\cos\theta\sin\theta)^2 C_{3311} + (\cos\theta)^4 C_{3333} \\ &+ (\cos\theta\sin\theta)^2 C_{3131} \\ &= (\sin\theta)^4 C_{1111} + 2(\cos\theta\sin\theta)^2 C_{1133} + (\cos\theta)^4 C_{3333} + (\cos\theta\sin\theta)^2 C_{2323} \end{aligned}$$

In particular, when calculating the stiffness components for the polar orientation $\theta = 0°$, we verify that $C' = C$ as expected.

Expression of the stiffness components C'_{pqrs} for the case of non-polar orientation: $\theta = 90°$.

$$C'_{1133}(90°) = C_{1133}$$

$$C'_{3131}(90°) = 0$$

$$C'_{1131}(90°) = 0$$

$$C'_{3331}(90°) = 0$$

$$C'_{2233}(90°) = C_{1122}$$

$$C'_{2231}(90°) = 0$$

$$C'_{3333}(90°) = C_{1111}$$

When the two tilt angles θ and ψ are used, the rotation matrix $R(\theta, \psi)$ to pass from the crystal coordinate $(\overrightarrow{e_x}, \overrightarrow{e_y}, \overrightarrow{e_z})$ to the epitaxial one $(\overrightarrow{e_x}'', \overrightarrow{e_y}'', \overrightarrow{e_z}'')$ is:

$$R\left(\theta,\psi\right)=\left[\begin{array}{ccc}\cos\theta\cos\psi & -\sin\psi & \sin\theta\cos\psi\\ \cos\theta\sin\psi & \cos\psi & \sin\theta\sin\psi\\ -\sin\theta & 0 & \cos\theta\end{array}\right]_{\left(\vec{e_x}'',\vec{e_y}'',\vec{e_z}''\right)}$$

Note that we find again that $R\left(\theta,\psi\right)=R\left(\theta\right)$ when $\psi=0°$. Then by applying the Hooke's law, we end with the following expression for the stiffness matrix in the epitaxial layer coordinate:

$$C''=\left[\begin{array}{cccccc}C''_{1111} & C''_{1122} & C''_{1133} & C''_{1123} & C''_{1131} & C''_{1112}\\ C''_{1122} & C''_{2222} & C''_{2233} & C''_{2223} & C''_{2231} & C''_{2212}\\ C''_{1133} & C''_{2233} & C''_{3333} & C''_{3323} & C''_{3331} & C''_{3312}\\ C''_{1123} & C''_{2223} & C''_{3323} & C''_{2323} & C''_{2331} & C''_{2312}\\ C''_{1131} & C''_{2231} & C''_{3331} & C''_{2331} & C''_{3131} & C''_{3112}\\ C''_{1112} & C''_{2212} & C''_{3312} & C''_{2312} & C''_{3112} & C''_{1212}\end{array}\right]$$

Expression of the stiffness components C''_{pqrs} in the epitaxial layer's coordinate as a function of the stiffness components C_{ijkl} in the crystal lattice coordinate with tilt angles θ and ψ.

$$\begin{aligned}C''_{1111}\left(\theta,\psi\right)=&\left(\cos\theta\right)^4C_{1111}\\ &+\frac{3}{4}\left(\cos\theta\right)^4\left(\cos\psi\sin\psi\right)^2C_{1122}\\ &+\left(\cos\theta\sin\theta\right)^2\left(1+\left(\sin\psi\right)^2\right)C_{1133}\\ &+\left(\sin\theta\right)^4C_{3333}\\ &+\left(\cos\theta\sin\theta\right)^2C_{2323}\end{aligned}$$

$$\begin{aligned}C''_{1122}\left(\theta,\psi\right)=&\frac{3}{4}\left(\cos\theta\cos\psi\sin\psi\right)^2C_{1111}\\ &+\left(\cos\theta\right)^2C_{1122}\\ &+\left(\sin\theta\right)^2C_{1133}\end{aligned}$$

$$\begin{aligned}C''_{1133}\left(\theta,\psi\right)=&\left(\cos\theta\cos\psi\sin\theta\right)^2C_{1111}\\ &+\left(\cos\theta\sin\theta\cos\psi\right)^2C_{1122}\\ &+\left(\left(\cos\theta\right)^4+\left(\sin\theta\right)^4\right)C_{1133}\\ &+\left(\cos\theta\sin\theta\right)^2C_{3333}\\ &-\left(\cos\theta\sin\theta\right)^2\left(\cos\psi\right)C_{2323}\end{aligned}$$

$$
\begin{aligned}
C''_{1123}(\theta,\psi) = &-(\cos\theta\cos\psi)^2(\sin\theta\sin\psi)\,C_{1111}\\
&-(\sin\psi)^3(\cos\theta)^2(\sin\theta)\,C_{1122}\\
&-(\sin\theta)^3(\sin\psi)\,C_{1133}\\
&-(\cos\theta)^2(\cos\psi\sin\psi\sin\theta)\,C_{2323}
\end{aligned}
$$

$$
\begin{aligned}
C''_{1131}(\theta,\psi) = &(\cos\theta)^3(\cos\psi\sin\theta)\left((\cos\psi)^2-\frac{1}{2}(\sin\psi)^2\right)C_{1111}\\
&+\frac{3}{4}(\cos\theta)^3(\sin\psi)^2(\sin\theta\cos\psi)\,C_{1122}\\
&+(\cos\theta\sin\theta)\left((\sin\theta)^2(\cos\psi)-(\cos\theta)^2\right)C_{1133}\\
&-(\sin\theta)^3(\cos\theta)\,C_{3333}\\
&-(\cos\theta)^3(\cos\psi)^2(\sin\theta)\,C_{2323}
\end{aligned}
$$

$$
\begin{aligned}
C''_{1112}(\theta,\psi) = &(\cos\theta)^3(\cos\psi\sin\psi)\left((\sin\psi)^2-\frac{3}{4}(\cos\psi)^2\right)C_{1111}\\
&+(\cos\theta)^3(\cos\psi\sin\psi)\left(\frac{3}{4}(\cos\psi)^2-(\sin\psi)^2\right)C_{1122}\\
&-(\sin\theta)^2(\cos\theta\cos\psi\sin\psi)\,C_{2323}
\end{aligned}
$$

$$
\begin{aligned}
C''_{2222}(\theta,\psi) = &\,C_{1111}\\
&+\frac{3}{4}(\cos\psi\sin\psi)^2\,C_{1122}
\end{aligned}
$$

$$
\begin{aligned}
C''_{2233}(\theta,\psi) = &(\sin\theta\sin\psi)^2\,C_{1111}\\
&+(\cos\psi\sin\theta)^2\,C_{1122}\\
&+(\cos\theta)^2\,C_{1133}
\end{aligned}
$$

$$
\begin{aligned}
C''_{2223}(\theta,\psi) = &-(\sin\psi)^3(\sin\theta)\,C_{1111}\\
&-(\cos\psi)^2(\sin\theta\sin\psi)\,C_{1122}
\end{aligned}
$$

$$C''_{2231}(\theta,\psi) = \frac{3}{4}(\sin\psi)^2(\cos\theta\sin\theta\cos\psi)C_{1111} + (\cos\theta\sin\theta\cos\psi)\left((\cos\psi)^2 + \frac{1}{2}(\sin\psi)^2\right)C_{1122} - (\cos\theta\sin\theta)C_{1133}$$

$$C''_{2212}(\theta,\psi) = (\cos\theta\cos\psi\sin\psi)\left(\frac{1}{2}(\cos\psi)^2 - (\sin\psi)^2\right)C_{1111} + (\cos\theta\cos\psi\sin\psi)\left(\frac{3}{2}(\cos\psi)^2 - (\sin\psi)^2\right)C_{1122}$$

$$C''_{3333}(\theta,\psi) = (\sin\theta)^4 C_{1111} + 2(\cos\theta\sin\theta)^2 C_{1133} + (\cos\theta)^4 C_{3333} + (\cos\theta\sin\theta)^2 C_{2323}$$

$$C''_{3323}(\theta,\psi) = -(\sin\theta)^3(\sin\psi)C_{1111} - (\cos\theta)^2(\sin\psi\sin\theta)C_{1133}$$

$$C''_{3331}(\theta,\psi) = (\sin\theta)^3(\cos\theta\cos\psi)C_{1111} + (\sin\theta\cos\theta)\left((\cos\theta)^2(\cos\psi) - (\sin\theta)^2\right)C_{1133} - (\cos\theta)^3(\sin\theta)C_{3333} + (\cos\theta)^3(\sin\theta\cos\psi)C_{2323}$$

$$C''_{3312}(\theta,\psi) = -(\sin\theta)^2(\cos\theta\cos\psi\sin\psi)C_{1111} + (\sin\theta)^2(\cos\theta\cos\psi\sin\psi)C_{1122} - (\sin\theta)^2(\cos\theta\sin\psi)C_{2323}$$

$$C''_{2323}(\theta,\psi) = (\sin\theta\sin\psi)^2 C_{1111} + (\cos\theta\cos\psi)^2 C_{2323}$$

$$C''_{2331}(\theta,\psi) = -(\sin\theta)^2(\cos\theta\cos\psi\sin\psi)C_{1111} + (\sin\theta)^2(\cos\theta\cos\psi\sin\psi)C_{1133}$$

$$C''_{2312}(\theta,\psi) = (\sin\psi)^2(\cos\theta\sin\theta\cos\psi)C_{1111} - (\sin\psi)^2(\cos\theta\sin\theta\cos\psi)C_{1122}$$

$$\begin{aligned} C''_{3131}(\theta,\psi) = {} & (\sin\theta\cos\psi)^2\left((\cos\psi)^2 + \frac{1}{2}(\sin\psi)^2\right)C_{1111} \\ & + 2(\cos\theta\sin\theta)^2(\cos\psi)C_{1133} \\ & - (\cos\theta\sin\theta)^2 C_{3333} \\ & + (\cos\theta)^3(\cos\psi)C_{2323} \\ & - \frac{1}{2}(\cos\theta\sin\theta\sin\psi)C_{1122} \end{aligned}$$

$$\begin{aligned} C''_{3112}(\theta,\psi) = {} & -\frac{1}{2}(\cos\theta\cos\psi)^2(\sin\theta\sin\psi)C_{1111} \\ & + \frac{1}{2}(\cos\theta\cos\psi)^2(\sin\theta\sin\psi)C_{1122} \\ & - 2(\cos\theta)^2(\sin\theta\cos\psi\sin\psi)C_{1133} \\ & + (\cos\theta)^2(\sin\theta\cos\psi\sin\psi)C_{2323} \end{aligned}$$

$$\begin{aligned} C''_{1212}(\theta,\psi) = {} & (\cos\theta\cos\psi)^2\left(2(\sin\psi)^2 + \frac{1}{2}(\cos\psi)^2\right)C_{1111} \\ & - (\cos\theta\cos\psi)^2\left(2(\sin\psi)^2 + \frac{1}{2}(\cos\psi)^2\right)C_{1122} \\ & + (\sin\theta\sin\psi)^2 C_{2323} \end{aligned}$$

Expression of deformations in the epitaxial layer coordinate $\varepsilon''_{xx}(\theta,\psi)$ and $\varepsilon''_{yy}(\theta,\psi)$.

We begin from the expression of the deformation vector in the crystal coordinate system ε:

$$\varepsilon = \begin{pmatrix} \varepsilon_a \\ \varepsilon_a \\ \varepsilon_c \end{pmatrix}_{\left(\vec{e}_x,\vec{e}_y,\vec{e}_z\right)}$$

We apply the rotation matrix $R(\theta,\psi)$ to have the expressions of ε in the epitaxial layer coordinate: $\varepsilon'' = R(\theta,\psi)\,\varepsilon$.

$$\varepsilon''_{xx}(\theta,\psi) = (\cos\theta)^2\,\varepsilon_a + (\sin\theta)^2\,\varepsilon_c$$

$$\varepsilon''_{yy}(\theta,\psi) = \varepsilon_a$$

$\varepsilon''_{xx}(\theta,\psi)$ and $\varepsilon''_{yy}(\theta,\psi)$ are independent of ψ. There is no change compared to the model with only the tilt angle θ.

Detailed expressions of the constants involved in the expression of ε''_{xz}, ε''_{yz}, ε''_{xy} and ε''_{zz}:

$$f_1 = -\frac{C''_{1212}C''_{3131}}{C''_{1212}C''_{3131} - \left(C''_{3112}\right)^2}$$

$$C_1 = \frac{C''_{2331}C''_{1212} - C''_{3112}C''_{2312}}{C''_{3131}C''_{1212}}$$

$$C_2 = \frac{C''_{2312}C''_{3131} - C''_{3112}C''_{2331}}{C''_{3131}C''_{1212}}$$

$$C_3 = -\frac{1}{C''_{2323} + C''_{2331}f_1C_1 + C''_{2312}f_1C_2}$$

$$C_\alpha = \frac{C''_{1131}}{C''_{3131}} - \frac{C''_{3112}C''_{1112}}{C''_{3131}C''_{1212}}$$

$$C_\beta = \frac{C''_{2231}}{C''_{3131}} - \frac{C''_{3112}C''_{2212}}{C''_{3131}C''_{1212}}$$

$$C_\gamma = \frac{C''_{3331}}{C''_{3131}} - \frac{C''_{3112}C''_{3312}}{C''_{3131}C''_{1212}}$$

$$C_\delta = \frac{C''_{1112}}{C''_{1212}} - \frac{C''_{3112}C''_{1131}}{C''_{3131}C''_{1212}}$$

$$C_\varepsilon = \frac{C''_{2212}}{C''_{1212}} - \frac{C''_{3112}C''_{2231}}{C''_{3131}C''_{1212}}$$

$$C_\eta = \frac{C''_{3312}}{C''_{1212}} - \frac{C''_{3112}C''_{3331}}{C''_{3131}C''_{1212}}$$

$$C_\lambda = C''_{1123} + C''_{2331}f_1C_\alpha + C''_{2312}f_1C_\delta$$

$$C_\mu = C''_{2223} + C''_{2331}f_1C_\beta + C''_{2312}f_1C_\varepsilon$$

$$C_o = C''_{3323} + C''_{2331}f_1C_\gamma + C''_{2312}f_1C_\eta$$

$$C_x = C''_{1133} + C''_{3323}C_3C_\lambda + C''_{3331}\left(f_1C_\alpha + C_1C_3C_\lambda\right) + C''_{3312}\left(f_1C_\delta + C_2C_3C_\lambda\right)$$

$$C_y = C''_{2233} + C''_{3323}C_3C_\mu + C''_{3331}\left(f_1C_\beta + C_1C_3C_\mu\right) + C''_{3312}\left(f_1C_\varepsilon + C_2C_3C_\mu\right)$$

$$C_z = C''_{3333} + C''_{3323}C_3C_o + C''_{3331}\left(f_1C_\gamma + C_1C_3C_o\right) + C''_{3312}\left(f_1C_\eta + C_2C_3C_o\right)$$

Expression of stiffness components for polar orientation: $\theta = 0°$ and ψ undefined:

$$C''_{1111}(0,\psi) = C_{1111} + \frac{3}{4}\left(\cos\psi\sin\psi\right)^2 C_{1122}$$

$$C''_{1122}(0,\psi) = \frac{3}{4}\left(\cos\psi\sin\psi\right)^2 C_{1111} + C_{1122}$$

$$C''_{1133}(0,\psi) = C_{1133}$$

$$C''_{1123}(0,\psi) = 0$$

$$C''_{1131}(0,\psi) = 0$$

$$C''_{1112}(0,\psi) = \left(\cos\psi\sin\psi\right)\left(\left(\sin\psi\right)^2 - \frac{3}{4}\left(\cos\psi\right)^2\right) C_{1111} + \left(\cos\psi\sin\psi\right)\left(\frac{3}{4}\left(\cos\psi\right)^2 - \left(\sin\psi\right)^2\right) C_{1122}$$

$$C''_{2222}(0,\psi) = C_{1111} + \frac{3}{4}\left(\cos\psi\sin\psi\right)^2 C_{1122}$$

$$C''_{2233}(0,\psi) = C_{1133}$$

$$C''_{2223}(0,\psi) = 0$$

$$C''_{2231}(0,\psi) = 0$$

$$C''_{2212}(0,\psi) = \left(\cos\psi\sin\psi\right)\left(\frac{1}{2}\left(\cos\psi\right)^2 - \left(\sin\psi\right)^2\right) C_{1111} + \left(\cos\psi\sin\psi\right)\left(\frac{3}{2}\left(\cos\psi\right)^2 - \left(\sin\psi\right)^2\right) C_{1122}$$

$$C''_{3333}(0,\psi) = C_{3333}$$

$$C''_{3323}(0,\psi) = 0$$

$$C''_{3331}(0,\psi) = 0$$

Expression of stiffness components for m-plane: $\theta = 90^\circ$ and $\psi = 0^\circ$:

$$C''_{1111}(90,0) = C_{3333} \qquad C''_{3333}(90,0) = C_{1111}$$

$$C''_{1122}(90,0) = C_{1133} \qquad C''_{3323}(90,0) = 0$$

$$C''_{1133}(90,0) = C_{1133} \qquad C''_{3331}(90,0) = 0$$

$$C''_{1123}(90,0) = 0 \qquad C''_{3312}(90,0) = 0$$

$$C''_{1131}(90,0) = 0 \qquad C''_{2323}(90,0) = 0$$

$$C''_{1112}(90,0) = 0 \qquad C''_{2331}(90,0) = 0$$

$$C''_{2222}(90,0) = C_{1111} \qquad C''_{2312}(90,0) = 0$$

$$C''_{2233}(90,0) = C_{1122} \qquad C''_{3131}(90,0) = C_{1111}$$

$$C''_{2223}(90,0) = 0 \qquad C''_{3112}(90,0) = 0$$

$$C''_{2231}(90,0) = 0 \qquad C''_{1212}(90,0) = 0$$

$$C''_{2212}(90,0) = 0$$

Expression of stiffness components for a-plane: $\theta = 90^\circ$ and $\psi = 30^\circ$:

$$C''_{1111}(90,30) = C_{3333}$$

$$C''_{1122}(90,30) = C_{1133}$$

$$C''_{1133}(90,30) = 0$$

$$C''_{1123}(90,30) = -\frac{1}{2}C_{1133}$$

$$C''_{1131}(90,30) = 0$$

$$C''_{1112}(90,30) = 0$$

$$C''_{2222}(90,30) = C_{1111} + \frac{9}{64}C_{1122}$$

$$C''_{2233}(90,30) = \frac{1}{4}C_{1111} + \frac{3}{4}C_{1122}$$

$$C''_{2223}(90,30) = -\frac{1}{8}C_{1111} - \frac{3}{8}C_{1122}$$

$$C''_{2231}(90,30) = 0$$

$$C''_{2212}(90,30) = 0$$

$$C''_{3333}(90,30) = C_{1111}$$

$$C''_{3323}(90,30) = -\frac{1}{2}C_{1111}$$

$$C''_{3331}(90,30) = 0$$

$$C''_{3312}(90,30) = 0$$

$$C''_{2323}(90,30) = \frac{1}{4}C_{1111}$$

$$C''_{2331}(90,30) = 0$$

$$C''_{2312}(90,30) = 0$$

$$C''_{3112}(90,30) = 0$$

$$C''_{1212}(90,30) = \frac{1}{4}C_{2323}$$

List of publications

- N. Le Biavan, M. Hugues, M. Montes Bajo, J. Tamayo-Arriola, A. Jollivet, D. Lefebvre, Y. Cordier, B. Vinter, F. H. Julien, A. Hierro and J.-M. Chauveau, "Homoepitaxy of non-polar ZnO/(Zn,Mg)O multi-quantum wells: From a precise growth control to the observation of intersubband transitions", Applied Physics Letters **111**, 231903 (2017)

- A. Hierro, M. Montes Bajo, J. Tamayo-Arriola, M. Hugues, J. M. Ulloa, N. Le Biavan, R. Peretti, F. H. Julien, J. Faist and J.-M. Chauveau, "Intersubband transitions and many body effects in ZnMgO/ZnO quantum wells", Proceedings SPIE **10533**, Oxide-based Materials and Devices IX, 105331K (2018)

- J. Tamayo-Arriola, M. Montes Bajo, N. Le Biavan, D. Lefebvre, A. Kurtz, J. M. Ulloa, M. Hugues, J.-M. Chauveau and A. Hierro, "Ga-doping of nonpolar m-plane ZnMgO with high Mg contents", Journal of Alloys and Compounds **766**, 436 (2018)

- M. Montes Bajo, J. Tamayo-Arriola, M. Hugues, J. M. Ulloa, N. Le Biavan, R. Peretti, F. H. Julien, J. Faist, J.-M. Chauveau and A. Hierro, "Multisubband plasmons in doped ZnO quantum wells", Physical Review Applied **10**, 024005 (2018)

- M. Montes Bajo, J. Tamayo-Arriola, N. Le Biavan, J. M. Ulloa, P. Vennéguès, D. Lefebvre, M. Hugues, J.-M. Chauveau and A. Hierro, "Breaking the intersubband selection rules for absorption with ZnO quantum wells: light polarization sensitivity under normal incidence", Physical Review Applied **10**, 034022 (2018)

- A. Jollivet, B. Hinkov, S. Pirotta, H. Hoang, S. Derelle, J. Jaeck, M. Tchernycheva, R. Colombelli, A. Bousseksou, M. Hugues, N. Le Biavan, J. Tamayo-Arriola, M. Montes Bajo, L. Rigutti, A. Hierro, G. Strasser, J.-M. Chauveau and F. H. Julien, "Short infrared wavelength quantum cascade detectors based on m-plane ZnO/ZnMgO quantum wells", Applied Physics Letters **113**, 251104 (2018)

- M. Montes Bajo, J. Tamayo-Arriola, N. Le Biavan, J. M. Ulloa, P. Vennéguès, D. Lefebvre, M. Hugues, J.-M. Chauveau and A. Hierro, "Intersubband absorption at normal incidence by m-plane ZnO/MgZnO quantum wells", Proceedings SPIE **10919**, Oxide-based Materials and Devices X, 109192C (2019)

- A. Jollivet, F. H. Julien, B. Hinkov, S. Pirotta, S. Derelle, J. Jaeck, M. Tchernycheva, R. Colombelli, A. Bousseksou, M. Hugues, N. Le Biavan, J. Tamayo-Arriola, M. Montes Bajo, G.

Strasser, J.-M. Chauveau and A. Hierro, "Short infrared wavelength quantum cascade detectors based on non-polar ZnO/ZnMgO quantum wells", Proceedings SPIE **10919**, Oxide-based Materials and Devices X, 1091919 (2019)

- A. Hierro, M. Montes Bajo, M. Ferraro, J. Tamayo-Arriola, N. Le Biavan, M. Hugues, J. M. Ulloa, M. Giudici, J.-M. Chauveau and P. Genevet, "Optical phase transition in semiconductor quantum metamaterials", Physical Review Letters **123**, 117401 (2019)

- B. Meng, J. Tamayo-Arriola, N. Le Biavan, M. Montes Bajo, Almudena Torres-Pardo, M. Hugues, A. Hierro, J.-M. Chauveau and J. Faist, "Observation of intersubband absorption in ZnO coupled quantum wells", Physical Review Applied **12**, 054007 (2019)

- M. Montes Bajo, J. Tamayo-Arriola, N. Le Biavan, M. Hugues, J.-M. Chauveau and A. Hierro, "Using interface phonon polaritons for alloy determination in ZnO/MgZnO multiple quantum wells", *submitted to Physical Review Applied (2019)*

Participation to conferences & Vulgarisation events

- "Science Festival", CNRS-CRHEA, Valbonne, France 2017
- Local final of "Ma Thèse en 180 secondes", Nice, France 2018
- Pint Of Science, Nice, France 2018
- "Group Research on Nanodevices for Terahertz and Mid Infrared" (GDR NanoTeraMIR), Montpellier, France (2018) - oral presentation
- "Condensed Matter Days" (JMC), Montpellier, France 2018 - oral presentation
- International Workshop on Zinc Oxide and other oxide seminconductors, Warsaw, Poland 2018 - oral presentation
- French German University Workshop (UFA) "Semiconductor nanostructures with band gap modulation", Bochum, Germany 2018 - oral presentation
- "Science Festival", CNRS-CRHEA, Valbonne, France 2018
- "Science Village", Valbonne, France 2019
- 19th Conference on II-VI Compounds and Related Materials, Zhengzhou, China 2019 - oral presentation
- French German University Workshop (UFA) "Semiconductor nanostructures with band gap modulation", Valbonne, France 2019 - oral presentation

Bibliography

A. Ohtomo, M. Kawasaki, T. Koida, K. Masubuchi, & H. Koinuma. 1998. Mg x Zn 1x O as a II–VI widegap semiconductor alloy. *Appl. Phys. Lett.*, **72**, 2466.

Akasaka, S., Nakahara, K., Tsukazaki, A., Ohtomo, A., & Kawasaki, M. 2010. MgxZn1-xO Films with a Low Residual Donor Concentration (<1015 cm-3) Grown by Molecular Beam Epitaxy. *Appl. Phys. Express*, **3**(7), 071101.

Al-Suleiman, M., El-Shaer, A., Bakin, A., Wehmann, H.-H., & Waag, A. 2007. Optical investigations and exciton localization in high quality Zn1xMgxO–ZnO single quantum wells. *Appl. Phys. Lett.*, **91**(8), 081911.

Alavi, K., Petroff, P. M., Wagner, W. R., & Cho, A. Y. 1983. Substrate rotation-induced compositional oscillation in molecular beam epitaxy (MBE). *Journal of Vacuum Science & Technology B: Microelectronics Processing and Phenomena*, **1**(2), 146–148.

Allen, S. J., Tsui, D. C., & Vinter, B. 1976. On the absorption of infrared radiation by electrons in semiconductor inversion layers. *Solid State Communications*, **20**(4), 425–428.

Alves, H., Pfisterer, D., Zeuner, A., Riemann, T., Christen, J., Hofmann, D. M., & Meyer, B. K. 2003. Optical investigations on excitons bound to impurities and dislocations in ZnO. *Optical Materials*, **23**(1), 33–37.

Andronov, A. A., Gavrilenko, V. I., Grishin, O. F., Murzin, V. N., Nozdrin, Yu. N., Stoklitskii, S. A., Chebotarev, A. P., & Shastin, V. N. 1982. Observation of population inversion of holes in Ge in crossed E and H fields from the spontaneous far-infrared emission. *Soviet Physics Doklady*, **27**(Nov.), 932.

Andronov, A. A., Valov, V. A., Kozlov, V. A., Nozdrin, Iu. N., & Pavlov, S. A. 1985. Tunable far-infrared laser using germanium hot holes. *Technical Physics Letters*, **11**(Aug.), 1000–1004.

Arguello, C. A., Rousseau, D. L., & Porto, S. P. S. 1969. First-Order Raman Effect in Wurtzite-Type Crystals. *Phys. Rev.*, **181**(3), 1351–1363.

Arthur, J. R. 2002. Molecular beam epitaxy. *Surface Science*, **500**, 189–217.

Asahara, H., Takamizu, D., Inokuchi, A., Hirayama, M., Teramoto, Akinobu, Saito, S., Takahashi, M., & Ohmi, T. 2010. Characterization of MgZnO films grown by plasma enhanced metal-organic chemical vapor deposition. *Thin Solid Films*, **518**(11), 2953–2956.

Ashkenov, N., Mbenkum, B. N., Bundesmann, C., Riede, V., Lorenz, M., Spemann, D., Kaidashev, E. M., Kasic, A., Schubert, M., Grundmann, M., Wagner, G., Neumann, H., Darakchieva, V., Arwin, H., & Monemar, B. 2002. Infrared dielectric functions and phonon modes of high-quality ZnO films. *Journal of Applied Physics*, **93**(1), 126–133.

Ashrafi, A. 2010. Exciton localization in inhomogeneously broadened ZnO/MgxZn1xO quantum wells. *Journal of Applied Physics*, **107**(12), 123527.

Ashrafi, A. B. M. A., Ueta, A., Avramescu, A., Kumano, H., Suemune, I., Ok, Y.-W., & Seong, T.-Y. 2000. Growth and characterization of hypothetical zinc-blende ZnO films on GaAs(001) substrates with ZnS buffer layers. *Appl. Phys. Lett.*, **76**(5), 550–552.

Azuhata, T., Matsunaga, T., Shimada, K., Yoshida, K., Sota, T., Suzuki, K., & Nakamura, S. 1996. Optical phonons in GaN. *Physica B: Condensed Matter*, **219-220**(Apr.), 493–495.

Barbieri, S., Alton, J., Beere, H. E., Fowler, J., Linfield, E. H., & Ritchie, D. A. 2004. 2.9THz quantum cascade lasers operating up to 70K in continuous wave. *Appl. Phys. Lett.*, **85**(10), 1674–1676.

Barker, A. S., & Ilegems, M. 1973. Infrared Lattice Vibrations and Free-Electron Dispersion in GaN. *Phys. Rev. B*, **7**(2), 743–750.

Bass, M., Franken, P. A., Ward, J. F., & Weinreich, G. 1962. Optical Rectification. *Phys. Rev. Lett.*, **9**(11), 446–448.

Bastard, Gerald. 1988. *Wave mechanics applied to semiconductor heterostructures*. Les Éditions de Physique.

Bateman, T. B. 1962. Elastic Moduli of Single-Crystal Zinc Oxide. *Journal of Applied Physics*, **33**(11), 3309–3312.

Baumbach, T., & Mikulik, P. 1999. X-ray Reflectivity by Rough Multilayers. *Pages 232–280 of:* Daillant, J., & Gibaud, A. (eds), *X-ray and Neutron Reflectivity: Principles and Applications*. Lecture Notes in Physics Monographs. Berlin, Heidelberg: Springer Berlin Heidelberg.

Béaur, L. 2011 (Dec.). *Propriétés excitoniques de puits quantiques ZnO/(Zn,Mg)O*. PhD Thesis, Université Montpellier 2.

Bayram, C., Vashaei, Z., & Razeghi, M. 2010a. Reliability in room-temperature negative differential resistance characteristics of low-aluminum content AlGaN/GaN double-barrier resonant tunneling diodes. *Appl. Phys. Lett.*, **97**(18), 181109.

Bayram, C., Vashaei, Z., & Razeghi, M. 2010b. Room temperature negative differential resistance characteristics of polar III-nitride resonant tunneling diodes. *Appl. Phys. Lett.*, **97**(9), 092104.

Beck, Mattias, Hofstetter, Daniel, Aellen, Thierry, Faist, Jérôme, Oesterle, Ursula, Ilegems, Marc, Gini, Emilio, & Melchior, Hans. 2002. Continuous Wave Operation of a Mid-Infrared Semiconductor Laser at Room Temperature. *Science*, **295**(5553), 301–305.

Beeler, M., Bougerol, C., Bellet-Amalric, E., & Monroy, E. 2014. Pseudo-square AlGaN/GaN quantum wells for terahertz absorption. *Appl. Phys. Lett.*, **105**(13), 131106.

Belkin, M. A., Fan, Jonathan A., Hormoz, S., Capasso, F., Khanna, S. P., Lachab, M., Davies, A. G., & Linfield, E. H. 2008. Terahertz quantum cascade lasers with copper metal-metal waveguides operating up to 178 K. *Opt. Express, OE*, **16**(5), 3242–3248.

Belkin, M.A., Qi Jie Wang, Pflugl, C., Belyanin, A., Khanna, S.P., Davies, A.G., Linfield, E.H., & Capasso, F. 2009. High-Temperature Operation of Terahertz Quantum Cascade Laser Sources. *IEEE Journal of Selected Topics in Quantum Electronics*, **15**(3), 952–967.

Bellotti, E., Driscoll, K., Moustakas, T. D., & Paiella, R. 2009. Monte Carlo simulation of terahertz quantum cascade laser structures based on wide-bandgap semiconductors. *Journal of Applied Physics*, **105**(11), 113103.

Belmoubarik, M., Ohtani, K., & Ohno, H. 2008. Intersubband transitions in ZnO multiple quantum wells. *Applied Physics Letters*, **92**(19), 191906.

Benveniste, E., Vasanelli, A., Delteil, A., Devenson, J., Teissier, R., Baranov, A., Andrews, A. M., Strasser, G., Sagnes, I., & Sirtori, C. 2008. Influence of the material parameters on quantum cascade devices. *Appl. Phys. Lett.*, **93**(13), 131108.

Berreman, D. W. 1963. Infrared Absorption at Longitudinal Optic Frequency in Cubic Crystal Films. *Phys. Rev.*, **130**(6), 2193–2198.

Bigenwald, P., Gil, B., Benharrats, F., Zitouni, K., & Kadri, A. 2012. The calculation of semipolar orientations for wurtzitic semiconductor heterostructures: application to nitrides and oxides. *Semicond. Sci. Technol.*, **27**(2), 024009.

Birman, J. L. 1959. Polarization of Fluorescence in CdS and ZnS Single Crystals. *Phys. Rev. Lett.*, **2**(4), 157–159.

Björck, M., & Andersson, G. 2007. *GenX* : an extensible X-ray reflectivity refinement program utilizing differential evolution. *Journal of Applied Crystallography*, **40**(6), 1174–1178.

Boemare, C., Monteiro, T., Soares, M. J., Guilherme, J. G., & Alves, E. 2001. Photoluminescence studies in ZnO samples. *Physica B: Condensed Matter*, **308-310**(Dec.), 985–988.

Borak, A. 2005. Toward Bridging the Terahertz Gap with Silicon-Based Lasers. *Science*, **308**(5722), 638–639.

Bosco, L., Franckié, M., Scalari, G., Beck, M., Wacker, A., & Faist, J. 2019. Thermoelectrically cooled THz quantum cascade laser operating up to 210K. *Appl. Phys. Lett.*, **115**(1), 010601.

Bründermann, E., Hübers, H.-W., & Kimmitt, M. F. 2012. *Terahertz Techniques*. Springer Series in Optical Sciences. Berlin Heidelberg: Springer-Verlag.

Brochen, S., Lafossas, M., Robin, I.-C., Ferret, P., Gemain, F., Pernot, J., & Feuillet, G. 2014. Residual and intentional n-type doping of ZnO thin films grown by metal-organic vapor phase epitaxy on sapphire and ZnO substrates. *Journal of Applied Physics*, **115**(11), 113508.

Brochen, S., Feuillet, G., Santailler, J.-L., Obrecht, R., Lafossas, Matthieu, Ferret, P., Chauveau, J.-M., & Pernot, J. 2017. Non-metal to metal transition in n-type ZnO single crystal materials. *Journal of Applied Physics*, **121**(9), 095704.

Bundesmann, C., Rahm, A., Lorenz, M., Grundmann, M., & Schubert, M. 2006. Infrared optical properties of MgxZn1xO thin films (0x1): Long-wavelength optical phonons and dielectric constants. *Journal of Applied Physics*, **99**(11), 113504.

Busby, Y., De Seta, M., Capellini, G., Evangelisti, F., Ortolani, M., Virgilio, M., Grosso, G., Pizzi, G., Calvani, P., Lupi, S., Nardone, M., Nicotra, G., & Spinella, C. 2010. Near- and far-infrared absorption and electronic structure of Ge-SiGe multiple quantum wells. *Phys. Rev. B*, **82**(20), 205317.

Campman, K. L., Schmidt, H., Imamoglu, A., & Gossard, A. C. 1996. Interface roughness and alloy-disorder scattering contributions to intersubband transition linewidths. *Appl. Phys. Lett.*, **69**(17), 2554–2556.

Capasso, F., Mohammed, K., & Cho, A. 1986. Resonant tunneling through double barriers, perpendicular quantum transport phenomena in superlattices, and their device applications. *IEEE Journal of Quantum Electronics*, **22**(9), 1853–1869.

Chauveau, J.-M., Vennéguès, P., Laügt, M., Deparis, C., Zuniga-Perez, J., & Morhain, C. 2008. Interface structure and anisotropic strain relaxation of nonpolar wurtzite (11-2^{-}0) and (10-10) orientations: ZnO epilayers grown on sapphire. *Journal of Applied Physics*, **104**(7), 073535.

Chauveau, J. M., Morhain, C., Teisseire, M., Laügt, M., Deparis, C., Zuniga-Perez, J., & Vinter, B. 2009. (Zn, Mg)O/ZnO-based heterostructures grown by molecular beam epitaxy on sapphire: Polar vs. non-polar. *Microelectronics Journal*, **40**(3), 512–516.

Chauveau, J.-M., Teisseire, M., Kim-Chauveau, H., Deparis, C., Morhain, C., & Vinter, B. 2010. Benefits of homoepitaxy on the properties of nonpolar (Zn,Mg)O/ZnO quantum wells on a-plane ZnO substrates. *Applied Physics Letters*, **97**(8), 081903.

Chauveau, J.-M., Xia, Y., Ben Taazaet-Belgacem, I., Teisseire, M., Roland, B., Nemoz, M., Brault, J., Damilano, B., Leroux, M., & Vinter, B. 2013. Built-in electric field in ZnO based semipolar quantum wells grown on (101^{-}2) ZnO substrates. *Appl. Phys. Lett.*, **103**(26), 262104.

Chen, C., Dutta, M., & Stroscio, M. A. 2004. Electron scattering via interactions with optical phonons in wurtzite crystals. *Phys. Rev. B*, **70**(7), 075316.

Chen, M., Zhu, Y., Su, L., Zhang, Q., Chen, Anqi, Ji, X., Xiang, R., Gui, X., Wu, T., Pan, B., & Tang, Z. 2013. Formation behavior of BexZn1xO alloys grown by plasma-assisted molecular beam epitaxy. *Appl. Phys. Lett.*, **102**(20), 202103.

Chiu, Y., Dikmelik, Y., Liu, P. Q., Aung, N. L., Khurgin, J. B., & Gmachl, C. F. 2012. Importance of interface roughness induced intersubband scattering in mid-infrared quantum cascade lasers. *Appl. Phys. Lett.*, **101**(17), 171117.

Colombo, D., Grilli, E., Guzzi, M., Sanguinetti, S., Marchionna, S., Bonfanti, M., Fedorov, A., von Känel, H., Isella, G., & Müller, E. 2007. Analysis of strain relaxation by microcracks in epitaxial GaAs grown on GeSi substrates. *Journal of Applied Physics*, **101**(10), 103519.

Curie, P. 1894. Sur la symétrie dans les phénomènes physiques, symétrie d'un champ électrique et d'un champ magnétique. *J. Phys. Theor. Appl.*, **3**(1), 393–415.

Damen, T. C., Porto, S. P. S., & Tell, B. 1966. Raman Effect in Zinc Oxide. *Phys. Rev.*, **142**(2), 570–574.

De Seta, M., Capellini, G., Busby, Y., Evangelisti, F., Ortolani, M., Virgilio, M., Grosso, G., Pizzi, G., Nucara, A., & Lupi, S. 2009. Conduction band intersubband transitions in Ge/SiGe quantum wells. *Appl. Phys. Lett.*, **95**(5), 051918.

Delteil, A., Vasanelli, A., Todorov, Y., Feuillet Palma, C., Renaudat St-Jean, M., Beaudoin, G., Sagnes, I., & Sirtori, C. 2012. Charge-Induced Coherence between Intersubband Plasmons in a Quantum Structure. *Physical Review Letters*, **109**(24), 246808.

Di Russo, E., Mancini, L., Moyon, F., Moldovan, S., Houard, J., Julien, F. H., Tchernycheva, M., Chauveau, J. M., Hugues, M., Da Costa, G., Blum, I., Lefebvre, W., Blavette, D., & Rigutti, L. 2017. Three-dimensional atomic-scale investigation of ZnO-MgxZn1xO m-plane heterostructures. *Appl. Phys. Lett.*, **111**(3), 032108.

Diehl, L., Bour, D., Corzine, S., Zhu, J., Höfler, G., Lončar, M., Troccoli, M., & Capasso, Federico. 2006. High-power quantum cascade lasers grown by low-pressure metal organic vapor-phase epitaxy operating in continuous wave above 400K. *Appl. Phys. Lett.*, **88**(20), 201115.

Dong, C. L., Persson, C., Vayssieres, L., Augustsson, A., Schmitt, T., Mattesini, M., Ahuja, R., Chang, C. L., & Guo, J.-H. 2004. Electronic structure of nanostructured ZnO from x-ray absorption and emission spectroscopy and the local density approximation. *Phys. Rev. B*, **70**(19), 195325.

Drouin, D., Hovington, P., & Gauvin, R. 1997. CASINO: A new monte carlo code in C language for electron beam interactions—part II: Tabulated values of the mott cross section. *Scanning*, **19**(1), 20–28.

Du, J., Hellicar, A. D., Li, L., Hanham, S. M., Macfarlane, J. C., Leslie, K. E., Nikolic, N., Foley, C. P., & Greene, K. J. 2009. Terahertz imaging at 77 K. *Supercond. Sci. Technol.*, **22**(11), 114001.

El-Shaer, A., Bakin, A., Al-Suleiman, M., Ivanov, S., Che Mofor, A., & Waag, A. 2007. Growth of wide band gap wurtzite ZnMgO layers on (0001) Al2O3 by radical-source molecular beam epitaxy. *Superlattices and Microstructures*, **42**(1), 129–133.

Encomendero, Jimy, Yan, Rusen, Verma, Amit, Islam, S. M., Protasenko, Vladimir, Rouvimov, Sergei, Fay, Patrick, Jena, Debdeep, & Xing, Huili Grace. 2018. Room temperature microwave oscillations in GaN/AlN resonant tunneling diodes with peak current densities up to 220 kA/cm2. *Appl. Phys. Lett.*, **112**(10), 103101.

Esaki, L., & Tsu, R. 1970. Superlattice and Negative Differential Conductivity in Semiconductors. *IBM Journal of Research and Development*, **14**(1), 61–65.

Evans, A., Yu, J. S., Slivken, S., & Razeghi, M. 2004. Continuous-wave operation of 4.8m quantum-cascade lasersat room temperature. *Appl. Phys. Lett.*, **85**(12), 2166–2168.

Faist, J., Capasso, F., Sivco, D. L., Sirtori, C., Hutchinson, A. L., & Cho, A. Y. 1994. Quantum Cascade Laser. *Science*, **264**(5158), 553–556.

Faist, J., Capasso, F., Sirtori, C., Sivco, D. L., Baillargeon, James N., Hutchinson, A. L., Chu, S.-N. G., & Cho, A. Y. 1996. High power mid-infrared (5 m) quantum cascade lasers operating above room temperature. *Appl. Phys. Lett.*, **68**(26), 3680–3682.

Faist, J., Hofstetter, D., Beck, M., Aellen, T., Rochat, M., & Blaser, S. 2002. Bound-to-continuum and two-phonon resonance, quantum-cascade lasers for high duty cycle, high-temperature operation. *IEEE Journal of Quantum Electronics*, **38**(6), 533–546.

Fathololoumi, S., Dupont, E., Chan, C. W. I., Wasilewski, Z. R., Laframboise, S. R., Ban, D., Mátyás, A., Jirauschek, C., Hu, Q., & Liu, H. C. 2012. Terahertz quantum cascade lasers operating up to 200 K with optimized oscillator strength and improved injection tunneling. *Opt. Express, OE*, **20**(4), 3866–3876.

Federici, J. F., Schulkin, B., Huang, F., Gary, D., Barat, R., Oliveira, F., & Zimdars, D. 2005. THz imaging and sensing for security applications—explosives, weapons and drugs. *Semicond. Sci. Technol.*, **20**(7), S266–S280.

Ferguson, B., & Zhang, X.-C. 2002. Materials for terahertz science and technology. *Nature Materials*, **1**(1), 26.

Fitzgerald, E. A. 1991. Dislocations in strained-layer epitaxy: theory, experiment, and applications. *Materials Science Reports*, **7**(3), 87–142.

Flores, Y. V., & Albo, A. 2017. Impact of Interface Roughness Scattering on the Performance of GaAs/AlxGa1–xAs Terahertz Quantum Cascade Lasers. *IEEE Journal of Quantum Electronics*, **53**(3), 1–8.

Franckié, M., Bosco, L., Beck, M., Bonzon, C., Mavrona, E., Scalari, G., Wacker, A., & Faist, J. 2018. Two-well quantum cascade laser optimization by non-equilibrium Green's function modelling. *Appl. Phys. Lett.*, **112**(2), 021104.

Gendron, L., Carras, M., Huynh, A., Ortiz, V., Koeniguer, C., & Berger, V. 2004. Quantum cascade photodetector. *Appl. Phys. Lett.*, **85**(14), 2824–2826.

Gerward, L., & Olsen, J. S. 1995. The High-Pressure Phase of Zincite. *J Synchrotron Rad*, **2**(5), 233–235.

Gibaud, A. 1999. Specular Reflectivity from Smooth and Rough Surfaces. *Pages 87–120 of:* Daillant, J., & Gibaud, A. (eds), *X-ray and Neutron Reflectivity: Principles and Applications*. Lecture Notes in Physics Monographs. Berlin, Heidelberg: Springer Berlin Heidelberg.

Giorgetta, F. R., Baumann, E., Hofstetter, D., Manz, C., Yang, Q., Köhler, K., & Graf, M. 2007. InGaAsAlAsSb quantum cascade detectors operating in the near infrared. *Appl. Phys. Lett.*, **91**(11), 111115.

Gomez, A., Péré-Laperne, N., de Vaulchier, L.-A., Koeniguer, C., Vasanelli, Angela, Nedelcu, A., Marcadet, X., Guldner, Y., & Berger, V. 2008. Dark current analysis of quantum cascade detectors by magnetoresistance measurements. *Phys. Rev. B*, **77**(8), 085307.

Graf, M., Scalari, G., Hofstetter, D., Faist, J., Beere, Harvey, Linfield, E., Ritchie, D., & Davies, G. 2004. Terahertz range quantum well infrared photodetector. *Appl. Phys. Lett.*, **84**(4), 475–477.

Grange, T., Stark, D., Scalari, G., Faist, J., Persichetti, L., Di Gaspare, L., De Seta, M., Ortolani, M., Paul, D. J., Capellini, G., Birner, S., & Virgilio, M. 2018. Room temperature operation of n-type Ge/SiGe terahertz quantum cascade lasers predicted by non-equilibrium Green's functions. *arXiv:1811.12879 [cond-mat]*, Nov.

Grundmann, M., & Zúñiga-Pérez, J. 2016. Pseudomorphic ZnO-based heterostructures: From polar through all semipolar to nonpolar orientations. *Physica status solidi (b)*, **253**(2), 351–360.

Han, P. Y., Cho, G. C., & Zhang, X.-C. 2000. Time-domain transillumination of biological tissues with terahertz pulses. *Opt. Lett., OL*, **25**(4), 242–244.

Helm, M. 1999. Chapter 1 The Basic Physics of Intersubband Transitions. *Pages 1–99 of:* Liu, H. C., & Capasso, F. (eds), *Semiconductors and Semimetals*, vol. 62. Elsevier.

Hofstetter, D., Giorgetta, F. R., Baumann, E., Yang, Q., Manz, C., & Köhler, K. 2010. Mid-infrared quantum cascade detectors for applications in spectroscopy and pyrometry. *Appl. Phys. B*, **100**(2), 313–320.

Hull, D., & Bacon, D. J. 2011. *Introduction to Dislocations*. 5 edition edn. Amsterdam: Butterworth-Heinemann.

Hutchinson, J. W., & Suo, Z. 1992. Mixed mode cracking in layered materials. *Advances in Applied Mechanics*, **29**, 63–191.

Im, J. S., Kollmer, H., Off, J., Sohmer, A., Scholz, F., & Hangleiter, A. 1997. Effects of Piezoelectric Fields in GaInN/GaN and GaN/AlGaN Heterostructures and Quantum Wells. *MRS Online Proceedings Library Archive*, **482**.

Jaffe, J. E., & Hess, A. C. 1993. Hartree-Fock study of phase changes in ZnO at high pressure. *Phys. Rev. B*, **48**(11), 7903–7909.

Jagadish, C., & Pearton, S. J. 2011. *Zinc Oxide Bulk, Thin Films and Nanostructures: Processing, Properties, and Applications*. Elsevier.

Jollivet, A., Hinkov, B., Pirotta, S., Hoang, H., Derelle, S., Jaeck, J., Tchernycheva, M., Colombelli, R., Bousseksou, A., Hugues, M., Le Biavan, N., Tamayo-Arriola, J., Montes Bajo, M., Rigutti, L., Hierro, A., Strasser, G., Chauveau, J.-M., & Julien, F. H. 2018. Short infrared wavelength quantum cascade detectors based on m-plane ZnO/ZnMgO quantum wells. *Appl. Phys. Lett.*, **113**(25), 251104.

Kawase, K., Ogawa, Y., Watanabe, Y., & Inoue, H. 2003. Non-destructive terahertz imaging of illicit drugs using spectral fingerprints. *Opt. Express, OE*, **11**(20), 2549–2554.

Kazarinov, R. F., & Suris, R. A. 1971. Possibility of the amplification of electromagnetic waves in a semiconductor with a superlattice. **5**(4), 707–709.

Köhler, R., Tredicucci, A., Beltram, F., Beere, H. E., Linfield, E. H., Davies, A. G., Ritchie, D. A., Iotti, R. C., & Rossi, F. 2002. Terahertz semiconductor-heterostructure laser. *Nature*, **417**(6885), 156.

Kim, M., Canedy, C. L., Bewley, W. W., Kim, C. S., Lindle, J. R., Abell, J., Vurgaftman, I., & Meyer, J. R. 2008. Interband cascade laser emitting at =3.75m in continuous wave above room temperature. *Appl. Phys. Lett.*, **92**(19), 191110.

Kim, S.-K., Jeong, S.-Y., & Cho, C.-R. 2003. Structural reconstruction of hexagonal to cubic ZnO films on Pt/Ti/SiO2/Si substrate by annealing. *Appl. Phys. Lett.*, **82**(4), 562–564.

Kim, W. J., Leem, J. H., Han, M. S., Park, I.-W., Ryu, Y. R., & Lee, T. S. 2006. Crystalline properties of wide band gap BeZnO films. *Journal of Applied Physics*, **99**(9), 096104.

Kisi, E. H., & Elcombe, M. M. 1989. u parameters for the wurtzite structure of ZnS and ZnO using powder neutron diffraction. *Acta Cryst C*, **45**(12), 1867–1870.

Ko, H.-J., Han, M.-S., Park, Y.-S., Yu, Y.-S., Kim, B.-I., Kim, S. S., & Kim, J.-H. 2004. Improvement of the quality of ZnO substrates by annealing. *Journal of Crystal Growth*, **269**(2–4), 493–498.

Kobayashi, M., Song, G. S., Kataoka, T., Sakamoto, Y., Fujimori, A., Ohkochi, T., Takeda, Y., Okane, T., Saitoh, Y., Yamagami, H., Yamahara, H., Saeki, H., Kawai, T., & Tabata, H. 2009. Experimental observation of bulk band dispersions in the oxide semiconductor ZnO using soft x-ray angle-resolved photoemission spectroscopy. *Journal of Applied Physics*, **105**(12), 122403.

Krishnamoorthy, S., Iliadis, A. A., Inumpudi, A., Choopun, S., Vispute, R. D., & Venkatesan, T. 2002. Observation of resonant tunneling action in ZnO/Zn0.8Mg0.2O devices. *Solid-State Electronics*, **46**(10), 1633–1637.

Kubis, T., Yeh, C., & Vogl, P. 2008. Quantum theory of transport and optical gain in quantum cascade lasers. *physica status solidi c*, **5**(1), 232–235.

Kumar, S., Hu, Q., & Reno, J. L. 2009. 186 K operation of terahertz quantum-cascade lasers based on a diagonal design. *Appl. Phys. Lett.*, **94**(13), 131105.

Kumar, S., Chan, C. W. I., Hu, Q., & Reno, J. L. 2011. A 1.8-THz quantum cascade laser operating significantly above the temperature of /kB. *Nat Phys*, **7**(2), 166–171.

Lambrecht, W. R. L., Rodina, A. V., Limpijumnong, S., Segall, B., & Meyer, B. K. 2002. Valence-band ordering and magneto-optic exciton fine structure in ZnO. *Phys. Rev. B*, **65**(7), 075207.

Laumer, B., Schuster, F., Stutzmann, M., Bergmaier, A., Dollinger, G., & Eickhoff, M. 2013. Accurate determination of optical bandgap and lattice parameters of Zn $_{1-\ x}$ Mg $_{\ x}$ O epitaxial films (0x0.3) grown by plasma-assisted molecular beam epitaxy on *a* -plane sapphire. *Journal of Applied Physics*, **113**(23), 233512.

Lautenschlaeger, S., Eisermann, Sebastian, Hofmann, M. N., Roemer, U., Pinnisch, M., Laufer, A., Meyer, B. K., Von Wenckstern, H., Lajn, A., Schmidt, F., Grundmann, M., Blaesing, J., & Krost, A. 2010. Morphological, structural and electrical investigations on non-polar a-plane ZnO epilayers. *Journal of Crystal Growth*, **312**(14), 2078–2082.

Le Biavan, N., Hugues, M., Montes Bajo, M., Tamayo-Arriola, J., Jollivet, A., Lefebvre, D., Cordier, Y., Vinter, B., Julien, F.-H., Hierro, A., & Chauveau, J.-M. 2017. Homoepitaxy of non-polar ZnO/(Zn,Mg)O multi-quantum wells: From a precise growth control to the observation of intersubband transitions. *Appl. Phys. Lett.*, **111**(23), 231903.

Leavitt, R. P., & Little, J. W. 1990. Simple method for calculating exciton binding energies in quantum-confined semiconductor structures. *Phys. Rev. B*, **42**(18), 11774–11783.

Lee, M., & Wanke, M. C. 2007. Searching for a Solid-State Terahertz Technology. *Science*, **316**(5821), 64–65.

Lee, Y.-S. 2009. *Principles of Terahertz Science and Technology*. Springer US.

Lelarge, F., Constantin, C., Leifer, K., Condo, A., Iakovlev, V., Martinet, E., Rudra, A., & Kapon, E. 1999. Effect of indium segregation on optical properties of V-groove InGaAs/GaAs strained quantum wires. *Appl. Phys. Lett.*, **75**(21), 3300–3302.

Leroux, M., Grandjean, N., Laügt, M., Massies, J., Gil, B., Lefebvre, P., & Bigenwald, P. 1998. Quantum confined Stark effect due to built-in internal polarization fields in (Al,Ga)N/GaN quantum wells. *Phys. Rev. B*, **58**(20), R13371–R13374.

Leuliet, A., Vasanelli, A., Wade, A., Fedorov, G., Smirnov, D., Bastard, G., & Sirtori, C. 2006. Electron scattering spectroscopy by a high magnetic field in quantum cascade lasers. *Phys. Rev. B*, **73**(8), 085311.

Levine, B. F., Choi, K. K., Bethea, C. G., Walker, J., & Malik, R. J. 1987. New 10 m infrared detector using intersubband absorption in resonant tunneling GaAlAs superlattices. *Appl. Phys. Lett.*, **50**(16), 1092–1094.

Levinshteĭn, M. E, Rumyantsev, Sergey L, & Shur, Michael. 2001. *Properties of advanced semiconductor materials: GaN, AlN, InN, BN, SiC, SiGe.* New York: Wiley. OCLC: 44174231.

Löffler, T., Bauer, T., Siebert, K. J., Roskos, H. G., Fitzgerald, A., & Czasch, S. 2001. Terahertz dark-field imaging of biomedical tissue. *Opt. Express, OE*, **9**(12), 616–621.

Li, L., Ye, H., Jiang, Y., Yang, R. Q., Keay, Joel C., Mishima, T. D., Santos, M. B., & Johnson, M. B. 2015. MBE-grown long-wavelength interband cascade lasers on InAs substrates. *Journal of Crystal Growth*, **425**(Sept.), 369–372.

Lim, C. B., Beeler, M., Ajay, A., Lähnemann, J., Bellet-Amalric, E., Bougerol, C., & Monroy, E. 2015. Intersubband transitions in nonpolar GaN/Al(Ga)N heterostructures in the short- and mid-wavelength infrared regions. *Journal of Applied Physics*, **118**(1), 014309.

Lockwood, D. J., Yu, Guolin, & Rowell, N. L. 2005. Optical phonon frequencies and damping in AlAs, GaP, GaAs, InP, InAs and InSb studied by oblique incidence infrared spectroscopy. *Solid State Communications*, **136**(7), 404–409.

Loudon, R. 1964. The Raman effect in crystals. *Advances in Physics*, **13**(52), 423–482.

Machhadani, H., Kotsar, Y., Sakr, S., Tchernycheva, M., Colombelli, R., Mangeney, J., Bellet-Amalric, E., Sarigiannidou, E., Monroy, E., & Julien, F. H. 2010. Terahertz intersubband absorption in GaN/AlGaN step quantum wells. *Applied Physics Letters*, **97**(19), 191101.

Machhadani, H., Tchernycheva, M., Sakr, S., Rigutti, L., Colombelli, R., Warde, E., Mietze, C., As, D. J., & Julien, F. H. 2011. Intersubband absorption of cubic GaN/Al(Ga)N quantum wells in the near-infrared to terahertz spectral range. *Phys. Rev. B*, **83**(7), 075313.

Maestrini, A., Ward, J., Chattopadhyay, G., Schlecht, E., & Mehdi, I. 2008. Terahertz Sources Based on Frequency Multiplication and Their Applications. *Frequenz*, **62**(5-6), 118–122.

Makino, T., Segawa, Y., Kawasaki, M., Ohtomo, A., Shiroki, R., Tamura, K., Yasuda, T., & Koinuma, H. 2001. Band gap engineering based on MgxZn1xO and CdyZn1yO ternary alloy films. *Appl. Phys. Lett.*, **78**(9), 1237–1239.

Mang, A., Reimann, K., & Rübenacke, St. 1995. Band gaps, crystal-field splitting, spin-orbit coupling, and exciton binding energies in ZnO under hydrostatic pressure. *Solid State Communications*, **94**(4), 251–254.

Matsui, H., & Tabata, H. 2005. Self-organized nanostripe arrays on ZnO (10-10) surfaces formed during laser molecular-beam-epitaxy growth. *Appl. Phys. Lett.*, **87**(14), 143109.

Matsui, H., & Tabata, H. 2006. Correlation of self-organized surface nanostructures and anisotropic electron transport in nonpolar ZnO (1010) homoepitaxy. *Journal of Applied Physics*, **99**(12), 124307.

Meng, Bo, Tamayo-Arriola, Julen, Le Biavan, Nolwenn, Montes Bajo, Miguel, Torres-Pardo, Almudena, Hugues, Maxime, Lefebvre, Denis, Hierro, Adrian, Chauveau, Jean-Michel, & Faist, Jérôme. 2019. Observation of Intersubband Absorption in $\mathrm{Zn}\mathrm{O}$ Coupled Quantum Wells. *Phys. Rev. Applied*, **12**(5), 054007.

Montes Bajo, M., Tamayo-Arriola, J., Le Biavan, N., Ulloa, J. M., Vennéguès, P., Lefebvre, D., Hugues, M., Chauveau, J.-M., & Hierro, A. 2018a. Breaking the Intersubband Selection Rules for Absorption with ZnO Quantum Wells: Light Polarization Sensitivity under Normal Incidence. *Phys. Rev. Applied*, **10**(3), 034022.

Montes Bajo, M., Tamayo-Arriola, J., Hugues, M., Ulloa, J. M., Le Biavan, N., Peretti, R., Julien, F. H., Faist, J., Chauveau, J.-M., & Hierro, A. 2018b. Multisubband Plasmons in Doped ZnO Quantum Wells. *Phys. Rev. Applied*, **10**(2), 024005.

Moram, M. A., & Vickers, M. E. 2009. X-ray diffraction of III-nitrides. *Rep. Prog. Phys.*, **72**(3), 036502.

Mourou, G., Stancampiano, C. V., Antonetti, A., & Orszag, A. 1981. Picosecond microwave pulses generated with a subpicosecond laser-driven semiconductor switch. *Appl. Phys. Lett.*, **39**(4), 295–296.

Narayan, J., & Larson, B. C. 2002. Domain epitaxy: A unified paradigm for thin film growth. *Journal of Applied Physics*, **93**(1), 278–285.

Narayan, J., Tiwari, P., Chen, X., Singh, J., Chowdhury, R., & Zheleva, T. 1992. Epitaxial growth of TiN films on (100) silicon substrates by laser physical vapor deposition. *Appl. Phys. Lett.*, **61**(11), 1290–1292.

Neumann, M. D., Esser, N., Chauveau, J.-M., Goldhahn, R., & Feneberg, M. 2016. Inversion of absorption anisotropy and bowing of crystal field splitting in wurtzite MgZnO. *Appl. Phys. Lett.*, **108**(22), 221105.

Nguyen-Van, H., Baranov, A. N., Loghmari, Z., Cerutti, L., Rodriguez, J.-B., Tournet, J., Narcy, G., Boissier, G., Patriarche, G., Bahriz, M., Tournié, E., & Teissier, R. 2018. Quantum cascade lasers grown on silicon. *Scientific Reports*, **8**(1), 7206.

Offermans, P., Koenraad, P. M., Wolter, J. H., Beck, M., Aellen, T., & Faist, J. 2003. Digital alloy interface grading of an InAlAs/InGaAs quantum cascade laser structure studied by cross-sectional scanning tunneling microscopy. *Appl. Phys. Lett.*, **83**(20), 4131–4133.

Ohtani, K., Belmoubarik, M., & Ohno, H. 2009. Intersubband optical transitions in ZnO-based quantum wells grown by plasma-assisted molecular beam epitaxy. *Journal of Crystal Growth*, **311**(7), 2176–2178.

Ohtani, Keita, Meng, Bo, Franckié, Martin, Bosco, Lorenzo, Ndebeka-Bandou, Camille, Beck, Mattias, & Faist, Jérôme. 2019. An electrically pumped phonon-polariton laser. *Science Advances*, **5**(7), eaau1632.

Orphal, L., Kalusniak, S., Benson, O., & Sadofev, S. 2017. Tunable intersubband transitions in ZnO/ZnMgO multiple quantum wells in the mid infrared spectral range. *AIP Advances*, **7**(11), 115309.

Ozgur, U., Hofstetter, D., & Morkoc, H. 2010. ZnO Devices and Applications: A Review of Current Status and Future Prospects. *Proceedings of the IEEE*, **98**(7), 1255–1268.

Page, H., Becker, C., Robertson, A., Glastre, G., Ortiz, V., & Sirtori, C. 2001. 300 K operation of a GaAs-based quantum-cascade laser at 9 m. *Appl. Phys. Lett.*, **78**(22), 3529–3531.

Paiella, R. 2006. *Intersubband Transitions In Quantum Structures*. Mc graw hill edn.

Park, W. I., Yi, Gyu-Chul, & Jang, H. M. 2001. Metalorganic vapor-phase epitaxial growth and photoluminescent properties of Zn1xMgxO(0x0.49) thin films. *Appl. Phys. Lett.*, **79**(13), 2022–2024.

Patimisco, P., Scamarcio, G., Santacroce, M. V., Spagnolo, V., Vitiello, M. S., Dupont, E., Laframboise, S. R., Fathololoumi, S., Razavipour, G. S., & Wasilewski, Z. 2013. Electronic temperatures of terahertz quantum cascade active regions with phonon scattering assisted injection and extraction scheme. *Opt. Express, OE*, **21**(8), 10172–10181.

Porterfield, D. W. 2007 (June). High-Efficiency Terahertz Frequency Triplers. *Pages 337–340 of: 2007 IEEE/MTT-S International Microwave Symposium*.

Preston, A. R. H., Ruck, B. J., Piper, L. F. J., DeMasi, A., Smith, K. E., Schleife, A., Fuchs, F., Bechstedt, F., Chai, J., & Durbin, S. M. 2008. Band structure of ZnO from resonant x-ray emission spectroscopy. *Phys. Rev. B*, **78**(15), 155114.

Redondo-Cubero, A., Hierro, A., Chauveau, J.-M., Lorenz, K., Tabares, G., Franco, N., Alves, E., & Muñoz, E. 2012. Single phase a-plane MgZnO epilayers for UV optoelectronics: substitutional behaviour of Mg at large contents. *Cryst. Eng. Comm.*, **14**(5), 1637–1640.

Reynolds, D. C., Look, D. C., Jogai, B., Litton, C. W., Collins, T. C., Harsch, W., & Cantwell, G. 1998. Neutral-donor–bound-exciton complexes in ZnO crystals. *Phys. Rev. B*, **57**(19), 12151–12155.

Reynolds, D. C., Look, D. C., Jogai, B., Litton, C. W., Cantwell, G., & Harsch, W. C. 1999. Valence-band ordering in ZnO. *Phys. Rev. B*, **60**(4), 2340–2344.

Roberts, J. S., Green, R. P., Wilson, L. R., Zibik, E. A., Revin, D. G., Cockburn, J. W., & Airey, R. J. 2003. Quantum cascade lasers grown by metalorganic vapor phase epitaxy. *Appl. Phys. Lett.*, **82**(24), 4221–4223.

Romanov, A. E., Young, E. C., Wu, F., Tyagi, A., Gallinat, C. S., Nakamura, S., DenBaars, S. P., & Speck, J. S. 2011. Basal plane misfit dislocations and stress relaxation in III-nitride semipolar heteroepitaxy. *Journal of Applied Physics*, **109**(10), 103522.

Rosencher, E., & Vinter, B. 2002. *Optoelectronics*. Sciences Sup. Cambridge University Press.

Ryu, Y. R., Lee, T. S., Lubguban, J. A., Corman, A. B., White, H. W., Leem, J. H., Han, M. S., Park, Y. S., Youn, C. J., & Kim, W. J. 2006. Wide-band gap oxide alloy: BeZnO. *Appl. Phys. Lett.*, **88**(5), 052103.

Sakr, S., Giraud, E., Dussaigne, A., Tchernycheva, M., Grandjean, N., & Julien, F. H. 2012. Two-color GaN/AlGaN quantum cascade detector at short infrared wavelengths of 1 and 1.7m. *Appl. Phys. Lett.*, **100**(18), 181103.

Scalari, G., Walther, C., Fischer, M., Terazzi, R., Beere, H., Ritchie, D., & Faist, J. 2009. THz and sub-THz quantum cascade lasers. *Laser & Photonics Reviews*, **3**(1-2), 45–66.

Schifano, R., Monakhov, E. V., Svensson, B. G., & Diplas, S. 2009. Surface passivation and interface reactions induced by hydrogen peroxide treatment of n-type ZnO (000-1). *Appl. Phys. Lett.*, **94**(13), 132101.

Schleife, A., Fuchs, F., Rödl, C., Furthmüller, J., & Bechstedt, F. 2009. Band-structure and optical-transition parameters of wurtzite MgO, ZnO, and CdO from quasiparticle calculations. *physica status solidi (b)*, **246**(9), 2150–2153.

Schröer, P., Krüger, P., & Pollmann, J. 1993. First-principles calculation of the electronic structure of the wurtzite semiconductors ZnO and ZnS. *Phys. Rev. B*, **47**(12), 6971–6980.

Schubert, M., Hofmann, T., & Šik, Jan. 2005. Long-wavelength interface modes in semiconductor layer structures. *Phys. Rev. B*, **71**(3), 035324.

Segnit, E. R., & Holland, A. E. 1965. The System MgO-ZnO-SiO2. *Journal of the American Ceramic Society*, **48**(8), 409–413.

Seta, M. D., Capellini, G., Ortolani, M., Virgilio, M., Grosso, G., Nicotra, G., & Zaumseil, P. 2012. Narrow intersubband transitions in n-type Ge/SiGe multi-quantum wells: control of the terahertz absorption energy trough the temperature dependent depolarization shift. *Nanotechnology*, **23**(46), 465708.

Shibata, H., Tampo, H., Matsubara, K., Yamada, A., Sakurai, K., Ishizuka, S., Niki, S., & Sakai, M. 2007. Photoluminescence characterization of Zn1xMgxO epitaxial thin films grown on ZnO by radical source molecular beam epitaxy. *Appl. Phys. Lett.*, **90**(12), 124104.

Siegel, P. H. 2002. Terahertz technology. *IEEE Transactions on Microwave Theory and Techniques*, **50**(3), 910–928.

Sirigu, L., Rudra, A., Kapon, E., Amanti, M. I., Scalari, G., & Faist, J. 2008. A terahertz quantum cascade laser grown by low-pressure metalorganic vapor phase epitaxy. *Appl. Phys. Lett.*, **92**(18), 181111.

Sirkeli, V. P., Yilmazoglu, O., Al-Daffaie, S., Preu, S., Kuppers, F., & Hartnagel, H. L. 2017. 1.33 THz room-temperature quantum cascade lasers based on ZnMgSe/ZnSe. *Pages 1–2 of: 2017 42nd International Conference on Infrared, Millimeter, and Terahertz Waves (IRMMW-THz)*. Cancun, Mexico: IEEE.

Sirtori, C., Faist, J., Capasso, F., Sivco, Deborah L., Hutchinson, A. L., Chu, S. N. G., & Cho, A. Y. 1996. Continuous wave operation of midinfrared (7.4–8.6 m) quantum cascade lasers up to 110 K temperature. *Appl. Phys. Lett.*, **68**(13), 1745–1747.

Sirtori, C., Kruck, P., Barbieri, S., Collot, P., Nagle, J., Beck, M., Faist, J., & Oesterle, U. 1998. GaAs/AlxGa1xAs quantum cascade lasers. *Appl. Phys. Lett.*, **73**(24), 3486–3488.

Sirtori, C., Page, H., Becker, C., & Ortiz, V. 2002. GaAs-AlGaAs quantum cascade lasers: physics, technology, and prospects. *IEEE Journal of Quantum Electronics*, **38**(6), 547–558.

Sobotta, H., Neumann, H., Franzheld, R., & Seifert, W. 1992. Infrared lattice vibrations of GaN. *physica status solidi (b)*, **174**(2), K57–K60.

Stachowicz, M., Pietrzyk, M. A., Sajkowski, J. M., Przezdziecka, E., Teisseyre, H., Witkowski, B., Alves, E., & Kozanecki, A. 2017. Asymmetric ZnO/ZnMgO double quantum well structures grown on m-plane ZnO substrates by MBE. *Journal of Luminescence*, **186**, 262–267.

Stroscio, M. A., Kisin, M., Belenky, G., & Luryi, S. 1999. Phonon enhanced inverse population in asymmetric double quantum wells. *Appl. Phys. Lett.*, **75**(21), 3258–3260.

Sun, G., Soref, R. A., & Khurgin, J. B. 2005. Active region design of a terahertz GaN/ Al0.15Ga0.85N quantum cascade laser. *Superlattices and Microstructures*, **37**(2), 107–113.

Sun, H. D., Makino, T., Segawa, Y., Kawasaki, M., Ohtomo, A., Tamura, K., & Koinuma, H. 2002. Enhancement of exciton binding energies in ZnO/ZnMgO multiquantum wells. *Journal of Applied Physics*, **91**(4), 1993–1997.

Suzuki, N., & Iizuka, N. 1999. Effect of Polarization Field on Intersubband Transition in AlGaN/GaN Quantum Wells. *Jpn. J. Appl. Phys.*, **38**(4A), L363.

Taboada, A. G., Kreiliger, T., Falub, C. V., Isa, F., Salvalaglio, M., Wewior, L., Fuster, D., Richter, M., Uccelli, E., Niedermann, P., Neels, A., Mancarella, F., Alén, B., Miglio, L., Dommann, A., Isella, G., & von Känel, H. 2014. Strain relaxation of GaAs/Ge crystals on patterned Si substrates. *Appl. Phys. Lett.*, **104**(2), 022112.

Taday, P. F. 2004. Applications of terahertz spectroscopy to pharmaceutical sciences. *Philosophical Transactions of the Royal Society of London. Series A: Mathematical, Physical and Engineering Sciences.*

Tanaka, M., & Sakaki, H. 1987. Atomistic models of interface structures of GaAs-AlxGa1xAs (x = 0.21) quantum wells grown by interrupted and uninterrupted MBE. *Journal of Crystal Growth*, **81**(1), 153–158.

Taïnoff, D., Al-Khalfioui, M., Deparis, C., Vinter, B., Teisseire, M., Morhain, C., & Chauveau, J.-M. 2011. Residual and nitrogen doping of homoepitaxial nonpolar m-plane ZnO films grown by molecular beam epitaxy. *Appl. Phys. Lett.*, **98**(13), 131915.

Teke, A., Özgür, Ü., Doğan, S., Gu, X., Morkoç, H., Nemeth, B., Nause, J., & Everitt, H. O. 2004. Excitonic fine structure and recombination dynamics in single-crystalline ZnO. *Phys. Rev. B*, **70**(19), 195207.

Terashima, W., & Hirayama, H. 2011. Spontaneous emission from GaN/AlGaN terahertz quantum cascade laser grown on GaN substrate. *physica status solidi c*, **8**(7-8), 2302–2304.

Terashima, W., & Hirayama, H. 2015. GaN-based terahertz quantum cascade lasers.

Thomas, D. G. 1960. The exciton spectrum of zinc oxide. *Journal of Physics and Chemistry of Solids*, **15**(1), 86–96.

Thonke, K., Gruber, Th., Teofilov, N., Schönfelder, R., Waag, A., & Sauer, R. 2001. Donor–acceptor pair transitions in ZnO substrate material. *Physica B: Condensed Matter*, **308-310**, 945–948.

Tonouchi, Masayoshi. 2007. Cutting-edge terahertz technology. *Nature Photonics*, **1**(2), 97–105.

Tredicucci, A., Capasso, F., Gmachl, C., Sivco, D. L., Hutchinson, A. L., & Cho, A. Y. 1998. High performance interminiband quantum cascade lasers with graded superlattices. *Appl. Phys. Lett.*, **73**(15), 2101–2103.

Tu, C. W., Miller, R. C., Wilson, B. A., Petroff, P. M., Harris, T. D., Kopf, R. F., Sputz, S. K., & Lamont, M. G. 1987. Properties of (Al,Ga)As/GaAs heterostructures grown by molecular beam epitaxy with growth interruption. *Journal of Crystal Growth*, **81**(1), 159–163.

Unterrainer, K., Colombelli, R., Gmachl, C., Capasso, F., Hwang, H. Y., Sergent, A. M., Sivco, D. L., & Cho, A. Y. 2002. Quantum cascade lasers with double metal-semiconductor waveguide resonators. *Applied Physics Letters*, **80**(17), 3060–3062.

Unuma, T., Takahashi, T., Noda, T., Yoshita, M., Sakaki, H., Baba, M., & Akiyama, H. 2001. Effects of interface roughness and phonon scattering on intersubband absorption linewidth in a GaAs quantum well. *Appl. Phys. Lett.*, **78**(22), 3448–3450.

Unuma, T., Yoshita, M., Noda, T., Sakaki, H., & Akiyama, H. 2003. Intersubband absorption linewidth in GaAs quantum wells due to scattering by interface roughness, phonons, alloy disorder, and impurities. *Journal of Applied Physics*, **93**(3), 1586–1597.

Verghese, S., McIntosh, K. A., & Brown, E. R. 1997. Highly tunable fiber-coupled photomixers with coherent terahertz output power. *IEEE Transactions on Microwave Theory and Techniques*, **45**(8), 1301–1309.

Vitiello, M. S., Scalari, G., Williams, B., & Natale, P. D. 2015. Quantum cascade lasers: 20 years of challenges. *Opt. Express, OE*, **23**(4), 5167–5182.

Wassner, T. A., Laumer, B., Maier, S., Laufer, A., Meyer, B. K., Stutzmann, M., & Eickhoff, M. 2009. Optical properties and structural characteristics of ZnMgO grown by plasma assisted molecular beam epitaxy. *Journal of Applied Physics*, **105**(2), 023505.

West, L. C., & Eglash, S. J. 1985. First observation of an extremely large-dipole infrared transition within the conduction band of a GaAs quantum well. *Appl. Phys. Lett.*, **46**(12), 1156–1158.

Williams, B. S. 2007. Terahertz quantum-cascade lasers. *Nature Photonics*, **1**(9), 517–525.

Williams, B. S., Kumar, S., Callebaut, H., Hu, Q., & Reno, J. L. 2003. Terahertz quantum-cascade laser at 100m using metal waveguide for mode confinement. *Appl. Phys. Lett.*, **83**(11), 2124–2126.

Williams, B. S., Kumar, S., Hu, Q., & Reno, J. L. 2005. Operation of terahertz quantum-cascade lasers at 164 K in pulsed mode and at 117 K in continuous-wave mode. *Opt. Express, OE*, **13**(9), 3331–3339.

Williams, G. P. 2002. FAR-IR/THz radiation from the Jefferson Laboratory, energy recovered linac, free electron laser. *Review of Scientific Instruments*, **73**(3), 1461–1463.

Wong, J. S., & Yen, Y.-S. 1988. Intriguing Absorption Band Behavior of IR Reflectance Spectra of Silicon Dioxide on Silicon. *Appl. Spectrosc., AS*, **42**(4), 598–604.

Worrall, C., Alton, J., Houghton, M., Barbieri, S., Beere, H. E., Ritchie, D., & Sirtori, C. 2006. Continuous wave operation of a superlattic quantum cascade laser emitting at 2 THz. *Opt. Express, OE*, **14**(1), 171–181.

Wu, F., Young, E. C., Koslow, I., Hardy, M. T., Hsu, P. S., Romanov, A. E., Nakamura, S., DenBaars, S. P., & Speck, J. S. 2011. Observation of non-basal slip in semipolar InxGa1-xN/GaN heterostructures. *Appl. Phys. Lett.*, **99**(25), 251909.

Yan, Q., Rinke, P., Winkelnkemper, M., Qteish, A., Bimberg, D., Scheffler, M., & Van de Walle, C. G. 2010. Band parameters and strain effects in ZnO and group-III nitrides. *Semicond. Sci. Technol.*, **26**(1), 014037.

Yang, R. Q. 1995. Infrared laser based on intersubband transitions in quantum wells. *Superlattices and Microstructures*, **17**(1), 77–83.

Yang, W. F., Wong, L. M., Wang, S. J., Sun, H. D., Ge, C. H., Lee, Alex Y. S., & Gong, H. 2011. Photoluminescence characteristics of ZnCdO/ZnO single quantum well grown by pulsed laser deposition. *Appl. Phys. Lett.*, **98**(12), 121903.

Yonenaga, I., Koizumi, H., Ohno, Y., & Taishi, T. 2008. High-temperature strength and dislocation mobility in the wide band-gap ZnO: Comparison with various semiconductors. *Journal of Applied Physics*, **103**(9), 093502.

Yu, N., & Capasso, F. 2010. Wavefront engineering for mid-infrared and terahertz quantum cascade lasers [Invited]. *J. Opt. Soc. Am. B, JOSAB*, **27**(11), B18–B35.

Özgür, Ü., Alivov, Ya. I., Liu, C., Teke, A., Reshchikov, M. A., Doğan, S., Avrutin, V., Cho, S.-J., & Morkoç, H. 2005. A comprehensive review of ZnO materials and devices. *Journal of Applied Physics*, **98**(4), 041301.

Zhang, H. H., Pan, X. H., He, H. P., Chen, W., Huang, J. Y., Ding, P., Lu, B., Ye, Z. Z., Lu, J. G., Chen, L. X., & Ye, C. L. 2014. Temperature dependence of exciton localization in ZnO/Zn1xMgxO multiple quantum wells with different barrier compositions. *Optics Communications*, **318**(May), 37–40.

Zhao, K., Chen, G., Li, B.-S., & Shen, A. 2014. Mid-infrared intersubband absorptions in ZnO/ZnMgO multiple quantum wells. *Applied Physics Letters*, **104**(21), 212104.